Nanosecond Repetitively Pulsed Plasmas in Preheated Air at Atmospheric Pressure

David Z Pai

CENTRALE PARIS

École Centrale Paris

THÈSE

présentée par

David PAI

pour l'obtention du

GRADE de DOCTEUR

Formation doctorale : ED 287 Sciences pour l'ingénieur, Energétique et Physique
Laboratoire d'accueil : Laboratoire EM2C, UPR 288 du CNRS situé à l'ECP

Etude des plasmas générés par impulsions électriques nanosecondes répétitives dans l'air préchauffé à pression atmosphérique

-

Nanosecond Repetitively Pulsed Plasmas in Preheated Air at Atmospheric Pressure

Soutenue le 31 janvier 2008

JURY :

Mme	Alix	Gicquel	Professeur à l'Univ. Paris 13
Mlle	Deanna	Lacoste	Ing. de Recherche CNRS, ECP
MM.	Christophe	Laux	Professeur à l'ECP
	Sergey	Macheret	Aeronautical Engineer, Lockheed Martin
Mme	Françoise	Massines	Dir. de Recherche CNRS, Lab. PROMES
MM.	Denis	Packan	Ing. de Recherche ONERA
	Antoine	Rousseau	Dir. de Recherche CNRS, Ecole Polytechnique

Ecole Centrale des Arts et Manufactures
Grand Etablissement sous tutelle
du Ministère de l'Education Nationale
Grande Voie des Vignes
92295 CHATENAY MALABRY
Cedex Tél. : 33 (1) 41 13 10 00
(standard)
Télex : 634 991 F EC PARIS

Laboratoire d'Energétique Moléculaire et Macroscopique, Combustion (E.M2.C.)
UPR 288, CNRS et École Centrale Paris
Tél. : 33 (1) 41 13 10 31
Télécopie : 33 (1) 47 02 80 35

2008 - 8

Résumé

Les plasmas d'air à pression atmosphérique ont des applications potentielles nombreuses dans le traitement biomédical et de surface, la décontamination chimique et biologique, le contrôle d'écoulement aérodynamique et la combustion. La plupart de ces applications nécessitent des plasmas à pression atmosphérique de grand volume, de faible coût énergétique et à des températures inférieures à 1000-2000 K. Les décharges Impulsionnelles Nanosecondes Répétitives (INR) sont particulièrement intéressantes car elles produisent des plasmas non-thermiques à des coûts énergétiques inférieurs de plusieurs ordres de grandeur à ceux des autres techniques. Cependant, à ce jour, les décharges INR n'ont pu être obtenues qu'à des températures élevées (2000 K). L'objectif de cette étude est d'étendre leur domaine de fonctionnement à plus basse température, inférieure à 1000 K.

Dans la première partie de ce mémoire, nous démontrons l'existence de trois régimes de fonctionnement de la décharge INR dans l'air à pression atmosphérique et à une température fixée de 1000 K. Nous en caractérisons les propriétés chimiques, électriques et thermiques par spectroscopie d'émission et par mesure courant-tension. Pour des conditions données, et par ordre d'apparition avec la tension, ces trois régimes ont un aspect de décharge couronne (C), diffuse (D) et filamentaire (F). Nous nous intéressons dans la suite aux régimes D et F car ils produisent l'activité chimique la plus importante. Nos mesures montrent que le régime D est caractérisé par de faibles niveaux d'émission lumineuse, de courant de conduction et de température, confirmant son caractère non-thermique. De plus, ce régime est créé par une onde d'ionisation initiale se propageant de l'anode vers la cathode, suivi d'une onde plus rapide dans la direction opposée. Pour caractériser l'activité chimique du régime D, nous avons mesuré la densité de plusieurs espèces chimiques excitées pendant et après les impulsions. Contrairement au régime D, le régime F est caractérisé par un rayonnement intense, un fort courant de conduction de l'ordre de la dizaine d'ampères et un échauffement significatif de l'air pouvant atteindre plusieurs milliers de Kelvins. En outre, les densités électroniques peuvent atteindre des niveaux élevés, de l'ordre de 10^{15} cm^{-3}.

Nous avons ensuite mené une étude paramétrique des effets de la température du gaz (300 à 1000 K), de la distance inter-électrodes (1 à 10 mm) et de la fréquence de répétition des impulsions (FRI) (1 à 30 kHz), sur les propriétés des régimes D et F, et sur la tension de transition D-F. Nous nous sommes attachés en particulier à déterminer les conditions requises pour étendre l'existence du régime D à tout le domaine 300-1000 K. La tension de transition entre les deux régimes augmente lorsque la température du gaz ou la FRI diminue. De plus, le régime D existe sur un domaine de tension plus étendu lorsque la FRI diminue. Dans les deux régimes, le délai entre l'impulsion haute tension et le claquage augmente quand la FRI diminue. La vitesse des ondes d'ionisation varie peu avec la FRI et la température du gaz. Enfin, nous avons déterminé que pour une température de gaz donnée, le régime D ne peut exister que pour une distance inter-électrodes minimale. Ceci nous a permis d'étendre le domaine d'existence de la décharge D jusqu'à la température ambiante.

Enfin, nous proposons une interprétation de la nature du régime D et des mécanismes de la transition D-F. L'ionisation est particulièrement forte dans la région proche des électrodes car le champ Laplacien y est très élevé en raison de la géométrie de pointes. Le régime D est initié dans la région anodique par un streamer dirigé vers la cathode, dont la tête se transforme en zone de chute cathodique, créant ainsi une décharge transitoire luminescente. Cependant, contrairement aux décharges luminescentes continues pour lesquelles une instabilité induisant le passage à l'arc peut se produire, le faible champ électrique réduit (E/N) présent dans la région inter-électrodes prévient la propagation de l'instabilité. La région inter-électrodes agit donc comme un élément résistif

limitant le courant. Cette propriété permet l'existence d'un régime D stable en évitant le passage au régime F.

En conclusion, nous avons démontré qu'il est possible de générer des plasmas d'air non-thermiques à pression atmosphérique entre 300 et 1000 K, en utilisant des décharges nanosecondes répétitives impulsionnelles. Leur domaine d'existence dépend de deux paramètres clés, la distance inter-électrodes et la fréquence de répétition des impulsions. L'étape importante suivante sera de continuer à quantifier la réactivité chimique de ces plasmas non-thermiques. Ceci impliquera la détermination des densités d'espèces actives, comme l'oxygène atomique, dans l'intervalle entre les impulsions. En raison de leur large domaine de fonctionnement en température, les plasmas d'air INR ont un fort potentiel pour les applications envisagées.

Abstract

Atmospheric pressure air plasmas have potential applications in biomedical and surface treatment, chemical and biological decontamination, aerodynamic flow control, and combustion. Many of these applications require large-volume low-power plasmas with high chemical reactivity at low gas temperature, i.e. non-thermal plasmas. One method to produce such plasmas, the Nanosecond Repetitively Pulsed (NRP) method, is particularly attractive because it can generate non-thermal plasmas for power budgets lower by several orders of magnitude than traditional plasma generation methods. To date, NRP plasmas in atmospheric pressure air have only been produced at the comparatively high temperature of 2000 K. This study seeks to enlarge the range of application of NRP plasmas to the 300 to 1000 K range of interest for the applications mentioned above.

In the first part of the thesis, we demonstrate the existence of three regimes of the NRP discharge in air at atmospheric pressure and at a fixed temperature of 1000 K, and then we characterize their chemical, electrical, and thermal properties through optical emission spectroscopy and current-voltage measurements. In order of increasing applied voltage for given conditions, the three regimes are corona-like (termed C), diffuse-like (D) and filamentary-like (F). We focus our study on the D and F regimes because they produce the highest levels of chemical activity. The measurements show that the D regime has low levels of emission, gas heating, and electrical conduction current, indicating that it is non-thermal. Furthermore, this regime develops through an initial ionization wave propagating from the anode to the cathode, followed by a faster return wave in the opposite direction. To characterize the D regime in terms of chemical activity, we measured the densities of several excited species. We inferred that the maximum electron density in the D regime is about 10^{13} cm^{-3}. In contrast to the non-thermal D regime, the thermal F regime emits strongly, heats the gas by several thousand degrees Kelvin, has tens of amperes of conduction current, and reaches maximum electron number densities of about 10^{15} cm^{-3}. Furthermore, we observed an ionization wave in the F regime that propagates from the anode to the cathode at about the same speed as the return wave in the D regime.

Second, we conduct a parametric study on the effects of gas temperature, gap distance, and Pulse Repetition Frequency (PRF), which ranges from 1 to 30 kHz in this study, on the properties of the D and F regimes and the D-F transition voltage. We wish in particular to determine the necessary conditions for producing the D regime at the lowest possible gas temperature. The transition between the regimes, in terms of emission intensity and energy deposited per pulse, shifts toward higher applied voltages as the gas temperature or PRF decreases. Furthermore, the D regime expands in applied voltage range with decreasing PRF. For both regimes, the delay between the application of the high-voltage pulse and breakdown shortens with increasing PRF. Ionization wave speeds do not vary with PRF or gas temperature. Finally, we find that at a given gas temperature, there is a minimum gap distance required for the existence of the D regime. Using this fact, we were able to extend the domain of existence of the D regime down to ambient temperature.

Finally, we propose hypotheses concerning the nature of the D regime and the D-F transition. The non-uniform Laplacian electric field generated by the pin-pin geometry is very high near

the electrodes where strong ionization occurs. We suggest that the D regime initiates in the anode high-field region with a cathode-directed streamer, whose head transforms into a cathode fall region, thus creating a transient glow discharge. The weakly ionizing low-field region between the electrodes can inhibit the spread of the glow-arc instability and prevent the D-F transition, thus acting as a current-limiting element.

In conclusion, we show that it is possible to generate low-power non-thermal plasmas in atmospheric pressure air from 300 to 1000 K using the NRP method, when parameters such as the gap distance and PRF are properly selected. An important next step will be to quantify further the chemical reactivity of the transient glow discharge plasma. This means determining the densities of active species of interest, such as atomic oxygen, in the interval between pulses. With its wide temperature range of operation, the NRP method holds promise as a flexible tool for air plasma applications at atmospheric pressure.

Remerciements

C’est à grâce aux nombreux individus que j’ai eu le privilège de faire ma thèse.

Tout abord, je remercie les membres du jury de thèse : Alix Gicquel, qui a présidé la soutenance, et également Denis Packan et Antoine Rousseau, pour une discussion très riche au niveau scientifique. J’ai aussi beaucoup apprécié les lectures détaillées de mes rapporteurs, Françoise Massines et Sergey Macheret.

J’ai apprécié la convivialité et l’amitié avec les membres du laboratoire EM2C, surtout les thésards. Mon apprentissage du français provient principalement de leur part.

Les membres de l’équipe plasma m’ont fait beaucoup rigoler et beaucoup travailler, toujours avec plaisir. Sans le conseil de la part de Deanna Lacoste, je n’aurai pas pu réaliser ce travail. J’ai acquis beaucoup d’expérience comme expérimentateur avec son aide. Je dois Christophe Laux plusieurs grands mercis : pour l’opportunité de travailler en thèse, pour toutes les astuces scientifiques et pour son soutiens toujours enthousiaste.

Pendant les moments frustrants en recherche, mes amis m’ont toujours remonté le moral, et donc je les compte essentiels à la réussite de cette thèse. Grâce à eux, mon séjour à Paris a été très riche en souvenirs.

Finally, I want to thank Henry, my dad, and my mom. Although my family found my decision to go to France rather unexpected, they nonetheless always supported me in any way possible.

Table of Contents

List of Figures

List of Tables

Chapter 1

Introduction

1.1 Motivation and context of the thesis

Plasmas are on the verge of becoming directly accessible for everyday use. Their release from the confines of television screens, clean rooms, and fusion reactors will be achieved when they become practical to use in open ambient air. Thus, atmospheric pressure air plasmas may function as a broad foundation upon which to build new technologies.

Today, atmospheric pressure air plasma science does not register much in the public consciousness. However, its backstage role in popular science in comparison to information technology or genetics, for example, belies its potential impact in a diverse set of public concerns: the environment, health care, energy, and manufacturing. Not only can atmospheric pressure air plasmas potentially redress the drawbacks of existing technologies, but they also raise the possibility of unanticipated innovations.

Fundamentally, the usefulness of plasmas rests upon their chemistry and electrodynamics. In terms of chemistry, large populations of electrons, ions, and neutral atoms and molecules can be generated to induce desired reactions at substantial rates. From the electrodynamics point of view, the forced motion of electrons and ions can produce special electromagnetic behavior in the plasma or couple energy into a bulk gas to influence fluid dynamics. Due to its gaseous nature, plasma activity can spread over large areas and volumes, or reach into otherwise inaccessible spaces. Furthermore, low additional mass is required.

Realizing such hopes for widespread use, however, requires that atmospheric pressure air plasma sources satisfy the following minimum criteria for versatility:

1. *High electron number density.* Because the chemical and electrodynamic properties that make plasmas useful depend mostly on electron behavior, the presence of a large number of electrons with sufficiently high energy to create other active particles through collisions should be made as high as possible.
2. *Operation at low gas temperature.* For a growing number of applications, the object in direct contact with the plasma is sensitive to temperature. The ultimate goal is to generate plasmas in air at room or low temperature.
3. *Significant length in at least one dimension*. Otherwise, plasmas can only be used at small scales.
4. *Low volumetric power*. Otherwise, the total power for generating large-scale plasmas is not practical. This is achieved by maximizing ionization efficiency.

There are other important challenges, such as the complexity and expense of the reactor. However, the above criteria concern fundamental plasma characteristics and are therefore unavoidable. Non-thermal (i.e. cold or non-equilibrium) plasmas, characterized by relatively low gas temperature and high electron temperature, are prime candidates for such sources. In particular, glow plasmas best meet the above requirements.

Unfortunately, at high pressure (typically 1 atm), non-thermal plasmas easily transform into thermal (i.e. hot or equilibrium) or quasi-thermal plasmas, for which both the gas and electron temperatures are high. Thermal plasmas include spark and arc discharges, which can have gas temperatures of several thousand Kelvins and form narrow, high-current filaments. Thermal plasmas are useful as well, but their high gas temperatures restrict their range of application.

The transition from the non-thermal to the thermal regime, specifically the glow-to-arc transition, usually occurs due to thermal instability. If the heat flux out of the plasma volume is sufficient to dissipate the heat buildup from within, then the non-thermal plasma remains stable. If not, the thermal instability causes excessive ionization that leads to the glow-arc transition. Because the ionization rate depends strongly on the electric field, the simplest way to avoid the transition is to lower the applied voltage, at the expense of ionization efficiency. These difficulties in producing non-thermal plasmas at atmospheric pressure stymied research and development until the 1980s.

Among the methods used to prevent the glow-to-arc transition, the most common involve inserting current-limiting resistors or insulating layers into the discharge circuit to control the ionization rate. In this case, the electric field and hence the ionization efficiency is higher, although still far from optimal. In 1988, Kanazawa *et al* [1.1] utilized an electrode covered with dielectric to generate the first stable atmospheric pressure glow plasma, in helium. Besides current limitation, other methods of generating atmospheric pressure air plasmas have also been explored in the laboratory, but none of them meet all of the criteria for versatility discussed above.

The ideal generation method is the use of electron beams. High-energy electrons injected into a body of air can achieve optimal ionization efficiency, which consequently also eliminates the problem of gas heating. Unfortunately, electron beam generation of air plasmas at atmospheric pressure poses several challenges, in particular the fabrication of transmission windows capable of sustaining high heat fluxes without breaking or causing too much power loss.

The Nanosecond Repetitively Pulsed (NRP) technique approaches the efficiency of electron beams. Instead of injecting external electrons, a strong applied electric field accelerates the plasma electrons to high velocity. This requires a short rise time to minimize the number of collisions at low energy. To avoid the glow-to-arc transition, the applied field is turned off before excessive ionization can occur. Repetitive pulsing results in the accumulation of metastable and active species, producing a rich chemistry. In fact, the NRP method meets all of the aforementioned minimum criteria for versatility. In 2003, Packan [1.2] experimentally demonstrated that a glow plasma can be produced by the NRP method for a specific condition in atmospheric pressure air at 2000 K. The next step is to explore the lower temperature limit of the NRP method and improve the understanding of the physics and chemistry of NRP plasmas.

In this study, the NRP method is implemented by applying short-duration (10 ns) high-voltage (5-10 kV) pulses at Pulse Repetition Frequencies (PRFs) of 1-30 kHz across a discharge gap (0.5-10 mm). In our experiments, the discharge occurs between two bare steel electrodes in a pin-pin configuration immersed in a pre-heated (300-1000 K) atmospheric pressure air flowing at 1-18 m/s into open ambient air.

We observe three regimes, which are corona-, diffuse-, and filamentary-like in appearance. They are labeled the C, D, and F regimes for reasons that will become clear in the course of this manuscript. This thesis deals with the D and F regimes, with the focus on the former. We are also interested in the transition between the D and F regimes.

In summary, our goals in this thesis are:

1. Study the properties of the NRP plasma regimes observed.
2. Demonstrate the versatility of the NRP method. Most importantly, we aim to generate non-thermal plasmas at the lowest possible gas temperature.

1.2 Scope of the thesis

Our work is mainly experimental, as we measure the optical emission and electrical characteristics of NRP plasmas to examine their chemistry and electrodynamics. We first present detailed background information in Chapter 2. This includes the development of applications using atmospheric pressure air plasmas and their methods of generation. Furthermore, we present the basic principles of the NRP method and summarize current research in NRP plasmas. Chapter 3 presents the detailed description of the experimental facility used for the present experiments.

Then, in Chapter 4, we present a characterization of the D and F regimes. Two representative D and F states are studied, which are generated at a gas temperature (T_g) of 1000 K and PRF=30 kHz. Voltage-current measurements permit us to distinguish the regimes according to their electrical characteristics. We use Optical Emission Spectroscopy (OES) for several purposes. First, we fit modeled spectra to measured spectra to deduce the time-resolved gas temperatures of the D and F states. Also, we construct spatio-temporal emission profiles of the D and F states during the breakdown phase using the measured emission intensity at points extending in both the radial and axial directions relative to the electrode axis. Finally, we deduce the time-resolved number densities of the D state at the discharge gap center for the excited species $N_2(C^3\Pi_u)$, $N_2(B^3\Pi_g)$, $N_2^+(B^2\Sigma_u^+)$, $NO(A^2\Sigma^+)$, and $O(3p^5P)$ using measured spectra.

Chapter 5 addresses the second priority of this study, which is to determine the influence of gas temperature, PRF, and gap distance on the D and F regimes. We establish how the applied voltages between regimes vary with temperature and PRF. Also, we use OES and voltage-current measurements to examine how the emission intensity and energy deposited per pulse change with gas temperature and PRF. Furthermore, we determine a relationship between the gap distance and gas temperature, which permits us to generate the D regime at temperatures down to 300 K.

Chapter 6 discusses an explanation for the experimental results of the D regime by linking our observations with established theories of streamers and glow discharges. In addition, we suggest reasons for which the gap distance plays a key role in preventing the D-F transition at a given gas temperature.

Finally, Chapter 7 summarizes the conclusions of this thesis and recommendations for future research.

This work was supported by the Agence Nationale de la Recherche (ANR) under the Interaction Plasma Ecoulement Réactif (IPER) project.

1.3 References

[1.1] S. Kanazawa, M. Kogoma, T. Moriwaki, and S. Okazaki, *J. Phys. D: Appl. Phys.* **21** (1988) 838-840.
[1.2] D. M. Packan, Ph.D. Thesis, Stanford University, 2003.

Chapter 2

Atmospheric Pressure Air Plasmas

2.1 Introduction

In this chapter we present topics in atmospheric pressure air plasmas relevant to the work in this thesis. We begin in Section 2.2 with an overview of current research in applications for atmospheric pressure air plasmas. Then, we summarize methods for generating atmospheric-pressure air plasmas in Section 2.3, covering thermal sources in Section 2.3.1 and non-thermal sources in 2.3.2. In Section 2.3.3, we introduce the Nanosecond Repetitively Pulsed (NRP) generation method, and in Section 2.4 we discuss current research involving this method.

2.2 Overview of low temperature non-equilibrium plasma applications

In this section, we discuss current engineering challenges that can be addressed by atmospheric pressure air plasmas, focusing on applications requiring low-temperature plasmas. In the past, plasma applications were limited to low-pressure or high-temperature conditions. The newfound feasibility of high-pressure low-temperature plasmas in air has attracted substantial research activity as well as growing interest from industry. The goal is economical and dependable operation in open ambient air.

We follow the discussion on applications from *Non-Equilibrium Air Plasmas at Atmospheric Pressure* by Becker *et al* [2.1], which reviews the principles of atmospheric-pressure air plasmas and research up to 2005. This section is divided by specific applications, starting with those that require plasma generation in ambient air and proceeding to those in higher temperature (up to 2000 K) air or air-like mixtures.

Medical technology

The need to provide doctors with less invasive medical tools, while improving accessibility and precision, has led to the use of lasers, electric cutting, and coagulation tweezers. Plasma-based tools can reduce invasiveness because the generator can remain at a distance while only the plasma flows onto the tissue. Furthermore, the gaseous nature of plasmas permits them to spread into regions difficult to access. The plasma chemistry can selectively act upon the target tissue or cells. Since living tissue cannot survive high temperature, low pressure, or electric shock, only atmospheric pressure glow plasmas can be used for medical purposes.

Recent advances in plasma medical technology include the plasma needle of Stoffels *et al* [2.2] for *in vivo* treatment. The plasma needle is a 13.56-MHz RF discharge generated at

the tip of a sharp needle, which is held at a distance from the patient as the plasma flows onto the treatment region, as shown in Figure 2.1.

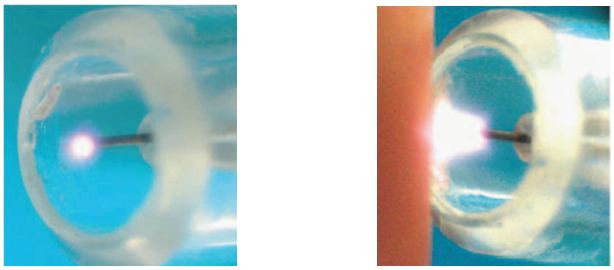

Figure 2.1: The plasma needle (left) when the grounded electrode is remote (>3mm away), and when plasma is in contact with dry skin (right). Plasma needles consist of a metal wire electrode (typical length 5 cm) placed in a casing and supplied with gas flow. Taken from [2.2].

When the plasma contacts the tissue, treatment occurs via active species generated in the plasma or in the tissue, such as O, OH, and NO. This may enable doctors to modify tissue, remove diseased tissue without damaging surrounding healthy tissue, and alleviate infection with a high level of finesse and precision. The plasma needle works best in helium, which has a low ignition voltage (200 V) and a high thermal conductivity (144 W/m/K), keeping the gas temperature below the cell thermal damage threshold. For a power budget of 140 W/cm^3, the plasma produced has a diameter of 3 mm, an electron density of about 10^{11} cm^{-3}, and a gas temperature of 323 K. The use of air as the vector for chemical activity would reduce cost by eliminating the need for additional feed gas.

Biological decontamination

Methods employed to kill harmful microorganisms sometimes have undesirable side effects. For example, Ultra-High Temperature (UHT) treatment sterilizes dairy products, but it also diminishes nutrient content. For heat-sensitive objects, such as plastic medical devices, chemical or radiation treatment is used instead. However, the most commonly used chemical sterilization agent, ethylene oxide, is toxic, highly flammable, and requires long treatment times. Some radiation sterilization devices, such as those employing gamma or X-rays, require heavy shielding to protect the user.

Atmospheric pressure air plasmas are also capable of biological decontamination, albeit via different mechanisms. In particular, reactive species produced by air plasmas, such as O, O_3, NO, NO_2, and OH interfere with the transport function of cell membranes. Charged particles may cause the rupture of the cell membrane, or lysis, through the electrostatic force of accumulated charge on the membrane. Also, gas heating and UV radiation resulting from plasma generation may also cause microorganism deactivation.

For example, the Atmospheric Pressure Plasma Jet (APPJ) pioneered by Schütze *et al* [2.3] is a uniform glow 13.56 MHz RF discharge that produces reactive species. A feed gas of a few percent O_2 diluted in He or Ar flows between a cylindrical outer ground electrode and a coaxial inner electrode, where the plasma is generated. Recombination depletes ions and electrons in the exiting jet but not metastable species (e.g. O_2*, He*)

and radicals (e.g. O, OH). In the jet, the gas temperature is 25-200ºC, charged particle densities are 10^{11}-10^{12} cm^{-3}, and reactive species concentrations are 10-100 ppm. Hermann *et al* [2.4] showed that the APPJ effectively deactivates surrogates for anthrax spores and mustard blister agent, as shown in Figure 2.2. Furthermore, the reactive species in the jet rapidly degrade into harmless byproducts.

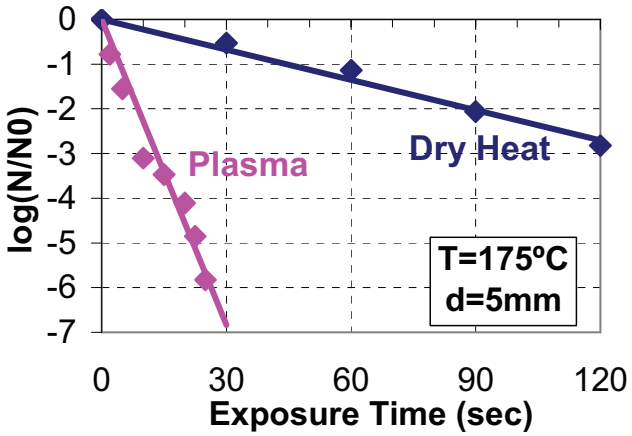

Figure 2.2: Kill curves for *Bacillus Globigii* (Anthrax simulant) using dry heat and plasma treatment using the APPJ (1% O_2 in He). Taken from [2.4].

However, the APPJ only works with less than 10% O_2 in a helium flow, which is very expensive and inconvenient. It requires carrying a supply of helium, which is not practical for portable systems required for on-site decontamination needs. Decontamination performed in pure air would eliminate these problems, but the gas temperatures of APPJ in air exceed 2000 K. Therefore, another method is needed to produce active species without heating the air.

Surface treatment

Low-temperature non-equilibrium plasmas are already widely used for surface treatment. For example, Plasma Enhanced Chemical Vapor Deposition (PECVD) is used in microelectronics to deposit thin silicon dioxide layers on wafers. One general advantage of gas-phase techniques is that they are "dry" processes, requiring relatively low amounts of additional materials that finish as waste. Among gas-phase techniques, those utilizing cold plasmas have the additional advantage that the electrons can be elevated to high temperature (several eV) to produce ionization, while the gas temperature remains low so as not to damage a temperature-sensitive surface under treatment.

One disadvantage of current plasma processes is that they require low pressure. Therefore, materials must be treated one batch at a time, with the treatment chamber de-pressurized and re-pressurized between batches. This method especially hurts cost-effectiveness for products with low profit margin, for which manufacturing in conveyer-belt fashion is the most economic solution. This would be possible if plasma-based surface treatment were performed at atmospheric pressure in ambient air.

At atmospheric pressure, however, cold discharges readily transform into arc discharges, whose high current levels may cause thermal and electrical damage. Furthermore, arcs are localized and thus are not well suited to treat large surfaces. One to avoid such problems is by using Dielectric Barrier Discharges (DBDs), which limit the current to prevent the formation of arcs and can generate large-area plasmas. There has been considerable work done recently in DBDs for surface treatment at atmospheric pressure, for example by Massines *et al* [2.5]. Either numerous filaments form from streamer breakdown, or a homogeneous discharge forms from Townsend breakdown. Although individual filaments are localized, a discharge with numerous filaments can nonetheless treat large surfaces in a statistical manner. Some applications, such as thin film deposition, require a truly diffuse discharge.

Chemical decontamination

Industries face mounting pressure to reduce air pollutant emission levels from production and from final products. Thus, there is interest in the decomposition of major industrial pollutants into harmless byproducts. Non-equilibrium air plasmas are interesting for chemical decontamination because energy is preferentially channeled into the production of energetic electrons. These electrons decompose the target pollutant either directly via impact or indirectly through the generation of radicals. The decomposition of NO_x, or the "de-NO_x" process, using plasmas has been a subject of considerable study.

Recently, Dorai and Kushner [2.6] computationally investigated the effect of repetitively pulsed plasmas on the de-NO_x process for diesel exhaust using DBDs. Chemical reactions on soot surfaces affect NO_x concentrations, and therefore the influence of soot is taken into account. Without soot, a 20-pulse series converts more NO to NO_2 compared to a single pulse. With soot, a single pulse initially oxidizes NO to form NO_2, followed by conversion of NO_2 back to NO on the soot. With a 20-pulse series and soot, a higher NO_2 gas phase density increases NO_2 flux to the soot surface, creating increased soot oxidation and larger conversion rates of NO_2 to NO. In the end, the proportion of removed NO_x is about the same, regardless of the pulsing scheme or the presence of soot.

Also, Chang *et al* [2.7] performed experiments on the removal of NO_x and SO_2 from coal boiler flue gases by a corona radical shower, which uses a corona discharge to produce ammonia radicals. The experiments were for gas temperatures of 62-80°C, applied voltages of 0-25 kV, and NO initial concentrations of 53-93 ppm with a fixed 800 ppm SO_2 concentration. Both NO_x and SO_2 removal rates increased with increased ammonia radical injection rate and input power. For 1 kWh of energy, 9 kg of SO_2 (99%) and 125 g of NO_x (75%) were removed.

Subsonic aerodynamic flow control

Significant progress has been made recently in the development of plasma actuators for airfoils. Their operation involves no moving parts, unlike that of mechanical actuators, and they can be activated over much shorter time scales than their mechanical analogues. An electric or magnetic field generates a plasma and exerts a force on charged species that is transferred to the gas through collisions. This bulk force, as well as gas heating

resulting from plasma generation, can alter flow. Flow control using DC corona discharges and DBDs has been successfully demonstrated. The modeling of DBD actuators is now fairly developed, following the recent work of Boeuf *et al* [2.8] and Likhanskii *et al* [2.9], with the latter concerning DBD actuators using the Nanosecond Repetitive Pulse (NRP) method investigated in this thesis.

Recently, Bérard *et al* [2.10, 2.11] performed a parametric experimental and numerical study of a DC corona in air at 1 atm and 300 K between two wires to quantify the effect of the discharge and geometry on flow velocity. The induced flow as a function of discharge current is shown in Figure 2.3.

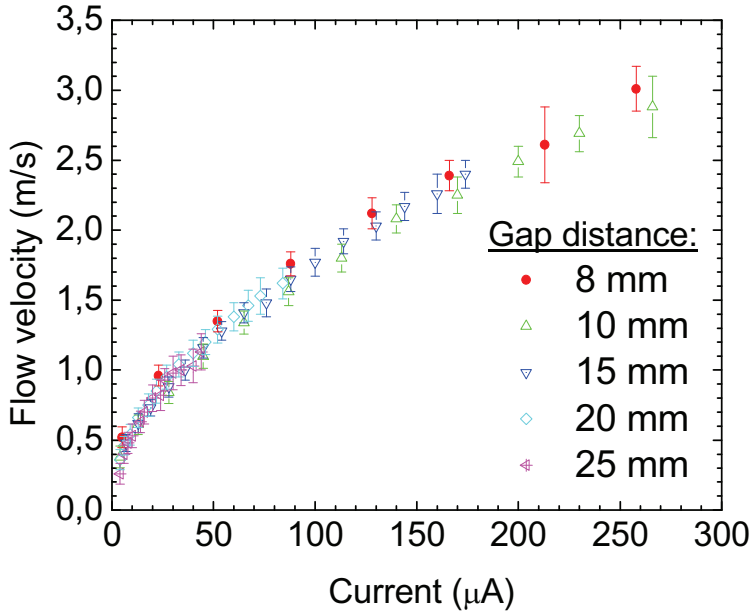

Figure 2.3: Ionic wind velocity measured in the middle plane located between the two wires as a function of the current for several gap distances. Positive DC discharge in air. Wire diameters: 0.35 and 2 mm. Electrode length: 20 cm. Taken from [2.10].

A corona discharge affects flow by producing ionic wind between two wires. The electric field around each wire is inversely related to the distance from the wire. Wires of small diameter are chosen to produce a high local field for ionization. As a result, the positive ions drift toward the cathode, transferring momentum through collisions along the way to the neutral species. Near the cathode, O_2^- generated via electron attachment drifts toward the anode, likewise transferring momentum to the neutrals. Thus, there are opposite charge currents, and the net flow of particles is the ionic wind. Using asymmetric wire diameters, one of the current flows can be favored, thus creating a wind in one direction.

Supersonic aerodynamic flow control

One major obstacle facing commercial supersonic flight is the bow shock layer that forms in front of the blunt-body profile of large passenger aircraft. The shock increases drag

and hence heat transfer to the aircraft body. Also, the shock wave generates a sonic boom that produces ground-level noise. To alleviate these problems, a physical spike placed at the nose of the aircraft modifies the bow shock into a conical oblique shock. This reduces drag, but a spike suffers from its own drag-induced heating and mechanical stress from changes in flight Mach number and in angle of attack.

To reproduce the effect of a physical spike while overcoming its drawbacks, various methods of energy deposition have been considered to heat the incoming flow [2.1]. By heating the flow, the local Mach number is reduced, and the bow shock layer moves upstream to form an oblique shock front. One potential method for energy deposition is plasma generation ahead of the aircraft body. Elias *et al* [2.12, 2.13] investigated drag reduction from localized heat deposition by discharges generated near steady bow shocks, as shown in Figure 2.4. Steady negative discharges were produced in front of a blunt body in M=3 supersonic flow using coaxial electrodes.

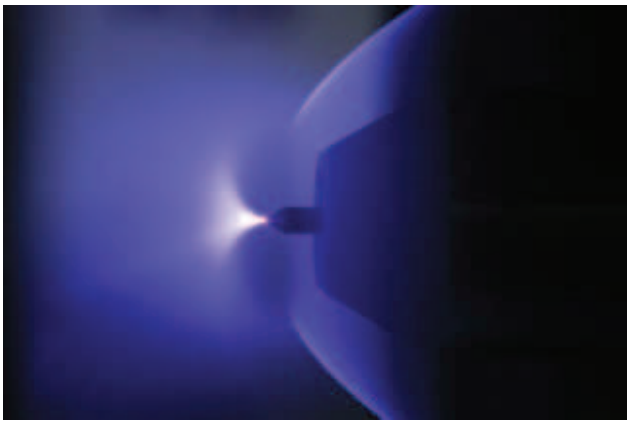

Figure 2.4: Plasma generation near bow shock layer. Taken from [2.13].

The corona, glow, and filamentary arc regimes were observed. The glow plasma dissipated up to 0.5 kW, but it did not change the drag coefficient. Simulations demonstrated that the plasma thermal power was insufficient for drag reduction, perhaps due to electron-impact N_2 vibrational excitation, whose subsequent long relaxation time may result in gas heating occurring primarily downstream instead of near the shock layer as intended. Thus, high plasma heating efficiency is necessary for efficient plasma-induced drag reduction.

In addition, Nishihara *et al* [2.14] performed magnetohydrodynamic (MHD) supersonic boundary layer control experiments combining repetitive high-voltage pulses with a B=1.5 T magnetic field to generate discharges in M=3 nitrogen and air flows. They showed that the boundary layer flow became more chaotic with increasing Reynolds number, with a transition occurring at stagnation pressures of 200-250 torr. DC voltage superimposed on the repetitive pulses resulted in stable, diffuse, and uniform plasmas along with the MHD effect.

Electromagnetic wave reflection, absorption, and phase shift

Stealth technology involves reducing the Radar Cross Section (RCS) of an aircraft by using unconventional body shapes and special materials and coatings. However, certain parts of the aircraft still leave detectable radar signatures, such as the air intakes. By placing a plasma in front of an intake, radar signals can be absorbed or reflected, as discussed by Vidmar [2.15]. For this to be practical, large volumes of air plasma with electron densities of 10^{13} cm^{-3} consuming less than 1 W/cm^3 of power must be produced in ambient air without heating the gas to temperatures much higher than 2000 K. Efficient plasma generation techniques to produce diffuse air plasmas are required.

Plasma-assisted combustion

Nitrogen oxides (NO_x) have numerous harmful effects on the environment and are produced primarily by combustion [2.16]. As a result, NO_x emissions reduction has become an active topic in combustion research. NO_x concentration decreases with decreasing flame temperature, which itself decreases with the fuel-air equivalence ratio. Therefore, the use of lean flames is a promising strategy for reducing NO_x emissions. Unfortunately, lean flames tend to be unstable or difficult to ignite. This limit is governed by the supply of radicals, notably O and OH, required as reactants in the combustion sequence of chemical reactions. Radicals are produced via reactions involving the fuel, and therefore radical production is dictated by the equivalence ratio. Below the flammability limit, radical production falls below the level needed to sustain combustion.

One way to extend the flammability limit is to boost radical production by generating a plasma in the combustion zone. The plasma generates radicals through hydrocarbon cracking and the air chemistry, although predominantly by the latter because even a stoichiometic mixture only contains a small fraction of fuel (<10%) and mostly air. Therefore, a better understanding of air plasma chemistry is important to the advancement of plasma-assisted combustion.

Recent progress in plasma-assisted combustion includes the work of Pilla *et al* [2.17, 2.18] in 2006 on the stabilization of a 12-kW lean turbulent premixed propane/air flame at atmospheric pressure. Stabilization was achieved with a plasma power of about 75 W, or 0.6% of the maximum flame power. In addition, at high flow rates that normally result in blow out, the plasma permits the existence of a small dome-shaped flame confined near the electrodes that can serve as a pilot flame to reignite the combustor. Figure 2.5 shows a flame regime map comparing the stability limit of combustion alone with those of plasma-assisted combustion.

Figure 2.6 is a comparison of the flame emission with and without application of the plasma for the same burner used in Figure 2.5. It demonstrates that the flame region is considerable larger when the plasma is applied, both visually and in terms of measurements of OH emission, which indicates that combustion is indeed enhanced by the plasma.

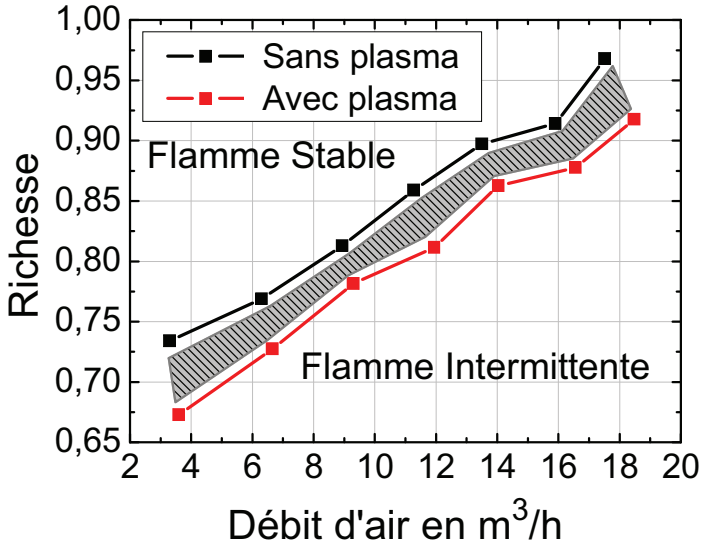

Figure 2.5: Flame regime map of a 12-kW lean turbulent premixed propane/air flame at atmospheric pressure. The discharge is filamentary, with an applied voltage of 6.7 kV, a pulse repetition frequency of 30 kHz, and a gap distance of 5 mm. The curves represent the equivalence ratios of the stable/intermittent flame transition, with and without plasma. Taken from [2.18].

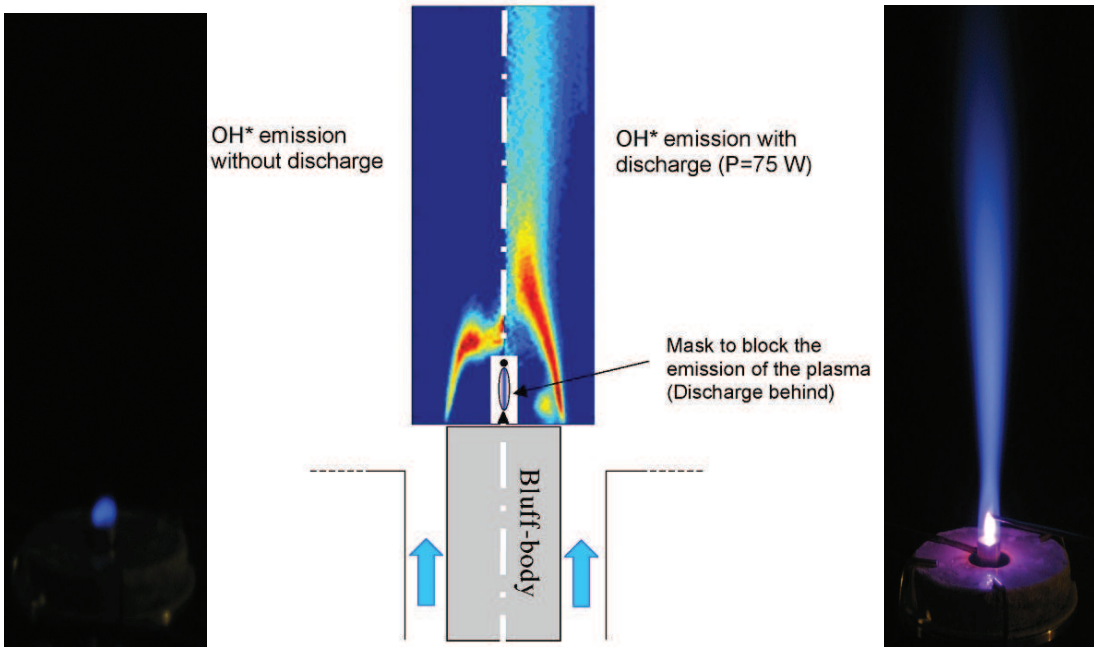

Figure 2.6: Comparison of the plasma-stabilized flame (right) and the pilot flame when no plasma is applied (left). Images of the flame are accompanied by emission profiles of the OH(A-X) transition. Flame power: 12 kW. Plasma power: 75 W. Flow rate: 15 m^3/h. Propane-air equivalence ratio: 0.8. Taken from [2.17].

In addition, Pancheshnyi *et al* [2.19] investigated the efficiency of the ignition of propane-air mixtures at pressures of 0.35-2.0 atm by NRP discharges using the same generator used in this thesis. The minimum energy for ignition decreased with the pressure, and a significant decrease of the ignition delay and the overall combustion duration were obtained by applying a series of high-voltage pulses. In air at 1 atm, only ten consecutive pulses over a total time of 300 μs and 10 mJ of energy were required to ignite a strongly diluted propane-air flame that a conventional spark plug could not ignite. For a summary of current research in plasma-assisted ignition and combustion, the interested reader is referred to the topical review written by Starikovskaia [2.20] in 2006.

Overview of temperature ranges for applications

We now consider the temperature ranges for the previously described applications together in Figure 2.7. Medical devices must operate at 290-320 K, which is safe for patients. Surface treatment and biological decontamination occur below 500 K. Chemical decontamination applications reach up to 1000 K, the temperature of exhaust gas that can be treated for VOC abatement. Stealth and flow control applications must operate at 100-2000 K, the temperature range of air in flight. Finally, combustion applications involve temperatures from 300 K for ignition to 2000 K for plasma-assisted combustion. Applications that require low temperature exclude the use of thermal plasmas, leaving non-thermal plasmas as the only option. Although non-thermal plasmas are more versatile than thermal plasmas, within the context of the applications discussed in this section, their power requirements must be minimized.

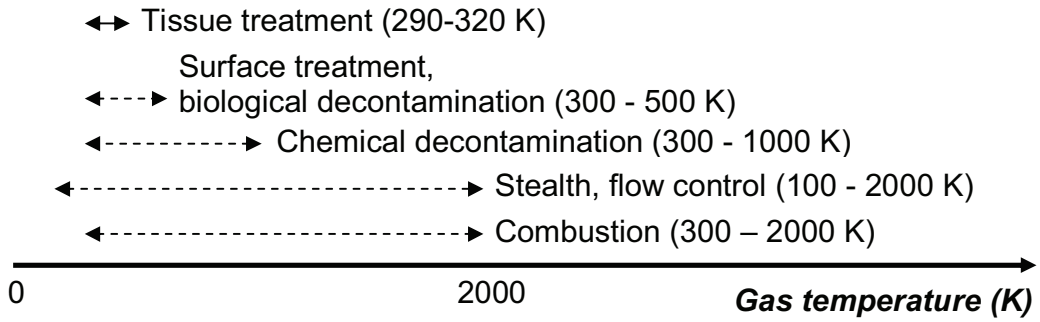

Figure 2.7: Temperature ranges under which air plasmas must be created for applications discussed in this section.

More precisely, high-temperature applications merely tolerate thermal plasma heating in exchange for their greater electrical and chemical activity, in general. In some cases, such as with supersonic flow control, a heating effect is sought, but it has not been proven that thermal plasmas serve as better heat sources than other methods. It remains to be seen whether the lower electrical and chemical activity of non-thermal plasmas is such a handicap that no amount of engineering can render them more advantageous at high temperatures than thermal plasmas.

2.3 Methods of producing plasmas in air at atmospheric pressure

In this section, we present a survey of methods for generating atmospheric-pressure air plasmas, both thermal and non-thermal, although the focus is on the latter. Only the most general operating principles are discussed, as we emphasize application design parameters: power budget, electron number density, and temperature range. This section is not a complete review, as we only provide examples of each method. We discuss thermal plasma sources in Section 2.3.1 and non-thermal sources in Section 2.3.2.

2.3.1 Thermal plasma sources

Direct Current

DC glow discharges in air at atmospheric pressure are problematic because they tend to transition to arc at high pressure. The glow-arc transition can be prevented by inserting a current-limiting resistor or by flowing the gas at high velocity to prevent gas heating through the release of the energy stored in the vibrational levels of N_2. This enabled Yu *et al* [2.21] to create stable diffuse glow discharges at gas temperatures of 1800-3000 K with electron densities in excess of 10^{12} cm^{-3} using 4-5 kW/cm^3 of power. The discharge did not appreciably affect the measured gas temperature. Thus, although these discharges could also be seen as constricted arcs, they fall into the glow discharge category according to the clarification by Raizer [2.22] by virtue of their non-equilibrium character (T_e>>T_g) and cathode fall voltages of about 300 V. Figure 2.8 shows measured and calculated values of the electric field, current density, power consumption, and electron number density.

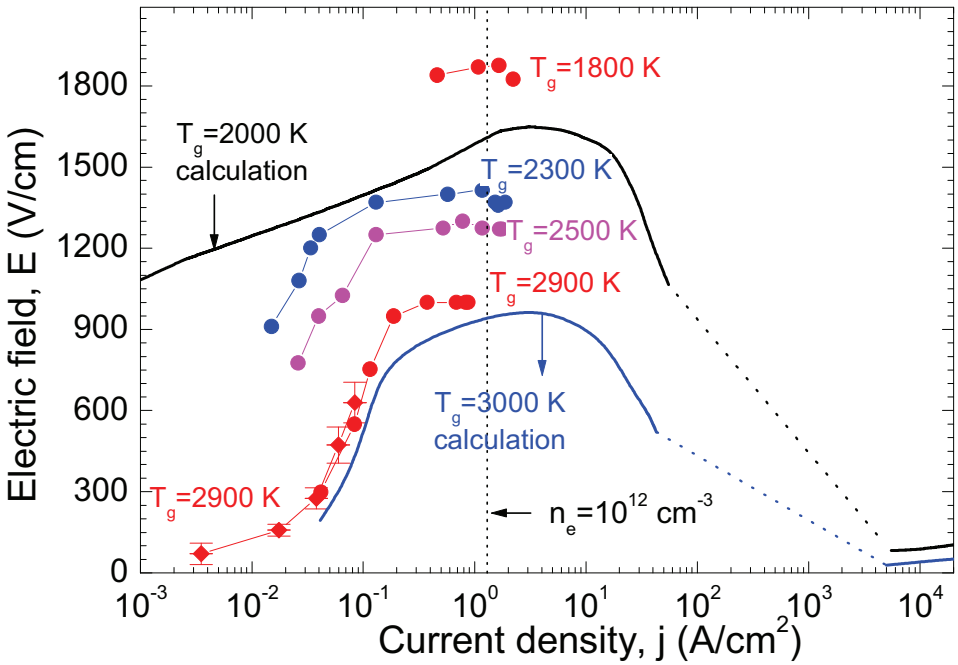

Figure 2.8: Measured (symbols) and predicted (solid lines) electrical discharge characteristics in atmospheric pressure air plasmas generated by DC electric discharges. Taken from [2.21].

Stark and Schoenbach [2.23, 2.24] proposed another method for DC glow plasma generation. In this case, the plasma is formed between a Micro-Hollow Cathode Discharge (MHCD) and a secondary anode, as shown in Figure 2.9. The MHCD serves as a source of electrons and thus, according to the authors, eliminates the cathode fall and provides a way to avoid the glow-to-arc transition. With this system, Stark and Schoenbach demonstrated the production of a stable atmospheric pressure glow in air for an inter-electrode distance of up to 1 cm, with a measured electron number density of up to 10^{13} cm^{-3} and a measured gas temperature of about 2000 K The current density and electric fields were respectively 3.8 A/cm^2 and 1.2 kV/cm, corresponding to a power density of about 5 kW/cm^3. The power consumption, gas temperatures, and attainable electron number densities are very similar to those obtained with the DC discharges presented earlier. Thus, this MHCD discharge system is very similar to a resistively ballasted DC discharge, with the MHCD playing the role of the ballast resistor.

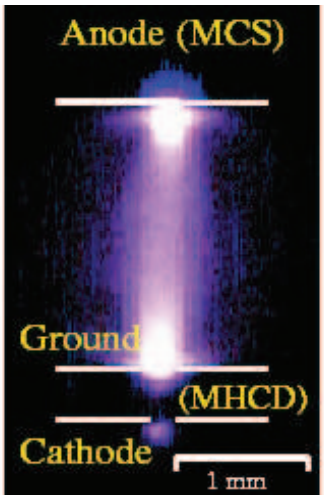

Figure 2.9: Cross-section of microplasma electrode geometry with a third positively biased electrode, the anode, with a superimposed photograph of an MHCD-sustained atmospheric-pressure air plasma. Taken from [2.24].

Radiofrequency

An example of atmospheric pressure air RF plasmas is the well-developed industrial standard Inductively Coupled Plasma (ICP) torch used to heat air to 1800-3000 K for the studies of DC discharges by Yu *et al* [2.21]. Figure 2.10 is an image of the ICP torch and the plasma it generates. A power supply operating at 4 MHz with a maximum output power of 50 kW is connected to the plasma torch head. Cold air is injected and heated in the induction region by the RF coil, which is wound around a quartz tube enclosing the induction region. The exiting thermal air plasma has a temperature of 4000-9000 K below 4000 K. Specifically, with an input power budget of 105 W/cm^3, a thermal plasma is produced with a gas temperature of 4000 K and an electron number density of about 10^{13} cm^{-3}.

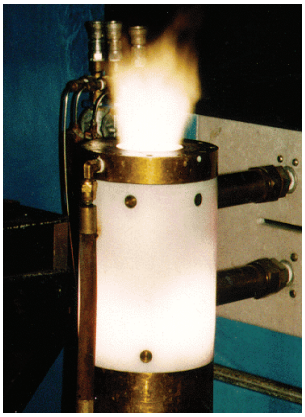

Figure 2.10: Image of the ICP torch used by Yu *et al* [2.25] to generate a thermal plasma. The plasma diameter is 5 cm.

Microwave

An example of a microwave generator for atmospheric-pressure air plasmas is the microwave torch used by Machala *et al* [2.26] to study DC glow discharges. Operating at a nominal power of 5 kW and a frequency of 2.45 GHz, this torch deposited up to 3.5 kW into the plasma. The thermal plasmas produced occupied a 10-cm^3 volume in open air, with gas temperatures up to 5000 K. The input power required to generate electron densities in excess of 10^{13} cm^{-3} was ~200 W/cm^3, which is comparable to that of the RF torch described previously.

Low-power microwave plasma reactors employ microstrips, such as the microstrip split-ring resonator designed by Iza and Hopwood [2.27], which operates at 900 MHz and at pressures of 0.05-760 torr. Over a relatively wide pressure range, argon and air discharges can be ignited using less than 3 W. Microstrips were also used by Kim and Terashima [2.28] to generate atmospheric-pressure microplasmas. A microwave power of 1 W was sufficient to sustain microplasmas in the discharge gap of 0.2 mm width and 6 mm length. The gas temperature was measured to be 800 K.

Laser

Lasers can be used to ignite the plasma, pre-ionizing the gas before another mechanism, such as RF excitation, sustains the plasma. One example is the UV laser-initiated plasma seeded by tetrakis (dimethyl-amino) ethylene (TMAE) investigated by Ding *et al* [2.29]. They were able to produce voluminous plasmas (~500 cm^3) with high electron densities of ~10^{13} cm^{-3} in atmospheric-pressure air for durations of about 5 ns and power in the 5 W/cm^3 range. Although non-thermal, the gas temperature increased to over 4000 K, and the power is consistent with those produced with thermal sources. Thus, these discharges appear to be in transition to thermalization.

2.3.2 Non-thermal plasma sources

Dielectric Barrier Discharges (DBDs)

Homogeneous discharges generated in the low frequency range (<100 kHz) generally are DBDs, as reviewed by Kogelschatz [2.30] in 2003. In 1993, Okazaki *et al* [2.31] produced homogenous discharges in air, argon, oxygen and nitrogen at atmospheric pressure using 50-Hz voltage generator and gap distances of 1.5 and 3 mm. The electrodes were composed of a fine metal wire mesh and a dielectric layer.

Massines *et al* [2.5, 2.32] used DBDs to generate Townsend and glow discharges at atmospheric pressure in N_2 and in helium, respectively. Figure 2.11 shows images of glow DBDs in He and N_2 taken with a 10-ns exposure time at the moment of maximum current. Initially, breakdown occurs in a uniform field. As the ion density increases, a cathode fall forms whose thickness decreases until the current maximizes. The compression of the cathode fall permits the discharge to sustain itself even when the applied voltage is halved. Following the current maximum, the cathode fall slowly re-expands, compressing the positive column. When the applied voltage changes polarity between two consecutive discharges, there is a residual memory current of the positive column. This indicates that there are enough electrons remaining in the gap for next breakdown to occur in low field, and models showed that a minimum pre-breakdown electron number density of 10^6 cm^{-3} is necessary to maintain the discharge. The maximum values of electron and ion densities are about 10^{11} cm^{-3}.

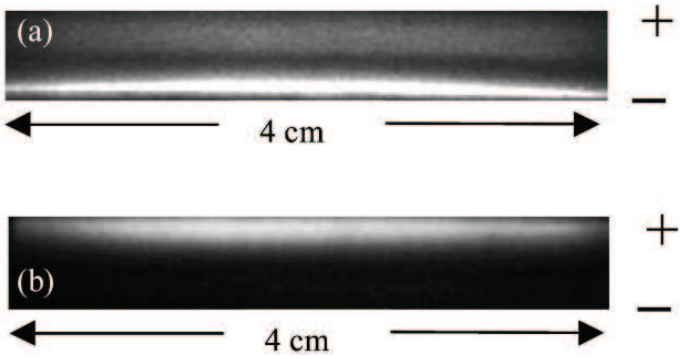

Figure 2.11: Images of the gas gap of a glow DBD in He (a) and N_2 (b). Taken from [2.5].

Kozlov *et al* [2.33] generated diffuse and filamentary DBDs in flowing N_2/O_2 mixtures between two semi-spherical electrodes covered by glass, as shown in Figure 2.12. They applied 6.5 kHz, 12–19 kV sinusoidal voltage. At oxygen volumetric concentrations greater than 0.1%, only the filamentary regime was observed, and variations of the oxygen concentration did not qualitatively change micro-discharge development or the cathode-directed ionization wave speeds. The micro-discharge decay time and the amount of transferred charge decreased monotonically with increased oxygen content, which is indicative of strong electron attachment.

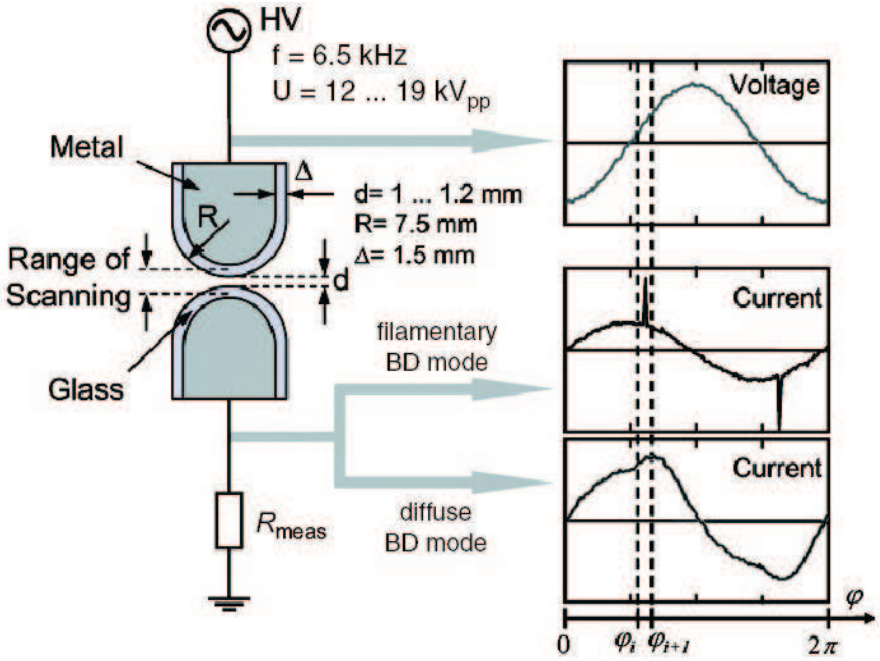

Figure 2.12: Schematic diagram and typical measured voltages and currents of the DBDs investigated by Kozlov *et al*. Taken from [2.33].

Another example of DBDs is the One Atmosphere Uniform Glow Discharge Plasma (OAUGDP™) created by Roth *et al* [2.34], which is in fact a Townsend discharge. Both diffuse and filamentary regimes were generated in dry air and helium. Surface charge appeared to play an important role in the growth and stability of the diffuse regime in air. In addition to maintaining the plasma, the input power dissipates by heating the dielectric covering the electrodes. This dielectric heating accounted for 10–100% of the total input power, indicating that low-loss dielectric materials were needed. Electron densities were in the 10^8-10^{10} cm^{-3} range.

Radiofrequency

High-power RF reactors such as the ICP torch described in Section 2.3.1 have been used for years, but novel low-power RF devices have recently been developed as non-thermal plasma sources. For example, Yalin *et al* [2.35] have created hollow slot microplasmas in open air. These discharges are uniform, with RF current densities of the order of A/cm^2. The inter-electrode distances are only 100–600 μm but with a much longer linear slot dimension, which resulted in plasmas 30 cm in length, suitable for wide-area surface treatment applications. Figure 2.13 shows the schematic diagram of the RF-driven hollow slot micro-discharge.

RF voltages at 4–60 MHz are applied to an interior electrode to ignite and sustain the plasma between electrodes, with the outer slotted electrode. To obtain uniform plasmas of dimensions greater than 30 cm, rare gas flow is inserted into the inter-electrode region and exits into open air. In one mode of operation, an afterglow plume extending 1–3 mm

from the grounded open slot permits treatment several millimeters away from the active plasma, where gas temperatures are lower.

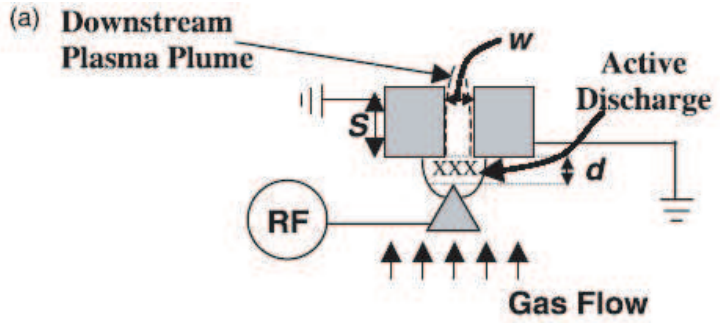

Figure 2.13: Schematic diagram of the RF-driven hollow slot micro-discharge. Gas flows in from the bottom, passes through the electrodes, and exits into open air. The slot width is *w*=200 μm, the inter-electrode gap is *d*=100 μm, and the extent of the open slots in the flow direction is *S*=5 mm. The wedge and slot electrodes are 1-30 cm long (dimension into page), creating a long plasma. Taken from [2.36].

Operation at 13.56 MHz with an argon flow generated diffuse non-equilibrium discharges with currents up to ~1.5A per centimeter of slot length. At this current level, the plasma power density was about 1 kW/cm^3, and energy per volume delivered to the flowing gas ~100–200 J/L. In this regime, the voltage remained roughly constant with increasing current. The glow-arc instability developed at higher currents without the occurrence of the abnormal glow.

Optical (Laser)

In a role reversal from the TMAE-seeded plasma described in Section 2.3.1, lasers can be used for plasma generation with RF field support. Plönjes *et al* and Adamovich [2.37, 2.38] have employed lasers to generate optically pumped non-thermal plasmas. An IR laser pumped CO-N_2 mixtures, which vibrationally excited CO through absorption, followed by near-resonant vibration-vibration (V–V) energy transfer from CO to N_2.

The pumping sustains a strongly vibrationally excited gas with a low power budget up to 200 W for a cw CO laser. Ionization occurs mainly via associative ionization, which is stable with respect to the heating instability that typically triggers the glow-arc transition at high pressure. Electron generation is stabilized with increasing gas temperature because the upper vibrational state populations decrease due to the exponential rise of vibration-translation (V-T) relaxation rates. Using a 10-W CO laser, they achieved maximum electron densities of 10^{10}-10^{11} cm^{-3}, with an absorbed power density of ~10 W/cm^3 that varied quadratically with the electron number density. The gas temperature is 400-700 K, whereas the CO vibrational temperature is 2000-4000 K.

While a plasma can be generated by optical pumping alone, an RF electric field can also be applied for additional pumping by using the free electrons generated by optical pumping to increase vibrational excitation via electron impact. The electric field is low such that electron-impact ionization rates are well below those of associative ionization,

thus retaining discharge stability. Because over 99.9% of the input power goes into N_2 vibrational excitation for low to moderate electric field strengths, RF pumping is efficient for sustaining high vibrational temperature.

While optical-RF pumped plasma generation is very effective for preventing the glow-arc transition, it suffers from two drawbacks. First, associative ionization is not an efficient process, with only about 0.1% of the input power channeled into ionization. Second, when the gas contains large proportions of species that rapidly relax vibrationally, such as O_2, much higher laser power is required to achieve substantial associative ionization.

Electron beams

Macheret *et al* [2.39-2.41] predicted the dynamics of plasmas generated in air by electron beams. In [2.39], they describe two regimes, distinguished by the removal mechanism of the negative charge generated by the ionizing beam. In the fountain regime, the back current of electrons toward the injection foil is responsible for charge removal. The thunderstorm regime is characterized by negative charge accumulation to form a cloud with a high local electric field, which instigates a streamer between the cloud and an electrode or between clouds created by separate beams.

In [2.40], Macheret *et al* have shown that the minimal energy cost of producing electron number densities of 10^{13} cm^{-3} with electron beams is about 34 eV per electron-ion pair. Electron energies in the tens to thousands of eV range are required, with about half of the energy spent on ionization cascades.

Due to practical difficulties with electron beams at atmospheric pressure, runaway electrons generated by sub-nanosecond high-voltage pulses were suggested as the next-best alternative. However, Macheret *et al* showed that runaway electrons are unable to penetrate deeply in air at atmospheric pressure, and thus this technique was also found to be impractical. Therefore, Macheret *et al* [2.40] performed further simulations of the NRP method of the Stanford group [2.47] (see next section) for generating diffuse plasmas. They confirmed that this method was the best experimentally proven alternative to the electron beam and runaway electron methods from a power budget perspective. In addition, they also showed that the cost of the NRP method, which is about 100 eV per electron-ion pair produced, is only three times higher than the electron beam method and two orders of magnitude lower than that for DC and RF ionization.

Most of the total applied voltage dropped across the physically thin cathode fall, which resulted in reduced electric fields much higher than the minimum value on Paschen's curve, otherwise known as Stoletov's point. This implies excessive ionization cost in the sheath. On the other hand, the reduced field in the positive column is near Stoletov's point, implying nearly ideal energy cost. Normally, in glow discharges, the opposite is true.

Comparison of different methods of generation

Having described the various methods to produce atmospheric pressure air plasmas, we now compare them to determine the best method for generating the most active plasma at the lowest temperatures and power budgets possible. We use the electron number density as an indicator of the "quality" of the plasma in terms of its electrical and chemical activity. We begin by comparing the gas temperatures of plasmas produced by various methods, as this is the immediate constraint for applications. Figure 2.14 summarizes the gas temperature ranges of the methods described in this section as a function of electron number density, and Figure 2.15 plots the corresponding volumetric power. We present approximate ranges, and the methods are grouped into general categories.

Thermal plasma sources cover the largest range of electron densities and are fairly energy efficient, but for electron number densities greater than 10^9 cm^{-3}, they have gas temperatures of 2500 K or higher, making them suitable only for combustion and flow control applications. DC plasma gas temperatures are lower, but they are the most inefficient because more than 99% of the power is lost to N_2 vibrational excitation. DBDs and laser-produced discharges are low power and can operate in near-ambient conditions, but their electron densities are relatively low. Electron beam sources, while theoretically able to achieve high electron number density, minimal gas heating, and low power consumption, have been difficult to demonstrate experimentally.

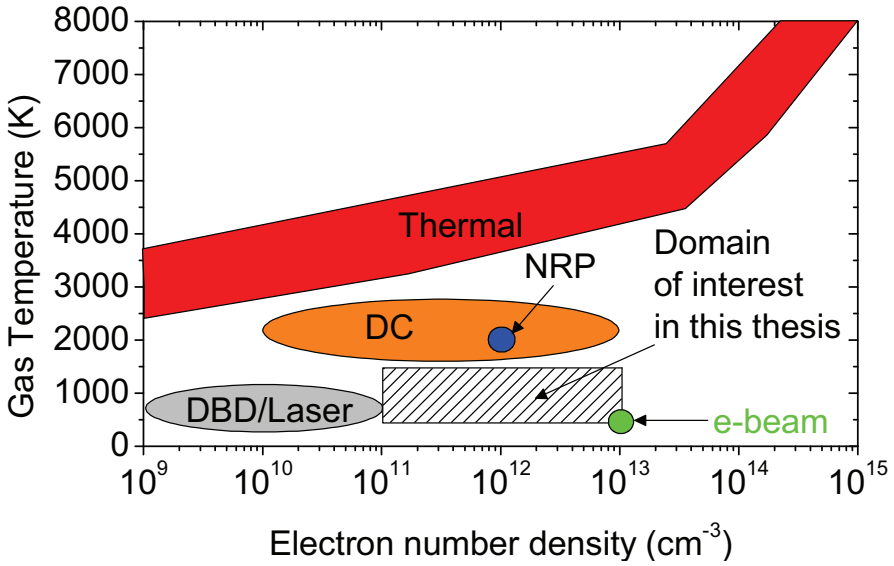

Figure 2.14: Gas temperatures of plasmas generated by the methods discussed in this section as a function of electron number density.

As we will discuss in the next section, non-thermal Nanosecond Repetitively Pulsed (NRP) glow plasmas have already been demonstrated to produce on average 10^{12} cm^{-3} of electrons at 2000 K for about 10 W/cm^3. From Figure 2.14 and Figure 2.15, we see that the NRP strategy is the only experimentally proven method capable of achieving high electron number density, temperatures under 2000 K, and low power consumption. In this study, we seek to extend the NRP non-thermal plasma regime to the lowest gas

temperature possible, which involves overcoming strong net electron attachment at lower temperatures. It is unknown at which temperature attachment eventually limits the production of non-thermal NRP plasmas. By achieving this goal, we could cover the widest range of applications shown in Figure 2.7.

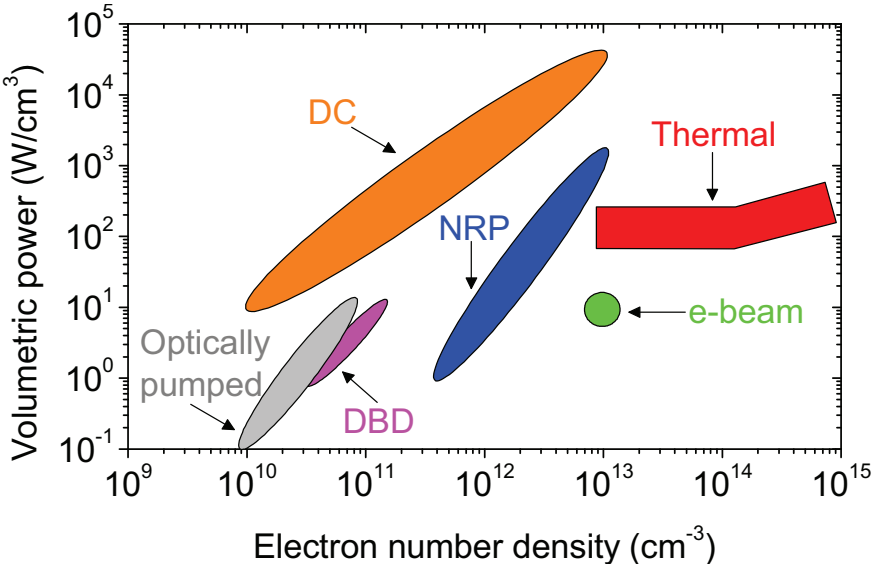

Figure 2.15: Power budgets of plasmas produced by methods discussed in this section as a function of electron number density. The power budget concerns the energy deposited in the plasma, not the total input power of the generator.

2.3.3 The Nanosecond Repetitively Pulsed (NRP) strategy

The use of high-voltage pulses for gas excitation first found application in low-pressure CO_2 mixtures for pulsed gas lasers in the 1970s [2.42, 2.43]. The possibility of using high-voltage nanosecond pulses to produce active species efficiently at higher pressures was demonstrated by Starikovskaia *et al* [2.44]. They investigated the spatio-temporal structure of Fast Ionization Waves (FIW) in discharges in air and N_2 at 0.5-100 torr produced by 10-15 kV negative pulses with FWHM=25 ns and rise/fall times of 3-5 ns, applied repetitively from 40-82 Hz. Electrons and excited particles are produced mostly behind the FIW front in relatively weak reduced electric fields of about 100 V/cm/torr.

The Stanford group [2.45-2.47] then proposed and demonstrated Nanosecond Repetitively Pulsed (NRP) plasmas as a way to reduce significantly the power budget required to sustain high electron number densities in atmospheric pressure air. The difference with earlier strategies lies in the very high repetition rate (10-100 kHz) chosen to match the recombination times of active species such as electrons. They showed in particular that power budget reductions of 2 to 3 orders of magnitude with respect to DC glow discharges were possible [2.47]. This work had been conducted from 1997-2002 with support from the "Air Plasma Ramparts Program" of the Air Force Office of Scientific Research (AFOSR) and the Department of Defense (DoD). Using a 10-ns, 10-kV, 100-kHz repetitive nanosecond pulse generator, they produced stable glow discharges in atmospheric pressure air at 2000 K with average electron densities of 1 to

2×10^{12} cm^{-3} and an experimental power budget of 12 W/cm^3, which is close to the theoretical value of 9 W/cm^3. The electrode gap was 1 cm and the pulsed electric field was ~5 kV/cm. Figure 2.16 is a schematic diagram of the NRP strategy, and Figure 2.17 shows time-resolved images of the development of the discharge in diffuse mode.

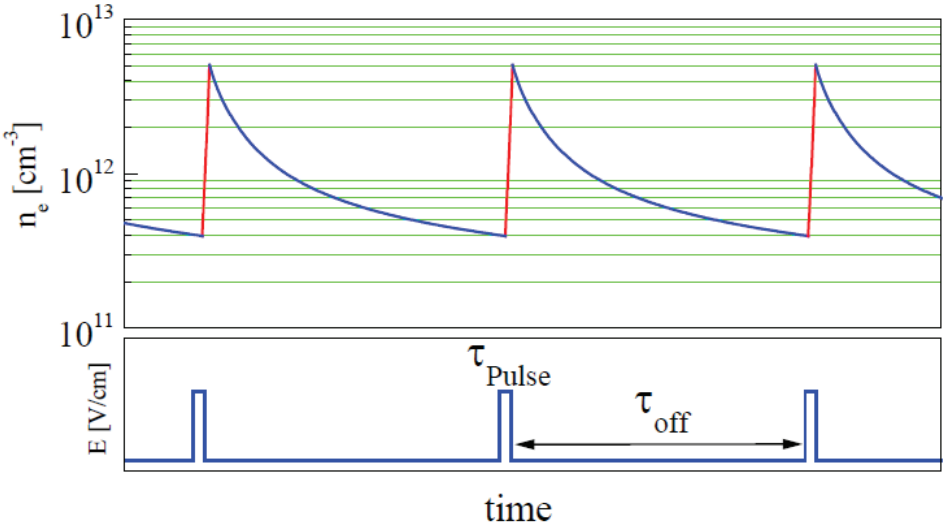

Figure 2.16: The Nanosecond Repetitively Pulsed (NRP) strategy for generating atmospheric pressure air plasmas. Taken from [2.46].

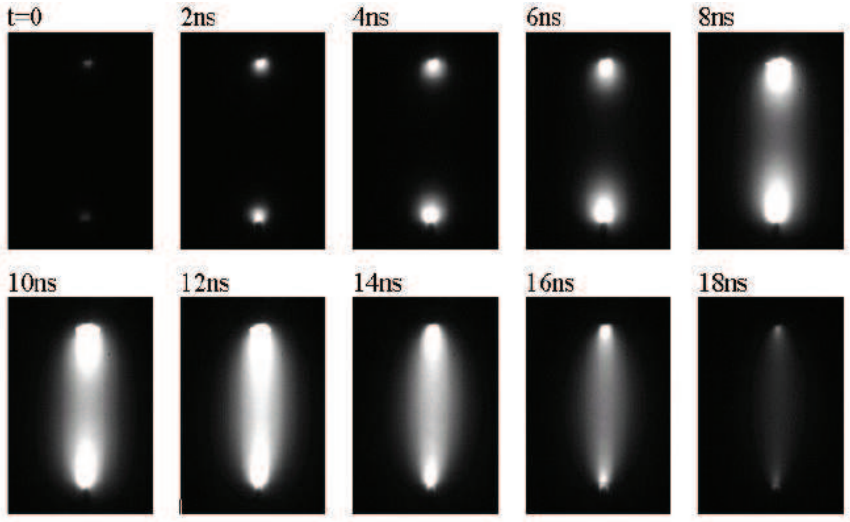

Figure 2.17: Time-resolved images of the NRP glow plasma in terms of the time after the beginning of high-voltage pulse. Taken from [2.46].

The NRP strategy consists of two parts:

1. The use of high-voltage nanosecond-duration pulses.
2. The application of these pulses at high Pulse Repetition Frequency (PRF). State-of-the-art generators are currently able to achieve PRFs up to 500 kHz.

The first part of the NRP strategy is the choice of using high-voltage nanosecond pulses to ionize efficiently without inducing the glow-arc transition. Applying a high electric field causes the Electron Energy Distribution Function (EEDF) to develop a large high-energy tail, such that significant numbers of electrons are accelerated to energies at which the electron-impact ionization cross-section (σ_i) is much greater than the cross-section for vibrational excitation (σ_v). Figure 2.18 shows electron-impact cross-sections for various processes in N_2.

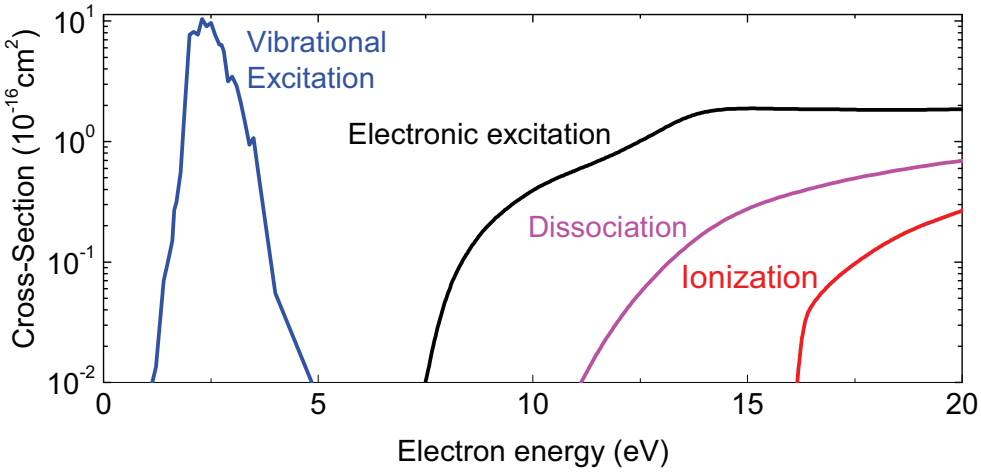

Figure 2.18: Cross-sections for electron-impact processes in N_2, taken from [2.22].

Figure 2.19 shows the EEDF at various times following the application of a 100-Td reduced electric field, calculated using the Boltzmann solver ELENDIF. Comparison of the graphs shows that after the field has been applied for just 100 ps, a much greater proportion of the electrons have energies greater than 10 eV, for which $\sigma_i > \sigma_v$.

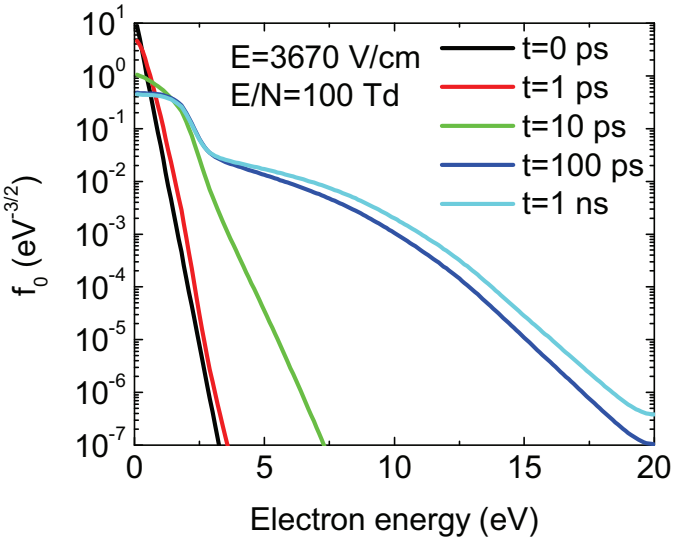

Figure 2.19: EEDF at times after the application of a 100-Td reduced electric field, calculated using ELENDIF.

When the electron-impact cross-sections for different modes of excitation from Figure 2.18 are multiplied by the EEDF from Figure 2.19, we obtain the fractions of the total power dissipated in each mode as a function of the reduced electric field (E/N), as shown in Figure 2.20. Relatively efficient ionization occurs for E/N>100 Td.

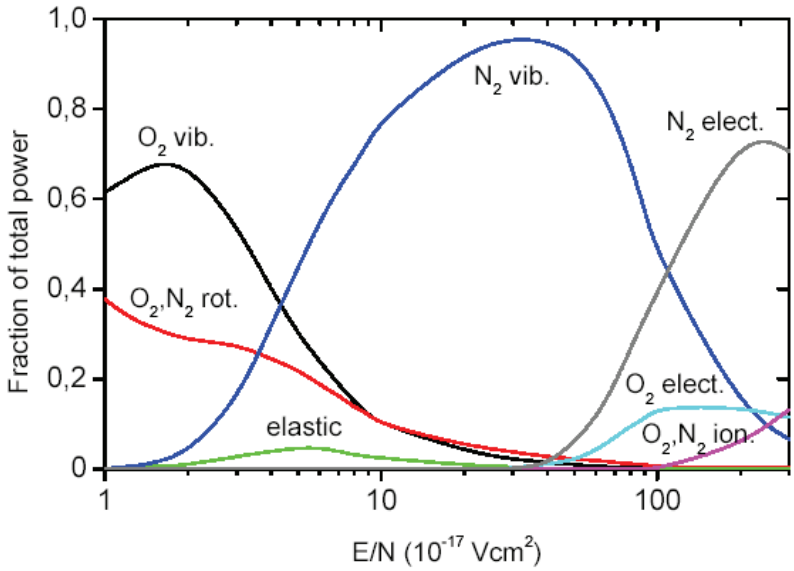

Figure 2.20: Fractions of power dissipated in different modes of excitation for air as a function of reduced electric field. Taken from [2.48, 2.49].

The NRP strategy involves applying a strong field to ionize efficiently and then turn it off after about 10 ns. If the field is not switched off, as is the case with DC discharges, the glow-arc transition quickly occurs. To avoid this in DC discharges, the electric field strength must be reduced, to the detriment of the ionization efficiency, as vibrational excitation of N_2 then consumes more than 99% of the input power.

Thus, to generate an average electron number density of 10^{12} cm^{-3} in 1-atm air at 2000 K, the DC field is 1.6 kV/cm, whereas the NRP field at PRF=30 kHz is 5.3 kV/cm [2.46]. Consequently, the volumetric power consumption for the NRP plasma to produce 10^{12} cm^{-3} of electrons is 10 W/cm^3, much less than the 3 kW/cm^3 dissipated by the DC plasma for the same electron number density. Figure 2.21 compares the power requirements for DC and NRP glow plasmas as a function of desired electron number density.

The second part of the NRP strategy is to choose the appropriate PRF such that the time interval between pulses is shorter than the characteristic recombination time of active species. In this way, the accumulative and synergetic effect of repeated pulsing achieves the desired steady-state behavior. This depends strongly on the electron recombination rate following a pulse, which determines the number of seed electrons available to the upcoming pulse for ionization. The electron recombination rate is the net rate of all the individual electron processes. At 2000 K, recombination is effectively due to a single reaction, the dissociative recombination of electrons with NO^+ [2.46]:

$$NO^+ + e \rightarrow N + O \tag{2.1}$$

As NO^+ is the dominant ion, the electron population can be approximated as:

$$\frac{dn_e}{dt} = -k_r n_e n_{NO^+} \approx -k_r n_e^2 \tag{2.2}$$

The reaction rate for dissociative recombination with NO^+ at 2000 K is $k_r=10^{-7}cm^3/s$. The solution in terms of the target maximum electron number density (n_{e1}), the target minimum electron number density (n_{e0}), and the recombination time (τ_r) is:

$$n_{e0} = \frac{n_{e1}}{1 + k_r \tau_r n_{e1}} \tag{2.3}$$

Thus, for $n_{e1}=10^{12}$ cm^{-3} and $n_{e0}=10^{11}$ cm^{-3}, the electron recombination time is $\tau_r=90$ μs. Hence, PRFs of 30 kHz and 100 kHz were chosen for the NRP plasmas generated at 2000 K, and Figure 2.22 demonstrates that these expectations were indeed met experimentally.

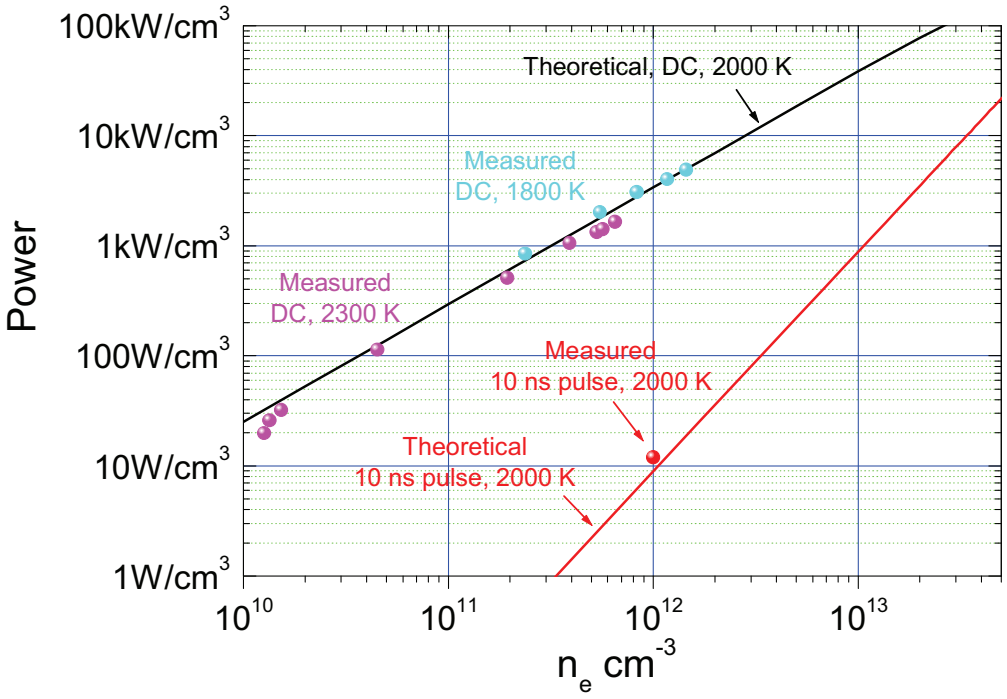

Figure 2.21: Measured and calculated power budgets for DC and NRP plasma generation as a function of the electron number density. Taken from [2.46].

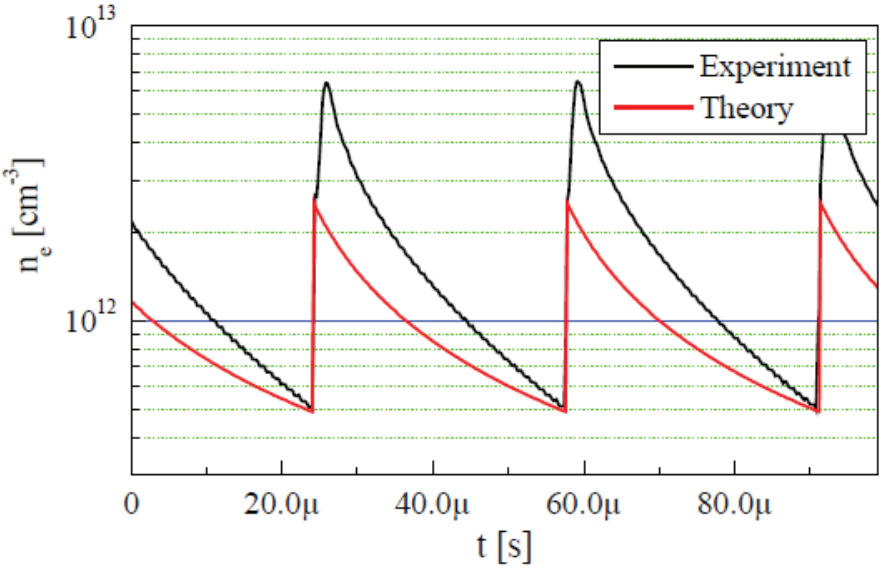

Figure 2.22: Electron number density as a function of time for an NRP atmospheric-pressure air glow plasma. T_g=2000 K, PRF=30 kHz. Taken from [2.46].

2.4 Recent developments in NRP plasma research

In this section we discuss research in NRP plasmas concerning their basic physics, methods for improving their performance in certain respects, and the measured active species that they produce.

Electrode array for multiple discharges

Takaki *et al* [2.50] generated NRP diffuse plasmas in N_2 using a needle-array electrode and a pulse generator capable of rise times under 30 ns. Multiple streamers occurred that prevented the glow-to-arc transition because thermalization was inhomogeneous. There were two discharge regimes: one at constant voltage with increasing current, indicative of a normal glow, and another increasing in voltage with increasing current, characteristic of an abnormal glow. They estimated the space- and time-averaged electron densities in the positive column to be 1.8×10^{11} cm^{-3}.

Ozone concentration

Williamson *et al* [2.51] investigated AC (0.3-2 kHz) and NRP (PRF=50-600 Hz) surface DBDs in atmospheric pressure air. The NRP discharge was more diffuse and did not have multiple cathode spots observed in the AC discharge, as shown in Figure 2.23. Although the pulses applied across the electrodes were over 100 ns long, a 10-ns FWHM pulse appeared over the discharge gap itself because of the voltage drop across the dielectric. In addition, the 600-A peak discharge current occurs about 10 ns after the voltage pulse in the discharge gap. To gauge plasma-chemical efficiency, Willamson *et al* measured the ozone number density by UV absorption and found that NRP ozone production increased faster with increasing average deposited power than that of the AC

plasma. The maximum ozone density for the AC plasma was 3×10^{15} cm^{-3} at 25 W, compared to 8.5×10^{15} cm^{-3} at 20 W for the NRP plasma. For the same PRF, the AC plasma consumes less power than the NRP plasma but also produces less ozone.

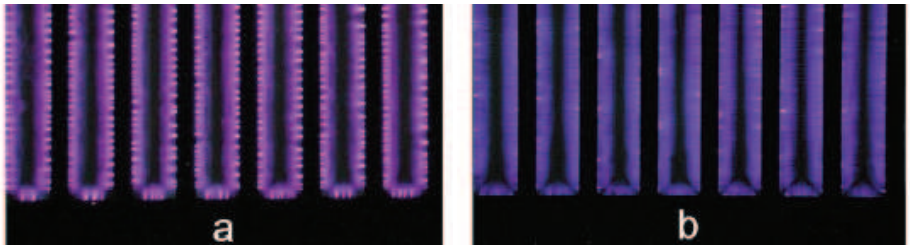

Figure 2.23: Images of surface DBDs in atmospheric air for (*a*) 7 kV, 3 kHz AC excitation and (*b*) 15 kV NRP negative polarity excitation at PRF=600 Hz. Taken from [2.51].

Atomic oxygen concentration

Ono *et al* [2.52] measured atomic oxygen in a pulsed DBD using two-photon absorption laser-induced fluorescence (TALIF). Negative (-40 kV) or positive (+30 kV) NRP DBDs at PRF=10 Hz were generated in an N_2-O_2 mixture at atmospheric pressure. Although the voltage pulses had long tails, the pulse width of the current was ~50 ns. The decay rate of atomic oxygen increased linearly with O_2 concentration, decaying mainly via third-body ozone creation, $O + O_2 + M \rightarrow O_3 + M$. The rate coefficient was estimated to be 2.2×10^{-34} cm^6/s for the negative DBD and 0.89×10^{-34} cm^6/s for the positive DBD. The atomic oxygen lifetimes were found to exceed 10 μs.

Ionization waves

Pancheshnyi *et al* [2.53] experimentally investigated cathode-directed streamer NRP plasmas in air at 300-760 torr and compared the measured anode current, streamer propagation velocity, and channel diameter with simulations. The pulses were of -12 kV amplitude, FWHM=22 ns, rise/fall times of 8 ns, and PRF=0.5-10 Hz. The electric field in the streamer head is roughly independent of pressure, while the electron number density decreases with increasing pressure by an order of magnitude. The measured streamer velocity decreased with gas pressure. In addition, the discharge branching pattern varied significantly with pressure, with a highly branched flash for p>680 torr, both branched and single channel streamers for p=500-900 torr, and only single channel streamers for p<470 torr.

Breakdown initiation and delay time

Shao *et al* [2.54] studied NRP breakdown in dry air, particularly in terms of the breakdown delay following pulse application and the Repetitive Stress Time (RST), which is the time of the first breakdown event after the first pulse. Their generator produced 60-100 kV pulses at PRF up to 1 kHz. The discharge gap distance was 5-20 mm. The breakdown delay and RST both deceased with increasing PRF. Shao *et al* postulated that runaway electrons played a role in their discharges, noting that the measured delay times were longer than those predicted by streamer theory.

2.5 Conclusion

In this chapter we discussed Nanosecond Repetitively Pulsed (NRP) plasmas in air at atmospheric pressure and how they can uniquely address the needs of potential applications. First, we summarized the applications and showed that many require a non-thermal plasma source operating within certain gas temperature limits. Therefore, the plasma source with the widest temperature range is the most versatile, in particular one that works at the lowest possible temperature. We then presented an overview of thermal and non-thermal plasma generation methods and showed that only the NRP method has been demonstrated to produce atmospheric pressure air plasmas with high electron densities at low temperature and for low power budgets. Finally, we outlined the basic principles of the NRP method and recent research in NRP plasmas.

2.6 References

[2.1] K. H. Becker, U. Kogelschatz, K. H. Schoenbach, and R. J. Barker 2004 *Non-Equilibrium Air Plasmas at Atmospheric Pressure* (Bristol: IOP Publishing).

[2.2] E. Stoffels, I. E. Kieft, R. E. J. Sladek, L. J. M. van den Bedem, E. P. van der Laan, M. Steinbuch, *Plasma Sources Sci. Tech.* **15** (2006) S169-S180.

[2.3] A. Schütze, J. Y. Jeong, S. E. Babayan, J. Park, G. S. Selwyn, and R. F. Hicks, *IEEE Transactions on Plasma Science* **26**(6) (1998) 1685-1694.

[2.4] H. W. Herrmann, I. Henins, J. Park, and G. S. Selwyn, *Phys. Plasmas* **6**(5) (1999) 2284-2289.

[2.5] F. Massines, P. Ségur, N. Gherardi, C. Khamphan, A. Ricard, *Surface and Coatings Tech.* **174-175** (2003) 8-14.

[2.6] R. Dorai and M. J. Kushner, *J. Phys. D: Appl. Phys.* **35** (2002) 2954-2968.

[2.7] J. S. Chang, K. Urashima, Y. X. Tong, W. P. Liu, H. Y. Wei, F. M. Yang, and X. J. Liu, *J. Electrostatics* **57** (2003) 313-323.

[2.8] J. P. Boeuf, Y. Lagmich, Th. Callegari, and L. C. Pitchford, *37th AIAA Plasmadynamics and Lasers Conference*, AIAA Paper 2006-3574, San Francisco, California, June 5-8, 2006.

[2.9] A. V. Likhanskii, M. N. Schneider, S. O. Macheret, and R. B. Miles, *45th AIAA Aerospace Meeting and Exhibit*, AIAA Paper 2007-633, Reno, Nevada, January 8-11, 2007.

[2.10] P. Bérard, D. A. Lacoste, C. O. Laux, AIAA Paper 2007-4611, *38th Plasmadynamics and Lasers Conference*, Miami, Florida, June 2007.

[2.11] P. Bérard, Ph.D. Thesis, Ecole Centrale Paris, 2007.

[2.12] P.-Q. Elias, B. Chaneutz, S. Larigaldie, D. Packan, *AIAA Journal* **45**(9) (2007) 2237-2245.

[2.13] P.-Q. Elias, Ph.D. Thesis, ONERA, 2007.

[2.14] M. Nishihara, N. B. Jiang, J. W. Rich, W. R. Lempert, I. V. Adamovich, S. Gogineni, *Phys. Fluids* **17**(10) (2005) 106102.

[2.15] R. J. Vidmar, *IEEE Transactions on Plasma Science* **18**(4) (1990) 733-741.

[2.16] U. S. Environmental Protection Agency Office of Air Quality Planning and Standards, "*NOx - How Nitrogen Oxides Affect the Way We Live and Breathe,"* 1998.

[2.17] G. Pilla, D. Galley, D. A. Lacoste, F. Lacas, D. Veynante, C. O. Laux, *IEEE Transactions of Plasma Science* **34**(6) (2006) 2471-2477.
[2.18] G. Pilla, Ph.D. Thesis, Ecole Centrale Paris, 2007.
[2.19] S. V. Panchenshnyi, D. A. Lacoste, A. Bourdon, and C. O. Laux, *IEEE Transactions of Plasma Science* **34**(6) (2006) 2478-2487.
[2.20] S. M. Starikovskaia, *J. Phys. D: Appl. Phys.* **39**(16) (2006) R265-R299.
[2.21] L. Yu, C. O. Laux, D. M. Packan, and C. H. Kruger, *J. Appl. Phys.* **91**(5) (2002) 2678-2686.
[2.22] Yu. P. Raizer, 1997 *Gas Discharge Physics* (Berlin: Springer).
[2.23] R. H. Stark and K. H. Schoenbach, *Appl. Phys. Lett.* **74**(25) (1999) 3770-3772.
[2.24] F. Leipold, R. H. Stark, A. El-Habachi and K. H. Schoenbach, *J. Phys. D: Appl. Phys.* **33** (2000) 2268-2273.
[2.25] C. O. Laux, T. G. Spence, C. H. Kruger, and R. N. Zare, *Plasma Sources Sci. Tech.* **12** (2003) 125-138.
[2.26] Z. Machala, C. O. Laux, C. H. Kruger, and G. V. Candler, *42th AIAA Aerospace Meeting and Exhibit*, AIAA Paper 2004-355, Reno, Nevada, January 5-8, 2004.
[2.27] F. Iza and J. A. Hopwood, *IEEE Transactions on Plasma Science* **31**(4) (2003) 782-787.
[2.28] J. Kim and K. Terashima, *Appl. Phys. Lett.* **86**(19) (2005) 191504.
[2.29] G. Ding, J. E. Scharer, and K. Kelly, *Phys. Plasmas* **8** (2001) 334-342.
[2.30] U. Kogelschatz, *Plasma Chem. and Plasma Proc.* **23**(1) (2003) 1-46.
[2.31] S. Okazaki, M. Kogoma, M. Uehara, and Y. Kimura, *J. Phys. D: Appl. Phys.* **26**(5) (1993) 889-892.
[2.32] F. Massines, A. Rabehi, P. Decomps, R. B. Gadri, P. Segur, C. Mayoux, *J. Appl. Phys.* **83**(6) (1998) 2950-2957.
[2.33] K.V. Kozlov, R. Brandenburg, H.-E. Wagner, A. M. Morozov, and P. Michel, *J. Phys. D: Appl. Phys.* **38** (2005) 518-529.
[2.34] J.R. Roth, J. Ráhel, X. Dai, and D. M. Sherman, *J. Phys. D: Appl. Phys.* **38** (2005) 555-567.
[2.35] A. P. Yalin, Z. Q. Yu, O. Stan, K. Hoshimiya, A. Rahman, V. K. Surla, and G. J. Collins, *Appl. Phys. Lett.* **83**(14) (2003) 2766-2768.
[2.36] A. Rahman, A. P. Yalin, V. Surla, O. Stan, K. Hoshimiya, Z. Yu, E. Littlefield, and G. J. Collins, *Plasma Sources Sci. Tech.* **13** (2004) 537-547.
[2.37] E. Plönjes, P. Palm, I. V. Adamovich, and J. W. Rich, *J. Phys. D: Appl. Phys.* **33** (2000) 2049-2056.
[2.38] I. V. Adamovich, *J. Phys. D: Appl. Phys.* **34** (2001) 319-325.
[2.39] S. O. Macheret, M. N. Shneider, R. B. Miles, *33rd AIAA Thermophysics Conference*, AIAA Paper 1999-3635, Norfolk, Virginia, June 28-July 1, 1999.
[2.40] S. O. Macheret, M. N. Shneider, R. B. Miles, *31st AIAA Plasmadynamics and Lasers Conference*, AIAA Paper 2000-2569, Denver, Colorado, June 19-22, 2000.
[2.41] S. O. Macheret, M. N. Shneider, and R. B. Miles, *Phys. Plasmas* **8**(5) (2001) 1518-1528.
[2.42] J. P. Reilly, *J. Appl. Phys.* **43** (1972) 3411-3416.
[2.43] A. E. Hill, *Appl. Phys. Lett.* **22** (1973) 670-673.
[2.44] S. M. Starikovskaia, N. B. Anikin, S. V. Pancheshnyi, D. V. Zatsepin, and A. Yu. Starikovskii, *Plasma Sources Sci. Tech.* **10** (2001) 344-355.

[2.45] C. H. Kruger, C. O. Laux, L. Yu, D. M. Packan, and L. Pierrot, *Pure Appl. Chem.* **74**(3) (2002) 337-347.
[2.46] D. M. Packan, Ph.D. Thesis, Stanford University, 2003.
[2.47] M. Nagulapally, G. V. Candler, C. O. Laux, L. Yu, D. M. Packan, C. H. Kruger, R. Stark, K. H. Schoenbach, *31st AIAA Plasmadynamics and Lasers Conference*, AIAA Paper 2000-2417, Denver, Colorado, June 19-22, 2000.
[2.48] N. L. Aleksandrov, F. I. Vysikailo, R. S. Islamov, I. V. Kochetov, A. P. Napartovich, V. G. Peygov, *Teplofiz. Vys. Temp. (translated in High Temperature)* **19**(1) (1981) 22-27.
[2.49] W. L. Nighan, *Phys. Rev. A* **2** (1970) 1989-2000.
[2.50] K. Takaki, H. Kirihara, C. Noda, S. Mukaigawa, and T. Fujiwara, *Plasma Proc. and Polymers* **3**(9) (2006) 734-742
[2.51] J. M. Williamson, D. Trump, P. Bletzinger, and B. N. Ganguly, *J. Phys. D: Appl. Phys.* **39**(20) (2006) 4400-4406.
[2.52] R. Ono, Y. Yamashita, K. Takezawa, and T. Oda, *J. Phys. D: Appl. Phys.* **38** (2005) 2812-2816.
[2.53] S. Pancheshnyi, M. Nudnova, and A. Starikovskii, *Phys. Rev. E* **71** (2005) 016407.
[2.54] T. Shao, G. Sun, P. Yan, J. Wang, W. Yuan, Y. Sun, and S. Zhang, *J. Phys. D: Appl. Phys.* **39** (2006) 2192-2197.

Chapter 3

Experimental Setup

3.1 Introduction

In this chapter, we present the experimental system used in this study and the performance characteristics of its most important components. We begin in Section 3.2 by describing the plasma generation and measurement systems. Sections 3.3, 3.4, and 3.5 present the technical details of the setup for spectrally resolved optical diagnostics (with a monochromator and an ICCD camera), the procedure for calibration in absolute intensity, and the scheme for synchronization between plasma generation and detection. This is followed in Sections 3.6, 3.7, and 3.8 by a discussion of the PMT module, including its calibration in relative intensity and its synchronization with plasma generation. In Section 3.9 we examine the output characteristics of the high-voltage pulse generator. Finally, in Section 3.10 we validate the high-speed performance of the passive high-voltage probe used to measure voltage.

3.2 Plasma generation and measurement system

In this section, we provide an overview of the experimental facility. Figure 3.1 and Figure 3.2 show an image and a diagram, respectively, of the experimental setup for plasma generation and the electrical and optical measurement systems.

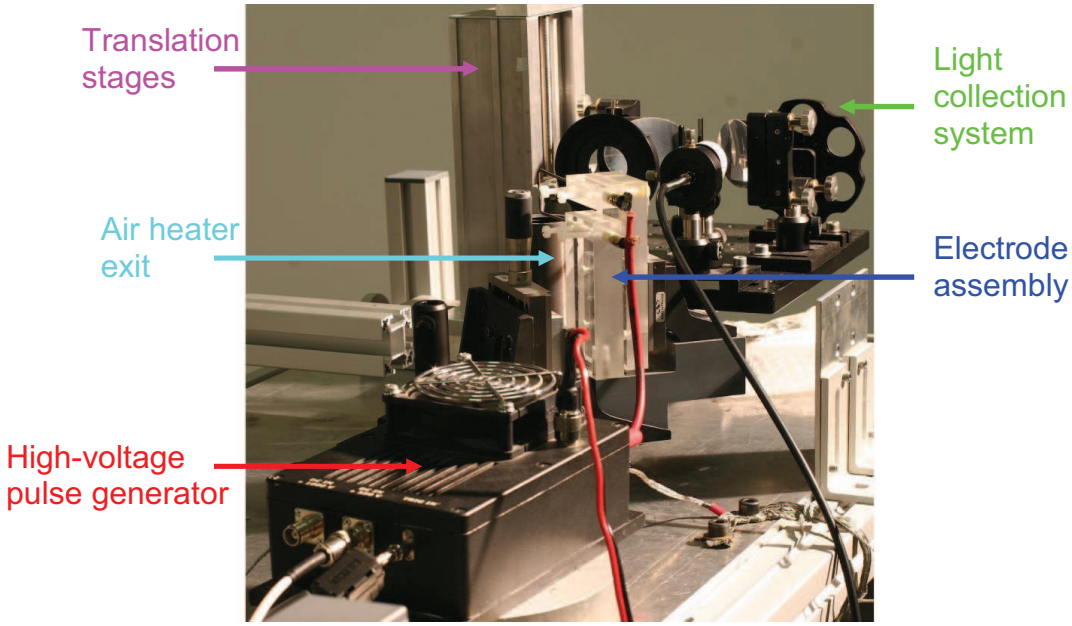

Figure 3.1: Image of several principal components of the experimental setup.

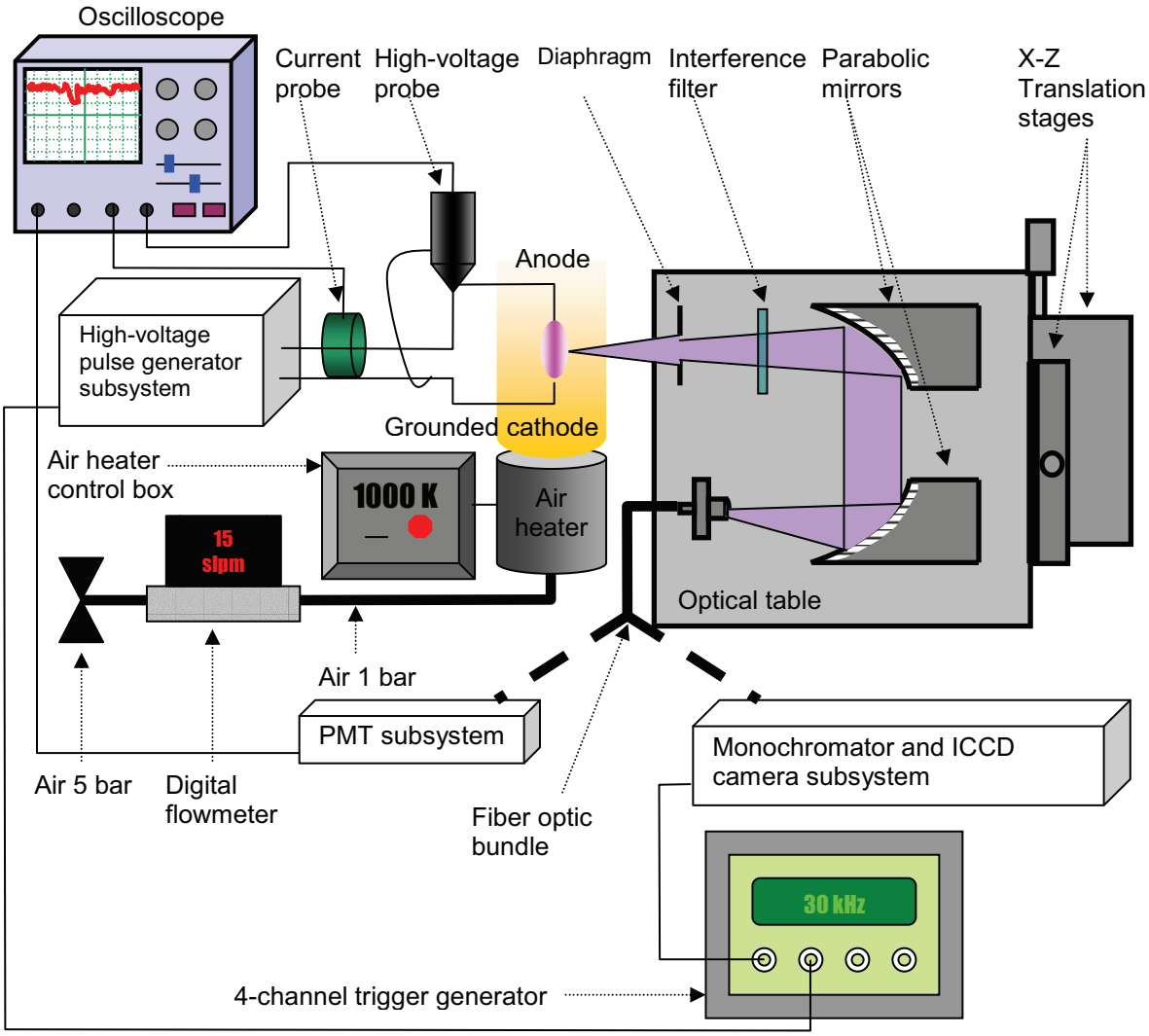

Figure 3.2: Schematic diagram of the experimental setup. The high-voltage generator, PMT, and monochromator-ICCD camera subsystems are discussed individually in later sections of this chapter. The thick dotted lines indicate that the fiber optic bundle connects either to the PMT or monochromator-camera subsystems.

Air heater subsystem

Figure 3.3 shows a digital camera image of the air heater exit and the electrode assembly. The discharge is generated in airflow pre-heated to 300-1000 K by a resistive heater (Osram Sylvania 8 kW Hot Air System). A Sierra Instruments Smart Trak digital mass flow meter calibrated for air regulates compressed laboratory-grade air from 5 atm down to 1 atm. Its flow rate can be adjusted up to 166 slpm. This air then flows into the resistive heater where it passes through a ceramic heating coil. An internal thermocouple located 2.5 cm before the heater exit measures the heated air temperature to feed the temperature regulation control loop. Separate thermocouple measurements ~2 cm downstream of the heater exit, where the discharge gap is located, confirmed that the temperature remained stable within 50°C of the reading of the internal thermocouple over run times of several hours.

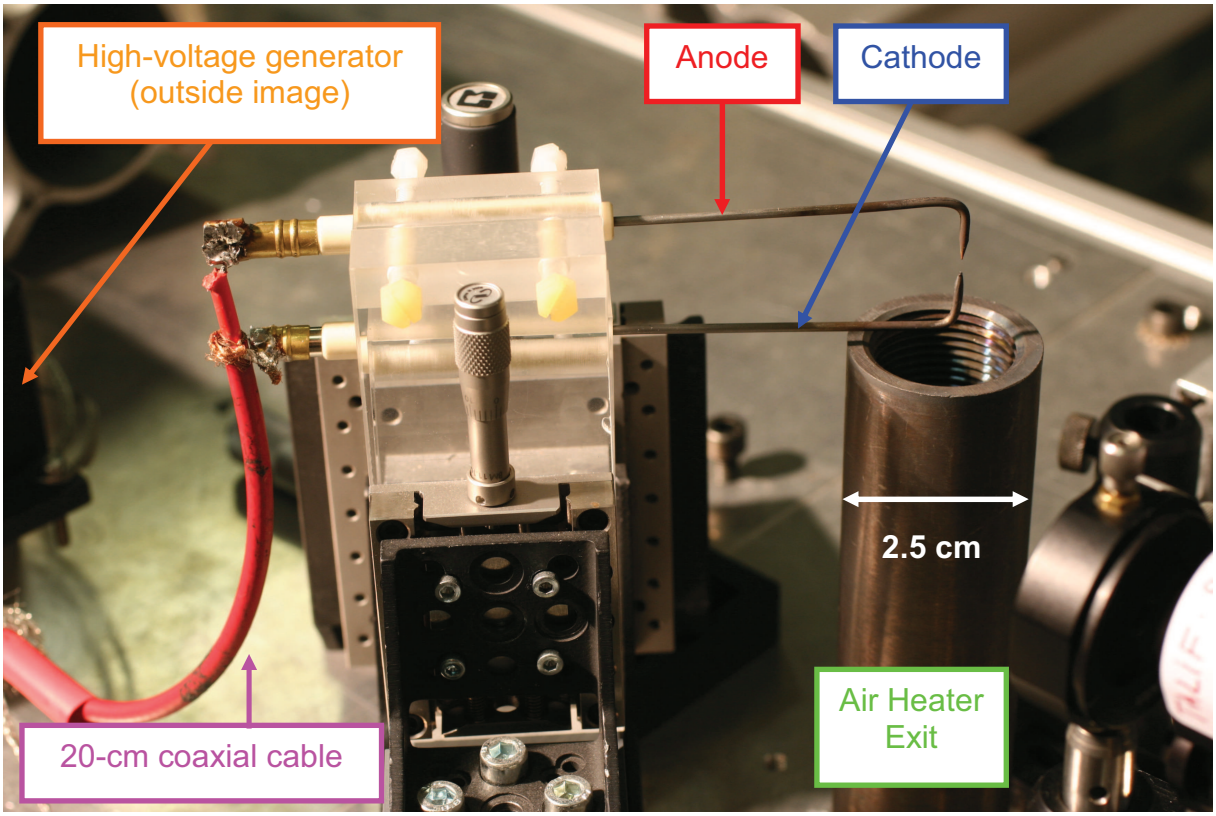

Figure 3.3: Image of air heater exit and electrode assembly.

High-voltage pulse generation subsystem

The plasma discharge is produced by applying nanosecond high-voltage pulses between two refractory steel electrodes, as shown in Figure 3.3. The pulses are produced by a generator (FID Technologies FPG 10-30MS) that produces pulses with rise/fall times of 5 ns, a flat top of 10 ns at greater than 90% of the maximum voltage, and amplitudes up to +5 kV into a matching 75 Ω impedance, or up to +10 kV into an open circuit. The pulse repetition frequency (PRF) ranges from 0-30 kHz. Section 3.9 describes the high-voltage pulse generator subsystem further, and Appendix A contains a summary of its operating principles. The electrodes are placed in a vertical pin-to-pin configuration with the anode above the grounded cathode. We re-sharpened the tips of each electrode manually as needed whenever they became worn.

Electrical measurement subsystem

Measurements of the voltage across the electrodes (V_p) were obtained using a 100-MHz bandwidth high-voltage probe (Lecroy PPE20kV). We measured the discharge current (I_p) using a Pearson coil current monitor (Model 6585) with a 3 dB cutoff low frequency of 400 Hz, a ±3 dB high frequency of 250 MHz, a 1.5 ns rise time, and a 1A/1V current-to-voltage conversion when terminated with a 1-MΩ impedance. A low-voltage attenuator (Barth Model 2-20) not shown in Figure 3.2 with 20 dB (10X) attenuation and 0-20 GHz bandwidth immediately followed the current monitor. The validation of the probes' high-speed performance is discussed in Section 3.10. A 350-MHz (maximum 1 or 2 GS/s) LeCroy Waverunner 434 or a 1-GHz (maximum 5 or 10 GS/s) LeCroy Wavepro 7000 oscilloscope was used to record the signals from the probes. Unless indicated otherwise, all measurements recorded with the oscilloscopes presented in this thesis are averaged over 100 samples.

Light collection subsystem

Figure 3.4 shows a digital camera image of the light collection subsystem. For optical emission spectroscopy, two 90° off-axis parabolic UV-grade MgF_2-coated aluminum mirrors of 50-mm diameter (Janos Technologies) collected and focused light into a UV solarization-resistant fiber optic bundle (Ocean Optics QP600-2-SR-BX). The mirrors were placed in mirror mounts (Ultima U200-A38) with adjustment knobs for 3-D movement.

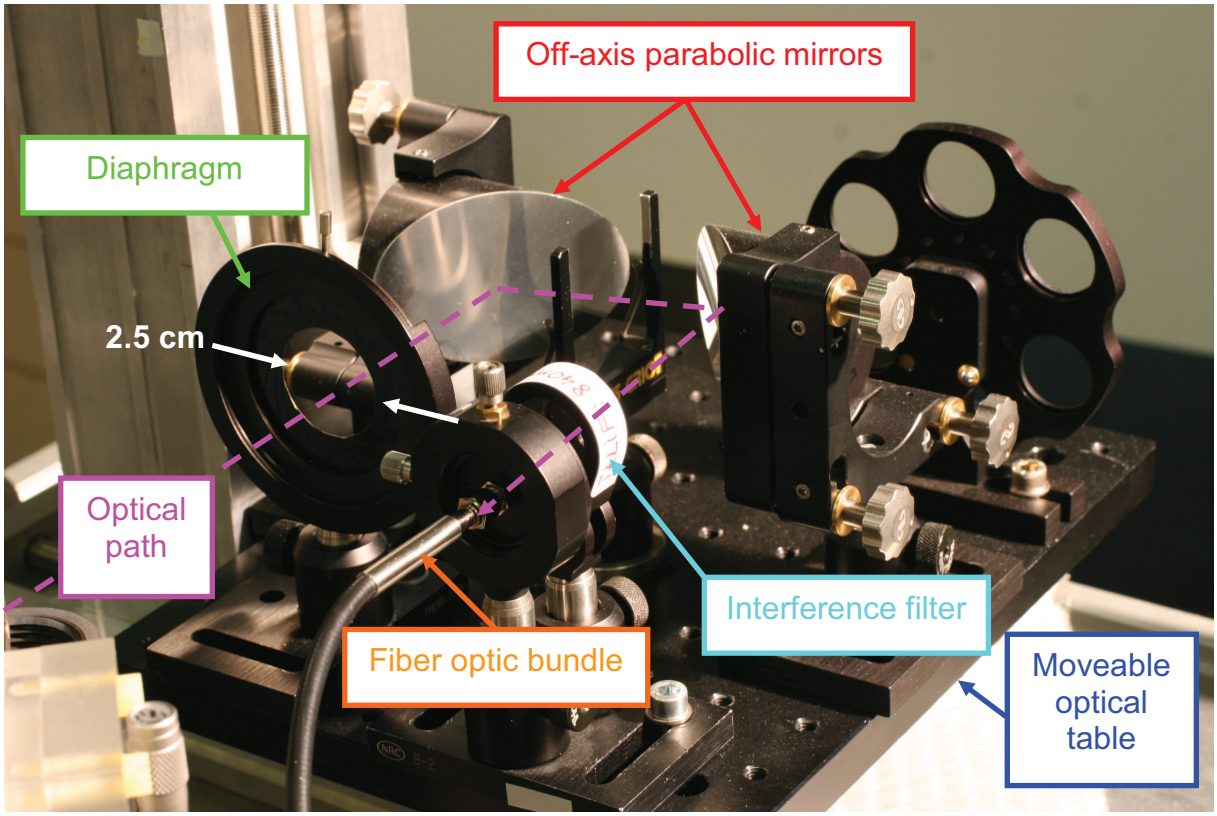

Figure 3.4: Image of the light collection subsystem.

A diaphragm placed before the collecting mirror was used to adjust the solid angle to control the intensity of the light collected. Whenever it was necessary to isolate a specific transition for photomultiplier tube measurements, a bandpass interference filter (e.g. Melles Griot 03 FIU 127 for the N_2 (C-B) 0-0 transition) was inserted into the optical path. The factory-tested characteristics of the N_2 (C-B) 0-0 filter are shown in Table 3.2. The above light collection system was placed on a 20×25 cm optical table that rested on an X-Z translation stage set (Velmex A4009K1-S4 UniSlide and B4909K1 Unislide), as shown in Figure 3.2.

Monochromator and ICCD camera subsystem

For some experiments, optical emission spectroscopy was performed using the monochromator and ICCD camera subsystem. The collected light entered a monochromator (Acton SpectraPro 2500i) for spectral filtering before final detection by an intensified CCD camera (Princeton Instruments PI-MAX). A detailed discussion of the monochromator-camera subsystem follows in Sections 3.3, 3.4, and 3.5.

PMT subsystem

For time-resolved optical emission measurements, a photomultiplier tube (PMT) module with a 1.4-ns rise time (Hamamatsu H9305-3) was used in place of the monochromator. Its signal was amplified using a 2-GHz high-speed amplifier (Hamamatsu C5594-44) and then recorded using the oscilloscope. A detailed discussion of the PMT module subsystem is presented in Sections 3.6, 3.7, and 3.8.

3.3 Specifics of the monochromator and ICCD camera subsytem

The Acton SpectraPro-2500i is a Czerny-Turner type monochromator whose specifications and nominal settings used in all experiments are listed in Table 3.1. Its schematic diagram is shown in Figure 3.5. Light from the fiber optic bundle enters the side entrance slit placed at the focal point of a collimating toroidal mirror. The collimated light is diffracted by the grating and then re-focused by a second toroidal mirror onto the CCD array of the PI-MAX camera. Each pixel of the CCD array serves as an exit slit, and an entire wavelength range can be scanned simultaneously. For the system used in this work, a typical scan covers 40 nm. Rotating the mirror or grating changes the wavelength range observed by the camera. Spectra from 200-900 nm can be measured with this system.

Table 3.1: Specifications and nominal settings used in all measurements for the monochromator-ICCD camera system.

SpectraPro2500i monochromator	
Optical path	90°
Mirrors	Original polished aspheric
Focal length	50 cm
Diffraction grating	600 grooves/mm blazed at 300 nm
Slit	100 μm at side entrance
Resolution	0.05 nm
Princeton PI-MAX Intensified CCD camera	
Image intensifier	Micro-channel plate (MCP)
Mode	Gate mode
CCD array dimensions	1024x1024 pixels
Shutter type	Electronic
Gain	255
Temperature control	Peltier-effect cooler at -20°C
Maximum background signal rejection ratio	5×10^{6}:1
Maximum image intensifier electronic gain	10,000
Minimum gate width	2 ns
Readout time	~1.2 s
Princeton Instruments ST-133 Controller with Programmable Timing Generator (PTG) Module	
ST-133 Timing mode	Internal sync
PTG Trigger	External
Operating mode	Gate mode

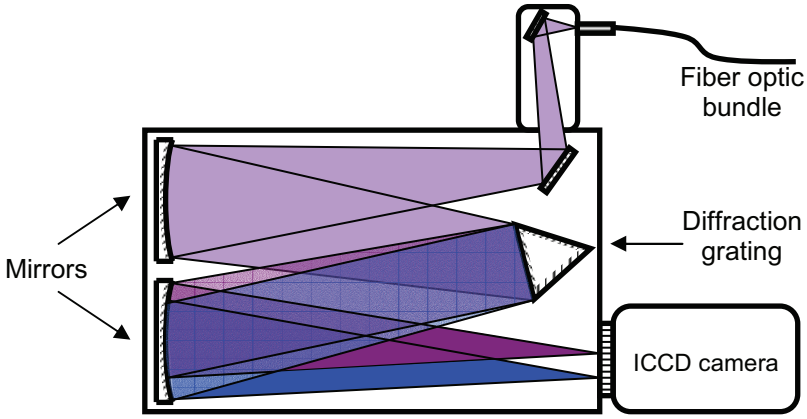

Figure 3.5: Schematic of monochromator and ICCD camera.

The Princeton Instruments PI-MAX intensified CCD camera can be used both for imaging and spectroscopy, and its key specifications are listed in Table 3.1. First, a photon that reaches the intensifier photocathode generates an electron via the photoelectric effect. This electron is subsequently accelerated through a Micro-Channel Plate (MCP), which is a type of high-gain Photo-Multiplier Tube (PMT). The electron multiplication amplifies the original signal. Upon striking a phosphor screen, the electrons produce visible photons that are detected by a CCD array. Thermally induced charge, or dark current, can build up in a CCD, and this statistical noise is known as dark noise. To reduce it, the CCD is cooled to -20°C with a Peltier-type thermo-electric cooler. The noise reduction factor achieved by cooling is significant: approximately a factor of 2 for every 6° reduction in temperature.

To take advantage of its fine time resolution and ensure a good signal-to-noise ratio, the camera is run in Gate mode. Figure 3.6 shows a timing diagram of camera operation in Gate mode. The bias voltage of the intensifier determines the gain, which can be switched on for desired time windows, or gate widths, as short as 2 ns. The intensifier opens this gate, i.e. switches to high gain, at a chosen gate delay following a trigger signal. Thus, the intensifier acts as a fast electronic shutter for the camera. Its exposure or acquisition time, during which charge collects in each CCD pixel, can be chosen to accumulate the light from a sequence of gates. The number of gates in such a sequence will be hereafter referred to as the number of "on-CCD accumulations." Increasing the number of on-CCD accumulations has the effect of increasing the signal-to-background ratio (S/B). This is because the dark noise originates primarily from the electronic noise generated from switching on the CCD array. For a single acquisition cycle, this occurs only once, and therefore the background noise is relatively constant. On-CCD accumulation is particularly effective for signal amplification when synchronized with repetitive phenomena, such as the plasmas studied in this work. The gate delay setting specifies the synchronization.

Following on-CCD accumulation, the CCD array is emptied of its charge for data collection during the readout phase. The data from repeated acquisition-readout cycles can be summed for "numerical accumulation" of the on-CCD accumulated signal, which serves to increase the signal-to-noise ratio (S/N) by averaging out random noise. Thus, to perform a particular measurement in Gate mode, four parameters must be specified: the gate width, the gate delay, the number of on-CCD accumulations, and the number of numerical accumulations. In the experiments reported in this thesis, we optimized these parameters for the highest possible S/B and S/N without saturation and within reasonable measurement times.

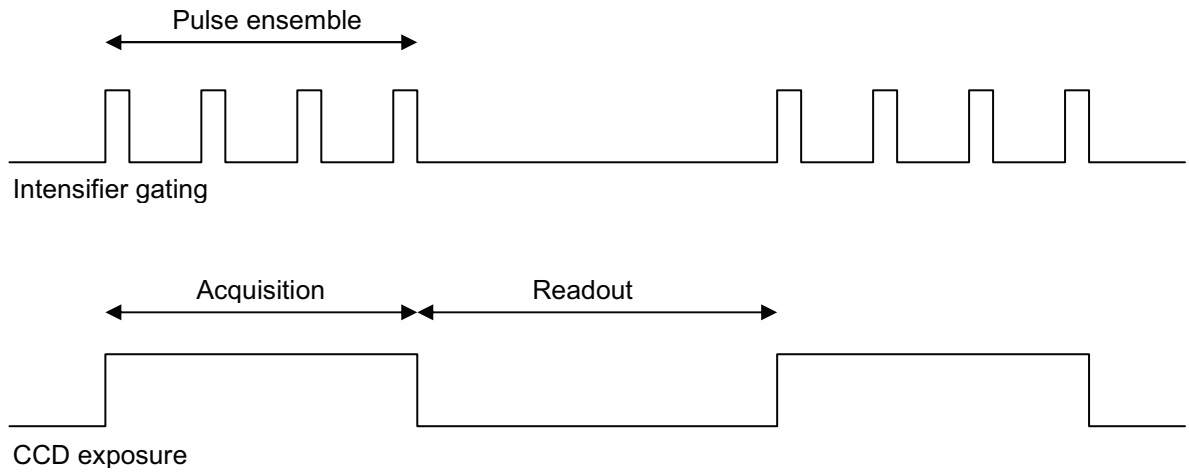

Figure 3.6: Timing diagram for the PI-MAX ICCD camera.

The ST-133 controller, which includes a Programmable Timing Generator (PTG) module, handles the coordination between the intensifier gating and the CCD exposure and readout. The PTG receives an external trigger signal, generates the signals to gate the intensifier, and also directs the ST-133 to handle the CCD acquisition and readout phases at the appropriate times. The ST-133 must be set in "Internal Sync" mode for the PTG to perform these tasks. These particular settings for the ST-133 and the PTG are summarized in Table 3.1. More details on synchronization of the camera with the discharge are found in Section 3.5.

Ideally, for measurements of a constant light source, the registered signal increases linearly with gate width and the number of on-CCD accumulations. This means that hypothetically if one photon is collected for a single 1-ns gate, then two photons should be registered for a single 2-ns gate or two 1-ns gates, and so on. Unfortunately, this is not exactly the case, and Figure 3.7 and Figure 3.8 show the actual number of photons counted as a function of the gate width and the number of on-CCD accumulations, respectively. We have therefore performed a calibration of the accumulation rate of the CCD system.

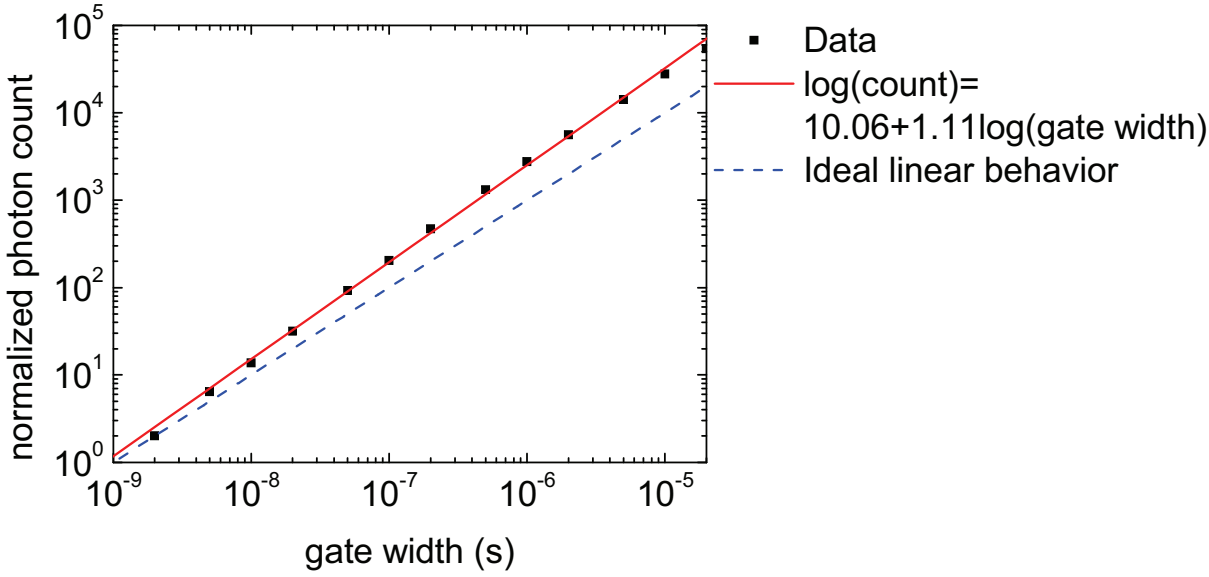

Figure 3.7: Measured photon count as a function of gate width (symbols) with a log-log fit (solid line) compared to ideal linear behavior (dotted line).

The data shown in Figure 3.7 are measurements of the emission of a stabilized radiation source (OL550 tungsten filament lamp) taken for different gate widths with a fixed number of on-CCD and numerical accumulations. Likewise, the data shown in Figure 3.8 are measurements of the lamp taken for different numbers of on-CCD accumulations with fixed gate width and number of numerical accumulations. If a measurement was taken near the CCD saturation limit, a second measurement was taken at reduced lamp intensity. The ratio between the two was used to normalize subsequent measurements at reduced lamp intensity. Finally, the measured data in Figure 3.7 were normalized to the 2-ns gate width data point such that two photons were counted for a single 2-ns gate. This is for the purpose of relating the photon counts registered for a given gate width to the hypothetical condition that one photon is counted per 1-ns gate. Note that a 2-ns gate width is the minimum achievable with our system. Likewise, the measured data in Figure 3.8 were normalized to the single on-CCD accumulation data point, such that one photon was counted for one on-CCD accumulation.

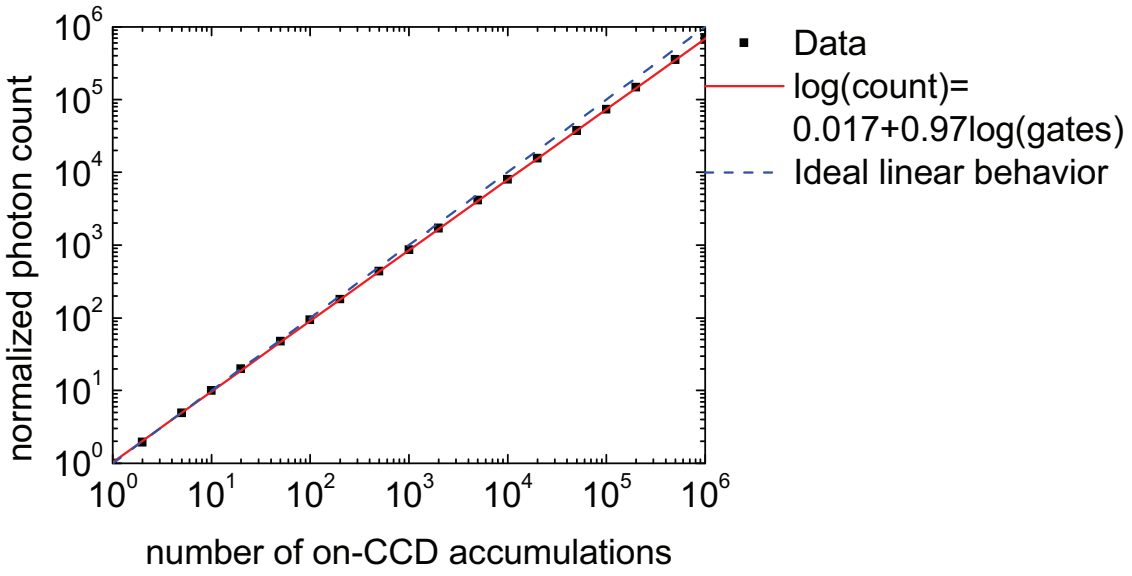

Figure 3.8: Measured photon count as a function of the number of on-CCD accumulations (symbols) with a log-log fit (solid line) compared to ideal linear behavior (dotted line).

Figure 3.7 and Figure 3.8 show that for small gate widths and numbers of on-CCD accumulations, the camera is nearly ideal. The deviation from linearity is minor for large numbers of on-CCD accumulations but significant for large gate widths. In both cases, the real behavior is well described by the fits given in the figures. Figure 3.7 and Figure 3.8 summarize the appropriate scaling factors for gate width and on-CCD accumulation, so that the calibration procedure discussed in Section 3.4 does not have to be repeated each time any of these parameters changes.

3.4 Calibration in absolute intensity of the monochromator and ICCD camera subsystem

This section presents the calibration in absolute intensity of the monochromator and ICCD camera subsystem. Each component of the measurement system has its own spectral response, beginning with the ambient air along the 4.5-m optical path from the discharge to the camera. Molecular oxygen absorbs strongly below 200 nm via its Schumann-Runge

continuum, which can be used to acquire the camera's dark noise by scanning the monochromator in this wavelength range.

The profile of the overall system spectral response above 200 nm is dominated by the response of the diffraction grating, which peaks at the blaze wavelength of 300 nm, and the radiant sensitivity of the photocathode. The UV-grade mirrors, solarization-resistant fiber optic bundle, and ICCD camera all have their lowest response around 200 nm. The system response (D_λ), in units of (counts/ns)/(W/cm^2/sr), is the product of the individual responses of each component.

To acquire the absolute system response, measurements were made with two standards of radiance with calibrations traceable to National Institute of Standards and Technology (NIST) standards. In the UV, an argon mini-arc manufactured by Arc Applications Research [3.1] was used, whose spectral radiance in the UV when supplied 40.0 A at about 35 V is shown in Figure 3.9.

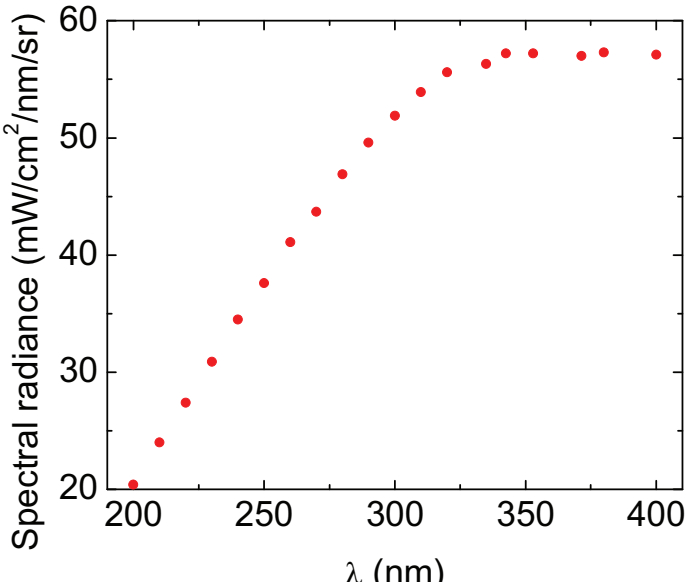

Figure 3.9: Spectral radiance of the argon miniarc supplied with 40 A at 35 V. Data taken from [3.1].

In the visible, a calibrated Optronic Laboratories OL550 tungsten ribbon-filament lamp with spectral radiance values traceable to NIST standards was used. The spectral radiance, when supplied with 15.0 A at about 5 V, is shown in Figure 3.10. The spectral radiance from a surface area A that emits a power Φ_λ over a solid angle Ω at an angle of incidence θ in the wavelength range $\Delta\lambda$ is defined as:

$$L = \frac{\mathrm{d}^5\Phi_\lambda}{\Delta\lambda \cdot \mathrm{d}A \cdot \mathrm{d}\Omega \cdot \cos\theta} \simeq \frac{\Phi_\lambda[\mathrm{W}]}{\Delta\lambda[\mathrm{nm}] \cdot A[\mathrm{cm}^2] \cdot \Omega[\mathrm{sr}]} \tag{3.1}$$

The approximation is valid for small A and Ω and at normal incidence. These conditions were true for all the measurements performed. The instrumental broadening of the monochromator is expressed by the spectral width $\Delta\lambda$, shown in Figure 3.11, and was measured using a Thorlabs HRP120 He-Ne laser. As shown in Table 3.1, the same entrance slit width and diffraction grating were used in all measurements. The effective exit slit width never changes, as it is the width of a CCD pixel. Therefore, the spectral width shown in Figure 3.11 is valid

for all measurements presented in this thesis. In Equation (3.1), $\Delta\lambda$=0.35 nm, the Full-Width Half-Maximum (FWHM) of the slit function. Finally, since the mirror collection system and iris aperture were in the same configuration for all discharge and calibration measurements, the solid angle was always the same. This meant that it did not have to be calculated explicitly to calibrate the system in absolute intensity.

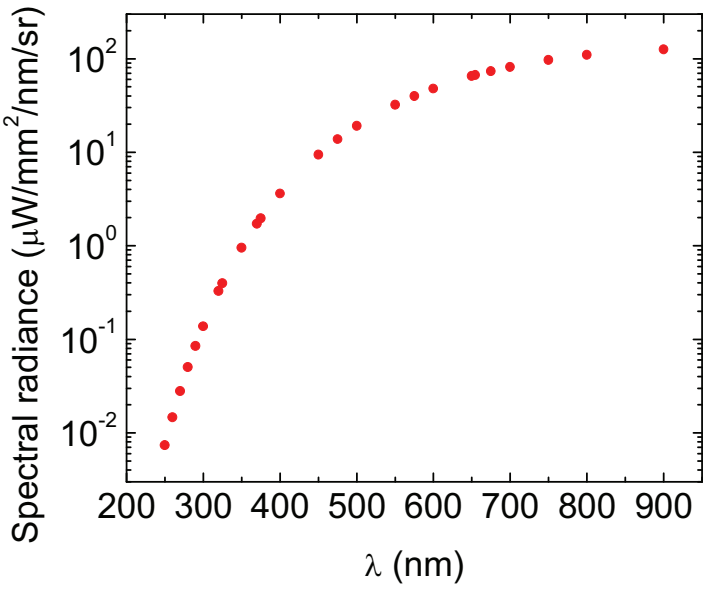

Figure 3.10: Spectral radiance of the OL550 tungsten lamp supplied with 15 A at about 5 V. Data taken from [3.2].

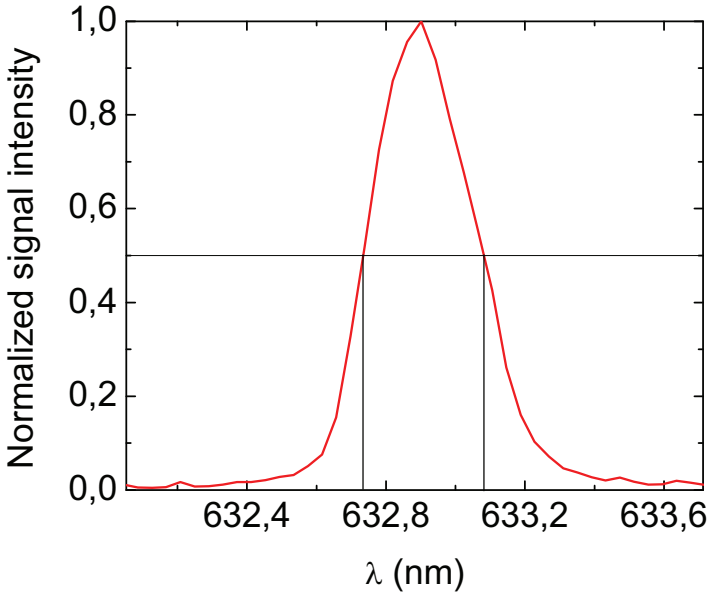

Figure 3.11: Measured slit function of the SpectraPro2500i monochromator with the settings shown in Table 3.1. It is approximated as a triangular profile with FWHM=0.35 nm.

The system response in intensity can be found for a particular set of measurement conditions by replacing the plasma under study with the standard of radiance. In this case, this involves placing the mini-arc or the tungsten lamp at the focal point of the collecting mirror and using

the same solid angle, monochromator, and camera settings as those for the corresponding discharge measurements.

Figure 3.12 shows the system response in the UV using the argon mini-arc for a given set of camera gating conditions. Using the scaling factors shown in Figure 3.7 and Figure 3.8, the measured data were reduced to count rate form and then divided by the argon mini-arc spectral response shown in Figure 3.9 to get the system response D_λ. This gives a direct relationship between the data count rate and the discharge's spectral radiance. The system loses considerable sensitivity in the deep UV, in part due to the fiber optic bundle's attenuation factor, which increases exponentially from 0.4 dB/m at 300 nm to 1.4 dB/m at 200 nm. In addition, the ICCD camera has low response at both ends of its 200-900 nm range. The lines that appear from 325-400 nm in the mini-arc spectrum are atomic lines that overlap the underlying continuum spectrum. The argon mini-arc spectral radiance data in Figure 3.9 concern only the continuum spectrum, avoiding wavelengths at which atomic lines appeared. Therefore, the calibration does not include the atomic lines.

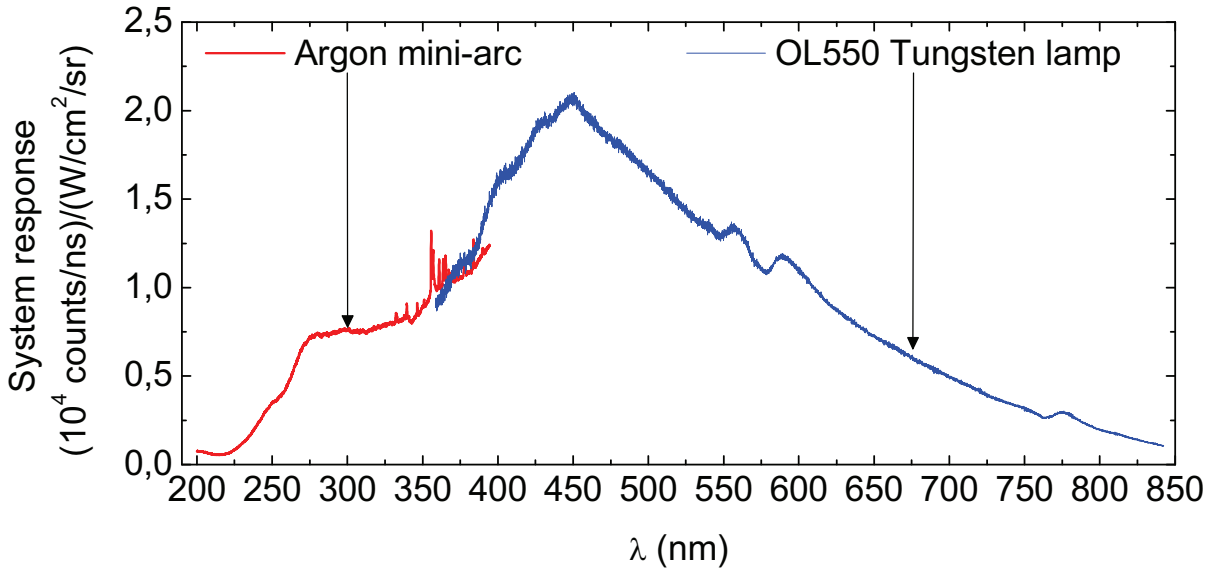

Figure 3.12: Response of the complete optical system to argon mini-arc (red) for calibration in the UV wavelengths using a 10-ns gate width, 20 on-CCD accumulations, and 1000 numerical accumulations. Response of complete optical system to tungsten lamp OL550 (blue) for calibration in the VIS wavelengths using a 10-ns gate width, 100 on-CCD accumulations, and 1000 numerical accumulations.

Figure 3.12 also shows D_λ in the visible using the OL550 tungsten lamp, following the same calibration procedure as for the argon mini-arc in the UV. The kinks at ~550 nm and ~775 nm are the result of grating ghosts. There is good agreement between the UV and VIS system responses in their overlapping wavelength range, 350-400 nm.

3.5 Synchronization of the ICCD camera with the discharge

In this section we discuss the synchronization of the ICCD camera with the discharge. Measurements of the pulsed discharge spectra required synchronizing the high-voltage pulse generator with the ICCD camera gate. Figure 3.13 is a block diagram of the devices involved. Synchronization was centralized with the Berkeley Nucleonics (BNC) 555 four-channel pulse delay generator, which triggered all devices. To reduce uncertainties in timing, the same 2-m BNC coaxial cables were always used to relay the BNC's trigger signals to other devices.

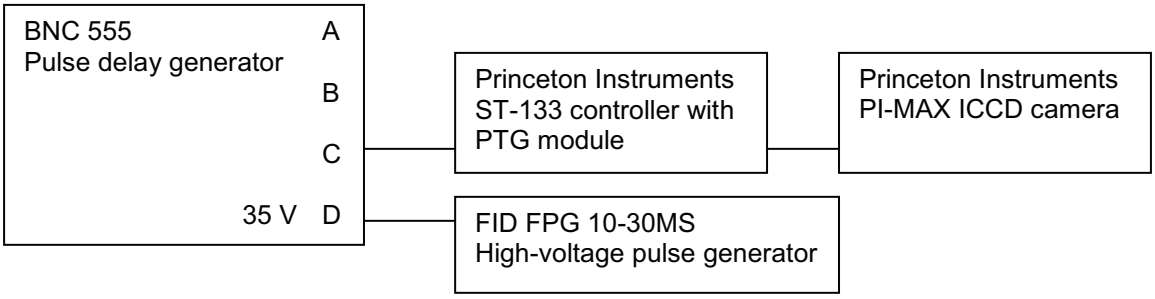

Figure 3.13: Block diagram of the synchronization scheme for the camera and the pulse generator.

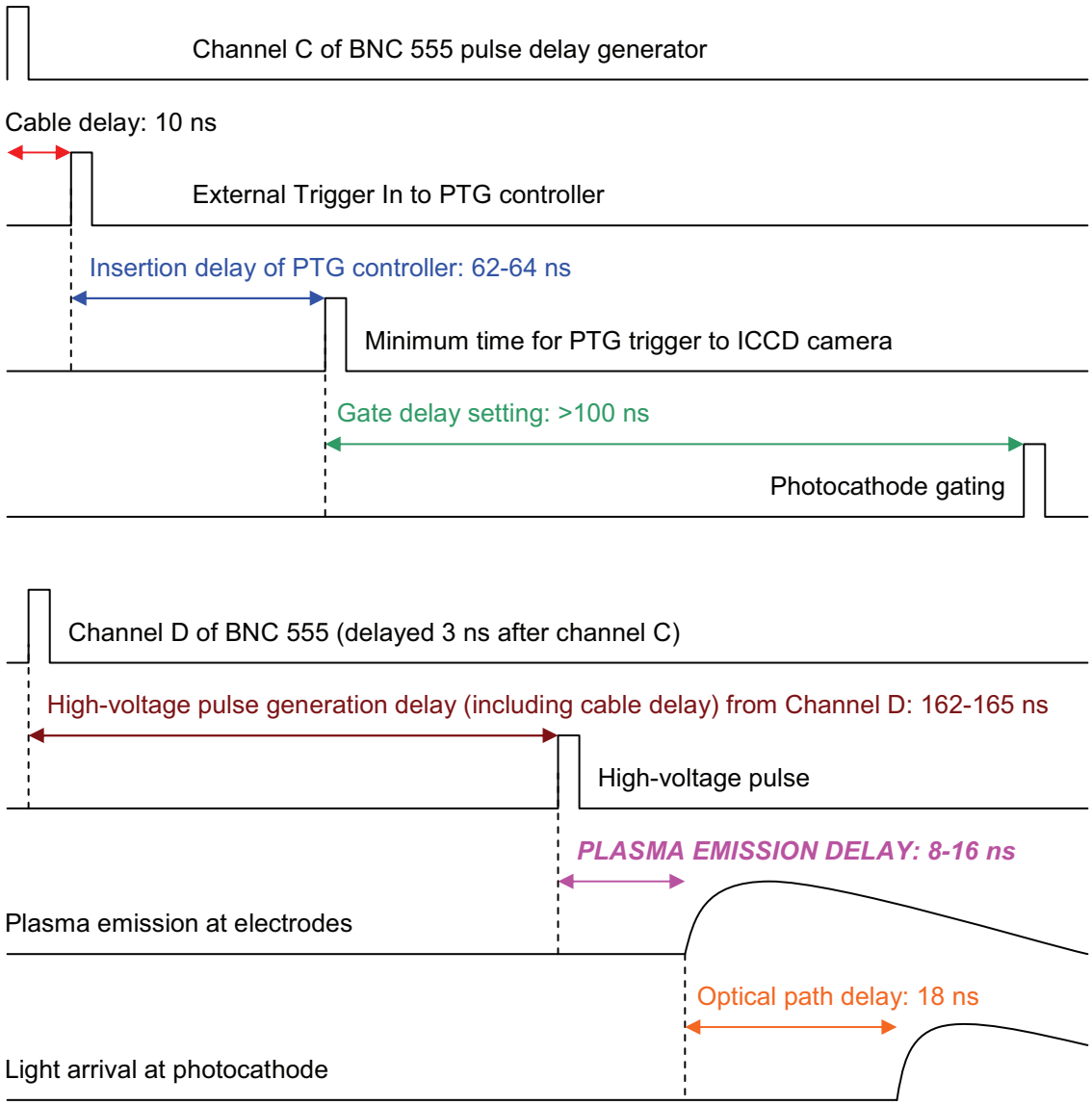

Figure 3.14: Timing diagram of the synchronization of the PI-MAX ICCD camera photocathode gating with the discharge.

Figure 3.14 is a timing diagram of all of the relevant delays. Channel C of the BNC was operated in TTL mode to trigger a Princeton Instruments ST-133 controller fitted with a Programmable Timing Generator (PTG) module, following a 10-ns delay of an interconnecting 2-m BNC coaxial cable. The PTG simplifies operation of the ST-133 via an

external synchronization signal. To operate the PI-MAX using the PTG, the ST-133 must be set in the "Internal Sync" timing mode. Each TTL trigger pulse from channel C received by the "Ext. Trig. In" input of the PTG initiates the desired PI-MAX gating and the subsequent readout cycle, which is also handled by the ST-133. The total insertion delay of 62-64 ns between the PTG's "Ext. Trig. In" input to the PI-MAX camera's photocathode gating time was measured using the camera's "Monitor" output, which provides a signal representing the photocathode gate period that lags behind the true gate by 4-6 ns. Following the PTG insertion delay, a gate delay is selected for the acquisition of plasma emission spectra during a desired period.

Meanwhile, channel D of the BNC delivers a 10 V, 100-ns square-pulse to trigger the high-voltage pulse generator, after the delay of an interconnecting 2-m BNC coaxial cable. Although the delay between channels C and D is set to zero, channel D actually delivers its trigger 3 ns after channel C does. The high-voltage pulse generation delay following its trigger signal changes slightly with the input DC voltage and considerably with Pulse Repetition Frequency (PRF). The reasons for this delay are explained in Appendix A. All of the measurements using the monochromator-ICCD camera subsystem were performed at PRF=30 kHz. High-voltage pulse generation delays following the moment of trigger signal delivery by the BNC generator were measured as a function of the input DC voltage with an error of less than 300 ps and ranged from 162 to 165 ns. This includes the interconnecting cable delay, which was not measured separately.

The plasma emission initiates 8-16 ns after the initiation of the high-voltage pulse. This light reaches the camera after following the path through the mirror optics (0.4 m), the fiber optic bundle (3 m), and the monochromator (2 m), for a total optical path delay of 18 ns. We assumed that light propagates at the same speed through the fiber as in air. The PI-MAX gate delay is selected to capture the emission at the desired moment during the plasma's emitting period. All delays for measurements presented in this thesis using the monochromator-ICCD camera subsystem are known with an uncertainty of 2 ns.

3.6 Specifics of the Photomultiplier Tube Module (PMT) subsystem

This section presents the Photomultiplier Tube Module (PMT) subsystem that was specifically built for this thesis. Figure 3.15 shows the block diagram. The Hamamatsu H9305-03 PMT was chosen for its broad spectral response and rapid rise time. It contains the Hamamatsu R6357 Photomultiplier Tube (PM), which is a 13-mm diameter side-on type PM with a reflection mode multi-alkali photocathode. An internal Cockcroft-Walton high-voltage power supply circuit provides up to 1250 V across nine dynode stages from anode to cathode. We did not measure the spectral response of the system because all PMT measurements presented in this thesis were performed at 337 nm, the N_2 (C-B) 0-0 emission band head.

To amplify the PMT output current, the Hamamatsu C5594-44 high-speed amplifier was chosen for its wide-band performance and adaptability to Hamamatsu PMTs. The Hamamatsu C7169 power supply powered both the PMT and its amplifier and controlled the PMT gain. Specifications for the PMT and the amplifier are shown in Table 3.2. Finally, the amplified PMT signal was recorded by an oscilloscope using a 50-Ω input impedance. Unless indicated otherwise, all measurements recorded with the oscilloscopes presented in this thesis are averaged over 100 samples.

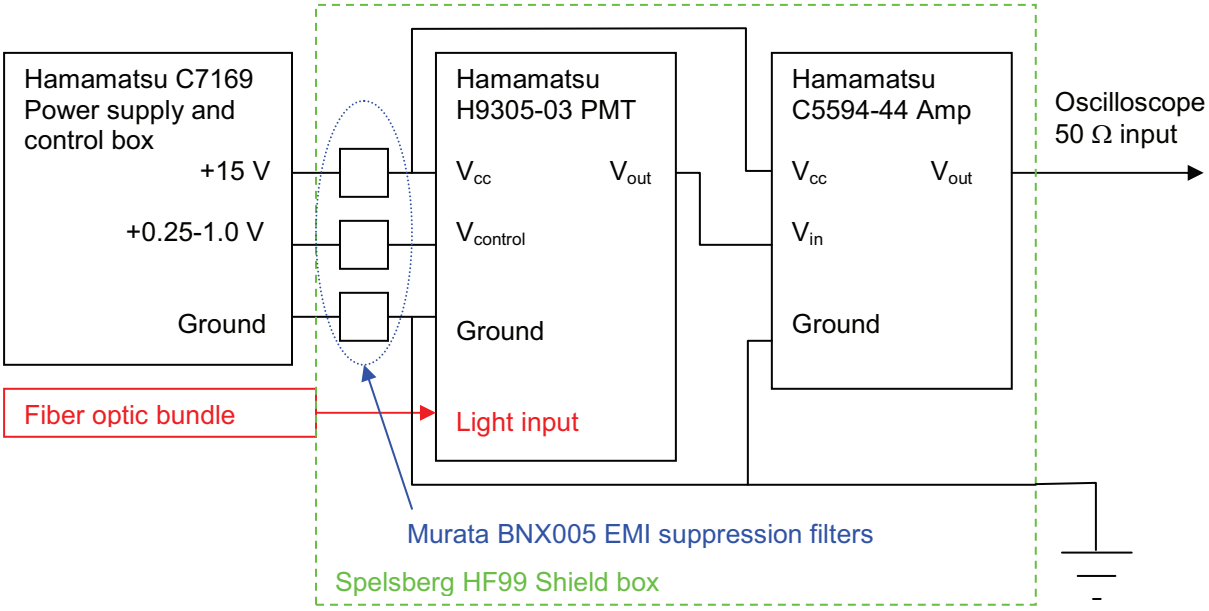

Figure 3.15: Block diagram of the PMT subsystem.

Table 3.2: Key specifications of the PMT module, its amplifier, and the interference filter.

Hamamatsu H9305-03 **Photomultiplier Tube Module (PMT)**	
Cathode radiant sensitivity at 337 nm	80 mA/W
Rise time	1.4 ns
Typical electron transit time	15 ns
Maximum output signal current	10 μA
Control voltage adjustment range ($V_{control}$)	+0.25 to +1.0 V
Maximum dark current	10 nA
Maximum gain	10^7
Hamamatsu C5594-44 High-speed amplifier	
Minimum upper cutoff (-3 dB) frequency	1.2 GHz
Maximum lower cutoff (-3 dB) frequency	100 kHz
Input current-to-voltage conversion factor	3.15 mV/μA
Minimum voltage gain at 100 MHz	34 dB (63 times)
Gain flatness from 200 kHz to 1 GHz	±1 dB
Measured amplification delay time	1 ns
Saturation output voltage at V_{cc}=+15 V	2.5 V
Melles Griot 03 FIU 127 Interference filter	
Diameter	25 mm
Center wavelength	338.13 nm
Peak transmission	27.94%
Half transmission wavelengths	333.13 nm and 343.13 nm
Bandwidth at 50%	10.01 nm
Bandwidth at 10%	14.35 nm
Bandwidth at 1%	20.99 nm

Unfortunately, the PMT subsystem was highly sensitive to Electro-Magnetic Interference (EMI) from the high-voltage pulse. Figure 3.16 shows the estimated power spectrum of a typical pulse, whose time domain signal is converted into the frequency domain using the fast Fourier transform. At a given frequency, the power is estimated as the square of the amplitude, divided by the number of sample points. The pulse repetition frequency in our range of interest (1-30 kHz) does not affect the normalized power spectrum, which is broadband and includes sidebands above 80 MHz with significant power.

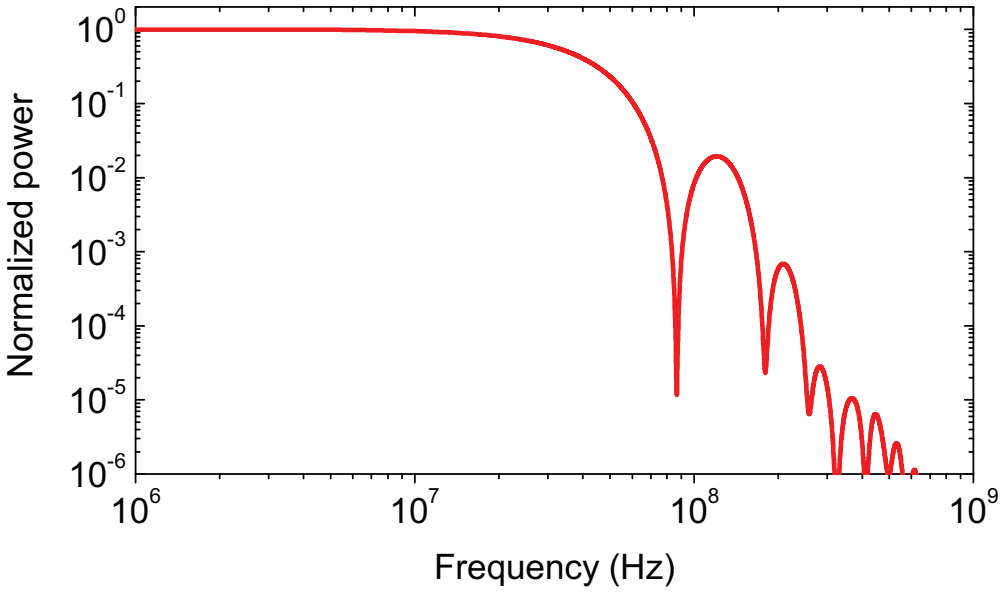

Figure 3.16: Normalized power spectrum of a typical 10-ns high-voltage pulse produced by the FID high-voltage pulse generator.

We used several techniques to attenuate the EMI. First, the PMT power supply transferred significant EMI to the PMT and the amplifier via its DC outputs. Thus, at the input side of the PMT and the amplifier, we installed Murata BNX0005 EMI suppression low-pass filters that provide up to 80 dB of insertion loss from 5-300 MHz. In addition, the complete PMT-amplifier assembly was enclosed in a Spelsberg HF99 polycarbonate aluminized 94×94×57 mm electromagnetic shielding box. It provides at least 40 dB of screening attenuation from 30 to 600 MHz. For further shielding, the entire PMT subsystem and the oscilloscope were enclosed in a 50×50×50 cm Faraday cage with a solid aluminum ground plane. This minimized the EMI induced on the cables between the PMT subsystem and the oscilloscope.

The above EMI suppression measures led to S/N of about 3, and a calculation was used to clean the signals further. For every PMT measurement of the discharge taken, another measurement was taken in exactly the same conditions except that no light from the discharge was allowed to reach the PMT by optically blocking the fiber optic bundle entrance. This second measurement effectively measured the EMI noise. Taking the difference of these two measurements resulted in a noise-filtered signal, as shown in Figure 3.17. With this procedure, we achieved S/N>10, which allowed accurate measurement of time-resolved emission profiles.

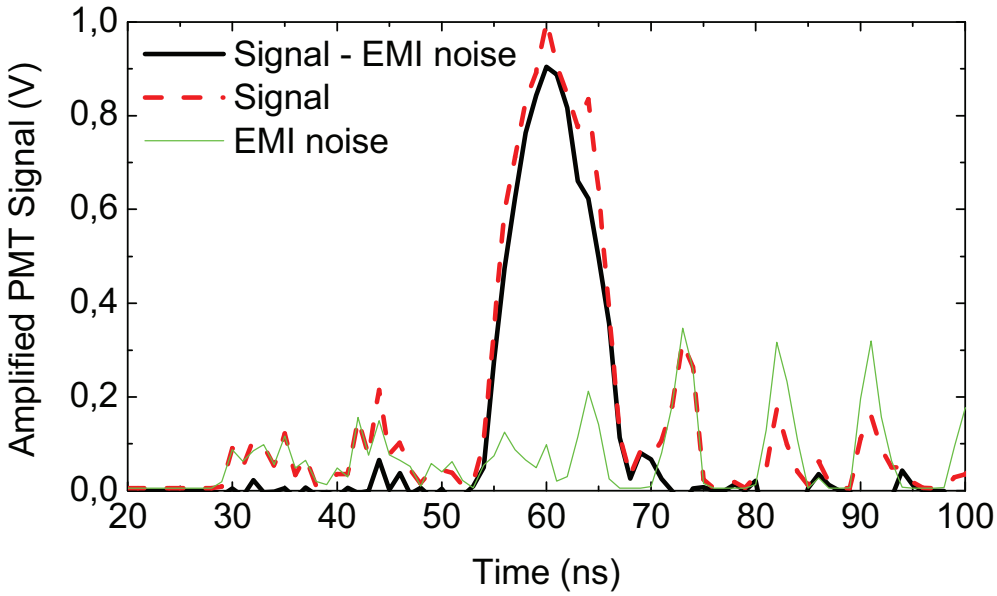

Figure 3.17: Example of a typical PMT signal (thick solid) obtained by subtracting the background EMI noise signal (thin solid) from the raw plasma emission signal (dashed).

3.7 Saturation and calibration in relative intensity of the PMT subsystem

The saturation limit of the PMT subsystem was determined by measuring the emission from the same discharge using variable gain, which is governed by the control voltage (V_{cont}). At the highest gain (V_{cont}=650 mV) shown in Figure 3.18, the PMT subsystem delivers a cropped signal because of amplifier saturation. The measured amplifier saturation voltage of 2.4 V agrees with the datasheet value of 2.5 V given in Table 3.2. At lower gain, saturation is due to the PMT, which does not crop the signal but instead responds non-linearly. Data points below the saturation limit are accurately measured, while those over it are underreported. For pulsed signals, this is apparent upon measuring their FWHM. Saturation suppresses the peak, which broadens the signal and results in a larger FHWM. In Figure 3.18, this occurs when V_{cont}=550 mV. But if the gain is too low (e.g. V_{cont}=450 mV), the noise floor contributes significantly to the total signal, again enlarging the FHWM. The most accurate measurement is made near the gain saturation limit (e.g. V_{cont}=500 mV), where the FWHM is minimized and the peak output voltage is 1.3 V. If we measure a different discharge, the V_{cont} for saturation may change but the peak output voltage does not. Therefore, for the PMT measurements presented in Chapters 4 and 5, we adjusted V_{cont} to achieve 1.3 V peak output.

After establishing its saturation limit, we calibrated the PMT subsystem in relative intensity by measuring plasma emission under fixed conditions using different V_{cont}. If a measurement was taken near the saturation limit, a second measurement was performed with the same V_{cont} but at reduced plasma emission intensity. The signal ratio between these two measurements was used as the normalization factor for subsequent measurements at the reduced plasma emission intensity. These measurements, shown in Figure 3.19, cover the range of V_{cont} for which the plasma emission did not need to be further attenuated by additional neutral density filters to avoid saturation.

The relative gain was calculated by using the signal voltage at V_{cont}=0.321 mV, the lowest measured value, as a normalization factor. Although this calibration did not cover the full range of V_{cont} as listed in Table 3.2, it did include the vast majority of V_{cont} values that were used in the discharge measurements. The occasional measurements outside of this range were

calibrated using extrapolated values of the log-log fit shown in Figure 3.19. These data points were for the weakest D states and the strongest F states. Even if the gain curve deviates from the log-log fit at these extremes, the calibration error would not change the conclusions drawn from the PMT measurement data since this study focuses primarily on those states near the D-F transition: the strong D states and the weak F states. The terms "strong" and "weak" will be defined in Section 4.8.

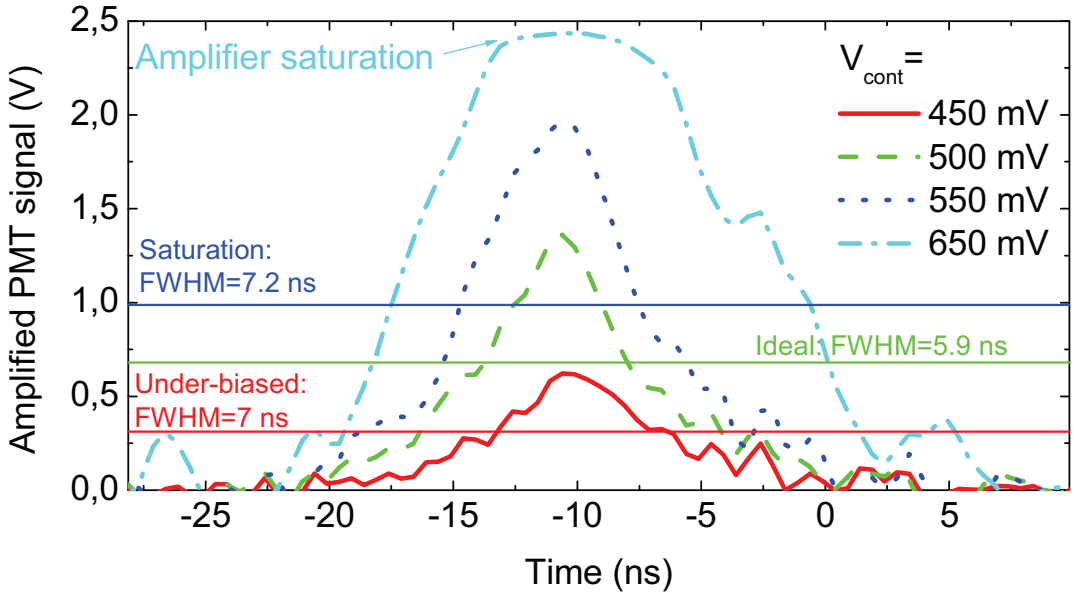

Figure 3.18: Measured PMT signal of a discharge for various control voltages (V_{cont}).

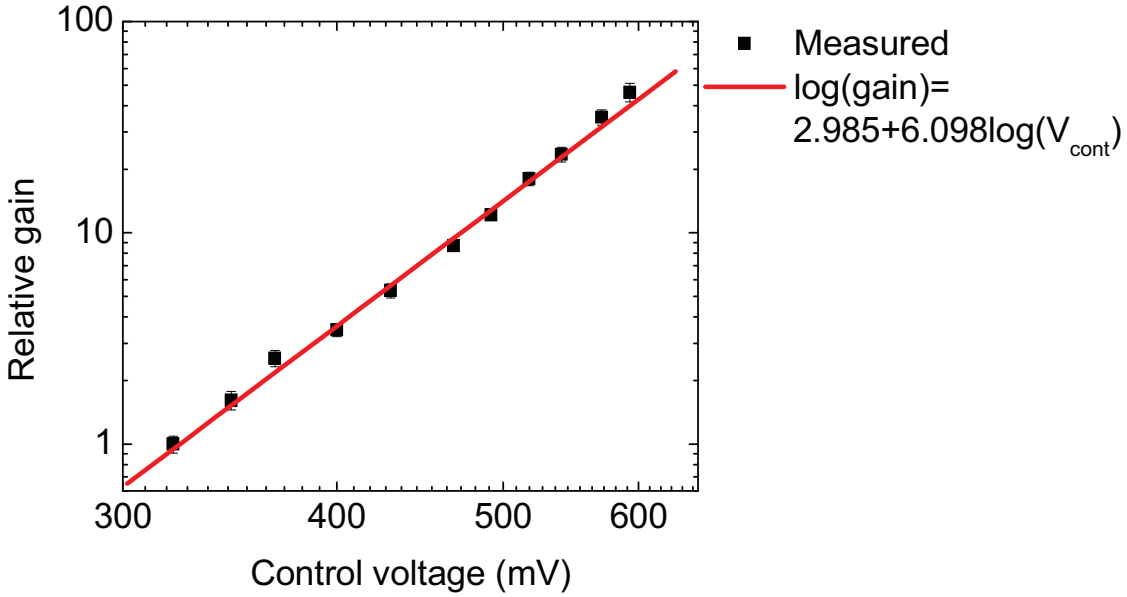

Figure 3.19: Relative intensity calibration of the PMT module and amplifier system gain: measurement (symbols) the log-log fit (solid).

3.8 Synchronization of the PMT subsystem with the discharge

In this section we present two methods used to synchronize the PMT subsystem with the discharge. Synchronization is necessary to determine the delay between the application of the high-voltage pulse and the plasma emission, which will be useful in Chapter 4. For measurements of the effect of the gas temperature (T_g) on the discharge regimes, the PRF was

fixed. On the other hand, for measurements of the effect of PRF on the discharges regimes, we fixed T_g and varied the PRF. Two different trigger mechanisms were used, depending on whether or not the PRF was fixed for a particular set of measurements.

Synchronization for fixed PRF

As mentioned in Section 3.5, The high-voltage pulse generation delay following its trigger signal varies only slightly with the DC supply voltage at fixed PRF, from 162 to 165 ns. This made it convenient to trigger the oscilloscope with the BNC generator. This minimizes EMI compared to triggering to the high-voltage pulse using the high-voltage probe, which introduces considerable EMI. Determining the delay between the high-voltage pulse and the plasma emission requires knowing the other system delays. Figure 3.20 shows the timing diagram used for this purpose.

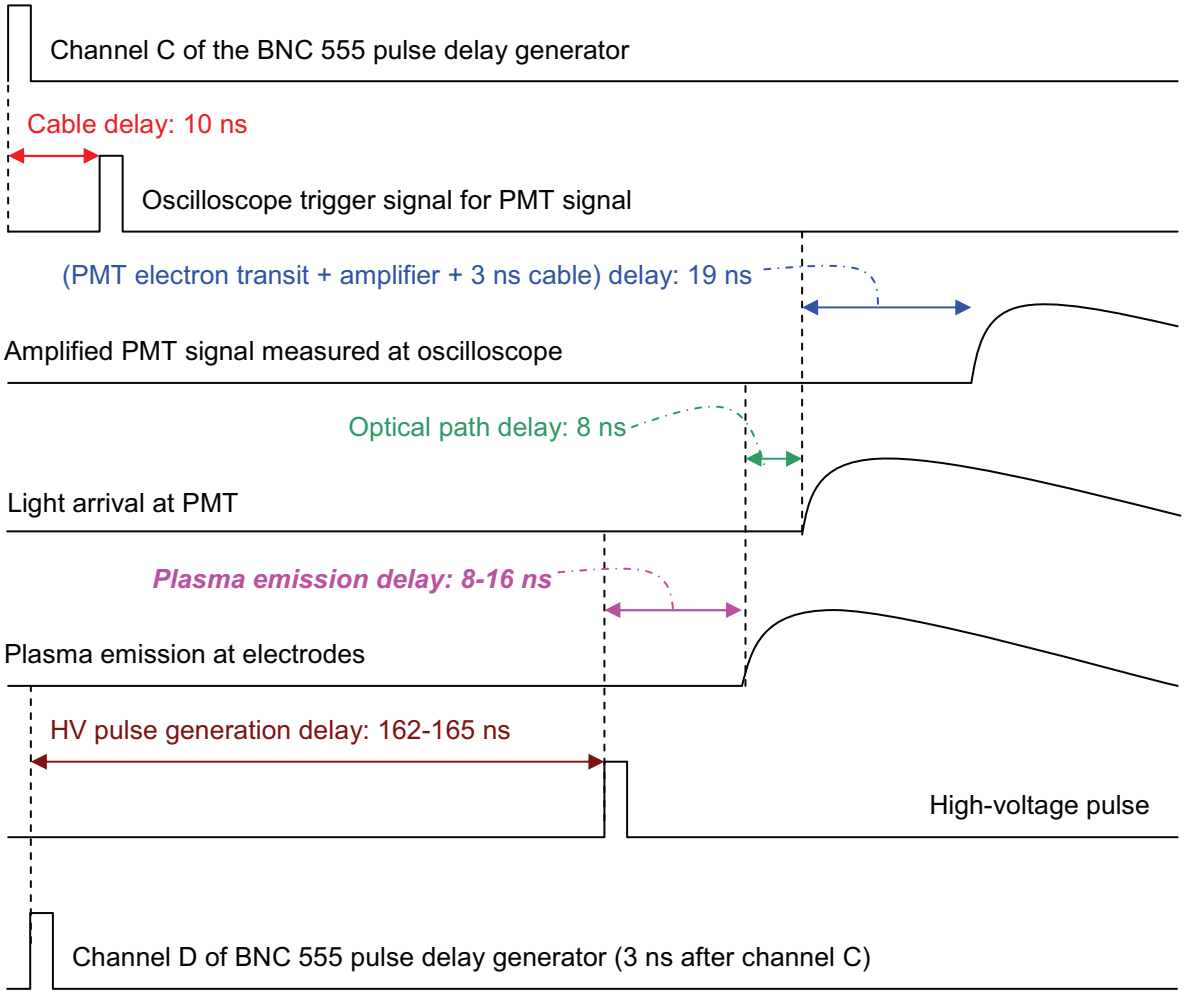

Figure 3.20: Timing diagram for synchronization of the PMT subsystem with the discharge, used for measurements at fixed pulse repetition frequency.

First, Channel C of the BNC generator delivers a TTL pulse, which is followed 3 ns later by a 10-V, 100-ns square wave pulse produced at Channel D. Following a 10-ns cable delay, the signal from Channel C triggers the oscilloscope. Meanwhile, the high-voltage pulse appears across the electrodes 162-165 ns after Channel D produces its signal. Some time later, the plasma is generated. Its emitted light passes through the mirror optics and the 2-m fiber optic bundle and reaches the PMT photocathode 8 ns later, assuming the speed of light in a vacuum

through the entire optical path. The subsequently generated photoelectrons require 15 ns for electron transit and multiplication, 1 ns for further amplification, and 3 ns through a cable before delivery to the oscilloscope as an electrical signal. Except for the electron transit time (taken from the manufacturer's datasheet) and the optical fiber delay, all of the delays mentioned above have been measured. By taking all of them into account, we can reconstruct the delay between the high-voltage pulse and the plasma emission within 300 ps. This uncertainty is primarily from that of the delay of high-voltage pulse generation following the trigger signal at Channel D.

Synchronization for variable PRF

When the PRF was varied between sets of measurements, using the BNC generator to trigger the oscilloscope was not convenient because the high-voltage pulse generation delay following its trigger varied with both PRF and input DC voltage, as discussed in Appendix A. Instead, the high-voltage pulse was directly used to trigger the oscilloscope. To measure the high-voltage pulse, the tip of the high-voltage probe was placed a few centimeters away from the anode. By avoiding direct contact, we reduced the EMI while still measuring an attenuated pulse via capacitive coupling with the anode. Figure 3.21 shows the timing diagram corresponding to this method.

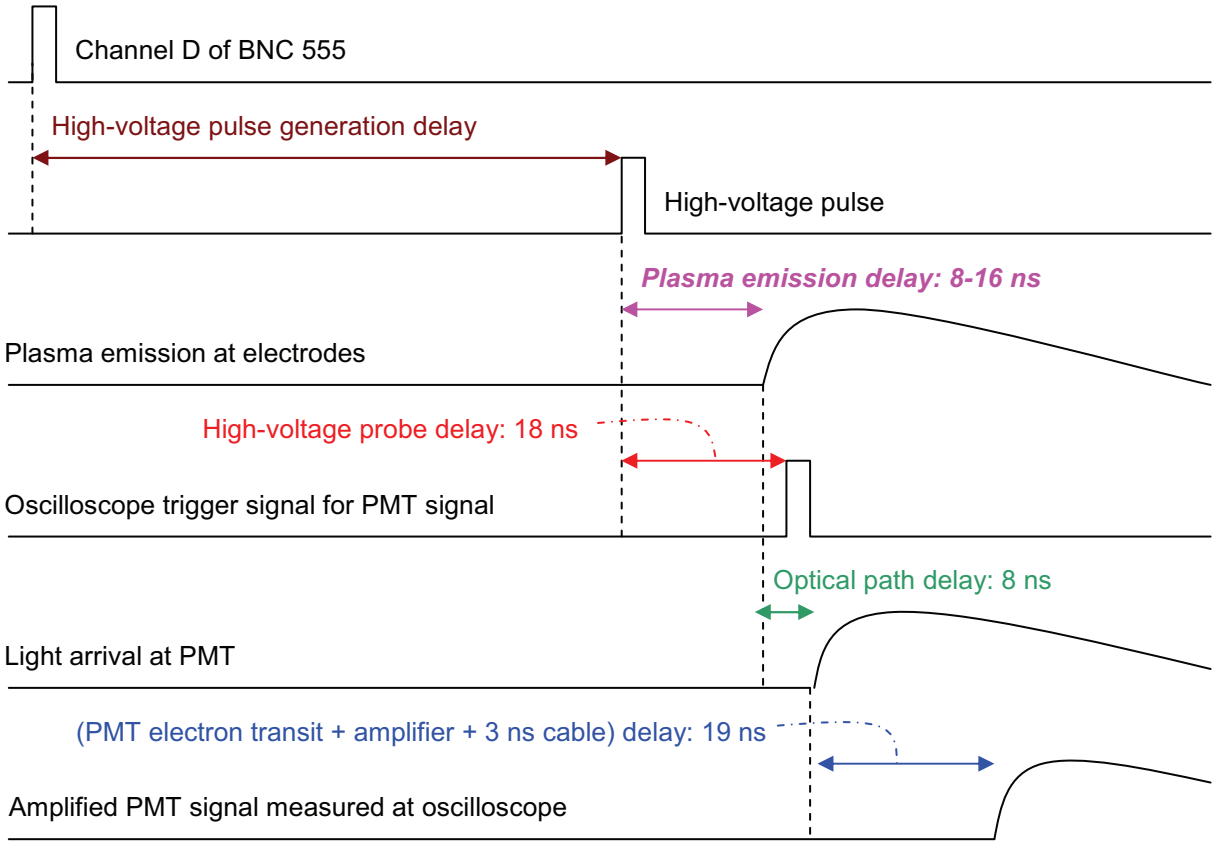

Figure 3.21: Timing diagram for synchronization of the PMT subsystem with the discharge, used for measurements at variable pulse repetition frequency.

First, a 10-V, 100-ns square wave pulse is produced at Channel D. After some time, the high-voltage pulse appears across the electrodes and is also detected by the high-voltage probe. After a propagation delay of 18 ns, the high-voltage probe signal triggers the oscilloscope. In addition, the high-voltage pulse generates the plasma some time later, producing emission.

The delay between plasma emission and its recording at the oscilloscope is identical to that already described for measurements at fixed PRF. By taking all delays into account, we can reconstruct the delay between the high-voltage pulse and the plasma emission within 300 ps. This uncertainty is mostly from that of the delay of high-voltage pulse generation following the trigger signal at Channel D.

3.9 Output characteristics of the high-voltage pulse generator

In this section we present the FID high-voltage pulse generator subsystem and examine the effect of the output load on its output. As described in Appendix A, high-voltage pulse generators capable of high PRF rely on a high-power Drift Step Recovery Diode (DSRD) with nanosecond reverse recovery time. Here we consider the FID generator as a "black box" and characterize its output as a function of its output resistance. This is important because the plasma output resistance changes rapidly in time, owing to changes in the plasma conductivity under the action of the applied field. Figure 3.22 shows a block diagram of the high-voltage pulse generator subsystem. Two Delta Elektronika ES 0300-0.45 DC power supplies connected in series power the generator through its DC input up to 600 V. A separate FID DC power supply powers the ventilation fan on top of the generator. The BNC pulse delay generator provides the trigger signal through its 35-V rear output panel.

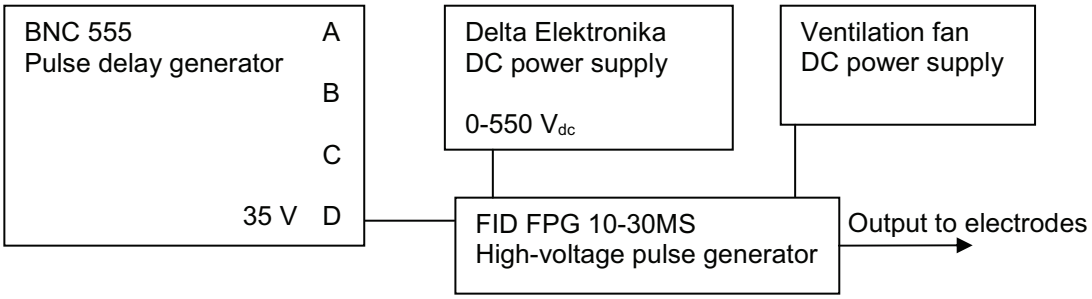

Figure 3.22: Block diagram of the high-voltage pulse generator subsystem.

We connected 1 or 3 W low-inductance metal-film resistors (Vishay BC Components PR01 and PR03) to the generator's output terminal. The voltage across them was measured with a 380-MHz 100X passive high-voltage probe (PMK PHV 641-L) instead of the 100-MHz PPE20kV probe used in the plasma measurements because of its superior bandwidth. The specifications and high-speed performance of the PMK PHV 641-L are presented in Section 3.10. We did not use it for plasma measurements because its maximum pulsed-input voltage is 4 kV, below the typical applied voltage for plasma generation. The high-voltage pulse generator was operated at relatively low power (PRF=1 kHz and 1.9 kV peak voltage under no-load conditions) to protect the test load resistors. Even without an external load, energy dissipates over an internal resistor R_{int}=3 kΩ connected in parallel with the output terminal. The measured voltages across the resistors are shown in Figure 3.23.

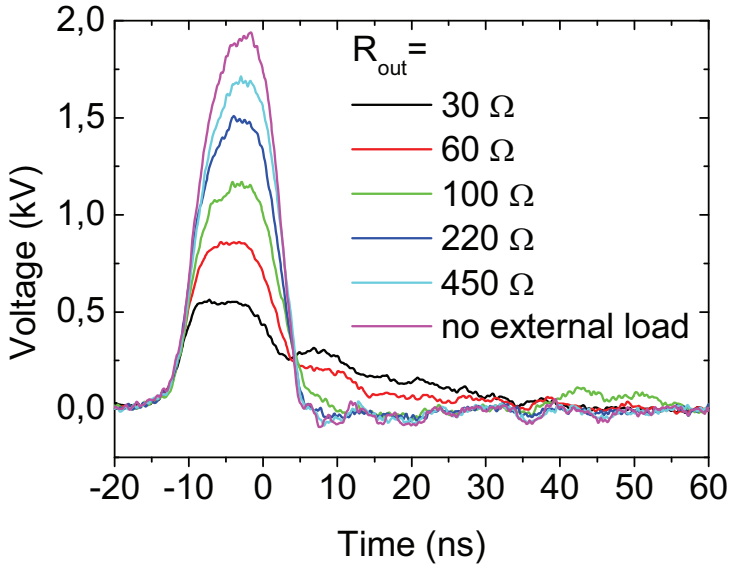

Figure 3.23: Measured high-voltage pulse generator output voltage waveforms for load resistances $R=R_{out}R_{int}/(R_{out}+R_{int})$=30-3000 Ω, where R_{int}=3 kΩ.

The waveforms are less square than those at high peak output voltages, but this does not affect the present discussion. For external load resistances (R_{out}) smaller than the internal transmission line impedance Z_0=75 Ω, the output pulse is elongated in time. Figure 3.24 shows the measured peak voltage (V), peak current ($I=V/R$), and peak power ($P=V^2/R$) corresponding to the waveforms shown in Figure 3.23. $R=R_{out}\|R_{int}$ is the total resistance at the output terminal.

The peak voltage, current, and power can also be determined using the following transmission line model. As mentioned above and in Appendix A, an internal coaxial cable coiled up against the output terminal acts as a transmission line. For an ideal pulse generator, the pulse waveform V_S propagates down a Z_0=75 Ω line and reflects at the load $Z_L=R$. The measured voltage at the load V_L is:

$$V_L=(1+\Gamma_L)V_S=\left(1+\frac{Z_L-Z_0}{Z_L+Z_0}\right)V_S=\frac{2Z_L}{Z_L+Z_0}V_S \tag{3.2}$$

Γ_L is the reflection coefficient at the load. The reflection coefficient at the source (Γ_S) is zero for all conditions in this thesis. Γ_S depends on whether the DSRD is in forward or reverse operation, as discussed Appendix A. Figure 3.24 is a comparison of the measured peak voltage, current, and power with the theoretical transmission line model. Their agreement supports using the transmission line model for describing the high-voltage pulse generator.

The transmission line model, however, fails to explain the measured pulse energy dependence on load resistance. If Γ_L were solely responsible for changes in V_L, the pulse energy would vary with R_L in the same way as the instantaneous power. Hence, the pulse energy and peak power would be maximized in the matched load case ($R_L=Z_0$), as shown in Figure 3.24. However, Figure 3.25 shows that the measured pulse energy continues to increase for R_L<60 Ω. This is because the output voltage waveforms spread out for R_L<60 Ω, which is most noticeable for the 30-Ω case in Figure 3.23. This pulse waveform degradation is

discussed in Appendix A. The load resistance couples to an internal RLC diode circuit that generates the pulse. Optimal pulse generation requires that this circuit be in a highly under-damped (oscillating) mode. If the external load resistance is too small, the circuit becomes too damped to produce a clean pulse. Thus, the pulse generator enters a sub-optimal mode when the external load resistance is less than about 60 Ω.

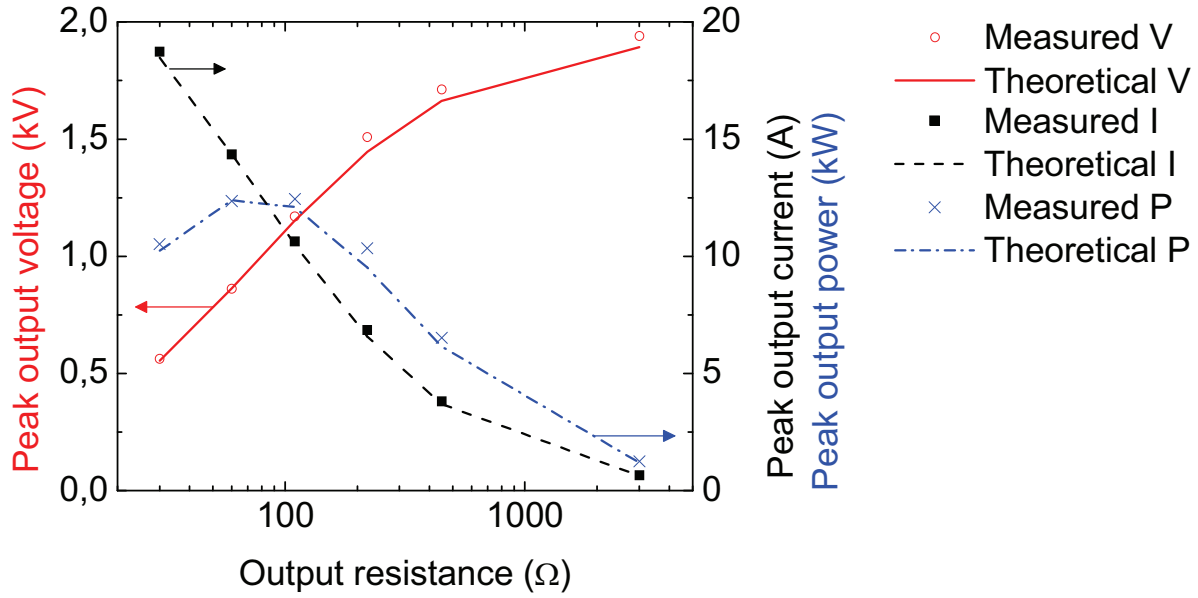

Figure 3.24: Measured (symbols) and theoretical (curves) peak output voltage, current, and power of the pulses from Figure 3.23 as a function of output resistance.

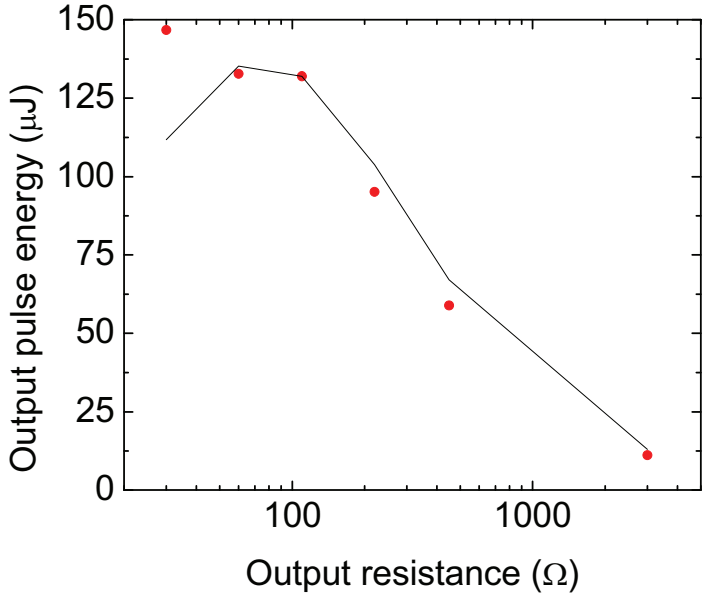

Figure 3.25: Measured (symbols) and theoretical (line) output energy as a function of the output resistance of the pulses from Figure 3.23.

Figure 3.26 shows the measured applied voltage V_p across the electrodes, the conduction current I_{cond}, and the plasma resistance $R_p=V_p/I_{cond}$ for a strong F state (which is defined in

Section 4.8). R_p is calculable this way only while both the voltage and current are non-negligible. The minimum measurable resistance is ~30 Ω, which is low enough to cause sub-optimal pulse generator performance. If we suppose that weaker F states have higher resistances, then 30 Ω is a lower bound for the plasma resistances reached in this study. Fortunately, the pulse generator operates sub-optimally only at the tail end of the high-voltage pulse. Therefore, sub-optimal operation of the high-voltage pulse generator only has a negligible effect on the discharges studied in this thesis.

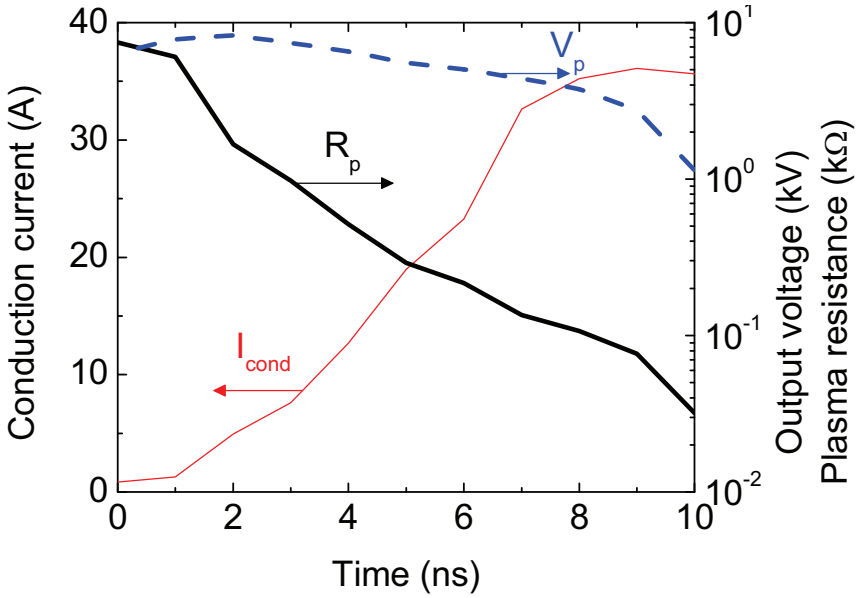

Figure 3.26: Measured applied voltage (dashed), conduction current (thin solid), and plasma resistance (thick solid) for a strong F state.

3.10 High-voltage probe detection of nanosecond pulses

In this section we verify the ability of the Lecroy PPE20kV 1000X high-voltage passive probe to measure the high-speed signals studied in this thesis. Its rated bandwidth is 100 MHz, but from Figure 3.16 we see that the typical high-voltage pulse's power spectrum extends further. We tested the performance PPE20kV using low-voltage pulses generated by the BNC pulse delay generator.

First, we needed a reference signal for comparison with measurements by the PPE20kV. We chose to set the BNC to produce 2.5-V TTL pulses with 2-ns rise/fall times and 10-ns or 20-ns pulse duration, which are time profiles similar to that of the high-voltage pulses for plasma generation. To use the TTL pulses as a reference, we had to measure them using a device with much greater bandwidth than the PPE20kV. Instead of using a probe, we chose a 2-m RG-58C/U cable, which typically has 0.18 dB/m of attenuation at 100 MHz and 0.76 dB/m of attenuation at 1 GHz [3.3]. It follows that the 2-m cable has 1.52 dB of attenuation at 1 GHz. Its bandwidth is therefore greater than 1 GHz, according to the standard definition of a -3 dB high frequency cutoff. In addition, the cable has BNC connectors, which typically produce negligible reflection below 4 GHz [3.4]. Thus, TTL pulses measured using the RG-58C/U cable are appropriate reference signals.

Figure 3.27 shows the schematic diagram of the TTL signal measurement setup using the coaxial cable. Since the PPE20kV requires a 1-MΩ output connection, we used a 1-MΩ

oscilloscope input impedance for all the measurements presented in this section to ensure the same frequency response by the oscilloscope. To prevent reflections due to the oscilloscope impedance, we connected a 50-Ω terminator in parallel using a BNC T-connector.

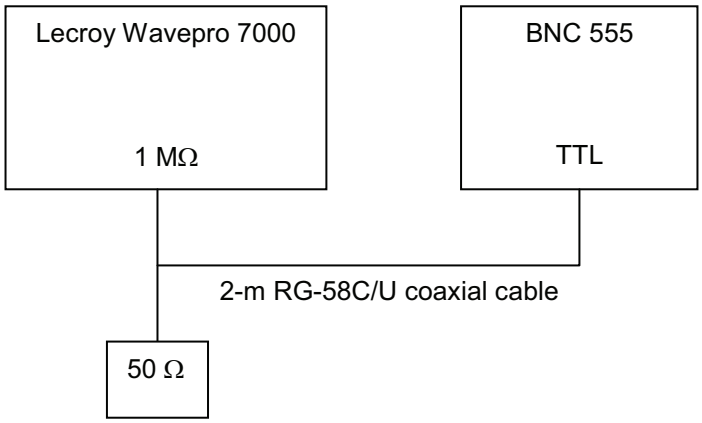

Figure 3.27: Schematic diagram of the TTL signal measurement setup using the coaxial cable.

The schematic diagram of the TTL signal measurement setup using the probe is shown in Figure 3.28. Again, the 50-Ω terminator was used to prevent reflections, but instead of connecting it in parallel at the oscilloscope input port as in Figure 3.27, we connected it in parallel with the PPE20kV at the TTL output port.

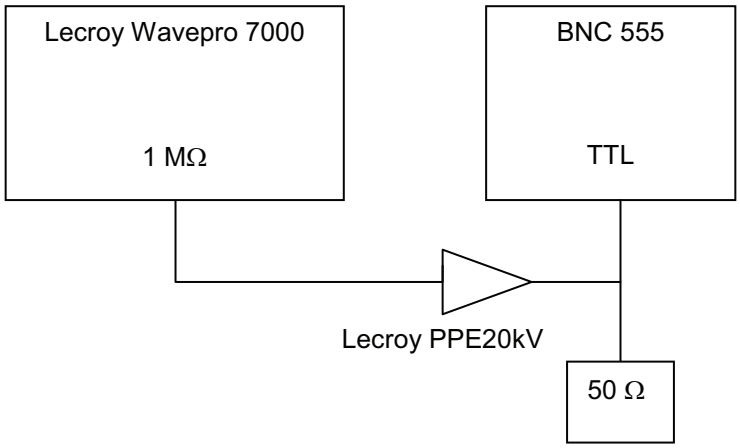

Figure 3.28: Schematic diagram of the TTL signal measurement setup using the PPE20kV 1000X probe or the PHV641-L 100X probe.

Figure 3.29 compares the cable-measured 20-ns TTL signal with the PPE20kV-measured signal. The PPE20kV is designed to have high S/N for measurements in the kilovolt range (S/N=95 at 7 kV). Its S/N is only about 2 at the TTL level of 2.5 V. Nevertheless, the shape of the fast TTL signal is well reproduced by the PPE20kV probe.

To improve the comparison, we went further and measured the TTL signal using the PMK PHV641-L 100X high-voltage passive probe. This served the dual purpose of evaluating its high-speed performance as well as serving as an intermediate standard for comparison with the PPE20kV. The PHV641-L has a maximum pulsed-input voltage of 4 kV, a bandwidth of 380 MHz, and a minimum rise-time detection of 0.95 ns. Thus, it is useful for medium-

voltage measurements in terms of the voltages applied in this thesis (up to 10 kV), such as in Section 3.9. Using the same setup as for the PPE20kV, shown in Figure 3.28, we measured the TTL signal using the PHV641-L. The result is shown in Figure 3.30, which demonstrates that the PHV641-L has a much lower noise level than the PPE20kV and therefore better approximates the reference signal measured by the cable.

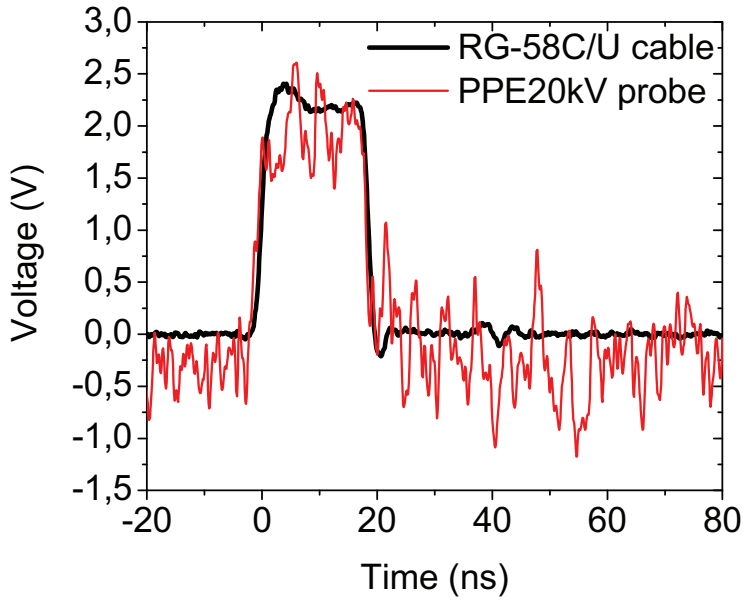

Figure 3.29: Measured TTL signals generated by the BNC 555 pulse delay generator using the coaxial cable (thick), the 100X probe (thin), and the Lecroy PPE20kV. PRF=30 kHz.

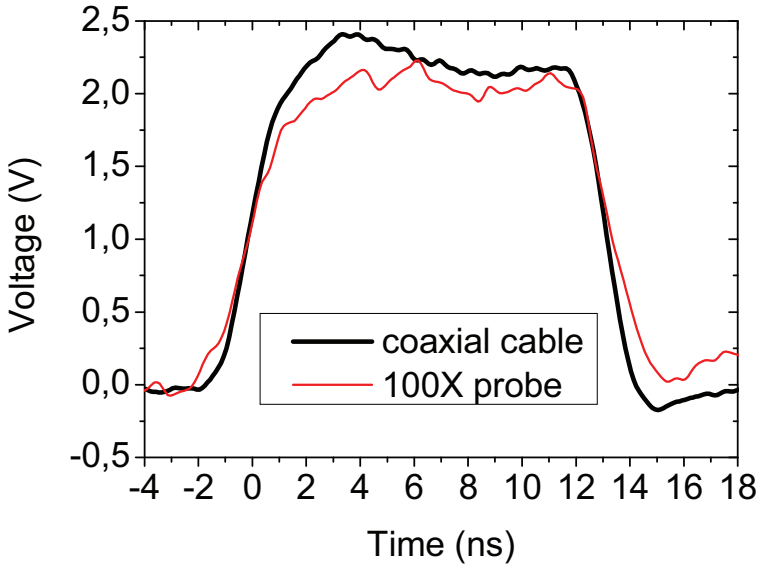

Figure 3.30: Measured TTL signals generated by the BNC 555 pulse delay generator using the coaxial cable (thick) and the PHV641-L 100X probe (thin). PRF=30 kHz.

We see that the lower bandwidth of the PHV641-L (380 MHz) compared to that of the cable (>1 GHz) results in lower measured voltages at the top of the pulse and slower rise and fall times. During the period when the cable signal is >90% of its maximum value, the PHV641-L signal is on average 7.7±3.8% lower than the cable signal. Thus, we have

effectively calibrated the frequency response of the PHV641-L against the reference signal measured by the cable.

Now we can calibrate the PPE20kV against the PHV641-L. To overcome the noise level of the PPE20kV, we used the 35-V output port of the BNC 555 to produce a 25-V pulse. For this pulse, the fall time (160 ns) is inherently slower than for the TTL pulse. However, its rise time is 6.6 ns, and therefore we only compare the measured rise times. We used the setup from Figure 3.28 for 25-V signal measurements using the PHV641-L and the PPE20kV, and the results are shown in Figure 3.31.

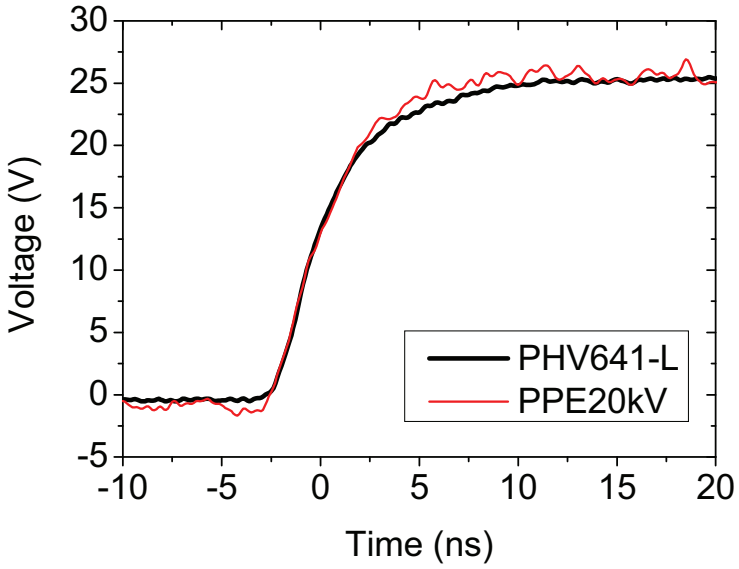

Figure 3.31: Measured 25-V signals generated by the BNC 555 pulse delay generator using the PHV641-L (bold) and the Lecroy PPE20kV. PRF=30 kHz.

The rise times agree, and the deviation between the measurements occurs at the top of the pulse, mainly because of the noise level of the PPE20kV. During the first 10 ns after the PHV641-L signal is >90% of its maximum value, the PPE20kV signal is on average 1.1±2.3% greater than that of the PHV641-L.

Finally, we relate the calibration of the PPE20kV against the PHV641-L with that of the PHV641-L against the original cable reference signal. First, we discuss the PPE20kV performance at the top of a pulsed signal. We relate the signal measured by the PPE20kV, V_{PPE}, to that measured by the PHV641-L, V_{PHV}, by the percent difference between the two, $\varepsilon_1=\mu_1 \pm \sigma_1=0.011 \pm 0.023$:

$$V_{PPE} = (1+\varepsilon_1)V_{PHV} = (1+\mu_1 \pm \sigma_1)V_{PHV} \tag{3.3}$$

V_{PHV} is related to the signal measured with the cable, V_C, by $\varepsilon_2=\mu_2 \pm \sigma_2=-0.077 \pm 0.038$:

$$V_{PHV} = (1+\varepsilon_2)V_C = (1+\mu_2 \pm \sigma_2)V_C \tag{3.4}$$

Thus, V_{PPE} is related to V_C by:

$$V_{PPE} = (1+\varepsilon_1)(1+\varepsilon_2)V_C = (1+\varepsilon_3)V_C \tag{3.5}$$

Where $\varepsilon_3=\mu_3 \pm \sigma_3$:

$$\mu_3 = \mu_1 + \mu_2 + \mu_1\mu_2 + \sigma_1\sigma_2 \tag{3.6}$$

$$\sigma_3 = \sigma_2 + \sigma_1 + \sigma_1\mu_2 + \sigma_2\mu_1 \tag{3.7}$$

Equations (3.6) and (3.7) yield μ_3=-0.066 and σ_3=0.017. Thus, the PPE20kV signal is on average 6.6±1.7% lower than the cable signal at the top of the pulse, which is an acceptable level of signal attenuation.

Finally, we have two ways to evaluate the 10-90% rise time of the PPE20kV. First, Figure 3.31 shows that its rise time is definitely shorter than 6.6 ns. Second, if we overlook the noise problem of the PPE20kV in Figure 3.29, then we see that it is able to match the 2.8-ns rise time measured by the cable. Thus, it is able to measure the 5-ns rise time of the high-voltage pulse. In conclusion, we have validated the high-speed performance of the PPE20kV high-voltage probe, in terms of its ability to reproduce faithfully the fast rise time and amplitude of the high-voltage pulses investigated here.

3.11 Conclusion

In this chapter we described the experimental system used in this study and the performance characteristics of its most important components. We presented the global description of the plasma generation and measurement system. Then we provided the procedure for calibration in absolute intensity and synchronization with plasma generation of the monochromator and ICCD camera. In addition, we discussed the calibration in relative intensity and the detection synchronization with plasma generation of the PMT module. Next, we showed that the high-voltage pulse generator output can be described by a transmission line model. Finally, we validated the high-speed performance of the passive high-voltage probes used to measure the nanosecond pulses.

3.12 References

[3.1] Arc Applications Research.
[3.2] Optronic Laboratories, *Report of Calibration for One Standard of Spectral Radiance OL 550.*
[3.3] http://www.radio-electronics.com/info/antennas/coax/coax_cable_types.php.
[3.4] http://www.amphenolconnex.com/products/bnc.asp

Chapter 4

Characterization of the Discharge Regimes

4.1 Introduction

This chapter presents the experimental results for the characterization of the D and F discharge regimes. First, Section 4.2 defines these regimes. Then, in Sections 4.3 to 4.9, we show spectroscopic measurements obtained using the monochromator-ICCD camera and PMT module subsystems described in Chapter 3 that provide information on the plasma chemistry, ionization wave propagation, and gas heating. After discussing the spectroscopic results, we present digital camera images of the discharge regimes in Section 4.10. In Section 4.11, we present results concerning the initiation and stability of the F regime. Finally, in Section 4.12 we discuss the electrical characteristics of the discharge regimes measured using the passive high-voltage and current probes.

4.2 General characterization of discharges and regimes

We start with a preliminary description of the discharges observed in this study. Due to their transient nature, Nanosecond Repetitively Pulsed (NRP) discharges challenge neat classification into the same categories as for DC discharges [4.1]. Visually, however, they strongly resemble their DC discharge counterparts. They also arise in the same order with increasing applied voltage, namely in the corona-glow-spark regime sequence. Figure 4.1 shows images of the discharge regimes in atmospheric pressure air at 1000 K, with PRF=10 kHz, a gap distance of 4.5 mm, and an airflow rate of 1 m/s.

From Table 4.1, the "C" regime, like a corona discharge, emits light only part of the gap distance, almost always near the anode. The "D" regime resembles the NRP glow discharge previously studied in atmospheric pressure air at 2000 K [4.2], since its emission occupies the entire gap in a diffuse manner, with bright spots near the electrodes suggesting anode and cathode space-charge layers. Finally, the "F" regime is reminiscent of a spark discharge, with the characteristic electrode heating, intense emission, and high conduction current.

Despite these similarities, the diversity of atmospheric pressure air plasmas that has been observed under various conditions, as discussed in Chapter 2, makes it difficult to associate them with NRP discharges. To avoid premature identification with previously studied plasmas, in this work C, D, and F refer to corona-, diffuse-, and filamentary-*like* discharge regimes. Transitions between the regimes, particularly the one between the D and F regimes, are typically quite sharp in terms of visual appearance and occur with minimal increases in applied voltage. These visual changes are always accompanied by the corresponding changes in energy, current, emission levels, and gas heating specified in Table 4.1.

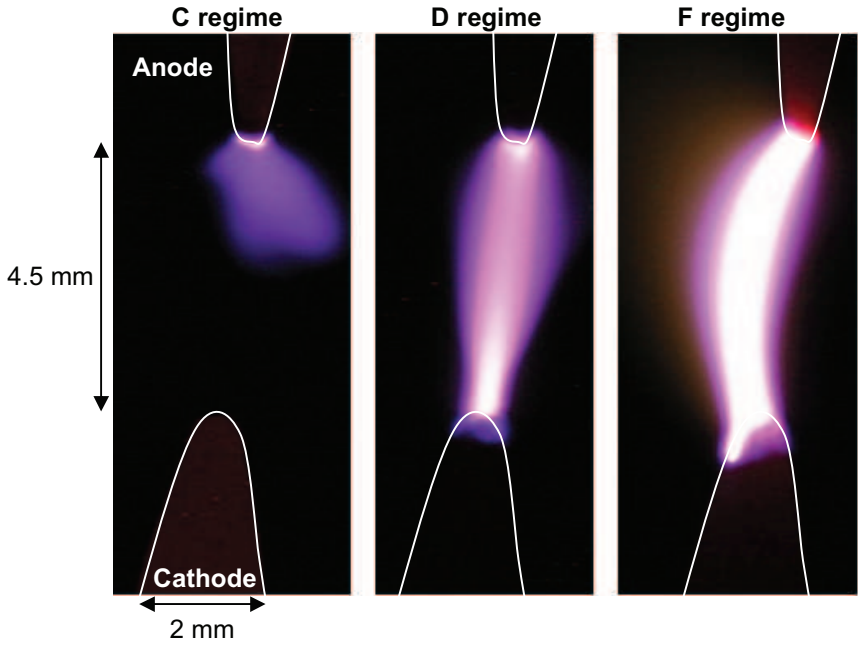

Figure 4.1: Images of the C, D, and F regimes in 1-atm air at 1000 K, with PRF=10 kHz, a gap distance of 4.5 mm, and an airflow rate of 1 m/s. The electrode shapes are outlined in white.

Table 4.1: Classification of observed discharge regimes.

Appearance	Energy deposited per pulse	Emission Levels	Gas Heating (+ΔT)	Name
Corona	<10 μJ	Low	~0	"C"
Diffuse	10-100 μJ	Medium	0-200 K	"D"
Filamentary	>100 μJ	High	2000-4000 K	"F"

At room temperature, one usually observes the C and F regimes. At higher temperatures, all three states are obtained. We will explore conditions for the appearance of the D regime and show that it can exist at room temperature, provided sufficient gap distance. This is important because the D regime has the potential for generating active species without significantly heating the gas, and its existence over the entire 300-2000 K range is critical for applications requiring such conditions. In this chapter, we will focus on experimental results characterizing the discharge states, and in Chapter 5, we will investigate the parameters controlling the transition between the D and F regimes.

4.3 Principal emission bands of the D regime from 200 to 800 nm

In this section we present examples of the spectra emitted in the D regime. The spectra presented in Figure 4.2 to Figure 4.5 were measured with the monochromator-ICCD camera subsystem described in Section 3.2. We wish to illustrate the general forms of the spectra, from which specific features are chosen in Sections 4.5 to 4.7 for analysis of the D regime. Each band head is labeled according to the vibrational transition (v',v'') that it

represents. Figure 4.8 will demonstrate that, of the systems shown from Figure 4.2 to Figure 4.5, only NO-γ persists more than ~50 ns after the application of the high-voltage pulse. Afterwards, no other emission systems emerge before the next pulse. The emission features used in following sections are the NO-γ (0,1), N_2 (C-B) (0,0), N_2 (B-A) (2,0), and N_2^+ (B-X) (0,0) bands as well as the O(3p ^{5}P-3s $^5S^0$) line. In each case, the intensity of the feature will be determined by subtracting the underlying background emission.

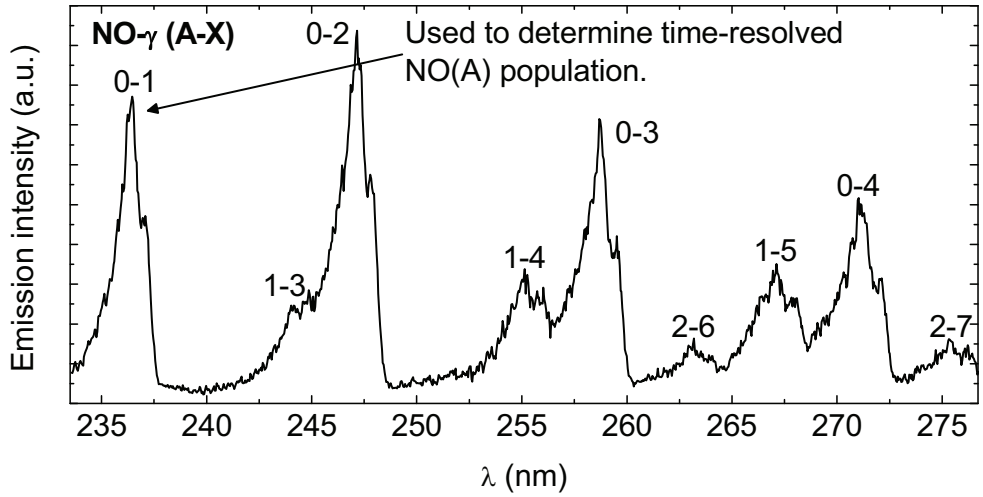

Figure 4.2: Typical experimental NO-γ spectrum of the D state, taken with a 2-ns gate width 52 ns after the rising half-maximum of the high-voltage pulse. T_g=1000 K, PRF=30 kHz, *d*=5 mm, v=1.55 m/s.

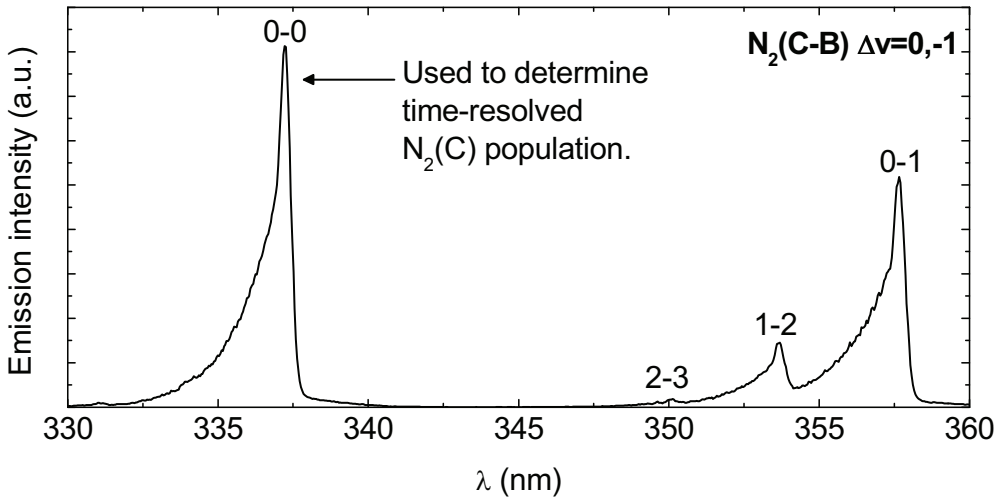

Figure 4.3: Typical experimental N_2 (C-B) Δv=0 and Δv=-1 spectrum of the D state, taken with a 2-ns gate width 36 ns after the rising half-maximum of the high-voltage pulse. T_g=1000 K, PRF=30 kHz, *d*=5 mm, v=1.55 m/s.

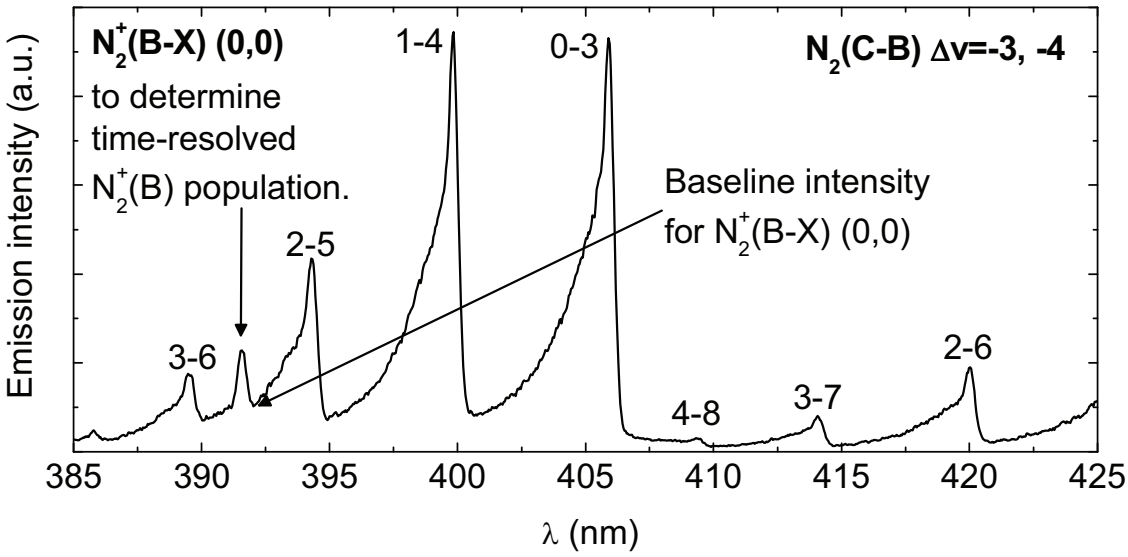

Figure 4.4: Typical experimental N_2 (C-B) Δv=-3,4 and N_2^+ (B-X) (0,0) spectrum of the D state, taken with a 2-ns gate width 34 ns after the rising half-maximum of the high-voltage pulse. T_g=1000 K, PRF=30 kHz, *d*=5 mm, v=1.55 m/s.

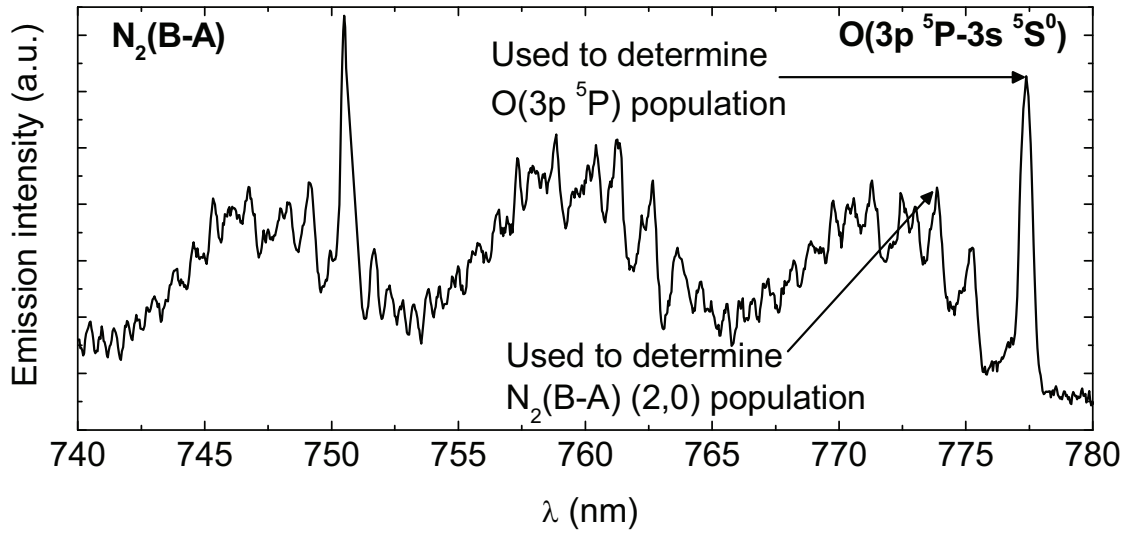

Figure 4.5: Typical experimental N_2 (B-A) and O(3p ^{5}P-3s $^5S^0$) spectrum of the D state, taken with a 2-ns gate width 34 ns after the rising half-maximum of the high-voltage pulse. T_g=1000 K, PRF=30 kHz, *d*=5 mm, v=1.55 m/s.

Note that the spectra of the D regime only contain emission features of air species, unlike the spectra of the F regime, which also contain atomic lines of metal. This indicates that the D regime causes negligible erosion of the electrodes.

4.4 Time-integrated spectra of the F regime from 200 to 800 nm

Here we present the emission spectra of an F state from 200 to 800 nm, which show numerous lines of atomic vapor. These are cathode region emission spectra, unlike the mid-gap region spectra from Section 4.3. Figure 4.6 and Figure 4.7 show the complete time-integrated spectrum of an F state for three different periods during the recombination period following the pulse. First, emission was accumulated during a 100-ns gate with a 300-ns gate delay, corresponding to 170 ns after application of the high-voltage pulse. Then, a 1-μs gate at 1 μs and a 10-μs gate at 10 μs after the high-voltage pulse were used.

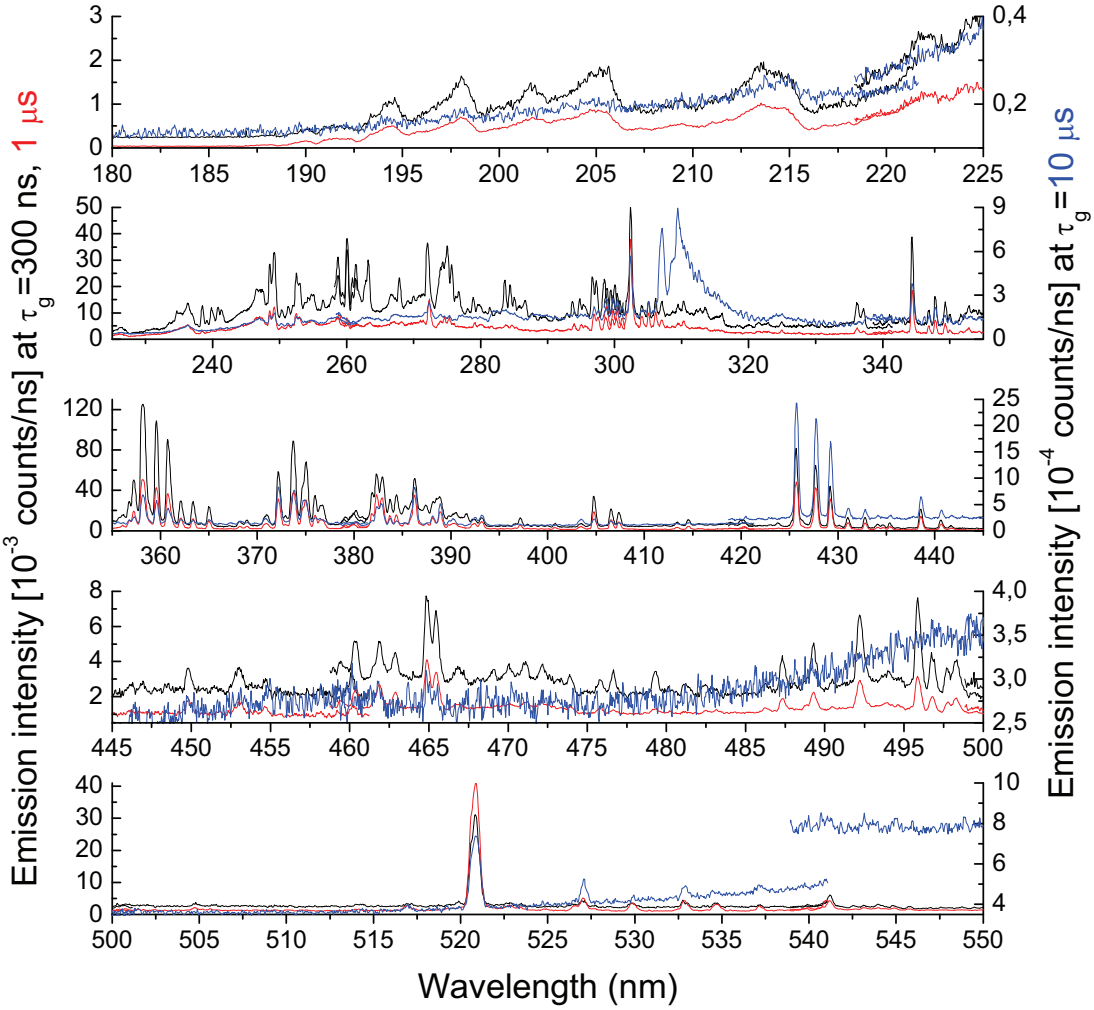

Figure 4.6: Time-integrated cathode region emission spectra from 180-550 nm of the F state at 300 ns, 1 μs, and 10 μs after the application of the high-voltage pulse. T_g=1000 K, PRF=30 kHz, *d*=5 mm, v=1 m/s.

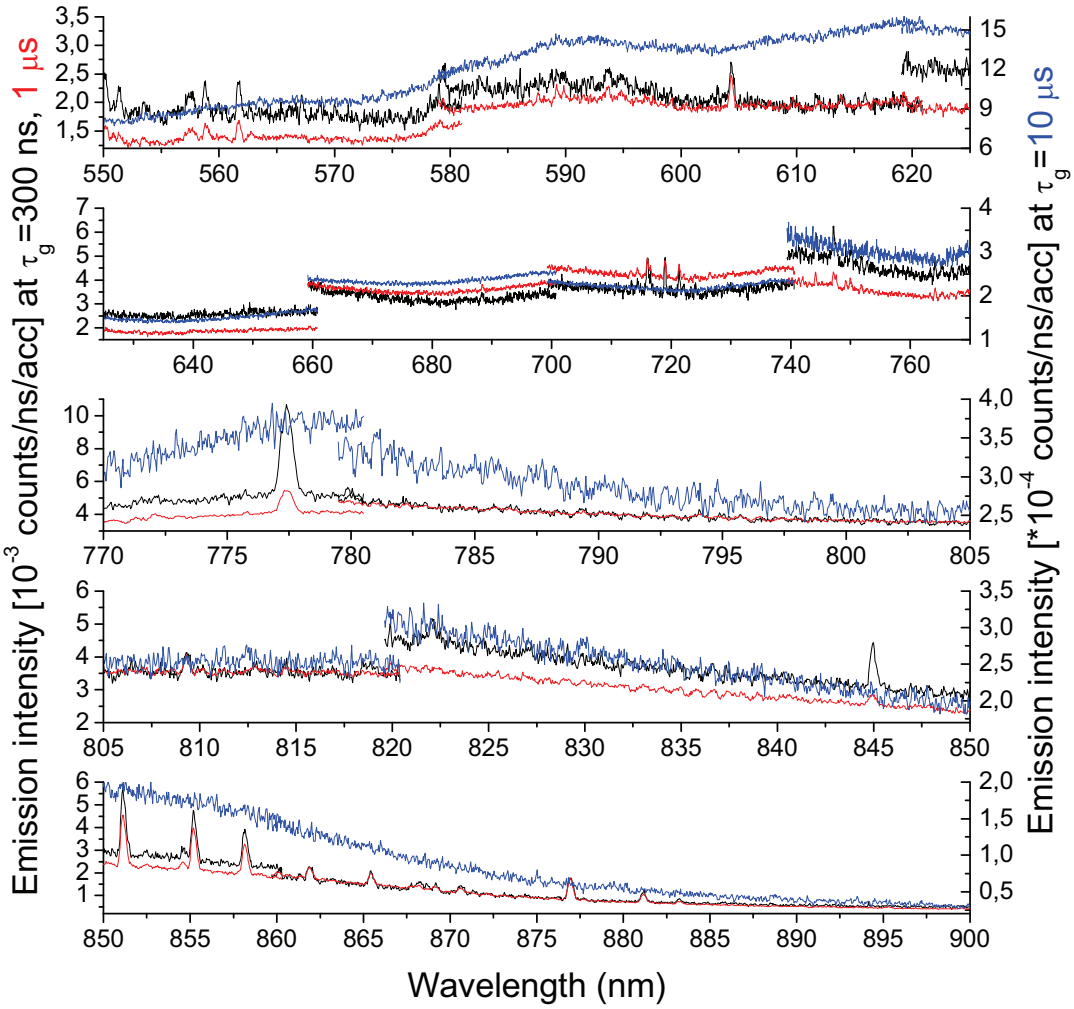

Figure 4.7: Time-integrated cathode emission spectra from 550-900 nm of the F state at 300 ns, 1 μs, and 10 μs after the application of the high-voltage pulse. T_g=1000 K, PRF=30 kHz, *d*=5 mm, v=1 m/s.

The mid-gap emission spectra of the F regime during the pulse and immediately thereafter did not differ qualitatively from those of the D regime and are therefore very similar to the D regime spectra shown in Figure 4.2 to Figure 4.5. Quantitatively, they were about one order of magnitude more intense. Unlike the D regime, however, numerous emission bands emerged in the F state once the initial burst of emission subsided. Some bands persisted and even emerged as late as 10 μs after the high-voltage pulse.

Note that Figure 4.6 and Figure 4.7 have not been calibrated in absolute intensity nor corrected for uneven pixel response across the CCD array. The pixels that record data at the low wavelength end of an acquisition spectral window register higher counts than those at the high wavelength end. This results in discontinuities between adjacent spectral windows. Thus, these figures serve only as a qualitative guide to the species observed for the F regime.

Aside from molecular features of NO and OH (A-X) (around 310 nm), it is clear that the spectra exhibited numerous atomic lines of air as well as of metallic vapor. This indicates erosion from the electrodes, which would be expected in a relatively hot spark or transient arc discharge.

4.5 Time-resolved excited species number densities of the D regime

Optical emission spectroscopy is a completely non-perturbing means of investigating plasma chemistry. The obtained spectra are calibrated in absolute emission intensity to yield time-resolved excited atomic and molecular species' number densities. This information is deduced from spontaneous emission, whose radiative transition probability is expressed as the Einstein A coefficient. This coefficient is approximated as the product of the transition probabilities between electronic, vibrational, and rotational levels, which are respectively described by the electronic transition moment R_e, the Franck-Condon factor $q_{v'v''}$, and the Hönl-London factor $S_{J''\Lambda''}^{J'\Lambda'}$:

$$A_{ul} = \frac{64\pi^4 \nu^3}{3hc^3} R_e^2 q_{v'v''} \frac{S_{J''\Lambda''}^{J'\Lambda'}}{2J'+1} \tag{4.1}$$

The local emissivity or volumetric radiation source strength, which describes the radiated power from a source volume per unit of solid angle, can then related to the upper state population N_u, the Einstein A coefficient, and the difference between the upper and lower state energies, also called the transition energy ΔE_{ul}:

$$\varepsilon\left[\mathrm{W/cm^3/sr}\right] = \frac{N_u A_{ul} \Delta E_{ul}}{4\pi} \tag{4.2}$$

Tabulated values of these various coefficients for the excited species studied in this work as well as an in-depth discussion on their calculation are found in the Ph.D. thesis of Laux [4.3]. Equation (4.2) implies that the upper level number density can be deduced if the local emissivity, Einstein A coefficient, and the transition energy are known.

We now discuss the procedure for time-resolved excited species number density measurements. In Chapter 3, we discussed the calibration procedure for the monochromator-ICCD camera subsystem, which provided a direct relationship between the measured count rate and the radiating power from the emitting source area, e.g. the tungsten ribbon lamp or the mini-arc. All the system parameters remained the same for measurements of the plasma, with the exception of the camera gating parameters, which were adjusted for optimum Signal-to-Background (S/B) and Signal-to-Noise (S/N) ratios within a reasonable real-time measurement period. To increase S/B, the gate width or the number of on-CCD accumulations was increased, or both. Increasing the gate width did not affect the real time for the measurement but decreased the time resolution of the measurement, whereas increasing the number on-CCD accumulations did not affect the time resolution but increased the real time required. Increasing the number of numerical accumulations increased S/N. Finally, the gate width was minimized to achieve the

highest time resolution possible. Table 4.3 lists the gating parameters used for each of the spectral features investigated.

Using a wavelength range that contained the spectral feature of interest, acquisitions were made for a progression of gate delays, until a minimum S/N of 2 was no longer possible within a 30-minute real-time measurement period. The spectral feature's emission intensity in raw count form was calculated by subtracting the line- or band-edge raw count, which represented the baseline spectrum. The line- or band-edge raw count is a good approximation for the baseline because it does not vary much in the narrow wavelength range overlapping the measured band. For example, Figure 4.4 illustrates how the N_2^+ (B-X) (0,0) band sits atop the N_2 (C-B) Δv=-3 band. Following the baseline correction, each data point was converted from raw count to count-rate form by dividing the raw count by the corrected gate width, number of on-CCD accumulations, and number of numerical accumulations. Section 3.3 discussed these corrected parameters. Then, each data point in count-rate form was divided by the system response (shown in Figure 3.9) at the appropriate wavelength, which gave the emission intensity of the plasma, in units of W/cm^2/sr. Note that the emission intensity cannot be directly used in Equation (4.2), which requires the local emissivity. Later in this section, we will discuss how to convert the former to the latter. Sections 3.3 and 3.4 explained the general procedures for camera gating and absolute emission intensity calibration.

For the present study, we chose a particular D state under the following operating conditions: T_g=1000 K, PRF=30 kHz, d=5 mm, and v=1.6 m/s. These conditions produced a very spatially and temporally stable D state. Also, the applied voltage was in the "middle" of the D regime at an applied voltage (V_p) of 6.7 kV, far from the C-D and D-F transition voltages. We selected several spectral features for investigation, which are shown in Figure 4.2 to Figure 4.5. These transitions were used to determine the populations of the upper states N_2(B), N_2(C), N_2^+(B), NO(A), and O(3p ^{5}P).

For each of the molecular electronically excited states N_2(B), N_2(C), N_2^+(B), and NO(A), the number density must be summed over all of its rotational and vibrational states. Therefore, to deduce the number density from a spectrum, it is necessary to calculate Equation (4.2) for all rovibronic transitions of a particular electronic transition. SPECAIR, a program for modeling air plasma spectra, performs this task. The excited state number density is calculated based on the gas, rotational, vibrational, and electronic temperatures that the user specifies as input. The modeled spectrum of the electronic transition of interest is then fitted to the measured spectrum, in absolute intensity. The excited state number density is found in a SPECAIR output file.

We seek to measure time profiles of number density, and fitting modeled spectra to measured spectra at each time step would not be practical. Instead, for each excited molecular species, we construct a time profile of the intensity at one wavelength. The wavelengths and their corresponding optical transitions are shown in Table 4.2. We determine a reference number density for each species by fitting a modeled spectrum to the measured spectrum for only one point in time, and then we normalize the rest of time profile by this reference number density. The reference number density is usually

determined at the time of maximum emission intensity, with the sole exception being for NO(A). In this case, the NO-γ bands are strongly overlapped by other NO bands at the time of maximum emission intensity, and therefore we use the spectrum measured 8 ns afterwards, where only the NO-γ bands are present, to determine the reference number density. There are errors associated with this normalization method, but they are not significant compared to the dynamic range of the measured intensities. In Appendix C, we will discuss these errors in detail.

For the excited atomic species O(3p ^{5}P), the use of Equation (4.2) is straightforward, as it does not have rotational or vibrational modes. The energy of the 3p ^{5}P-3s ^{5}S transition is shown in Table 4.2, and its Einstein A coefficient is 3.69×10^7 s^{-1} [4.3].

Table 4.2: Optical transitions selected for D state time-resolved measurements.

Excited (Upper) state	Transition	Wavelength (nm)	Transition energy (cm^{-1})
NO(A)	NO-γ (0,1)	236.27	42324.30
N_2(C $^3\Pi_u$)	N_2 (C-B) (0,0)	337.03	29671.10
N_2^+(B)	N_2^+ (B-X) (0,0)	391.14	25566.10
N_2(B $^3\Pi_g$)	N_2 (B-A) (2,0)	773.21	12933.10
O(3p ^{5}P)	3p ^{5}P – 3s ^{5}S	777.42	12857.6

Table 4.3: Camera gating parameters for the acquisition of D state emission spectra.

Excited (Upper) state	Gate delay range (ns)	Gate width range (ns)	on-CCD accumulation range	numerical accumulations range
NO(A)	129-2.7×10^4	2-5000	10^5-5×10^6	10-50
N_2(C)	129-1050	2-1000	50-5×10^5	25-100
N_2^+(B)	129-789	2-50	1000-5×10^5	25-100
N_2(B)	133-415	2-50	5×10^4-10^6	20-40
O(3p ^{5}P)	131-415	2-50	5×10^4-10^6	20-40

Figure 4.8 presents the results for these selected excited states. We define t_{RHM} as the time following the Rising Half-Maximum (RHM) of the initial high-voltage pulse. First, we address the chemistry that occurs starting at t_{RHM}~250 ns, boxed in by the shaded region in the top graph. It is due to secondary high-voltage pulses that are inherent to the generator and are not reflections from the load of a transmission line. The origins of these secondary high-voltage pulses are discussed in Appendix A. There are several of them, but they are of progressively lower amplitudes and do not generate as much chemical activity as the initial pulse. The long-term (t_{RHM} >1 μs) presence of NO(A) is boosted by the secondary pulses but not dependent on them. Instead, the persistence of NO(A) is largely due to its long recombination time. N_2(C), however, recombines fast enough to nullify the secondary pulse effect immediately, and eventually it resumes recombining as if these pulses never occurred. The other fast-recombining species were

not measurable in the long-term, but we surmise that they behave like $N_2(C)$, since their initial recombination times are about as short.

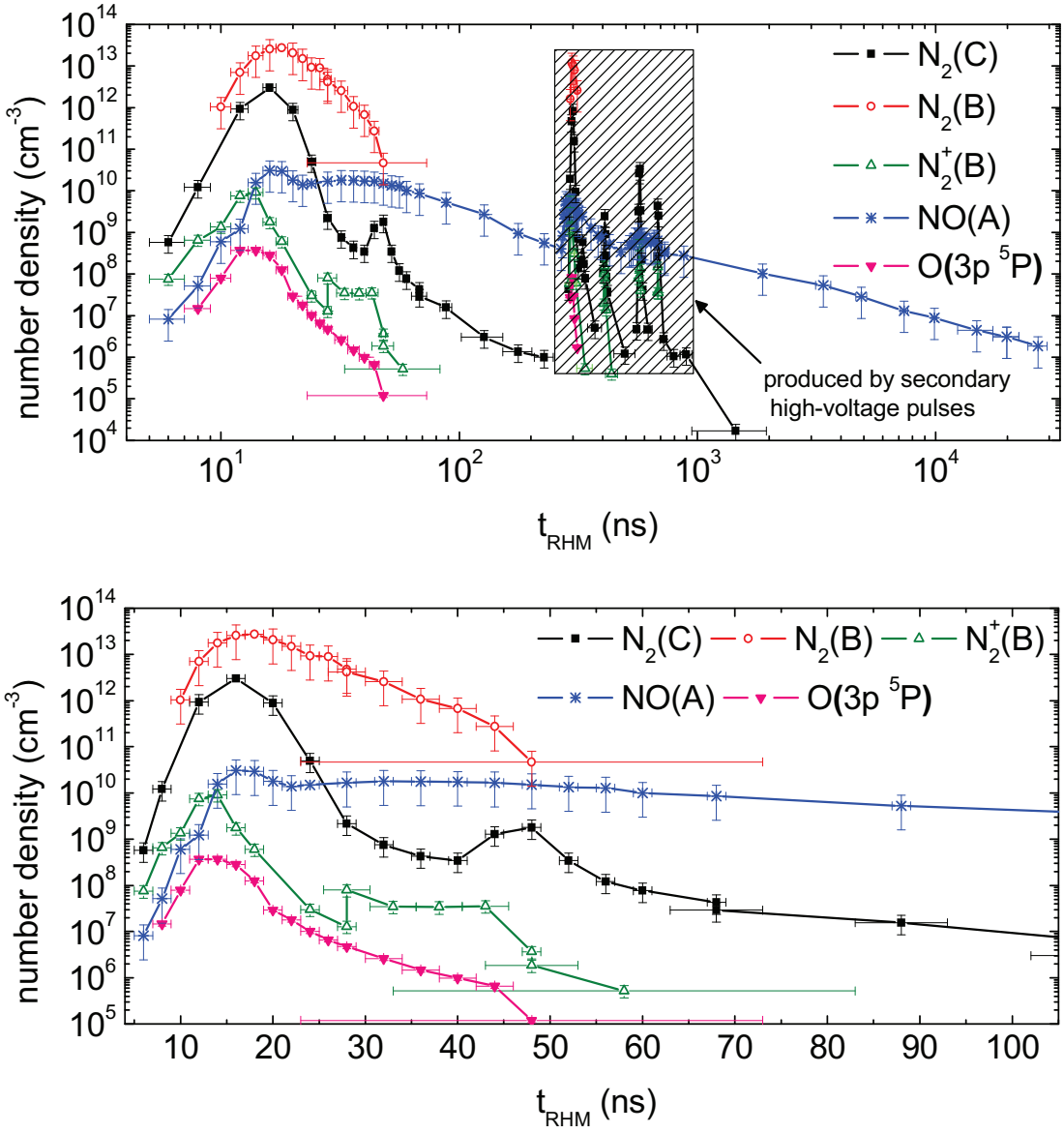

Figure 4.8: Measured excited species populations in the middle of the discharge gap for a D state throughout the pulse period (top) and a zoom of the first 100 ns after the high-voltage pulse (bottom). The data points were centered in the gate width time, which is represented by the horizontal error bars. T_g=1000 K, PRF=30 kHz, V_p=6.7 kV, d=5 mm, v=1.6 m/s.

During the initial pulse, the excited states' number densities reach values of 3×10^{12} cm^{-3} for $N_2(C)$, 2.8×10^{13} cm^{-3} for $N_2(B)$, 9.1×10^{9} cm^{-3} for $N_2^+(B)$, 1.5×10^{10} cm^{-3} for NO(A), and 3.7×10^{8} cm^{-3} for O(3p ^{5}P). All of the species recombine within 50 ns, except for NO(A), which is measurable throughout the repetition period. This is in agreement with results in atmospheric pressure air at 2000 K [4.2]. The populations of $N_2^+(B)$ and

$O(3p\ ^5P)$ reach their maximum values simultaneously and slightly sooner than the other species. Their recombination behavior is similar, with the exception of a second peak for $N_2^+(B)$ population at t_{RHM} =27 ns, which is not due to a secondary high-voltage pulse. The populations of $N_2(B)$, $N_2(C)$, and NO(A) reach their maximum values several nanoseconds later, with $N_2(B)$ recombining more slowly than $N_2(C)$. Like the population of $N_2^+(B)$, that of $N_2(C)$ peaks a second time, albeit later at t_{RHM} =47 ns. The second peaks observed for $N_2(C)$ and $N_2^+(B)$ could be ionization/excitation back waves (as discussed in Section 4.7). A 0-D chemical kinetic model by Caillault [4.5] does not predict these second peaks, which further suggests that they are the result of spatial rather than chemical effects.

As will be discussed in Section 4.6, the measured emission intensity is the sum, through an effective emitting source surface, of the radiating powers from each infinitesimal volume along the line-of-sight. However, we need the local emissivity to solve for the excited state number density using Equation (4.2). SPECAIR calculates the line-of-sight emission intensity for a cube of uniform emissivity. The cube is chosen to have a side length of 2 mm, the Full-Width Half-Maximum (FWHM) of the discharge, as will be shown in Section 4.6. Thus, by fitting a modeled spectrum to a measured spectrum in absolute intensity, we measure the average number density of an excited species in the volume from which emission is detected.

To obtain the number density at the center of the discharge, we use a mathematical de-convolution procedure called Abel inversion to convert the measured line-of-sight emission intensity into the local emissivity. This will be discussed in detail in Section 4.6. The volume of emission detection is approximately a cylinder whose radius and length are both 2 mm. The emitted power in W/sr can be computed by integrating the Abel-inverted emissivity over this cylindrical volume. In SPECAIR, we calculate spectra using a cube of uniform emissivity with a side length of 2 mm. To have the same power as the discharge emission collected from the cylinder, the uniform emissivity of the cube must be about 90% of the maximum Abel-inverted emissivity found at the center of the discharge. Thus, the line-of-sight emission intensity is normalized by 0.9 for conversion to emissivity at the center of the discharge. As a result, all of the number densities shown in Figure 4.8 are for the center of the discharge.

Using this single normalization factor for all data points implies two assumptions. First, we assume that all measured transitions had the same local emissivity radial profile as N_2 (C-B) (0,0) when normalized to unity, as shown in Figure 4.9. Without this assumption, we would have had to perform the Abel inversion for each measured species. Given the real-time cost of radial profile measurements (see Section 4.6), this would not have been practical. The error associated with this assumption depends on the deviation of the radial profiles of the various detected species from that of $N_2(C)$. However, this error should be fairly small, at least for the fast-decaying species. For NO(A), the profile is likely to be affected by diffusion, but only at long time scales. The second assumption is that the radial profile only scales in amplitude with time and does not change shape, which is approximately true upon observation of Figure 4.9.

4.6 Time-resolved radial emission profiles of the D regime

All spectroscopic measurements presented in this work are line-of-sight and collect light from a thin slice of the plasma's emitting volume, as opposed to a point within the volume. Since the plasma's emitting radius is at most only about 2 mm, which is small compared to the focal length of the collecting mirror (20 cm), the solid angle for light emitted from the point in the plasma closest to the mirror along the line of sight is very similar to that of light from the farthest point. In addition, no point along the line of sight is much out of focus. Therefore, there is no lateral spatial resolution. If, for instance, the plasma had a 1-m emitting radius, then most of the light emitted along the line of sight would be very out of focus, and we could claim to be collecting light from a spot within the plasma.

To address this problem, measurements were performed laterally (in the x direction) at the gap center (in the vertical z direction), and the set of line-of-sight data was converted to a radial local emissivity profile via Abel inversion. This technique requires radial symmetry such that the line-of-sight emission intensity $I(x)$ decomposes into a summation of the radial local emissivity profile $\varepsilon(r)$ times the length of each ring through which it intersects. This is the Abel transform:

$$I(x) = 2\int_{r}^{R} \frac{r\varepsilon(r)}{\sqrt{r^2 - x^2}}\, dr \tag{4.3}$$

Conversely, a lateral sweep of $I(x)$ reconstructs $\varepsilon(r)$ via Abel inversion:

$$\varepsilon(r) = \frac{1}{\pi}\int_{-x_R}^{x_R} \frac{dI/dx}{\sqrt{x^2 - r^2}}\, dx \tag{4.4}$$

The error in calculating $I(r)$ depends strongly upon dL/dx, making fine lateral spatial resolution necessary. Given the 1-2 mm emitting radius of the D state, increments of 0.125-0.25 mm proved satisfactory, where the emitting radius x_R was defined as the radial distance at which the emission intensity has dropped to 10% of its maximum value. The POLAB4 program written by Laux [4.3] was used to generate a polynomial fit of the lateral profile, calculate Equation (4.4), and calculate the error propagation. A detailed description of this algorithm is provided in [4.3].

Figure 4.9 shows the radial local emissivity profiles of $N_2(C)$ for the same D state studied in Figure 4.8 measured using the monochromator. The camera gate width was 2-ns for measurements, taken at fixed gate delays corresponding to emission occurring at t_{RHM}=8 ns, 16 ns, and 24 ns. These times correspond to the emission intensity rise, peak, and immediate fall times, respectively. A 180-ns gate width centered at t_{RHM}=169 ns was used to measure the radial profile during the early recombination period. The discharge is widest at t_{RHM}=8 ns, where the FWHM is 2.6 mm, and this is probably due to the diffuse Townsend avalanche phase of the discharge, as will be discussed in Section 4.8 as

well as in Chapter 6. At t_{RHM}=16 ns and 24 ns, the FWHM of the discharge reduces to 2 mm. Finally, at t_{RHM}=169 ns, the FHWM reduces slightly, down to 1.8 mm.

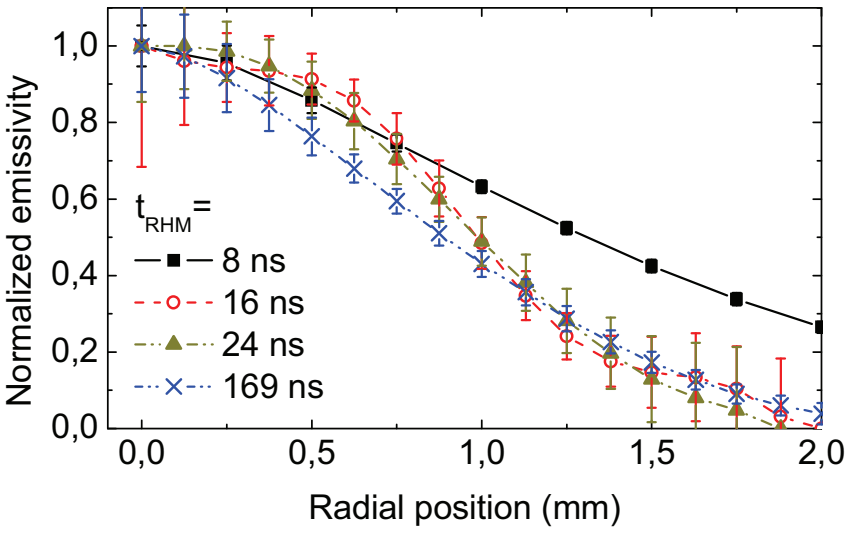

Figure 4.9: Abel-inverted radial local emissivity profiles of the N_2 (C-B) (0,0) band head in the center of the gap for the D state at various times t_{RHM}. T_g=1000 K, PRF=30 kHz, d=5 mm, v=1.6 m/s.

4.7 Spatio-temporal emission profiles of the D and F regimes using the monochromator – the presence of ionization waves

Now we consider the behavior of the D and F regimes in the axial direction. The results presented in Sections 4.3 to 4.5 describe the plasma only at mid-gap (r=0, z=d/2). Section 4.6 provided information in the radial direction. In this section we present the results of time-resolved monochromator measurements taken along the inter-electrode gap axis (the z direction) at each vertical 1-mm increment. These experiments were performed in the same fashion as the time-resolved emission measurements of the D state in Section 4.5. Unlike in those experiments, we fixed the camera gating parameters and did not calibrate the data in absolute intensity because our objective here is to determine the relative difference in behavior along the inter-electrode gap axis. Because the emission levels decreased by several orders of magnitude after only tens of nanoseconds, measurements were performed only down to 10% of the maximum intensity value. Measuring lower intensities would have required impractically long acquisition times.

Acquiring time profiles using the monochromator is time-consuming because each point in time is a separate measurement, whereas the PMT module registers all points in time at once. On the other hand, the monochromator is more sensitive, owing to the ICCD camera's accumulation capability. Its main advantage over the PMT module, however, is that it enables us to isolate spectral features sitting atop a significant background. For example, the time profiles for N_2 (C-B) (0,0), NO-γ (0,1), and O (3p ^{5}P-3s $^5S^0$) measured

in Section 4.5 could also be acquired using the PMT module, albeit over a smaller dynamic range, by choosing the appropriate narrowband interference filter. Figure 4.2, Figure 4.3, and Figure 4.5 show that these transitions do not sit atop any baseline spectra. On the other hand, the N_2^+ (B-X) (0,0) and N_2 (B-A) (2,0) transitions sit atop baselines uneven in intensity that are difficult to measure accurately using a second interference filter in a narrow band adjacent to the transition of interest. The monochromator, however, is capable of such fine filtering.

For these measurements along the electrode axis, the data processing steps were the same as in Section 4.5 except for the calibration. To provide information on the level of ionization, we measured the N_2^+ (B-X) (0,0) transition and corrected for the N_2 (C-B) (2,5) band baseline. To gauge the level of excitation, we also measured the N_2 (C-B) (0,0) transition, which does not require baseline subtraction. Measuring N_2 (C-B) (0,0) also enabled comparison with the PMT measurements in Section 4.8. Table 4.4 shows the camera gating parameters used for these measurements.

Table 4.4: Camera gating parameters for the acquisition of emission spectra of D and F states at various points along the electrode axis.

State	Transition	Gate width (ns)	On-CCD accumulations	Numerical accumulations
D	N_2^+ (B-X) (0,0)	2	300	100
F	N_2^+ (B-X) (0,0)	2	25	100
D	N_2 (C-B) (0,0)	2	30	100
F	N_2 (C-B) (0,0)	2	2	100

Figure 4.10 shows the measured emission profiles for representative D and F states with the same experimental conditions. The D state on the left-hand graph shows two distinct phases of discharge formation. Both $N_2(C)$ and $N_2^+(B)$ are generated at the anode initially and propagate as a wave toward the cathode. The N_2 (C-B) wave lags behind that of N_2^+ (B-X) by about 2 ns initially, at the anode. The average $N_2^+(B)$ wave velocity is 10^8 cm/s, similar to those reported by Aleksandrov *et al* [4.6] but lower than those of Marode [4.7]. Both waves diminish in strength as they propagate, and by the time they reach the middle of the gap, the $N_2(C)$ wave is no longer detectable. However, the $N_2^+(B)$ wave proceeds to gather strength and reach its maximum intensity at the cathode. The second phase consists of a back wave for $N_2(C)$. The overlapping N_2 (C-B) (2-5) band may obscure a similar back wave for N_2^+ (B-X). This back wave propagates from the cathode to the anode at 2.5×10^8 cm/s, considerable faster than the initial wave. Figure 4.10 (right) does not show waves for the F state, although the camera would not resolve a very fast wave, as its gate width is limited to a minimum of 2 ns. In Chapter 5, we will present F regime measurements using the PMT module to determine if ionization waves are present.

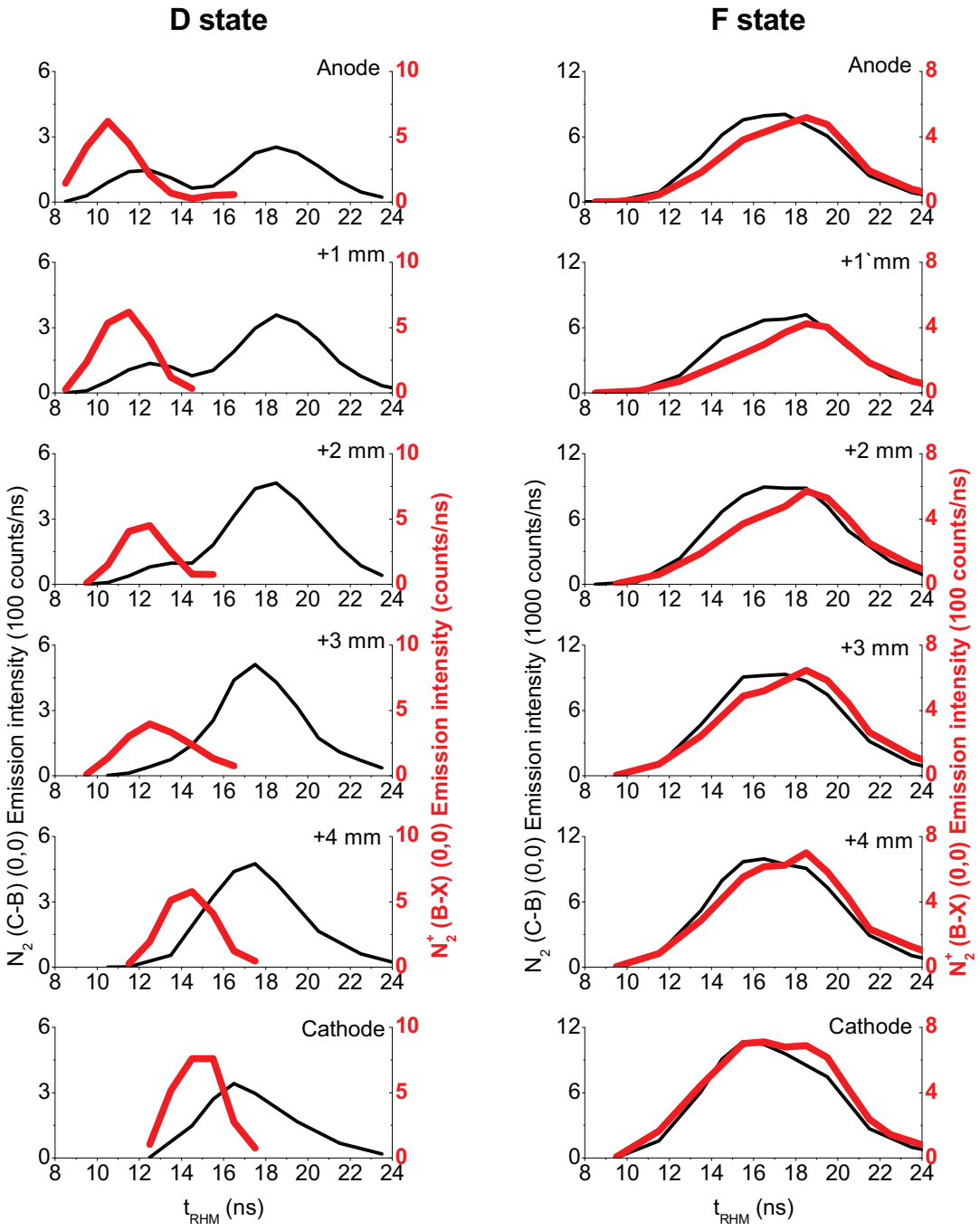

Figure 4.10: Measured N_2 (C-B) (0,0) (black and thin) and N_2^+ (B-X) (0,0) (red and thick) intensities along electrode axis of a D state at V_p=7 kV (left) and an F state (right) at V_p=7.3 kV. T_g=1000 K, PRF=30 kHz, d=5 mm, v=2.3 m/s. Positions along electrode axis are marked.

Despite the uncertainty surrounding the presence of an ionization wave for the F state, we can draw a key conclusion. In Section 4.12, we will show that the F regime conduction current is on the order of tens of amperes. Pilla [4.8] measured the emission radius of the

F regime operated in flames to be on the order of 1 mm. Using these estimates, we see that the F state produces current densities in the 1-kA/cm² range, which is characteristic of arc discharges [4.1]. In Section 4.9 it will be shown that under continuous pulsed operation (as opposed to duty-cycle pulsed operation), such as was the case for the acquisition of the data shown in Figure 4.10 (right), the F state maintains T_g>2000 K at all times. Recalling that the recombination time for an NRP glow discharge in atmosphere pressure air at 2000 K is 90 μs [4.2], it follows that the electron density should not decay significantly between two consecutive pulses. Thus the F regime generates high electron densities characteristic of arc discharges, which subsequently undergo slow recombination. An ionization wave may not be necessary for breakdown since the gap remains highly conductive. Subsequent pulses may maintain a high level of ionization through a series of local avalanches.

Another important observation from Figure 4.10 comes from comparing the relative intensities of the N_2 (C-B) and the N_2^+ (B-X) transitions. The N_2 (C-B) transition is about 20 times more intense in the F state than for the D state. On the other hand, the N_2^+ (B-X) transition is about 100 times more intense in the F state than for the D state. Therefore, assuming electron-impact excitation generates $N_2(C)$ and ionization creates $N_2^+(B)$, we see that the F state produces proportionally much more ionization than excitation. This corresponds well with observations in Section 4.12 that the F regime conduction current is significantly higher than that of the D regime. We will draw further conclusions in Section 4.12 from the fact that ionization is about 100 times stronger in the F regime than it is for the D regime.

4.8 Temporal emission profiles at the anode using the PMT module – the influence of the applied voltage on ionization waves in the D regime

In the previous section, ionization waves were shown to propagate back and forth across the discharge gap for the D state chosen for investigation. In this section, we present PMT measurements of N_2 (C-B) (0,0) emission across the D regime to demonstrate the effect of applied voltage on these ionization waves. Although the PMT module cannot be used to measure N_2^+ (B-X) (0,0), it was combined with the appropriate interference filter to measure $N_2(C)$ (see Sections 3.6-3.8 for details of the measurement system). As mentioned in the previous section, the PMT module lacks the monochromator's sensitivity, but its S/N is sufficient to distinguish ionization wave behavior. Moreover, its ability to collect an entire time profile at once permits the acquisition of data for many states across the D regime. Measurements were performed for several applied voltages, with all other operating conditions fixed: T_g=1000 K, PRF=30 kHz, d=5 mm, and v=1.6 m/s. Since the PRF was fixed, the PMT module was triggered using the BNC timing generator. The various system delays discussed in Section 3.8 were accounted for during data processing. We adjusted the PMT gain to optimize S/N without saturation and calibrated in relative intensity, as shown in Section 3.7.

Figure 4.11 shows measurements for the D regime taken at the anode for applied voltages of 5.8, 6.1, and 6.4 kV. These applied voltages respectively generated D states just above

the C-D transition, in the middle of the D regime voltage domain, and just below the D-F transition.

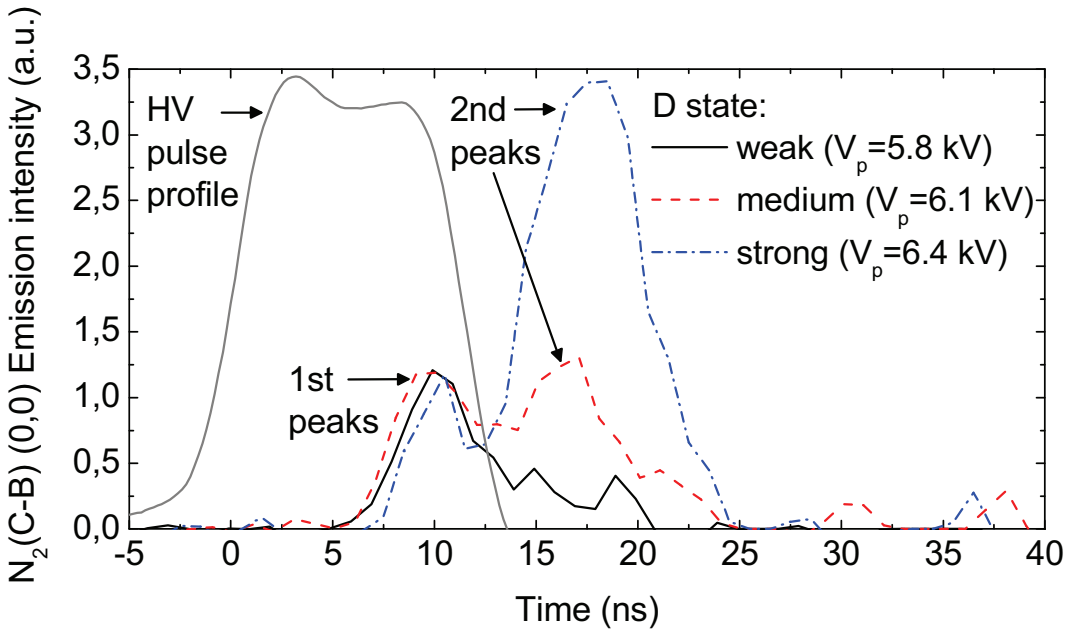

Figure 4.11: Measured N_2 (C-B) (0,0) emission intensity at the anode as function of time for weak, medium, and strong D states. The grey-colored HV pulse is strictly a profile in relative amplitude and serves only to orient the timing of the emission. T_g=1000 K, PRF=30 kHz, *d*=5 mm, v=1.6 m/s.

Hereafter, D states at these operating points are respectively referred to as the "weak," "medium," and "strong" D states, in the order of increasing applied voltage, as shown in Figure 4.12. Since these operating points are common to all D regimes, they are more useful for comparisons between different operating conditions than specific applied voltages. We also define similar common operating points for the F regime, as shown in Figure 4.12.

Two peaks of emission are distinguishable for the medium and strong D state cases. Their temporal spacing of about 10 ns and relative intensities agree with the measurements at the anode shown in Figure 4.10 (left), which was for a medium D state. The weak D state exhibits a single peak, which coincides with the first peak of the other two states. Interestingly, this first peak does not vary in time delay or intensity, regardless of the applied voltage. Figure 4.10 showed that this first peak appears first at the anode and then propagates toward the cathode, which suggests that it is an ionization wave and possibly a cathode-directed streamer. Therefore, we reason that the first peaks observed in Figure 4.11 represent the same phenomenon and conjecture that this streamer evolves in the same manner across the discharge gap as shown in Figure 4.10 for all applied voltages. Unlike the first peaks, the second emission peaks of the medium and strong D states depend strongly on the applied voltage. In Figure 4.11, the second peaks' intensities increase as a function of the applied voltage. In addition, these peaks occur at

the same time that the return wave reaches the anode in Figure 4.10. Thus, we presume that we are again measuring the return wave with the PMT module.

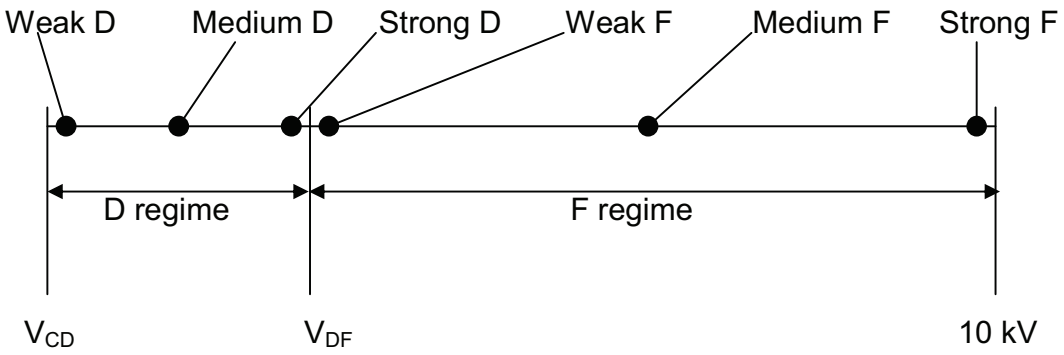

Figure 4.12: Definition of weak, medium, and strong states of the D and F regimes, which are defined by the C-D transition voltage (V_{CD}), D-F transition voltage (V_{DF}), and the maximum output of the high-voltage pulse generator (10 kV). The values of V_{CD} and V_{DF} depend on T_g, PRF, gap distance (d), and airflow velocity (v), as discussed in Chapter 5. The relative positions of weak, medium, and strong states, however, remain the same.

Figure 4.13 plots the first and second peak intensities as a function of the applied voltage across the D regime for the same operating conditions as Figure 4.11, except that PRF=20 kHz. It again demonstrates the independence of the first peak from the applied voltage, as well as a quadratic dependence of the second peaks.

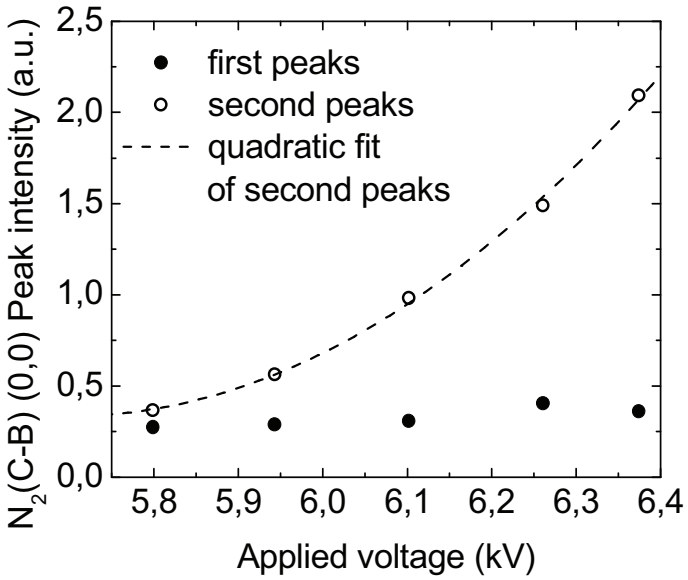

Figure 4.13: Measured first and second peaks of N_2 (C-B) (0,0) emission intensity at the anode as function of applied voltage across the range of the D regime. T_g=1000 K, PRF=20 kHz, d=5 mm, v=1.6 m/s.

This suggests a linear relationship between the second peak intensity and discharge power, as power is proportional to the square of the applied voltage. This is reasonable because the principal process for electronic excitation is via electron impact. The reaction rate for electron-impact electronic excitation is related to the electron energy, which is directly transferred from the electric field energy during the high-voltage pulse period.

The waves observed in Figure 4.10 and Figure 4.11 suggest a possible explanation of the physics of the D regime, which is summarized here and fully presented in Chapter 6. First, the high-voltage pulse initiates Townsend avalanches. A space-charge layer forms near the anode, generating a space-charge field that eventually meets Meek's criterion for the avalanche-to-streamer transition. As a result, a cathode-directed streamer initiates at the anode, which we observe as the first emission peak at the anode. The emission delays relative to the high-voltage pulse observed in Figure 4.8, Figure 4.10, and Figure 4.11 may be interpreted as the time required to meet Meek's criterion at the anode or the time required for the generation of emission. The initial streamer creates an ionized channel as it propagates across the gap. Once it reaches the cathode, the streamer head induces secondary electron emission from the cathode. These electrons cause a redistribution of potential in the cathode fall region until the final cathode fall voltage is reached. At this point, a glow discharge is established. The potential redistribution propagates across the gap, generating a return wave observed in Figure 4.10 and as the second emission peak at the anode in Figure 4.11.

4.9 Time-resolved gas temperature measurements of the D and F regimes

In this section we discuss time-resolved gas temperature (T_g) measurements at mid-gap made using the monochromator-ICCD camera subsystem to demonstrate that the D and F regimes exhibit very different degrees of gas heating. To measure T_g, T_g=T_r was assumed due to fast rotational-translational energy transfer. Then, T_r was found by fitting the measured N_2 (C-B) (0,0) band spectra to spectra produced by SPECAIR, a program for modeling air plasma spectra. We chose the N_2 (C-B) (0,0) band for fitting T_r because its shape is relatively simple, and it is sensitive to changes in T_r. Furthermore, its shape is independent of T_v because the superimposed hot Δv=0 bands (e.g. (1,1), (2,2), etc.) have much smaller Einstein A coefficients than the (0,0) band. Changes in the electronic temperature, T_{elec}, affect the emission intensity but not the shape of the N_2 (C-B) (0,0) band, and therefore fitting modeled spectra to experiment does not require knowledge of T_{elec}. Laux *et al* [4.9] discuss the details of this method.

The experimental procedure and modeling parameters were as follows. The measurements were performed in the same fashion as in Section 4.5 at mid-gap for both the D and F regimes at various times. The fixed conditions were T_g=1000 K, PRF=30 kHz, d=5 mm, and v=1.6 m/s. The applied voltage (V_p) was varied to explore different discharge regimes. We recorded N_2 (C-B) (0,0) spectra for weak and strong states in the D and F regimes, which were defined in Figure 4.12. Special care was taken to maximize S/B and S/N through on-CCD and numerical accumulation, because the entire band needed to be accurately measured for fitting with the modeled spectra.

The measured N_2 (C-B) (0,0) spectra and SPECAIR fits demonstrate that the D regime generates minimal gas heating, whereas the F regime greatly increases T_g. The top graph in Figure 4.14 shows the results for the weak D, strong D, and weak F states for a 2-ns gate width at t_{RHM}=7 ns. "Weak" and "strong" were defined in Figure 4.12. This is the earliest time with detectable emission for the weak D state, when the gas is at minimum T_g after 1/PRF=33 μs of cooling and before the upcoming high-voltage pulse heats it again.

The bottom graph in Figure 4.14 shows the results for the weak D, strong D, and weak F states for a 2-ns gate width at t_{RHM}=15 ns, the time of maximum emission for the weak D state. These graphs show that the weak D state does not heat the gas, which remains at T_g=1000 K both at t_{RHM}=7 ns and 15 ns. The strong D state maintains T_g=1200 K both at t_{RHM}=7 ns and t_{RHM}=15 ns. On the other hand, the weak F state starts at T_g=1900±100 K at t_{RHM}=7 ns before heating up to T_g=2500±300 K at t_{RHM}=15 ns. Thus, we have demonstrated that the F regime induces greater gas heating than the D regime at t_{RHM}=7 ns and 15 ns.

To obtain a better picture of F regime gas heating, we performed more measurements to construct a time profile of T_g. The measurements shown in Figure 4.14 and all results previously presented in this chapter were performed in "continuous pulsed" mode, which means that a pulse was delivered with each 1/PRF=33 μs period. The disadvantage of this mode is the ambiguity of the moment when the plasma and the electrodes reach steady state temperature behavior in the F regime. We visually observed that the electrodes glow brighter over the course of minutes, which indicates the time scale for gradual heating.

Furthermore, bright spots develop at the anode and cathode tips that increase in intensity over this time scale. The electrode tips erode as well, which is generally a problem in the F regime but greatly accelerated in continuous pulsed mode. Although we have not formally studied the effect of the electrode state on plasma behavior, we have noticed that the discharges become less stable temporally and spatially with damaged electrodes. In addition, the regime transition voltages generally increase. Thus, we had to clean and to re-sharpen the electrodes occasionally to ensure the repeatability of the experiments.

To alleviate electrode damage for the following measurements, we triggered the high-voltage pulse generator in "duty cycle pulsed" mode, in which pulses were applied for 700 consecutive 1/PRF=33 μs periods but none for the next 700 periods. This "700 pulsed, 700 non-pulsed" scheme was chosen for two reasons. First, 700 consecutive pulses sufficed to initiate and stabilize the behavior of the desired F state when applied to air unaffected by previous pulses. In Section 4.11 we will elaborate on the F regime's temporal stability. Second, the 700 consecutive non-pulsed periods was enough time for the electrodes to cool before the next 700 pulses such that they never glowed. The duty cycle pulsed mode was not used for previous measurements because they were performed before we began to consider the heating effect at large time scales.

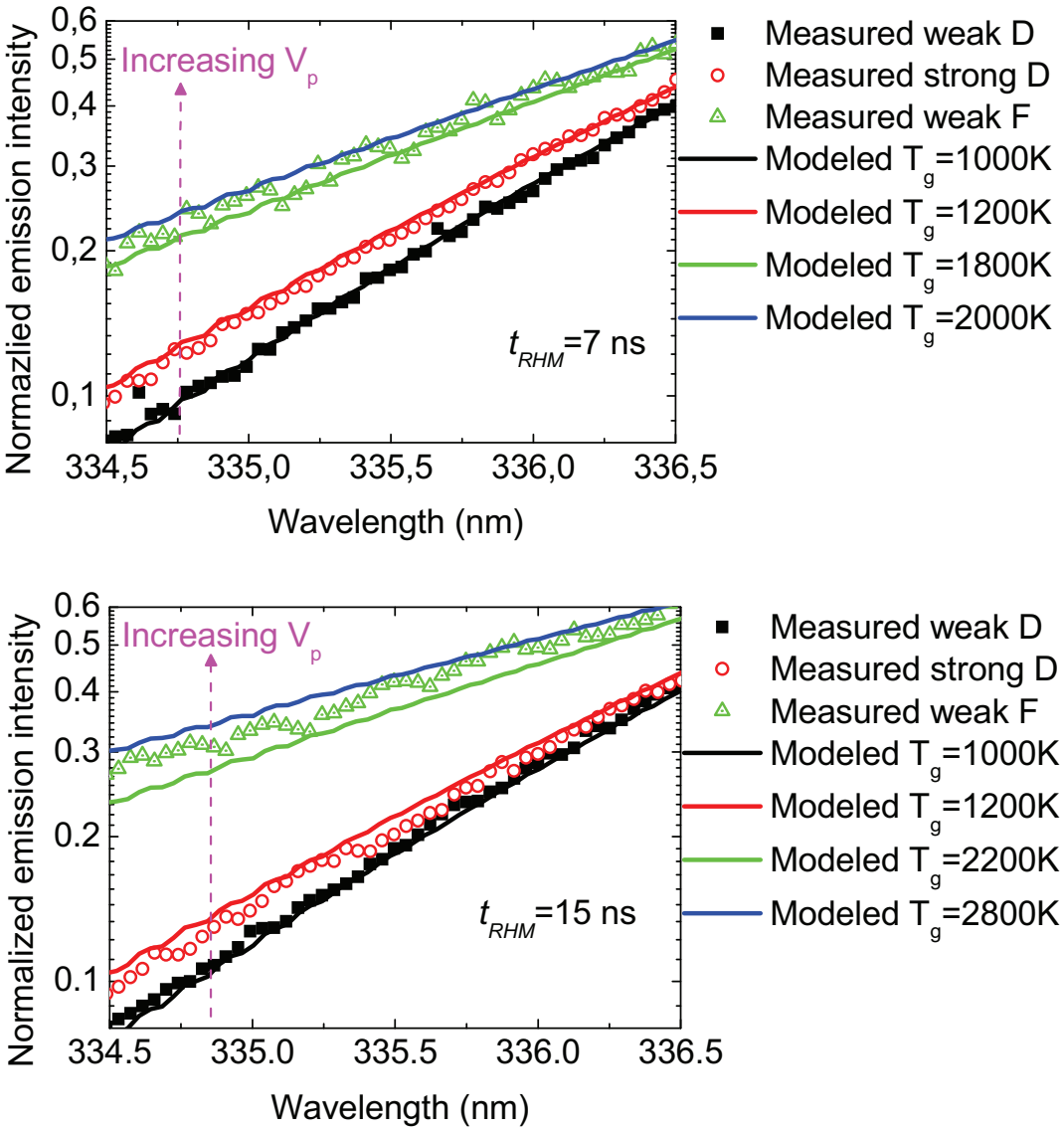

Figure 4.14: Measured N_2 (C-B) (0,0) spectra (symbols) and modeled spectra produced by SPECAIR (lines) at t_{RHM}=7 ns (top) and t_{RHM}=15 ns (bottom). T_g=1000 K, *d*=5 mm, v=1.6 m/s, PRF=30 kHz.

Figure 4.15 shows time-resolved rotational temperature measurements for the weak and strong F states for t_{RHM}=7-100 ns. "Weak" and "strong" were defined in Figure 4.12. The weak F state reaches a maximum temperature of 3800±200 K at t_{RHM}=32 ns. A similar rapid gas heating effect has also been observed by Popov [4.10]. The initial T_g at t_{RHM}=6 ns is 1450±50 K, which is ~400 K lower than that of the weak F state presented in Figure 4.14. This could be because the measurements from Figure 4.14 were performed in continuous pulsed mode instead of duty cycle pulsed mode, which may have resulted in a larger long-term temperature increase. The cooling of the weak F state also occurs very rapidly, returning to 1600±400 K at t_{RHM}=59 ns. This is in contrast with the 0-D

chemical kinetics model by Caillault [4.5], which predicts a much longer cooling period at the μs-scale.

One reason for such disagreement could be that the rotational levels of the $N_2(C)$ state might quench at different rates, thus distorting the rotational distribution. Although such preferential quenching has never been observed in N_2, Crosby and Crosley [4.11] measured such an effect in OH. Another possible explanation could be the occurrence of a fast expansion wave, suggested by Marode [4.12]. Indeed, if the gas heats up to 3800 K within 10 ns, this would produce a local pressure rise up to about 4 atm in the small filament channel that has a radius of about 1 mm. The pressure difference between the filament and the surrounding air at 1 atm would result in a pressure expansion wave and cool the filament adiabatically.

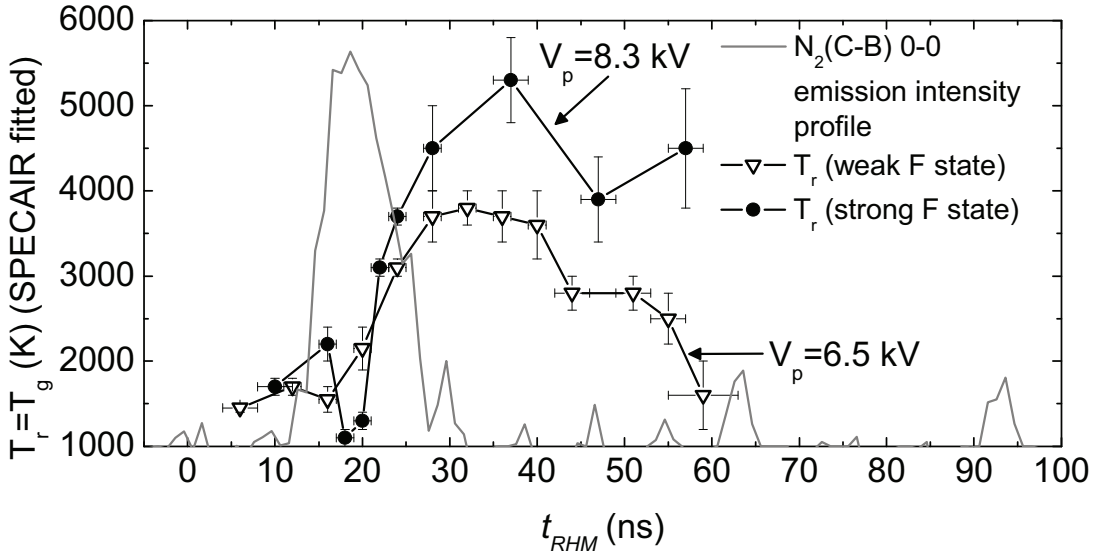

Figure 4.15: Measured gas temperatures for the weak and strong F states (symbols) and the time profile for N_2 (C-B) (0,0) emission intensity (solid line). The errors bars in time indicate the camera gate width for each data point. T_g=1000 K, PRF=30 kHz, *d*=5 mm, v=2 m/s.

Figure 4.15 also includes a representative N_2 (C-B) (0,0) emission intensity time profile for the F regime using the PMT module subsystem. The intensity is in arbitrary units and linear scale. It does not correspond to the y-axis units and is intended only to show that the moment of the peak emission intensity clearly occurs before that of the peak temperature for the F regime. This might be explained by the exothermic production of oxygen atoms through dissociative quenching [4.10].

The strong F state experiences a more substantial gas heating effect. Its T_g is initially 1700±100 K at t_{RHM}=10 ns and reaches a maximum of 5300±500 K at t_{RHM}=37 ns. A rapid cooling effect also occurs at about the same time as for the weak F state, although it less definitive because the error is significant at the latter times,. The strong F state also experiences an unexplained drop in temperature at t_{RHM}=15-20 ns, which coincides with the emission intensity maximum. With the exception of weak F states, we observed this

drop for other F states in a variety of operating conditions. Because the camera acquisitions required several minutes, we suspected that the discharge's behavior drifted at this time scale, thus distorting the time-resolved measurements. However, leaving the discharge in continuous pulsed mode operation for over an hour still resulted in momentary temperature drops at the same t_{RHM}. Moreover, they occurred regardless of the duty cycle pulsed mode scheme used. Thus, this behavior is not a result of instrumental or systematic error. Such a drastic dip in T_r over 5 ns is probably not a thermal effect and thus does not reflect T_g.

There are several sources of error that could explain the large uncertainties for some of the data points on the temperature curves shown in Figure 4.15. We have not yet carefully examined the spatial stability of the F regime. Under some circumstances, particularly for strong F states at low T_g, the spark filaments did not always follow the same path across the gap. It is not guaranteed that each camera gate measured the same part of the discharge. Typically, when the discharge was visually unstable, the camera registered data inconsistently. When the discharge was visually stable, successive acquisitions dependably agreed within 10%. In addition, we have not extensively determined if the same regime is produced with each pulse. Preliminary experiments on the temporal stability of the F regime will be discussed in Section 4.11. Finally, despite using the duty cycle mode for maintaining steady state, the discharge behavior may drift nonetheless. This may result in large errors for accumulated acquisitions taken over several minutes.

Another issue surrounding this measurement method may involve self-absorption of the N_2 (C-B) (0,0) band. Self-absorption reduces the band-head intensity in absolute terms and relative to the rest of the band. One way to gauge its effect is to compare the band-head intensity of the N_2 (C-B) (0,0) band ($I_{(0,0)}$) which is strongly self-absorbed, to the band-head intensity of the N_2 (C-B) (0,1) band ($I_{(0,1)}$), which is less self-absorbed. We have modeled spectra using SPECAIR to examine the effect of self-absorption on the band-head intensity ratio $I_{(0,1)}/I_{(0,0)}$ as a function of the various temperatures: T_g, T_r, T_v, and T_{elec}. We assumed an absorption length of l_a=1 mm because Pilla [4.8] measured this conductance radius for an F state generated in a flame, which was also measured to have T_r=2700 K and T_v=4000 K on average during the high-voltage pulse period, using the N_2 (C-B) (1,3) band.

As an example, Figure 4.16 shows two pure N_2 modeled spectra of the N_2 (C-B) (0,0) and (0,1) bands at T_r=T_g=2700 K, T_v=4000 K, and T_{elec}=50,000 K, one of which includes self-absorption. Note that the band-head intensity $I_{(0,0)}$ of the self-absorbed spectrum is almost completely suppressed. The rest of the band is relatively less self-absorbed. This would result in an overestimation of T_r=T_g if normalized and used for fits using SPECAIR. $I_{(0,1)}$ is absorbed as well because we have chosen T_v=4000 K, at which the N_2(B) v=1 state is populated enough to absorb substantially.

Figure 4.17 displays the modeled $I_{(0,1)}/I_{(0,0)}$ as a function of T_{elec}. T_v=4000 K was used for all the simulations. As indicated for the case of T_g=1000 K, if there is no self-absorption, $I_{(0,1)}/I_{(0,0)}$ is independent of T_{elec}. With self-absorption, $I_{(0,1)}/I_{(0,0)}$ increases with increasing

T_{elec} since the ground state for absorption of N_2 (C-B) (0,0) emission, N_2(B) v=0, becomes more populated. Figure 4.17 also shows that the deviation of $I_{(0,1)}/I_{(0,0)}$ from its value without self-absorption decreases with increasing T_r=T_g. To explain this, we consider the transmission, expressed as the ratio of the optically thick to the optically thin emission intensities (I_{thick}/I_{thin}), for each band head. Transmission is inversely related to the degree of absorption.

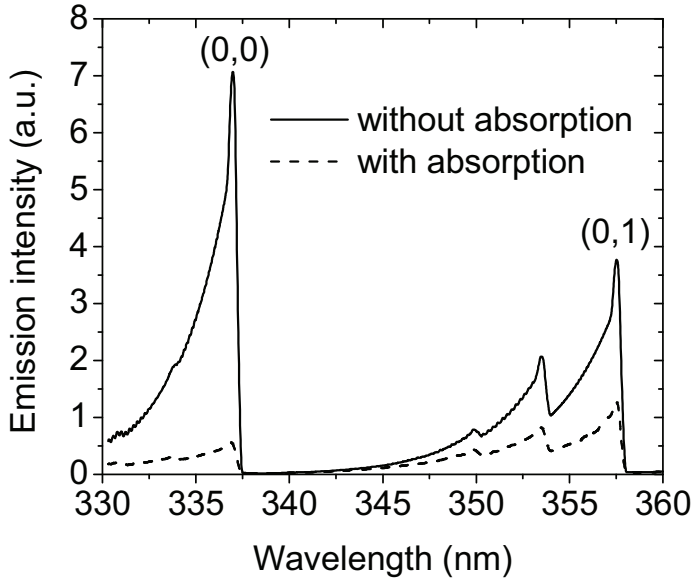

Figure 4.16: Simulated N_2 spectra of the N_2 (C-B) v=0,-1 bands showing (0,0) and (0,1) band head suppression due to self-absorption. T_r=T_g=2700 K, T_v=4000 K, T_{elec}=50,000 K. The absorption length is l_a=1 mm.

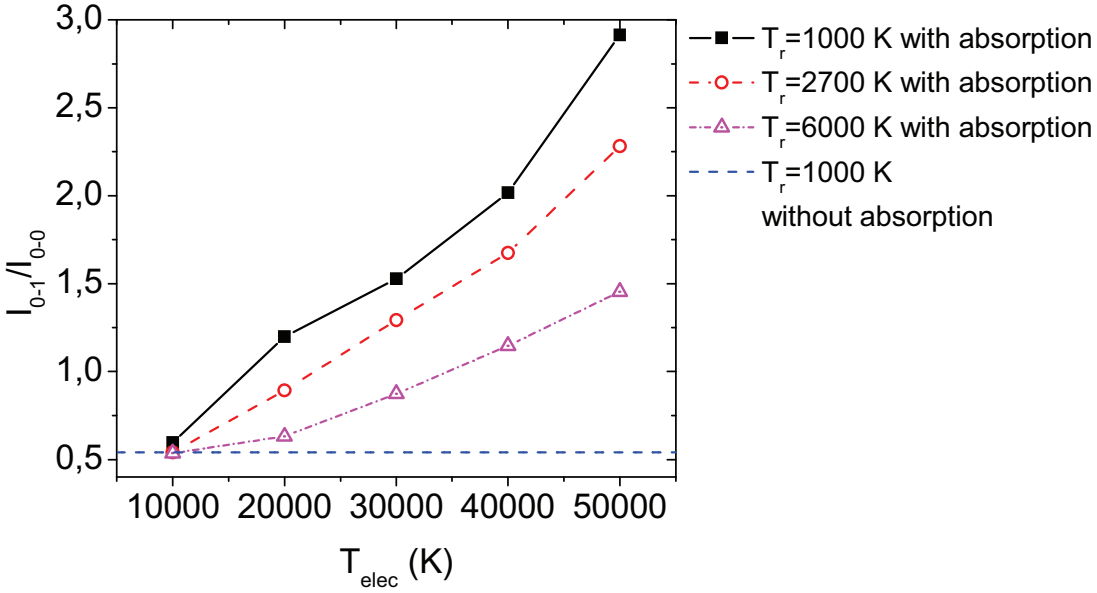

Figure 4.17: Ratios of intensities between the N_2 (C-B) (0,0) and (0,1) band heads of modeled N_2 spectra as a function of T_{elec} for several T_r=T_g. T_v=4000 K. The absorption length is l_a=1 mm.

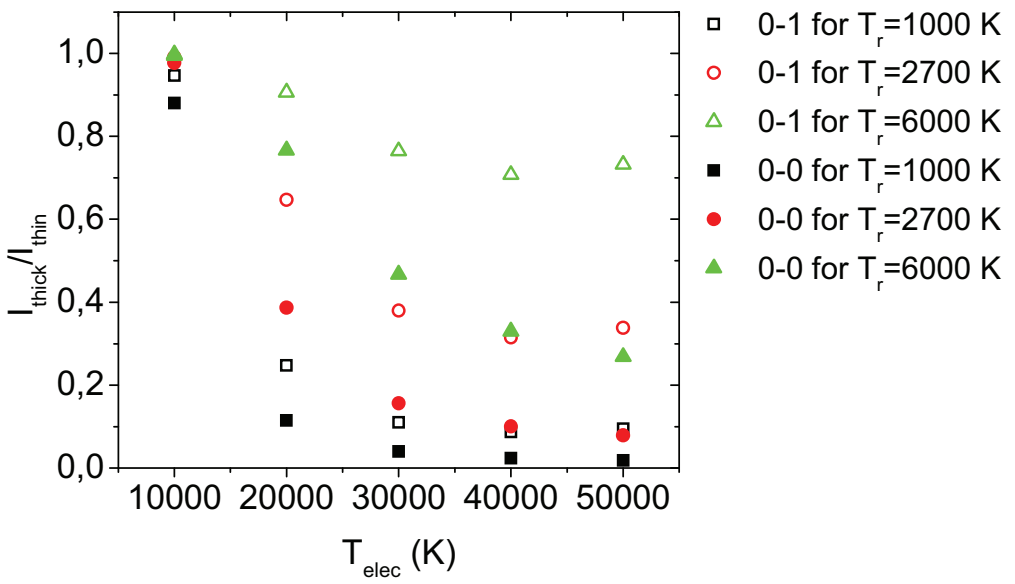

Figure 4.18: Ratio of optically thick to optically thin band-head emission intensities of modeled N_2 (C-B) (0,1) (hollow) and (0,0) (solid) spectra as a function of T_{elec} for several T_r=T_g. T_v=4000 K. The absorption length is l_a=1 mm.

Figure 4.18 shows the transmission as a function of T_{elec} for both the (0,0) and (0,1) band heads, for the cases of T_r plotted in Figure 4.17. For the same T_r, I_{thick}/I_{thin} for the (0,1) band head is always greater than that for the (0,0) band head, and thus the latter is more absorbed. With increasing T_r=T_g, I_{thick}/I_{thin} increases for both band heads because the J states forming the band head depopulate as more molecules occupy the higher J states forming the band tail. For the absorbing ground states of both bands, this depopulation of the J states with increasing T_r counters the increase in the population of the N_2(B) state with increasing T_{elec}. This reduces self-absorption and narrows the deviation between $I_{(0,1)}/I_{(0,0)}$ with and without absorption.

Now we address the self-absorption of the acquired F state spectra. Figure 4.19 (top) shows the measured spectra for the strong F state shown in Figure 4.15, normalized to the (0,0) band head. Some data points from Figure 4.15 are not shown since their spectra are overlapped by NH emission; these points are the three latest ones in Figure 4.19 (bottom). Figure 4.19 (bottom) presents $I_{(0,1)}/I_{(0,0)}$ corresponding to the spectra of the top graph as a function of t_{RHM}, and it shows that $I_{(0,1)}/I_{(0,0)}$ maintains nearly a constant value of about 0.57 at t_{RHM}=10-30 ns. This is very close to $I_{(0,1)}/I_{(0,0)}$ for the case of no absorption. In addition, Figure 4.15 shows that the SPECAIR temperature fits ranged from 1000-4500 K during the t_{RHM}=10-30 ns period. From Figure 4.17, it is clear that if self-absorption is present, such large differences in T_r must be accompanied by noticeable changes in $I_{(0,1)}/I_{(0,0)}$, except if T_{elec} is as low as 10,000 K, at which little self-absorption occurs. Otherwise, the plasma is optically thin and no absorption occurs regardless of the value of T_{elec}. In either case, negligible self-absorption of the N_2 (C-B) (0,0) transition occurs during the t_{RHM}=10-30 ns period.

The level of absorption becomes more difficult to determine during t_{RHM}=30-60 ns, when $I_{(0,1)}/I_{(0,0)}$ rises slightly above 0.57. These data points correspond to the spectra that are not shown in Figure 4.19 (top) because they are contaminated by NH emission that emerges during this period. Using SPECAIR simulations, we confirmed that NH emission did not hinder temperature fits using the (0,0) band. On the other hand, NH emission obscures the (0,1) band, which causes the rise in $I_{(0,1)}/I_{(0,0)}$ at t_{RHM}=30-60 ns. In any case, $I_{(0,1)}/I_{(0,0)}$ never exceeds 0.66, which is still very close to the non-absorbed value. It follows that the above arguments against absorption during the t_{RHM}=10-30 ns period also apply here. Thus, for t_{RHM}=30-60 ns, the self-absorption of the N_2 (C-B) (0,0) transition is negligible based on the low $I_{(0,1)}/I_{(0,0)}$ measured during this period.

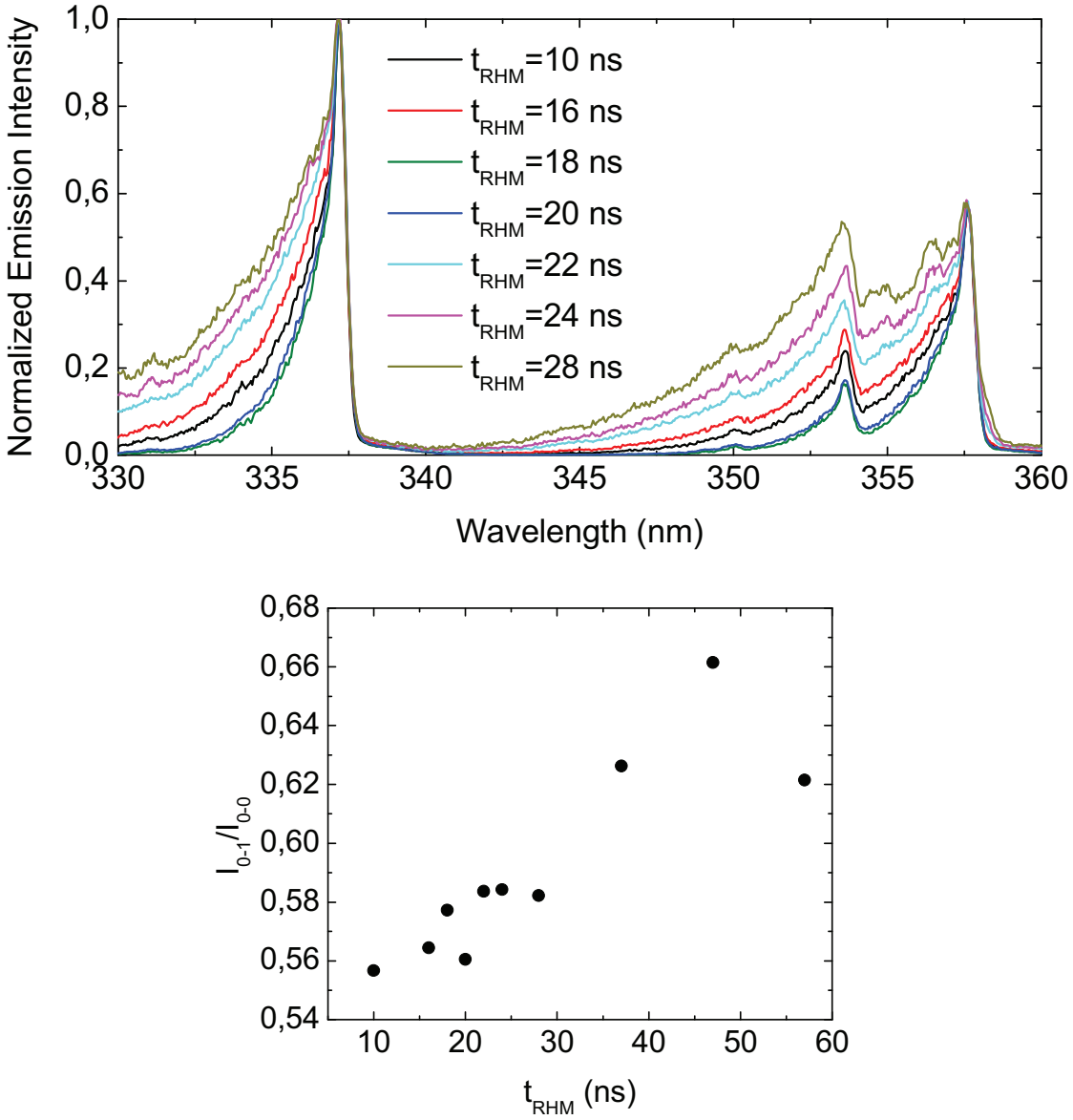

Figure 4.19: Measured N_2 (C-B) spectra (top) and the ratios of intensities between the (0,0) and (0,1) band peaks as a function of electronic temperature (bottom) for the strong F state shown in Figure 4.15. T_g=1000 K, PRF=30 kHz, *d*=5 mm, and v=2 m/s.

In conclusion, we have determined that self-absorption is a minor effect for all of the experimental spectra used to measure T_g. Therefore, the use of optically thin modeled spectra yields the true T_r when fitted to the experimental spectra. For more a more detailed analysis of self-absorption, see Appendix D.

4.10 Images of the D and F regimes

Having presented a series of spectroscopic measurements from Sections 4.3 to 4.9, we now finish the discussion on plasma optical emission in this section by presenting a series of images of the D and F regimes. Figure 4.20 shows digital camera images of the C, D, and F regimes in atmospheric pressure air at 1000 K, with PRF=10 kHz, d=4.5 mm, and v=1 m/s. The camera exposures were continuous, with exposure times ranging from 4 s for the weakest C state photographed to 10 ms for the weak F state. The exposure times were adjusted to avoid camera saturation and to obtain images representative of how the discharges appear to the eye. The light captured in the images is primarily from the N_2 (C-B) Δv=-3 and Δv=-4 band transitions in the 385-435 nm spectral range, which extends into the violet range. Thus, these images are also representative of the emission from the N_2 (C-B) (0,0) transition studied previously in this chapter. The difference is that emission from the N_2 (C-B) (0,0) band in the UV is considerably more intense than that from the N_2 (C-B) Δv=-3 and Δv=-4 bands in the visible.

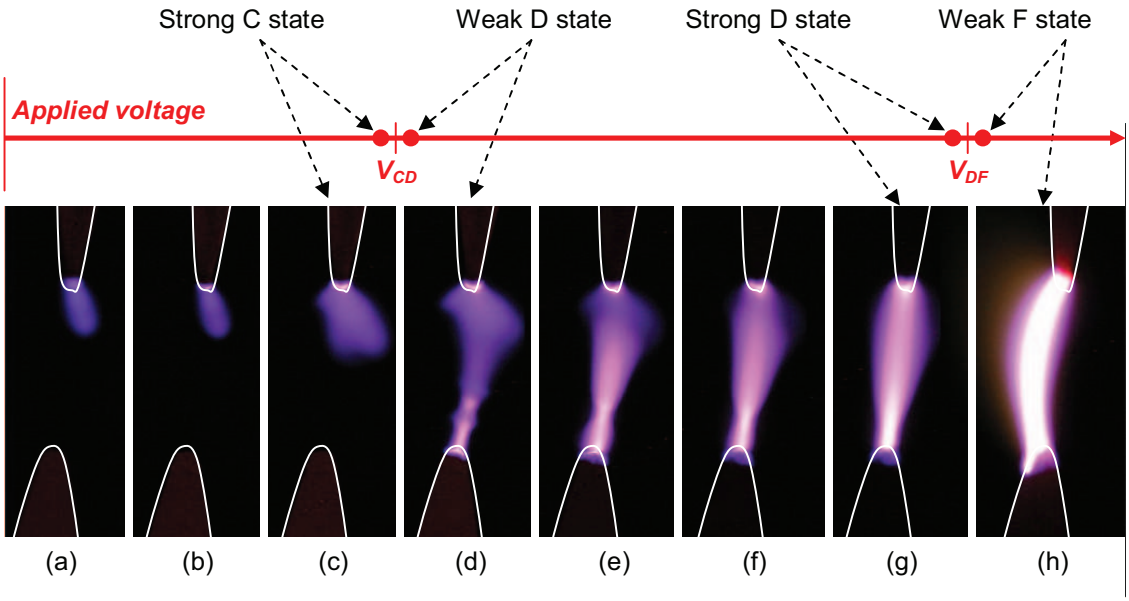

Figure 4.20: Digital camera images of the C (images (a)-(c)), D (images (d)-(g)), and F (image (h)) regimes in 1-atm air with T_g=1000 K, PRF=10 kHz, d=4.5 mm, and v=1 m/s. The anode shape is outlined in white at the top of each image, and the cathode shape is outlined at the bottom. Above the images is an axis of applied voltages with the C-D transition voltage (V_{CD}) and the D-F transition voltage (V_{DF}) indicated. The applied voltages and corresponding images for the strong C, weak D, strong D, and weak F states are indicated by dashed arrows.

The images in Figure 4.20 are accompanied by an axis of the applied voltage, with the voltages for the C-D transition (V_{CD}) and the D-F transition (V_{DF}) indicated. V_{CD} is about 6 kV, and V_{DF} is about 7 kV. Furthermore, the applied voltages and corresponding images for the strong C (image (c)), weak D (image (d)), strong D (image (g)), and weak F (image (h)) states are indicated, in accordance with the definitions from Figure 4.12. We emphasize that unlike the discharges observed previously and afterwards in this chapter, the discharges in this section were generated with PRF=10 kHz and d=4.5 mm instead of with PRF=30 kHz and d=5 mm. However, as will be shown in Chapter 5, the difference in plasma characteristics between these two operating conditions is not significant.

Images (a)-(c) of Figure 4.20 show that as the applied voltage increases, the C regime emission zone expands both in the axial and radial directions from the anode. In addition, a thin brightly emitting region develops very close to the anode surface. Upon reaching the C-D transition, the discharge bridges the gap with a narrow connection to the cathode, as seen in image (d). The anode region of the weak D state has the same shape as that of the strong C state shown in image (c). As the voltage increases in the D regime, the discharge becomes more spatially uniform, with the radial extent of the anode region decreasing and that of the cathode region increasing. In addition, the plasma appears to partially cover the electrode surfaces, more so on the cathode.

Recalling the preliminary explanation of the nature of the D regime from Section 4.8 (and fully discussed in Chapter 6), we note that the measured emission for the weak D state is primarily from the initial streamer, whereas that for the strong D state is primarily from the return wave. In Section 4.8, we found that the initial streamer remains constant in emission intensity throughout the D regime, although the return wave intensity increases with increasing applied voltage. Therefore, images (d)-(f) progressively show more emission from the return wave. Furthermore, the emission zone in image (d) sometimes extends to a radius of greater than 1 mm, which is larger than the typical 10-100 micron radii of streamers in air at atmospheric pressure. However, these images are not resolved in time, and it is possible that an initial streamer of typical radius takes a different path from the anode to the cathode with each applied voltage pulse. The accumulation of light from each of these streamers over a long exposure time would result in a large effective emission zone, as seen in image (d) of Figure 4.20.

Another possible explanation is that the large emission zone near the anode in image (d) is not from the streamer but instead from Townsend avalanches in volume near the anode. In Chapter 6, we will discuss how such avalanches may precede streamer formation in the D regime. This explanation is supported by the similarity of the emission zones near the anode of images (c) and (d). It is possible that the C regime involves only avalanche ionization, and that V_{CD} is the critical voltage for the avalanche-to-streamer transition. In this case, the narrow emission zone near the cathode in image (d) may be from the streamer following the avalanche-to-streamer transition. Therefore, we may consider images (c)-(g) as composite images of Townsend avalanches, the initial streamer, and the return wave that are progressively superimposed as the applied voltage increases.

Finally, image (h) of Figure 4.20 shows the weak F state. We adjusted the exposure time of the digital camera to show the least saturated image while still capturing the faint trail of light seen to the left of the discharge. This trail is commonly witnessed in the F regime, and it becomes more prominent with increasing applied voltage. It is perhaps due to glowing metallic particles that have been sputtered off of the electrodes by the discharge. This is consistent with the fact that the F regime erodes the electrodes, as discussed in Section 4.9. We also mentioned before that the electrodes glow when the discharge is in the F regime due to heating. This is not seen in image (h) because the camera exposure time had to be reduced to lessen the degree of saturation.

4.11 F regime initiation and stability

In this section, we discuss measurements of the minimum number of pulses required to achieve the F regime and the number of subsequent pulses needed to reach a stable state. We address this subject primarily to determine the appropriate number of consecutive pulses per duty cycle. This was relevant for the gas temperature measurements discussed in Section 4.9, which were performed in pulsed duty cycle mode. For the experiments discussed in this section, we fixed the operating conditions T_g=1000 K, d=5 mm, and v=1.6 m/s. The minimum number of pulses required for the initiation of the F regime was determined by applying a single burst sequence of high-voltage pulses, starting with one pulse and increasing in number until the F state was visually observed. Figure 4.21 shows the measured minimum number of pulses as a function of the applied voltage across the F regime, for PRF=1-30 kHz. Although there is significant variation, the overall trend is toward fewer pulses with increasing applied voltage. Up to 400 pulses are required near the D-F transition voltage. At the maximum voltage the generator can provide, 10.5 kV, only 2-3 pulses are needed.

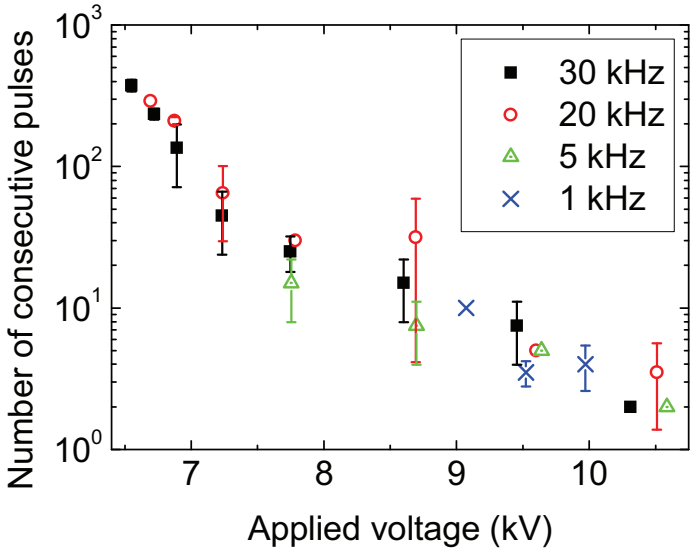

Figure 4.21: The minimum number of pulses required for initiation of the F regime as a function of the applied voltage for PRF=1-30 kHz. T_g=1000 K, d=5 mm, v=1.6 m/s.

In pulsed duty cycle mode, we must not only initiate the F regime but also achieve stable repetitive behavior before ending the pulse sequence. To determine the number of pulses required following initiation, we used the PMT module to determine when the emission intensity reached steady state. The PMT gain was adjusted to avoid saturation for any F state emission peak during the pulse sequence. To capture a sufficient number of consecutive pulses in a single acquisition, the oscilloscope was set to its maximum time window. As the oscilloscope was limited by a maximum number of samples per acquisition, the maximum time resolution for this time window was less than that required to guarantee capturing the nanosecond-scale emission signal. To ensure that the signal was not missed, we used the optional low-pass filter of the oscilloscope to elongate the PMT output in time. Although this distorted the time profile, proportional changes in signal amplitude were retained.

Figure 4.22 shows the results of these measurements for the conditions T_g=1000 K, PRF=30 kHz, *d*=5 mm, and v=1.6 m/s for several pulse sequence modes. First, the continuous pulse mode emission intensity was measured as a reference, and it varies from pulse to pulse with a 0.07 standard deviation about a mean value of 0.7. Next, the noise signal, which includes the EMI induced by the high-voltage pulses, was measured by setting T_g=300 K while running the high-voltage pulse generator in the same conditions. No discharge is generated, and the measured signal is only noise. The noise signal has a mean of 0.1 with a standard deviation of 0.02.

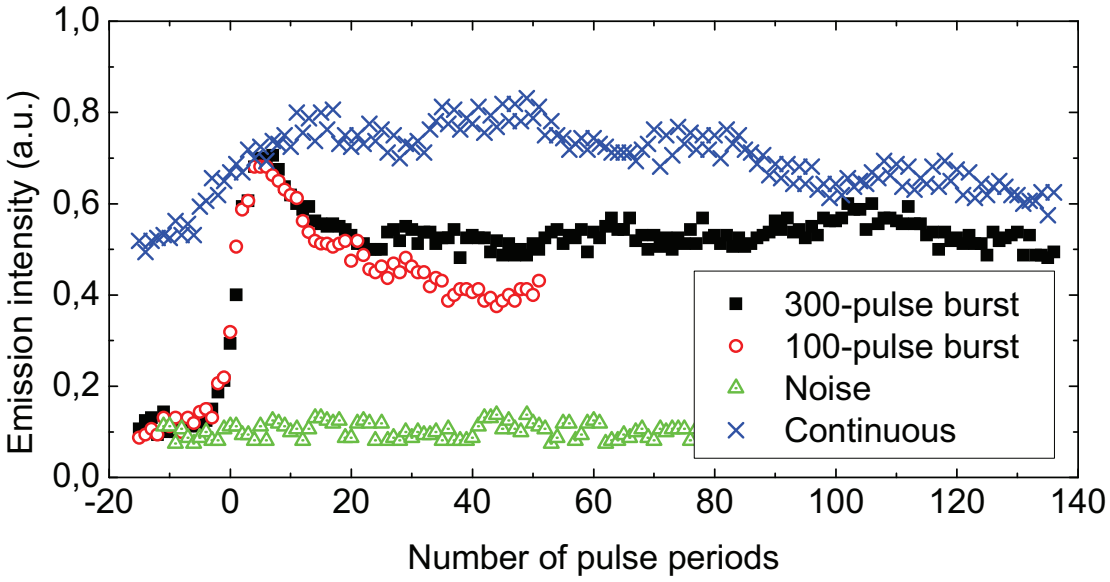

Figure 4.22: The filtered emission intensity of an F state as a function of the number of consecutive applied pulses for a single 100-pulse burst, a single 300-pulse burst, continuous pulsed mode, and the noise signal with no plasma present. T_g=1000 K, PRF=30 kHz, *d*=5 mm, v=1.6 m/s. The noise signal was acquired with high-voltage pulses applied but at T_g=300 K to avoid plasma generation.

Finally, single 100- and 300-pulse bursts were applied. The F state initiation cannot be measured because the PMT gain was adjusted for the maximum signal intensity over the

whole pulse sequence. Weakly emitting F states or even D states probably escaped detection. Thus, we can only claim that the emission rises above the noise floor to the maximum signal level in ~7 consecutive pulses. Afterwards, the emission intensity settles down to a steady value. For the 100-pulse burst, a steady state mean emission intensity of 0.4 is reached after ~10 pulses following the peak emission period. The continuation of this steady behavior for subsequent pulses is confirmed by the 300-pulse burst measurement, which has a mean steady state intensity of 0.5. The 100- and 300-burst steady state mean emission intensities are 57% and 71% of the continuous pulsed mode mean, respectively. This means that the continuous pulsed mode still reaches a more energetic F state due to processes at millisecond time scales or longer, such as heating.

In conclusion, we chose a 700-pulse sequence for the pulsed duty cycle mode measurements in Section 4.9 based on the number of consecutive applied pulses required to initiate and then stabilize the F state. From Figure 4.21, we see that up to 400 pulses are required to initiate the F state. The 100-burst sequence shown in Figure 4.22 implies that within 100 pulses following pulse initiation, the F state has reached steady state. To guard against variations in the number of pulses required for F state stabilization, we chose to buffer the sequence with 200 additional pulses.

4.12 Voltage and current characteristics of the D and F regimes

In this section, we present measurements of the discharge voltage and current during the application of the high voltage pulse to determine the electrical characteristics of the D and F regimes. To measure voltage, we used a Lecroy PPE20kV passive high-voltage probe with a 1000:1 voltage attenuation factor. Its ability to measure the high-voltage pulses investigated here was discussed in Section 3.10. The probe tip was attached to the anode, and the ground clip was attached to the cathode. To measure current, a Pearson Model 6585 Rogowski-type current probe was placed in a break in the shield of the 20-cm coaxial cable connecting the pulse generator to the electrodes and measured the current flowing in the inner conducting wire of the cable. It has a rise-time of 1.5 ns and a current-to-voltage ratio of 1 A to 1 V. Figure 4.23 shows an example of a current measurement made in ambient air with no discharge. The measured total current (I_{total}) is ideally only displacement current (I_{disp}), dictated by the electrode impedance (Z_{elec}):

$$I_{total} = I_{disp} = \frac{V_p}{Z_{elec}} \tag{4.5}$$

The electrode capacitance Z_{elec} is dominated by the capacitance of the 20-cm coaxial cable. Figure 4.23 displays the calculated I_{disp} derived from the applied voltage measured by the Lecroy probe. In this example, the capacitance was chosen as 9.15 pF to scale the calculated current to the same positive maximum value as the measured current. Using this scaling method, the electrode capacitance always remained in the 9-10 pF range for a 5-mm gap. Some variation is expected because the electrode configuration changed slightly each time the electrodes were dismounted for polishing.

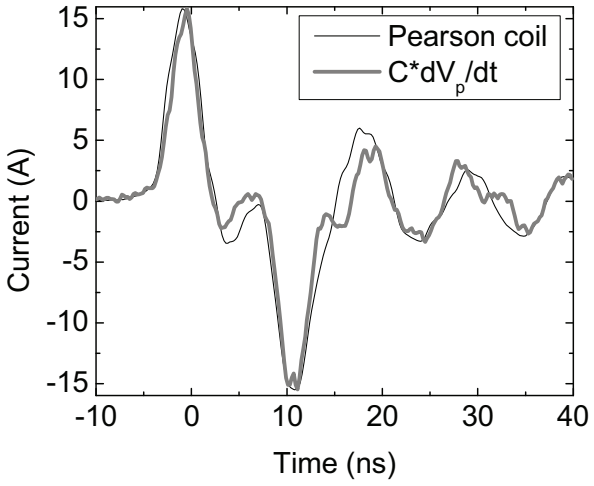

Figure 4.23: Typical measured current waveform in ambient air without plasma, using the Pearson coil (thin) and capacitive displacement current calculated from applied voltage measured by the Lecroy probe (thick). The inferred electrode capacitance is C=9.15 pF.

Figure 4.23 demonstrates good agreement between the measured and calculated currents, confirming that the Pearson coil can function at high speed. This also confirms that Z_{elec} is principally capacitive. The discrepancy between the curves is due to parasitic currents (I_{para}), notably from probe loading. The true I_{total} includes such parasitic effects:

$$I_{total} = I_{disp} + I_{para} = \frac{V_p}{Z_{elec}} + \frac{V_p}{Z_{para}} \tag{4.6}$$

In addition, the current ringing shown is real and not simply due to probe ringing. It is unlikely that two different types of probes would exhibit such similar ringing if it were not the true behavior of the circuit under measurement. However, since we are interested in the high-voltage pulse's ability to generate a discharge, all the following measurements strictly concern the pulse period. Figure 4.24 shows typical measured total current and voltage waveforms of the D and F regimes. The F regime current includes significant conduction current (I_{cond}) superimposed on I_{disp}, such that the total current is:

$$I_{total} = I_{cond} + I_{disp} + I_{para} \tag{4.7}$$

I_{cond} peaks during the second half of the high-voltage pulse, which itself experiences a drop. Thus, the plasma resistance (R_p) decreases sharply while the pulse is still applied.

Figure 4.25 shows an example of $I_{cond} \approx I_{total} - I_{disp}$ of the F regime. I_{cond} ranged from 20 to 40 A in the F regime, depending mostly on the applied voltage (V_p). The D regime current is almost entirely I_{disp}, as it closely resembles the current shown in Figure 4.23. With small I_{cond}, the D regime voltage and current waveforms are nearly indistinguishable from the corresponding waveforms when no plasma is present. The D regime I_{cond} did not rise above the ringing noise level and therefore will not be investigated further.

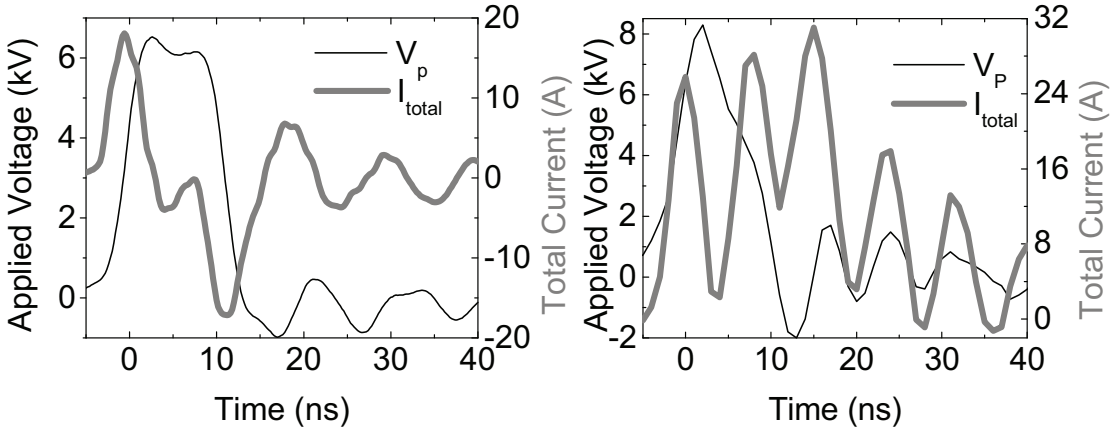

Figure 4.24: Typical measured current (thick) and voltage (thin) waveforms for a typical D state (left) and F state (right). T_g=1000 K, PRF=30 kHz, *d*=5 mm, v=1.6 m/s.

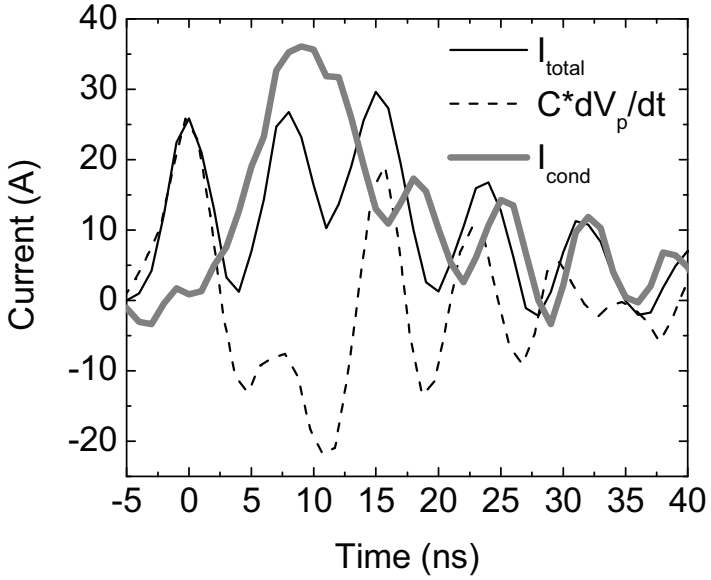

Figure 4.25: Measured total current, calculated displacement current, and calculated conduction current as a function of time for the typical F state corresponding to Figure 4.24 (right). T_g=1000 K, PRF=30 kHz, *d*=5 mm, v=1.6 m/s.

We calculate the plasma resistance R_p in the F regime by dividing the measured applied voltage by I_{cond}. Figure 4.26 presents R_p for the representative F state studied so far. Error due to noise becomes significant when I_{cond} is low, and therefore we must quantify the error. The current and voltage noise were determined using the data points preceding the pulse. It was found that the noise current had a mean value of -164 mA, with a standard deviation σ_I=123 mA. The noise voltage had a mean of 63.6 V and a standard deviation σ_V=25.8 V. Before they were used to calculate R_p, the raw signals were corrected for the noise offsets. The error in the resistance ΔR_p is:

$$\Delta R_p = \Delta\left(\frac{V_p}{I_{cond}}\right) = \frac{\left|I_{cond}\Delta V_p\right| + \left|V_p \Delta I_{cond}\right|}{I_{cond}^2} = \frac{\left|I_{cond}\sigma_V\right| + \left|V_p \sigma_I\right|}{I_{cond}^2} \tag{4.8}$$

We removed the data points with large ΔR_p from the plot in Figure 4.26. After retaining only the precise data, another problem remained: sometimes we measure negative R_p. For Figure 4.25, we calculated I_{cond} by subtracting I_{disp} arising strictly due to capacitance, but Figure 4.23 demonstrates that this does not account for I_{para}. Furthermore, parasitic reactive components can phase shift the current from the voltage. Since R_p<0 is clearly incorrect, we instead only focus on the data points in Figure 4.26 for which R_p>0.

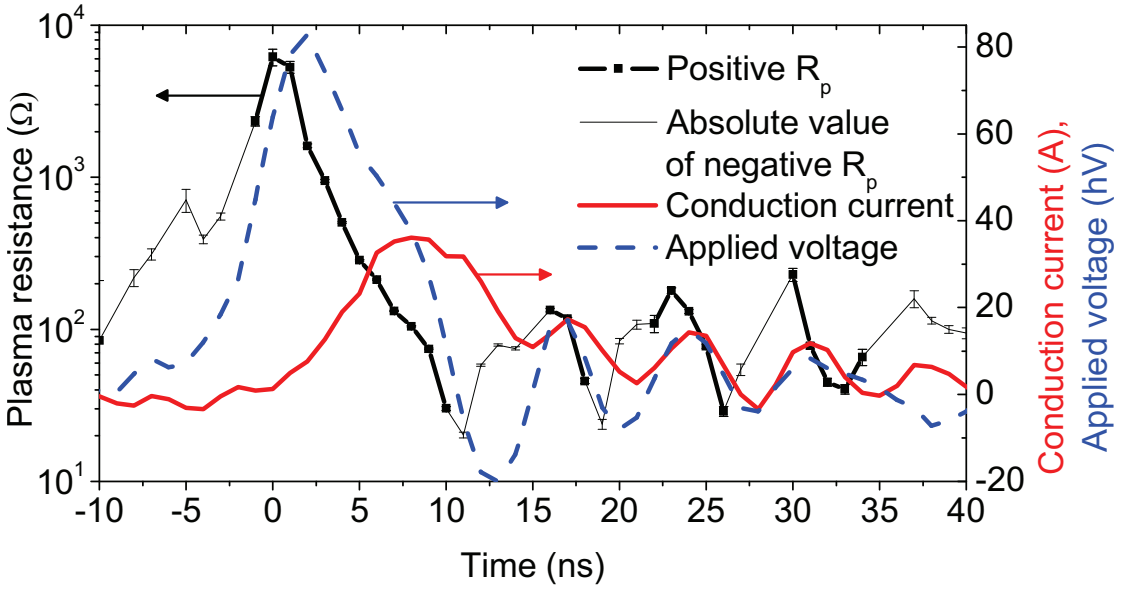

Figure 4.26: Measured plasma resistance, conduction current, and applied voltage as a function of time for the typical F state from Figure 4.24 and Figure 4.25. The plasma resistance plot includes those points for which R_p>0 (symbols and thick line) and those for which R_p<0 are plotted in absolute value (thin line). T_g=1000 K, PRF=30 kHz, d=5 mm, v=1.6 m/s.

At t=0, the high-voltage pulse is near its peak while I_{cond} is just beginning to climb above the noise floor. R_p at this time is at a maximum value of 6.2 kΩ and decreases as I_{cond} increases. As the voltage drops, R_p continues to decrease, down to a minimum of 30 Ω at t=10 ns. This is explained by ionization induced by the high-voltage pulse, which increases the electron density. This increases electrical conductance, which decreases R_p. The current and voltage oscillation phase ensues, and R_p also fluctuates during this period with a slight overall increasing trend. This indicates that the voltage oscillations after the pulse generate some ionization.

The dampening of the high-voltage pulse upon the appearance of I_{cond} is due to transmission line reflection at the plasma. We use R_p to calculate the reflection coefficient (Γ_R), knowing that the characteristic impedance of the cable connecting the pulse generator to the electrodes is Z_0=75 Ω:

$$\Gamma_R = \frac{R_P - Z_0}{R_P + Z_0} \tag{4.9}$$

The pulse delivered by the generator is the forward wave V^+ propagating toward the plasma load. Upon reflection at this load, a backward wave $V^- = \Gamma_R V^+$ propagates back towards the generator. The voltage measured at the load is the sum of the forward and backward waves:

$$V_p = V^+ + V^- = (1+\Gamma_R)V^+ = \left(\frac{2R_p(t)}{R_p(t)+Z_0}\right)V^+ \tag{4.10}$$

Therefore, we can reconstruct V^+, as shown in Figure 4.27. V^+ is closer to the trapezoidal pulse delivered by the generator than V_p measured by the probe. When R_p is high, $\Gamma_R \approx 1$ and $V_p \approx 2V^+$. As R_p decreases, Γ_R approaches the matching condition for R_p=75 Ω, for which Γ_R=0 and V_p=V^+. Finally, as R_p decreases further, Γ_R<0 and thus V_p<V^+.

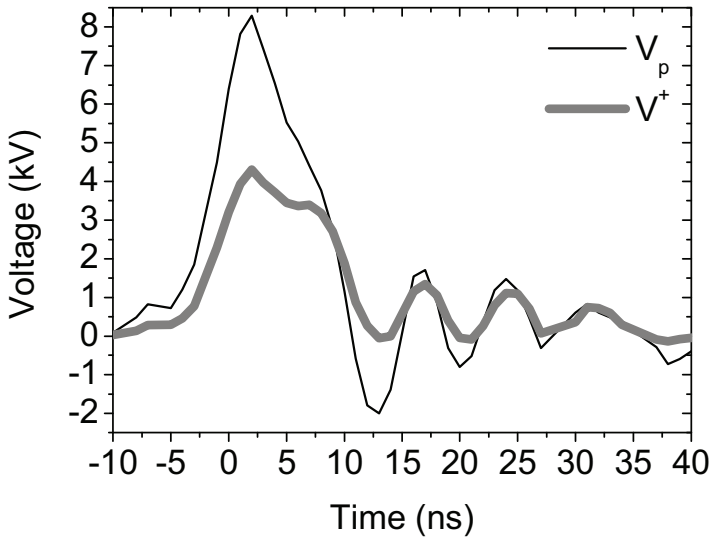

Figure 4.27: The measured high-voltage pulse (thin) and the reconstructed forward pulse delivered by the high-voltage pulse generator (thick) for the F state studied in Figure 4.26. T_g=1000 K, PRF=30 kHz, *d*=5 mm, v=1.6 m/s.

Finally, we can use R_p shown in Figure 4.26 to calculate the electron number density (n_e) as a function of time. R_p is related to the plasma resistivity (ρ_p) by $R_p = \rho_p l/A$, where l and A are the length and cross-sectional area of the resistor, respectively. We use the gap distance (d) as the length l and $A = \pi r_p^2$, where the plasma radius (r_p) is about 1 mm, as seen in Figure 4.9. We can then use the plasma conductivity (σ_p), which is $\sigma_p = 1/\rho_p$, to calculate the electron number density:

$$\sigma_p = \frac{n_e e^2}{m_e \nu_{e-h}} \tag{4.11}$$

where e and m_e are the electron charge and mass, respectively, and ν_{e-h} is the electron-heavy collision frequency, given by:

$$\nu_{e-h} \approx n_h Q_{e-h} \sqrt{\frac{8k_B T_e}{\pi m_e}} \tag{4.12}$$

where n_h is the gas density, Q_{e-h} is the electron-heavy cross-section for momentum transfer, k_B is Boltzmann's constant and T_e is the electron temperature. Using Q_{e-h}~10^{-15} cm^2 and T_e~30,000 K, we find that ν_{e-h} is about 10^{12} s^{-1} at T_g=1000 K. Figure 4.28 shows the electron number densities for the typical F state that has been studied in this section, calculated using Equation (4.11) the data for R_p in Figure 4.26 for which R_p>0.

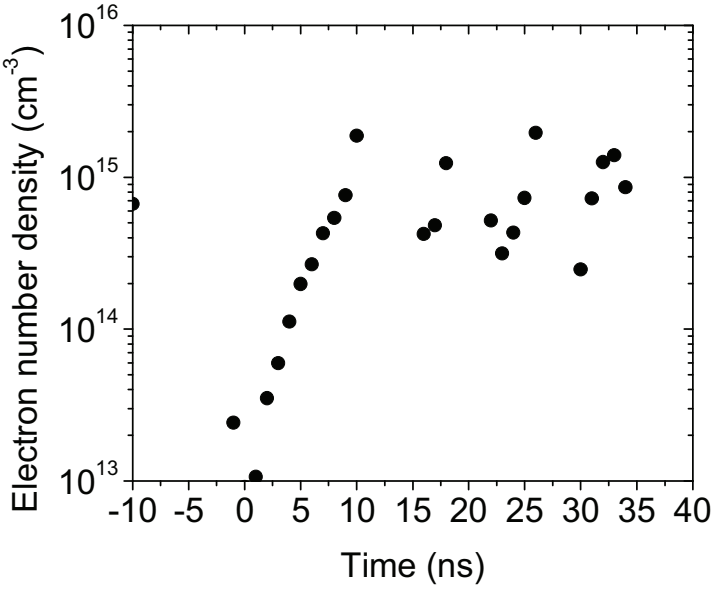

Figure 4.28: Measured electron number density as a function of time for the typical F state, derived from the data points in Figure 4.26 for which R_p>0. T_g=1000 K, PRF=30 kHz, d=5 mm, v=1.6 m/s.

We see that the lowest value of n_e measured is 10^{13} cm^{-3}, although we do not know if this is the minimum value after the recombination period because of the error in R_p for t<0 associated with the low measured conduction current during this time, as discussed previously. The maximum value of n_e is 2×10^{15} cm^{-3}, which means that the high-voltage pulse causes n_e to increase at least two orders of magnitude. It remains around this maximum value for at least 25 ns, although the spread of values for n_e during this early recombination period is quite large. It is expected that n_e remain near its maximum value up to t=40 ns, given that the gas temperature is high in the F regime, as discussed in

Section 4.9. In air at atmospheric pressure around 2000 K, the electron recombination time is on the order of microseconds [4.2].

Previously, in Section Figure 4.7, we observed that the emission intensity of the N_2^+ (B-X) (0,0) transition for the F regime is about 100 times greater than that of the D regime. Ionization should result primarily from electron-impact ionization of N_2, which means that the number densities of N_2^+ in the ground state and of the electrons should be about the same. Although it is not clear how much of the N_2^+(B) state should be produced compared to the ground state, it is reasonable to assume that the populations of ground state N_2^+ of the D and F regimes should also differ by a factor of about 100. Therefore, we estimate that the maximum electron density of the D regime is about 10^{13} cm^{-3} because that of the F regime is about 10^{15} cm^{-3}. This agrees with the maximum electron density measured by Kruger *et al* [4.2] for an NRP glow discharge in air at atmospheric pressure and at T_g=2000 K.

4.13 Conclusion

In this chapter, we have presented the experimental results for the characterization of the D and F discharge regimes. For the D regime, we measured the populations of the excited species N_2(B), N_2(C), N_2^+(B), NO(A), and O(3p ^{5}P), which all recombined within nanoseconds except for NO(A), which was detectable throughout the pulse period. Concerning the spatio-temporal properties of the D regime, it was found that the emission radius was about 1 mm during the application of the high-voltage pulse. An initial ionization wave of constant emission intensity was found to propagate from the anode to the cathode, followed by a return wave whose intensity varied with the applied voltage. In addition, we showed that the D regime does not induce significant gas heating. Finally, the measured current and voltage waveforms were not distinguishable from those with no discharge present, indicating that very little conduction current was generated. Despite the lack of direct measurements of the electron density, we were able to infer that the maximum electron number density was about 10^{13} cm^{-3}. Comparing the results of these measurements with previous research, we proposed that the observed behavior of the D regime correlated well with the initial stages of streamer-induced glow discharge formation.

Concerning the F regime, we found that it remained chemically active long after the application of the high-voltage pulse, including as yet unidentified species that emerge about 10 μs afterwards. Emission filled the discharge gap nearly instantaneously upon application of the high-voltage pulse, in contrast to the ionization wave propagation witnessed in the D regime. Furthermore, the F regime heated the gas up to ~5000 K within a few nanoseconds after the pulse. We also found that F regime was characterized by significant conduction current, from which we determined that the plasma resistance was lowered significantly by the high-voltage pulse. Furthermore, we used the measured plasma resistance to determine that the maximum electron number density was about 10^{15} cm^{-3}. All of these observations point to the conclusion that the F regime is a spark discharge.

4.14 References

[4.1] Yu.P. Raizer 1991 *Gas Discharge Physics* (Berlin: Springer).

[4.2] C.H. Kruger, C.O. Laux, L. Yu, D.M. Packan, and L. Pierrot, *Pure Appl. Chem.* **74** (2002) 337–347.

[4.3] C.O. Laux, Ph.D. Thesis, Stanford University, 1993.

[4.4] D. Pai, G. Pilla, D. A. Lacoste, and C. O. Laux, *2nd AAAF Conference for On-board Energy Systems,* Avignon, France, June 26-28, 2006.

[4.5] L. Caillault, private communication, (2007).

[4.6] N.L. Aleksandrov, A.A. Kirpichnikov, S.V. Kindusheva, I.N. Kosarev, and A.Yu. Starikovskii, AIAA Paper 2007-997, *45th AIAA Aerospace Sciences Meeting and Exhibit (Reno) 2007*.

[4.7] E. Marode, *J. Appl. Phys.* **46**(5) (1975) 2005-2015.

[4.8] G. Pilla, Ph.D. Thesis, Ecole Centrale Paris, 2007.

[4.9] C.O. Laux, T.G. Spence, C.H. Kruger, and R.N. Zare, *Plasma Sources Sci. Technol.* **12** (2003) 125-138.

[4.10] N. A. Popov, *Plasma Physics Reports* **27**(10) (2001) 886-896.

[4.11] R. A. Copeland and D. R. Crosley, *Chem. Phys. Lett.* **107** (1984) 295-300.

[4.12] E. Marode, private communication, (2007).

Chapter 5

Influence of Gas Temperature, Pulse Repetition Frequency, and Gap Distance on Discharge Regimes and Properties

5.1 Introduction

In Chapter 4, we studied the D and F regimes at T_g=1000 K, PRF=30 kHz, and d=5 mm. By fixing the operating conditions, we isolated those properties that were unique to the two regimes. In this chapter, we seek to characterize the dependence of the properties of the D and F regimes on T_g, PRF, and the gap distance (d). This extends the study of discharge regime properties begun in Chapter 4, and it also provides insight on how to choose T_g, PRF, and d to achieve a particular plasma state with desired properties. Sections 5.2, 5.3, and 5.4 discuss how PRF affects the regimes, emission intensity at different points along the electrode axis, and energy deposited in the discharge per pulse. Sections 5.5, 5.6, and 5.7 discuss how T_g affects the regimes, emission intensity, and energy deposited in the discharge per pulse. In Section 5.8, we discuss the influence of gap distance on the discharge regimes. Finally, in Section 5.9, we discuss the coupled effect when both the gap distance and T_g are varied. This permits us to choose the operating conditions to generate the D regime down to T_g=300 K.

5.2 Influence of pulse repetition frequency on discharge regimes

In this section we present measurements to determine the voltage ranges over which D and F states occur, as a function PRF. For all of these measurements, we fixed T_g=1000 K. For each PRF under study, we measured the C-D transition voltage V_{CD} and D-F transition voltage V_{DF} using the Lecroy PPE20kV high-voltage probe as the applied voltage (V_p) was increased from 0 V. In the C regime, the emission zone in the anode region progressively enlarges across the discharge gap as V_p increases, until it fully connects with the cathode, thus transitioning to the D regime. The luminosity of the discharge noticeably jumps when this occurs. The D-F transition is also distinct, as the luminosity greatly increases, accompanied by a crackling sound. Both the C-D and D-F transitions usually occur abruptly with V_p. At high PRF, the regime transitions are very distinct visually. At low PRF, however, the average luminosity of the discharge is low, requiring the use of the monochromator to monitor the plasma emission.

We assembled the transition voltage data measured for each PRF into a regime "map" of the discharge regimes as a function of the PRF. The D regime is lower-bounded by V_{CD} and upper-bounded by V_{DF}, and the F regime is lower-bounded by V_{DF}, with no upper bound found up to 10 kV, the maximum output of the high-voltage pulse generator. As a byproduct of these studies, the transition voltage from the discharge-less "N" regime to the C regime V_{NC} was also measured. The C regime, lower-bounded by V_{NC}, is also shown in the regime maps to follow. We consider the N-C, C-D, and D-F transitions to

be "regular" transitions, as they predominantly occur. In addition, they follow the traditional order of DC discharge regime formation with increasing energy: corona, glow, and arc. Occasionally, "irregular" transitions occurred, in particular the N-F transition, which was the only transition witnessed at small gap distances. Other irregular transitions such as C-F and N-D happened rarely, and it is not clear whether they actually occurred or if the discharge passed through the intermediate regimes too quickly for detection. The only irregular transition studied in this chapter is the N-F transition, which sometimes defined the lower bound of the F regime.

Before proceeding further, we must also mention that the regimes are sensitive to the sharpness of the electrode tips and their surface condition, although we did not perform a rigorous study of this issue. In Section 4.9, we also mentioned how the electrode condition affected gas temperature measurements. Specifically, the cathode was easily blunted or damaged by exposure to the F regime, and color changes on the surface could be discerned after only a few seconds of operation. In general, damaged electrodes lead to higher regime transition voltages. For the regime map measurements presented in this section and in Section 5.5, we sharpened and cleaned the electrodes as often as possible. In addition, we stopped operating the high-voltage pulse generator immediately after the F regime was attained to minimize electrode damage.

Figure 5.1 is a discharge regime map as a function of PRF with fixed T_g=1000 K, d=5 mm, and v=1.6 m/s. V_{NC}, V_{CD}, and V_{DF} were recorded for PRF=1-30 kHz. The regimes do not show much sensitivity to PRF, except at low PRF, where the D regime expands in applied voltage (V_p) range.

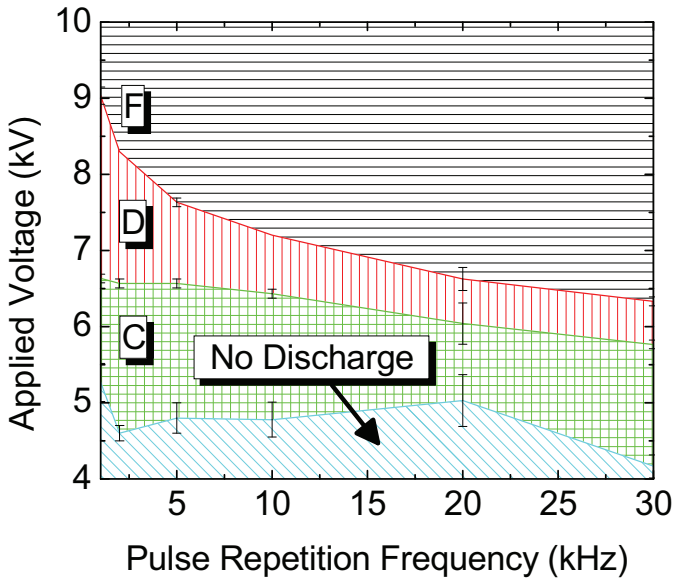

Figure 5.1: Discharge regime map according to applied voltage (V_p) as a function of PRF. T_g=1000 K, d=5 mm, v=1.6 m/s.

5.3 Spatio-temporal emission profiles using the PMT module – the influence of pulse repetition frequency

In this section we present results of PMT measurements of N_2 (C-B) (0,0) emission intensity at different points along the electrode axis to examine the influence of PRF. The setup and method used for these measurements were presented in Section 4.8. Figure 5.2 shows the peak emission intensity of D and F regimes as a function of V_p at the center of the discharge gap for PRF=1-30 kHz, with T_g=1000 K, d=5 mm, and v=1.6 m/s fixed. Within the D or F regime, the emission intensity follows the weak-medium-strong state path described in Section 4.8. Comparing with the regime map presented in Figure 5.1, we find that the jumps in emission correspond to the D-F transition at each PRF. These jumps are about a factor of 10 at high PRF but gradually reduce until there is virtually no jump at 1 kHz. Thus, the D-F transition becomes "softer" with decreasing PRF. Within each regime, there up to one decade of variation in the peak emission intensity.

Furthermore, we saw in Figure 5.1 that the applied voltage range corresponding to the D regime increases with decreasing PRF. We see from Figure 5.2 that the range of emission of the D regime increases in similar fashion with decreasing PRF. By using lower PRF, we can obtain D states that emit at intensities above the range attainable at higher PRF. Overall, the emission intensity in the D regime is more sensitive to changes in V_p than in PRF, and in the F regime the emission is practically independent of PRF.

If we interpret the emission intensity of the N_2 (C-B) (0,0) transition as a general indicator of the chemical activity of the plasma, then we see that the PRF does not so much affect the chemistry of the D regime as it determines the D-F transition. V_p still principally drives the degree of chemical activity. Thus, the accumulative effect of repetitive pulsing on the chemistry of both regimes is not as significant as the influence of the applied electric field, within the range of PRF and V_p studied here.

In addition to measurements at the center of the discharge gap, we also investigated the emission from the anode and cathode regions. This continues the discussion on the ionization waves of the D regime begun in Sections 4.7 and 4.8, where we showed that an initial cathode-directed streamer departs from the anode, followed by a return wave. Emission from both waves appeared as two distinct peaks at the anode, where enough time separated the two for detection by the PMT. In the middle of the gap and at the cathode, the PMT could not resolve two waves and only one emission peak appeared. For PRF=20 kHz, the intensity of the first peak remained constant for all V_p, whereas the intensity of the second peak increased with increasing V_p. Now we again examine the emission at the anode, but here we consider a range of PRF from 2 to 20 kHz.

Figure 5.3 shows the intensity of the first and second emission peaks measured at the anode using the PMT module for PRF=2-20 kHz, with T_g=1000 K, d=5 mm, and v=1.6 m/s fixed. For a given PRF, the second peak intensities always increase as a function of V_p. The intensity curves shift to higher V_p with decreasing PRF, which was observed in Figure 5.2 also. The first peak intensities, however, do not vary appreciably

with V_p or PRF. Note that the first peak intensities do not appear at higher V_p because the intensity of the second peak is strong enough to obscure it. Finally, as discussed in Sections 4.7 and 4.8, the F regime does not exhibit two emission peaks at the anode.

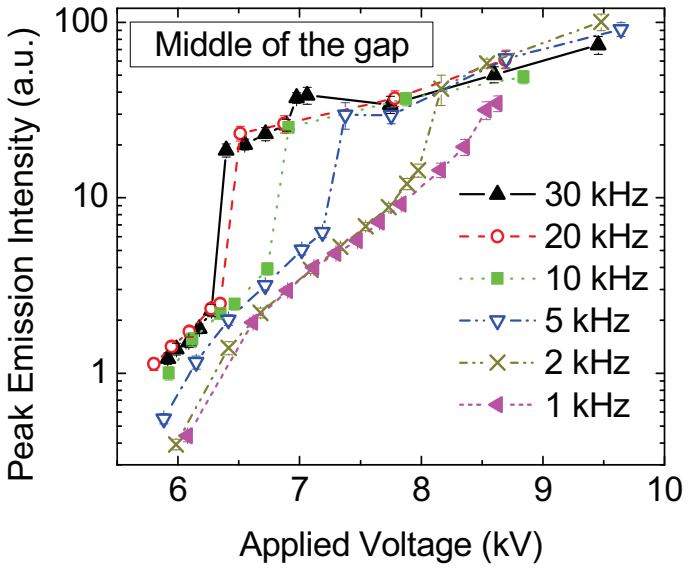

Figure 5.2: Measured N_2 (C-B) (0,0) emission intensity peaks in the middle of the discharge gap as a function of V_p for PRF=1-30 kHz. T_g=1000 K, d=5 mm, v=1.6 m/s.

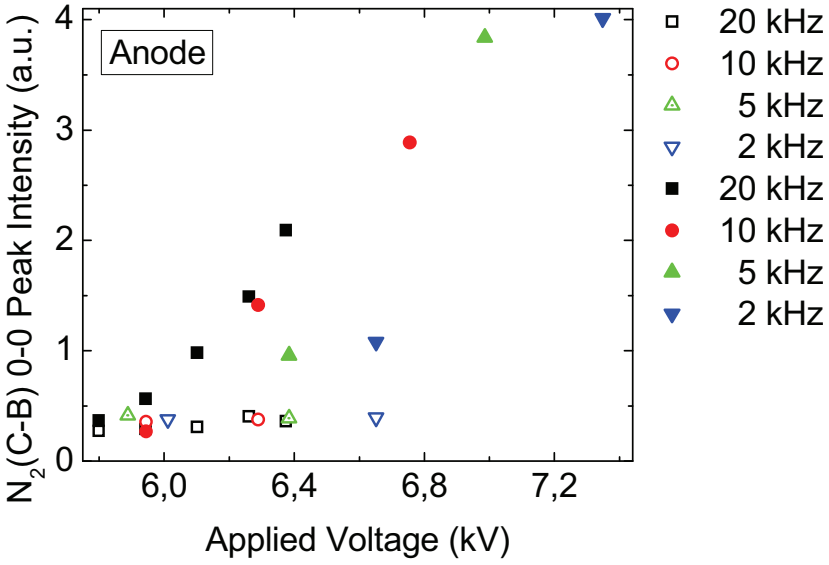

Figure 5.3: Measured N_2 (C-B) (0,0) emission peak intensities at the anode of the D regime for PRF=2-20 kHz for the first peaks (filled) and second peaks (hollow). T_g=1000 K, d=5 mm, v=1.6 m/s.

In addition to the N_2 (C-B) (0,0) emission intensity, the PMT measurements yielded information on the delay of the emission after the high-voltage pulse. In Section 4.8, we proposed that the first emission peak of the D regime is an initial streamer leading to the

formation of a transient glow discharge. The formation time for the streamer is dictated by Meek's criterion for the avalanche-to-streamer transition. We explore the validity of this explanation by measuring the delay of the emission relative to the high-voltage pulse, which is defined as the time between the rising half-maximum of the emission and the rising half-maximum of the high-voltage pulse (t_{RHM}).

Figure 5.4 (left) shows the measured delay of the first and second emission intensity peaks after the high-voltage pulse at the anode for the weak, medium, and strong D states. Although there is not very much variation in this delay, it is clear that both the first and second peak delays increase with increasing applied voltage, and that the second peak delays decrease slightly with increasing PRF. Figure 5.4 (right) shows the emission delay measured at the cathode, which does not demonstrate any trend with applied voltage and a weaker tendency to decrease with increasing PRF.

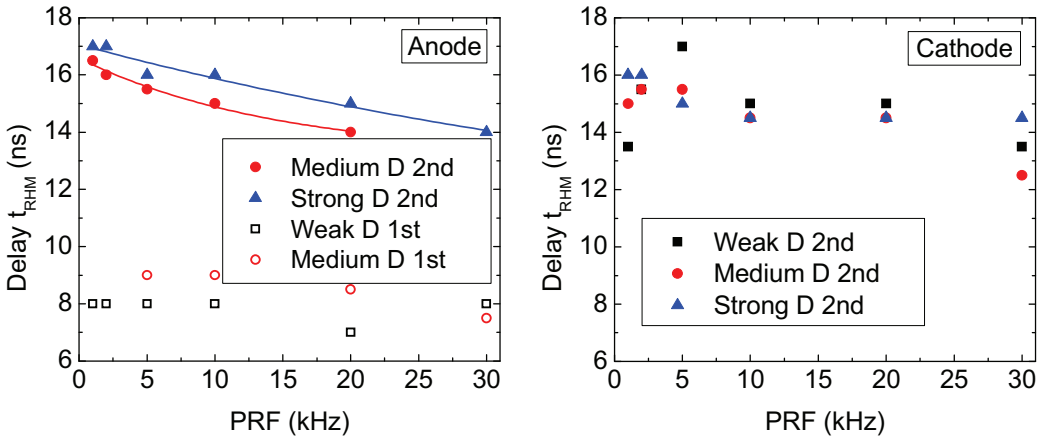

Figure 5.4: Measured delays of N_2 (C-B) (0,0) emission for first peaks (hollow) and second peaks (filled) as function of PRF for weak, medium, and strong D states at the anode (left) and cathode (right). T_g=1000 K, *d*=5 mm, v=1.6 m/s.

Due to the lack of a trend in the cathode peak delay data, it is only possible to calculate a global average for ionization wave speeds over all PRFs and applied voltages. Table 5.1 shows the average over all PRF and V_p. Since the standard deviation of the cathode and anode second peak delays is larger than their difference, we cannot calculate a return wave speed. We can conclude, however, that the cathode peak occurs before the anode second peak. These observations are in agreement with Figure 4.10 (left), in which the same sequence of events occurs. Thus, the difference between the cathode peak and anode first peak average delays is interpreted as the average initial streamer speed over all PRFs, which is 8×10^7 cm/s. This agrees with the speed of 10^8 cm/s measured in Section 4.7.

Now we proceed to analyze the F regime emission delay. As shown in Figure 4.10 (right), only one emission peak appears at all points along the electrode axis. This is true for all PRF and V_p of the F regime. The strong F state measurements are not presented here since the discharge generally is unsteady in space and time, as it takes different paths

between the electrodes with each pulse. The weak and medium F states, however, are more stable and thus can be analyzed.

Table 5.1: Measured average delays of N_2 (C-B) (0,0) emission intensity peaks in the D regime over PRF=1-30 kHz. T_g=1000 K, *d*=5 mm, v=1.6 m/s.

Emission location	Mean (ns)	Standard deviation (ns)
Anode first peak	8.2	0.7
Cathode	14.9	1.0
Anode second peak	15.6	1.1

Figure 5.5 shows the PMT measurements of the anode and cathode emission of the F regime for PRF=1-30 kHz, with T_g=1000 K, *d*=5 mm, and v=1.6 m/s fixed. The trends with PRF are difficult to ascertain, although linear and second-order polynomial fits indicate that the delays generally decrease with increasing PRF, with the exception at 30 kHz. The weak F states generally have longer delays, in the same range as the D state second peak delay times. Also, it is apparent that emission appears first at the anode. The average delays for the F states are shown in Table 5.2. Finally, the ionization wave speed appears to decrease with increasing PRF. The average value for the F regime over all PRF is 6×10^8 cm/s, with a standard deviation of 3×10^8 cm/s.

Table 5.2: Measured average delays of N_2 (C-B) (0,0) emission intensity peaks in the F regime over PRF=1-30 kHz. T_g=1000 K, *d*=5 mm, v=1.6 m/s.

Emission location	Mean (ns)	Standard deviation (ns)
Anode	15.0	1.0
Cathode	15.6	0.6

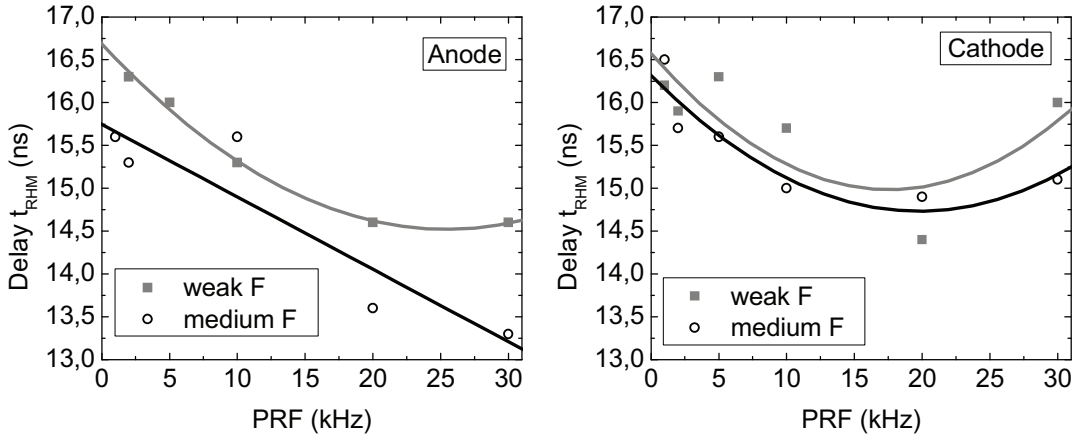

Figure 5.5: Measured delays of N_2 (C-B) (0,0) emission peaks for weak and medium F states as a function of PRF at the anode (left) and cathode (right). T_g=1000 K, *d*=5 mm, v=1.6 m/s.

5.4 Energy deposited per pulse – influence of pulse repetition frequency

In this section, we discuss the energy deposited per pulse in the plasma for the D and F regimes and its dependence on PRF. To obtain the energy, the applied voltage and

discharge current were measured. Using the Lecroy PPE20kV high-voltage probe and the Pearson Model 6585 current probe, following the procedure described previously in Section 4.12. Here, we will focus on the issues that pertain to energy measurement.

The total energy is calculated by multiplying the measured voltage and current waveforms to obtain the power, which is then integrated in time during the pulse duration to yield the energy. The integration time (τ_p) begins with the rise of the high-voltage pulse and ends when it falls back below 0 V, thus excluding the subsequent ringing. It is legitimate to neglect the ringing because it results from probe loading and not from reflections of the high-voltage pulse. Following the discussion from Section 4.12, the total measured current (I_{total}) includes the conduction (I_{cond}), the displacement (I_{disp}), and parasitic (I_{para}) currents:

$$I_{total} = I_{cond} + I_{disp} + I_{para} \tag{5.1}$$

We assume that the energy associated with the displacement current is zero over the integration time. Thus, the measured total energy per pulse (E_{total}) is the sum of the energy dissipated into the plasma (E_{plasma}) and the parasitic energy loss (E_{para}):

$$E_{total} = \int_0^{\tau_p} V_p I_{total} dt = E_{plasma} + E_{para} = \int_0^{\tau_p} V_p I_{cond} dt + \int_0^{\tau_p} V_p I_{para} dt \tag{5.2}$$

As mentioned before, the D regime I_{cond} is very small, and D regime voltage and current waveforms are nearly indistinguishable from the corresponding waveforms when no plasma is present. However, the accumulated effect of small I_{cond} can be rendered measurable by integrating the power $V_p I_{total}$ in time to obtain the energy. Figure 5.6 shows the energy determined for D states at different V_p. They are compared to "no-plasma" energies ($E_{no\text{-}plasma}$), measured with the high-voltage pulse generator operated using the same settings but in ambient air such that no discharge was created.

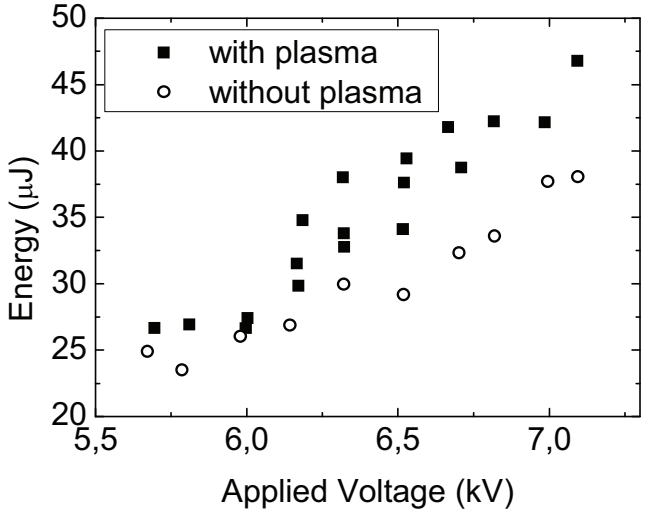

Figure 5.6: Measured total energy for the D regime at T_g=700-1000 K and corresponding no-plasma energy at 300 K as a function of applied voltage. PRF=30 kHz, *d*=5 mm, v=2 m/s.

Without plasma, no conduction current flows, and we measure the total current $I_{no\text{-}plasma}=I_{para}+I_{disp}$. Only I_{para} is responsible for dissipating $E_{no\text{-}plasma}$. The D regime I_{cond} is very small, indicating high plasma impedance that is close to the no-plasma load impedance. We can then assume that the V_p of a D state is negligibly different from its corresponding no-plasma V_p. It follows that $E_{no\text{-}plasma}\approx E_{para}$. We approximate the energy of the D regime using Equation (5.2):

$$E_{plasma} \approx E_{total} - E_{no-plasma} = \int_0^{\tau_p} V_p I_{total} dt - \int_0^{\tau_p} V_p I_{no-plasma} dt \tag{5.3}$$

Therefore, for the D regime, two sets of energy measurements were acquired: one with the plasma and another without the plasma, and the difference was taken to obtain E_{plasma}.

The F regime energy cannot be determined using Equation (5.3) because the voltage waveforms between the cases with and without plasma are very different. In Section 4.12, we demonstrated that this pulse distortion was due to the rapidly changing plasma resistance in response to ionization, hence modifying the reflection coefficient. Thus, the measured applied voltage waveform, which is the sum of the forward propagating and reflected waveforms, is distorted from the corresponding waveform without plasma. For example, Figure 5.7 shows a comparison of an F state's V_p with its no-plasma counterpart's V_p. They initially agree but begin to diverge as this F state's I_{cond} becomes significant. Thus, we cannot assume $E_{para}\approx E_{no\text{-}plasma}$ because V_p for the no-plasma case is not a good approximation of the F regime V_p seen by the parasitic impedance elements.

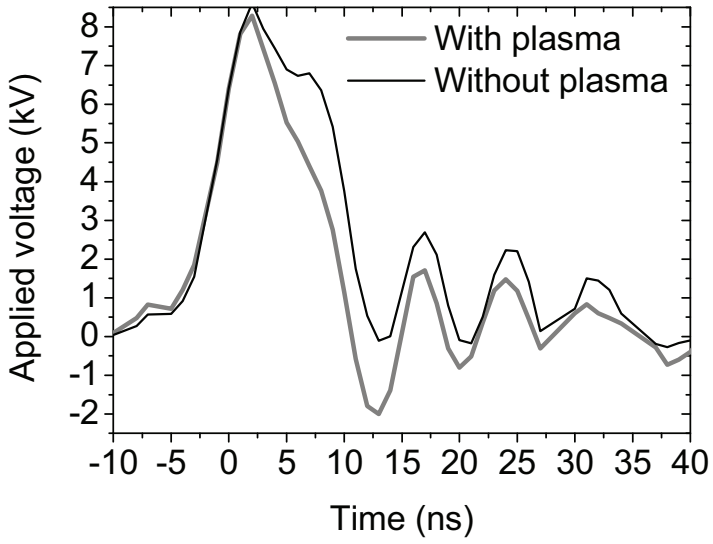

Figure 5.7: Measured applied voltage for an F state and the reconstructed no-plasma applied voltage. This figure uses the same measured data shown in Figure 4.27.

To properly calculate E_{para} for the F regime we would need to reproduce F regime voltage waveforms such as the one in Figure 5.7 and measure the resulting current in no-plasma

conditions. Unfortunately, the high-voltage pulse generator does not allow for manipulation of its output voltage waveform. A way to calculate this current would be to construct a detailed circuit model of the electrode system including all of the relevant parasitic impedances and simulate the current using the measured F regime voltage waveform. However, the determination of the parasitic impedances is far from trivial.

Instead of developing a complex circuit model, we assumed that $E_{plasma}>>E_{para}$ for the F regime, and thus $E_{plasma}\approx E_{total}$. To prove that $E_{plasma}>>E_{para}$, we consider $E_{no\text{-}plasma}$ for the V_p corresponding to those applied for the F regime. In Figure 5.8, we present $E_{no\text{-}plasma}$ corresponding to F regimes from PRF=1-30 kHz, with T_g=300 K, d=5 mm, and v=2 m/s fixed. It shows that the no-plasma energy increases linearly with increasing voltage and is independent of PRF.

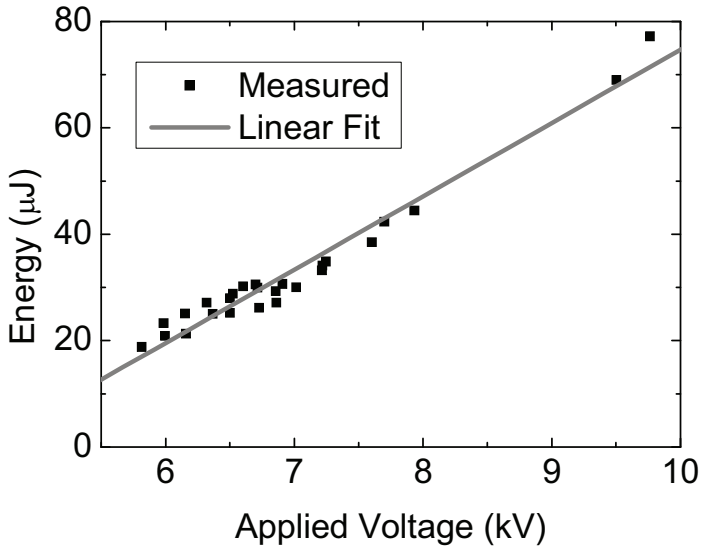

Figure 5.8: Measured no-plasma energy for the F regime as a function of the applied voltage for PRF=1-30 kHz. T_g=300 K, d=5 mm, v=2 m/s.

Comparison with Figure 5.9, which presents the E_{total} of the corresponding F states from PRF=1-30 kHz, with T_g=1000 K, d=5 mm, and v=1.6 m/s fixed, shows that for a given applied voltage, E_{total} measured for the F state is always about 10 times greater than the corresponding $E_{no\text{-}plasma}$. Furthermore, as shown in Figure 5.7, the formation of the F state causes the voltage to decrease, and this effect becomes more pronounced with increasing V_p. Because $E_{no\text{-}plasma}$ decreases with decreasing V_p, E_{para} is less than $E_{no\text{-}plasma}$ because of the decrease in V_p in the F regime. Thus, for the F regime, E_{plasma} differs from E_{total} by less than 10%.

Finally, having taken into account the parasitic energy losses, we can present the results of energy measurements for the D and F regimes. Figure 5.9 shows the measured energies per pulse of the D and F regimes as a function of applied voltage for PRF=1-30 kHz, with T_g=1000 K, d=5 mm, and v=1.6 m/s held constant.

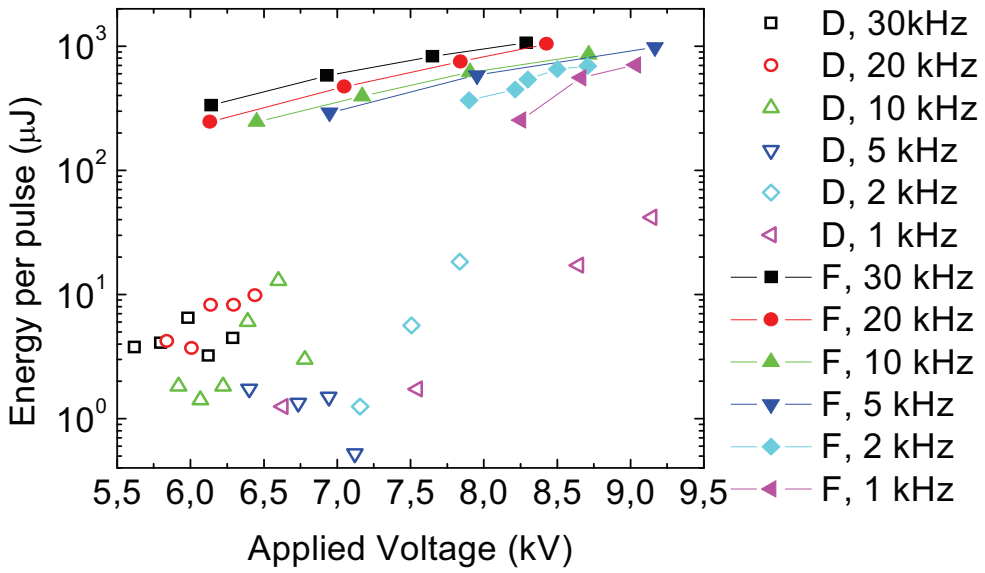

Figure 5.9: Measured energy per pulse for the D (hollow) and F (solid) regimes as a function of applied voltage for PRF=1-30 kHz. T_g=1000 K, *d*=5 mm, v=1.6 m/s.

The D-F transition is marked by an abrupt increase in energy that grows with increasing PRF, from a factor of 6 to 51. Another important feature is that the energy curves shown for the F regimes shift downward in V_p with increasing PRF. This shift also seems to occur for the D regime, although the trend is not as clear because the energies are much smaller and the measurement uncertainty is higher. Overall, E_{plasma} is about 1-10 μJ for the D regime and about 100-1000 μJ for the F regime.

The sensitivity of the regime transition voltages to electrode conditions gives the impression that the regimes overlap considerably, such that D and F states can sometimes occur simultaneously at V_p far from V_{DF}. We discussed the issue of electrode damage in Section 5.2. In reality, for two separate experiments with different electrode conditions, the same V_p can generate a D state in one experiment and an F state in the other. However, during one experiment, if we increased V_p from 0 V, we always observed that the D regime transitioned into the F regime at V_{DF} without any sustained period of both regimes occurring simultaneously. To minimize the effects of electrode damage, we performed all of the D regime measurements before proceeding to the F regime measurements. F regime experiments progressively damaged the electrodes, resulting in changes in V_{DF}. Thus, the overlapping of the regimes shown in Figure 5.9 and Figure 5.12 is indicative of changes in V_{DF}, not the co-existence of the D and F regimes.

5.5 Influence of gas temperature on discharge regimes

We now apply the same analysis as in Section 5.2 to determine the influence of gas temperature on the discharge regimes. Figure 5.10 presents the regime map as a function of T_g, with PRF=30 kHz, *d*=5 mm, and v=1.6 m/s fixed.

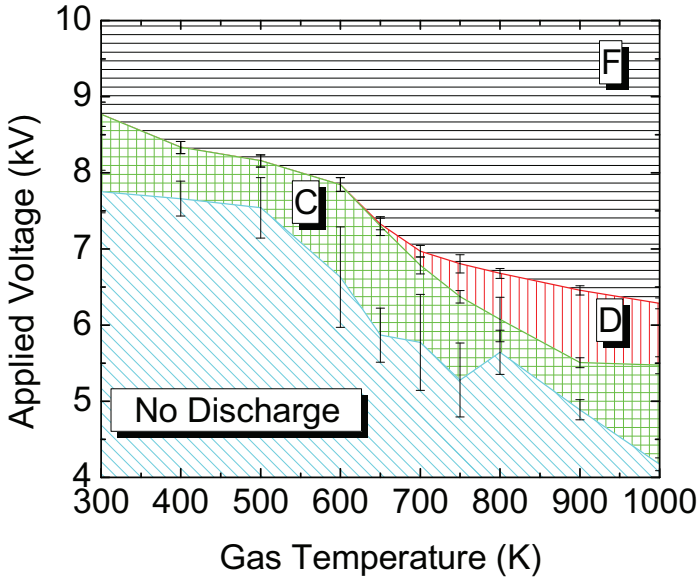

Figure 5.10: Discharge regime map according to applied voltage as a function of T_g. PRF=30 kHz, *d*=5 mm, v=1.6 m/s.

The regime map shown in Figure 5.10 shows a much more pronounced dependence on gas temperature than did Figure 5.1 for PRF. There is again the D regime expansion phenomenon with increasing T_g. Below 650 K, the D regime disappears altogether. From T_g=300-650 K, only the C and F regimes are observed. As we will see in Section 5.9, this is because the gap distance is 5 mm, which prevents the formation of the D regime below 650 K.

5.6 Spatio-temporal emission profiles using the PMT module – influence of gas temperature

In this section we present results of PMT measurements of N_2 (C-B) (0,0) emission intensity at different points along the electrode axis to examine the influence of the gas temperature. They were performed in the manner discussed in Section 5.3, except that we varied T_g instead of PRF. For these measurements, we fixed PRF=30 kHz, *d*=5 mm, and v=1.6 m/s. Figure 5.11 shows the peak emission intensity of the D and F regimes as a function of V_p at the middle of the discharge gap for T_g=300-1000 K. Comparing with the regime map presented in Figure 5.10, we see that the jumps in emission correspond to the D-F transition. Unlike the case with varying PRF, the jumps are always by about a factor of 10. Also, the D does not exist below 750 K for these experimental conditions, and thus only the emission for the F regime is available for the 300 K and 500 K cases.

PMT measurements were also performed at the anode and cathode. Emission from the initial streamer and the return wave appeared as two distinct peaks at the anode, where enough time separated the two for detection by the PMT. In the middle of the gap and at the cathode, the PMT could not resolve two waves and only one emission peak appeared. As mentioned above, the D regime could only be generated at T_g>750 K. Its emission intensity did not vary much from 750 to 1000 K. Only a couple of conclusions can be

drawn from these measurements. First, the first and second anode emission delays do not vary in this temperature range. The average initial streamer speed was 8×10^7 cm/s, which agrees with the speed of 10^8 cm/s reported in Section 3.7. Second, the first anode peak intensity remains approximately constant from 750 to 900 K, then increases abruptly at 1000 K, as shown in Table 5.3. As expected, the applied voltage does not affect the first peak intensity. However, its dependence on temperature is in contrast to its independence from PRF.

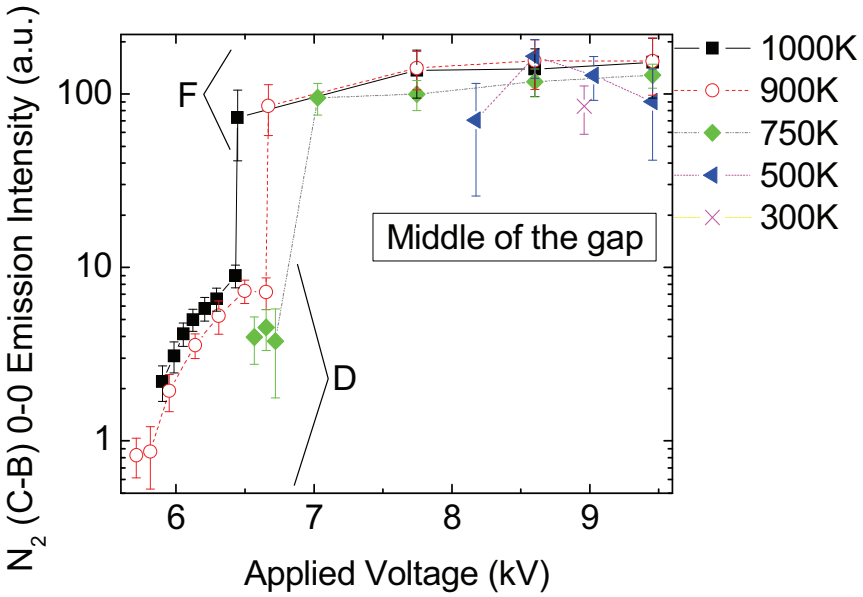

Figure 5.11: Measured N_2 (C-B) (0,0) peak emission intensity in the middle of the discharge gap as a function of V_p for T_g=300-1000 K. PRF=30 kHz, d=5 mm, v=1.6 m/s.

Table 5.3: Measured average intensities of the N_2 (C-B) (0,0) first emission peak in the D regime at the anode over all V_p for several T_g. PRF=30 kHz, d=5 mm, v=1.6 m/s.

Gas temperature (K)	Weak D state intensity (a.u.)	Medium D state intensity (a.u.)
750	1	1
900	0.97	1.1
1000	1.7	1.7

Likewise, the F regime anode and cathode emission measurements did not show any discernable T_g dependence. Table 5.4 shows the mean delays measured for all T_g=300-1000 K, with PRF=30 kHz, d=5 mm, and v=1.6 m/s fixed. As expected, the means are very close to the measured values in Table 5.2, but the standard deviations are smaller. This could be because the dynamic range of T_g studied was much smaller than that of PRF.

The average ionization speed of the F regime over all T_g was 7×10^8 cm/s, with a standard deviation of 3×10^8 cm/s. Thus, although there are not trends in emission delay or

ionization wave speed, we can say that their average values are consistent with the measurements over PRF discussed in Section 5.3.

Table 5.4: Measured average delay N_2 (C-B) (0,0) emission in the F regime at the anode and cathode over all V_p and T_g=300-1000 K. PRF=30 kHz, d=5 mm, v=1.6 m/s.

Emission location	Mean (ns)	Standard deviation (ns)
Anode	15.1	0.4
Cathode	15.8	0.6

5.7 Energy deposited per pulse – influence of gas temperature

We now apply the same analysis as in Section 5.4 to determine the influence of gas temperature on the energy deposited per pulse for the D and F regimes. Figure 5.12 shows the measured energies per pulse of the D and F regimes as a function of applied voltage for T_g=500-1000 K, with PRF=1-30 kHz d=5 mm, and v=1.6 m/s fixed.

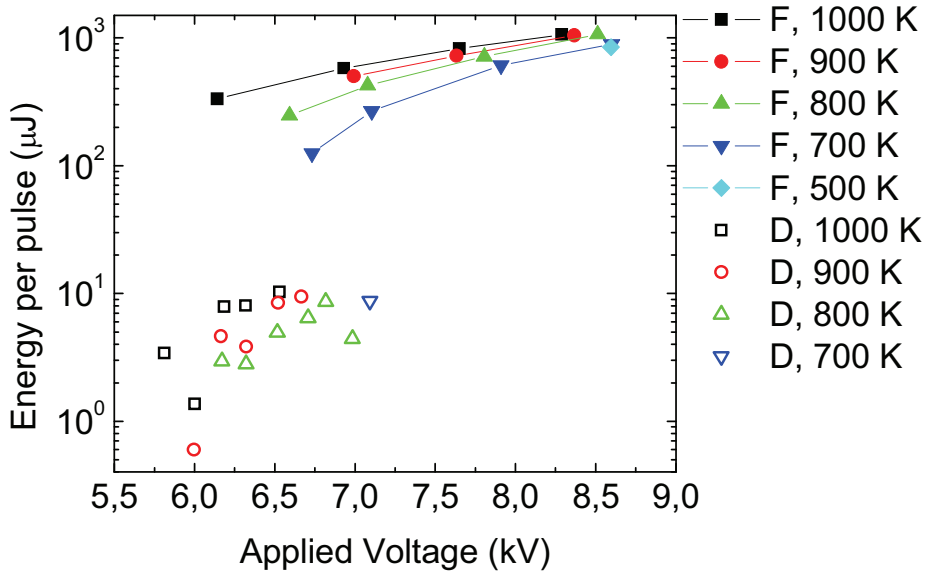

Figure 5.12: Measured energy per pulse for the D (hollow) and F (solid) regimes as a function of applied voltage for T_g=500-1000 K. PRF=30 kHz, d=5 mm, v=1.6 m/s.

The D-F transition is marked by an abrupt increase in energy that grows with increasing T_g, from a factor of 14 to 32. Another important feature is that the energy curves shown for the F regimes shift downward in V_p with increasing T_g. This shift also seems to occur for the D regime, although the trend is not as clear because the energies are much smaller and the measurement uncertainty is higher. Overall, E_{plasma} is about 1-10 μJ for the D regime and about 100-1000 μJ for the F regime.

5.8 Influence of gap distance on discharge regimes

We now apply the same analysis as in Sections 5.2 and 5.5 to determine the effect of gap distance on the discharge regimes. We performed experiments to determine regime map as a function of gap distance, shown in Figure 5.13, with T_g=1000 K, PRF=30 kHz and v=1.6 m/s fixed. Under the critical gap distance of d=2 mm, only the F regime exists, and above it "branching" to the C and D regimes occur.

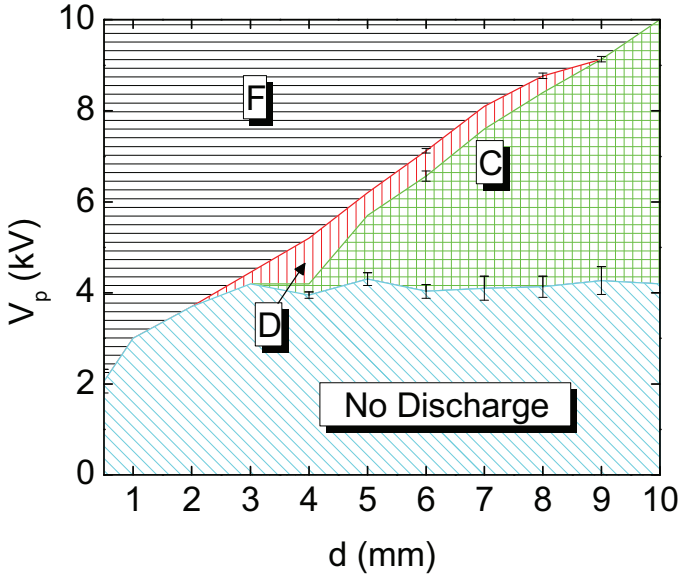

Figure 5.13: Discharge regime map according to applied voltage as a function of gap distance. T_g=1000 K, PRF=30 kHz, v=1.6 m/s.

Furthermore, suppose that the D regime is a glow discharge (we will discuss this hypothesis in Chapter 6). The average electric field in the positive column (E_{PC}) is equal to $(V_p - V_c)/d$, where V_c is the cathode fall voltage. The positive column length is approximately the gap distance because the anode and cathode fall regions of a glow discharge are typically only microns thick for atmospheric pressure air, as discussed by Raizer [5.1]. For the weak D states, a linear fit of V_{CD} as a function of gap distance has a slope equal to E_{PC} and an extrapolated value of V_p at d=0 equal to V_c, as shown in Figure 5.14. Likewise, E_{PC} and V_c for the strong F states is found by using a linear fit of V_{DF} as a function of gap distance.

Both the weak and strong D states have E_{PC}=9 kV/cm, which is probably the value throughout the D regime, as these states bound the regime. The average reduced electric field is 30.6 kV/cm/atm (122 Td), which is about equal to the DC breakdown field (E_{br}) for ambient air in gaps smaller than several centimeters [5.1]. The cathode fall voltage increases from 1.2 kV for the weak D states to 1.9 kV for the strong D states, and then the D-F transition occurs. This is similar to an abnormal DC glow discharge, for which V_c increases as the applied voltage increases up to the glow-arc transition voltage.

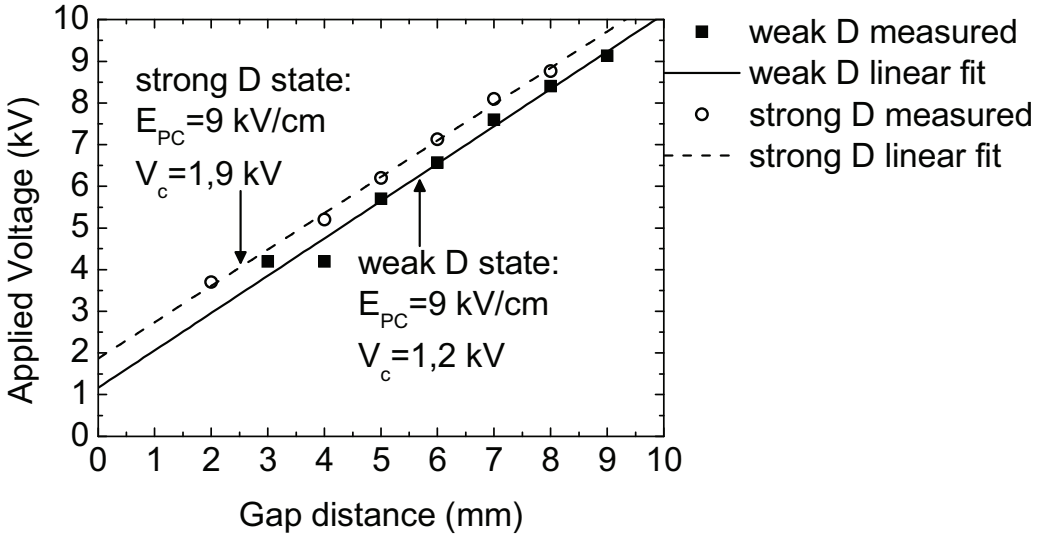

Figure 5.14: Linear fits and extrapolations of the measured applied voltages as a function of the gap distance for the weak and strong D states shown in Figure 5.13. The slope of the lines equals the average electric field in the positive column. The intercept at *d*=0 is the cathode fall voltage.

5.9 Combined influence of gap distance and gas temperature

In this section we present a coupled effect of gap distance and gas temperature on the discharge regimes. We performed experiments to determine regime maps as a function of gap distance for T_g=700-1000 K, with PRF=30 kHz and v=1.6 m/s fixed. Figure 5.15 shows these regime maps for fixed gas temperatures of 700, 800, and 1000 K. For a given T_g, there is a critical gap distance under which only the F regime occurs and above which "branching" to the C and D regimes occur. As T_g decreases, this critical gap distance and the transition voltages increase. At 700 K, V_{CD} exceeds the maximum output of the high-voltage pulse generator, such that the D regime is unattainable.

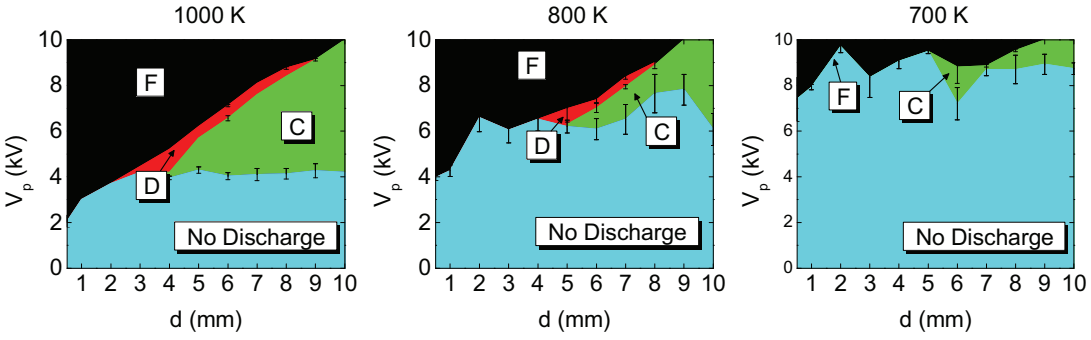

Figure 5.15: Discharge regime map according to applied voltage of gap distance d for T_g=700 K, 800 K, and 1000 K. PRF=30 kHz, v=1.6 m/s.

Extrapolating these trends to ambient conditions, we used a more powerful high-voltage pulse generator, used primarily for the experiments of Pilla [5.2], to obtain the following preliminary result: an unstable D state was achieved at T_g=300 K, PRF=56 kHz, V_p=19 kV, and d=17 mm. While the increased PRF and applied voltage were perhaps

anticipated as requirements to attain the D regime at 300 K, needing a larger gap was not expected. In Chapter 6, we will present an explanation for the minimum gap distance required for generating the D regime at a particular gas temperature.

5.10 Conclusion

In this chapter, we have examined the effect of gas temperature and pulse repetition frequency on the discharge regimes. First, we described the C, D, and F regimes in terms of regime maps in PRF and T_g, which showed that the regimes were much more sensitive to T_g than to PRF in the range investigated (T_g=300-1000 K, PRF=1-30 kHz). Also, with the other operating conditions fixed, there is a critical T_g above which the D regime can be generated. The regime maps were considered in conjunction with the measured N_2 (C-B) (0,0) emission intensity and the energy deposited in the plasma per pulse. The emission intensity and energy curves as a function of the applied voltage V_p shifted to higher V_p with decreasing PRF and T_g. Shifting behavior indicated that two states occupying the same relative place within a regime were equivalent in terms of their emission intensity and energy. For example, all the weak F states, regardless of PRF or T_g, were roughly equivalent by this definition. In addition to the shifts, we observed that the D regime existed over a narrower range of applied voltages and that the D-F transition became more abrupt with increasing PRF, accompanied by larger differences in emission intensity and energy between the D and F regimes. Furthermore, we discovered that the N_2 (C-B) (0,0) emission delay following application of the high-voltage pulse decreased noticeably with increasing PRF, whereas no trend as a function of T_g was found. This was interpreted in terms of a faster initiation of the streamer at higher PRF, owing to a higher level of pre-ionization in the gap at higher PRF. Finally, the regime maps in gap distance for several T_g showed that for a given T_g, there is a minimum gap distance for the generation of the D regime. Using this fact, we generated a D state in ambient air. Thus, it appears that it is possible to observe a stable D discharge at all temperatures from 300 to 1000 K with careful selection of electrode gap distance, applied voltage, and PRF.

5.11 References

[5.1] Yu. P. Raizer, 1997 *Gas Discharge Physics* (Berlin: Springer)
[5.2] G. Pilla, Ph.D. Thesis, Ecole Centrale Paris, 2007.

Chapter 6

Nature of the D regime

6.1 Introduction

In this chapter, we discuss a possible explanation of the physics of the D regime and its transition to the F regime, based upon the experimental results presented in Chapters 4 and 5. In Section 6.2, we present an approximation of the non-uniform Laplacian electric field produced by a pin-to-pin electrode geometry. Section 6.3 discusses how the Laplacian field separates the discharge gap into strongly and weakly ionizing zones. In Section 6.4, we explain the sequence of events observed in the D regime in terms of the known physics of streamers and streamer-cathode interaction. Finally, in Section 6.5, we propose an explanation of why a minimum gap distance for D regime generation exists.

6.2 Laplacian electric field generated by electrodes in a pin-to-pin configuration – analytic approximation

In this section we examine the influence of the Laplacian electric field generated by a pin-to-pin electrode configuration using an analytic calculation. We idealize the two electrodes as an infinite two-sheet hyperboloid surface. Sharp tip electrodes are commonly approximated as hyperboloid surfaces because an exact solution to Laplace's equation exists for its potential [6.1-6.3]. The solution is found using the prolate spheroidal coordinate system, which is defined by the orthogonal coordinates (η, ξ, ϕ). Hyperboloid surfaces are found when η is constant, prolate-spheroidal surfaces are found when ξ is constant, and ϕ is the azimuthal angle of rotation about the major axis. Physically, η-surfaces are equipotential surfaces, and ξ- and ϕ-lines are electric field lines.

Figure 6.1 shows the hyperboloid electrodes in prolate spheroidal coordinates. The origin (η=0, ξ=1) is in the center of the discharge gap. We consider the problem in one dimension along the inter-electrode (z) axis, for which ξ=1 and $z=a\eta$, where $2a$ is the distance between the foci. R is the radius of curvature of the electrode tips, which are located at $z=+d/2$ for the anode and $z=-d/2$ for the cathode. Here, R and d are free parameters related to the foci distance by $a=[(d/2)(d/2+R)]^{1/2}$. R and d also determine the equipotential surface of the electrodes, $\eta_0=[(d/2)/(d/2+R)]^{1/2}$, such that $V(\eta_0)=V_p$ at the anode and $V(-\eta_0)=0$ at the cathode. V_p is the applied voltage.

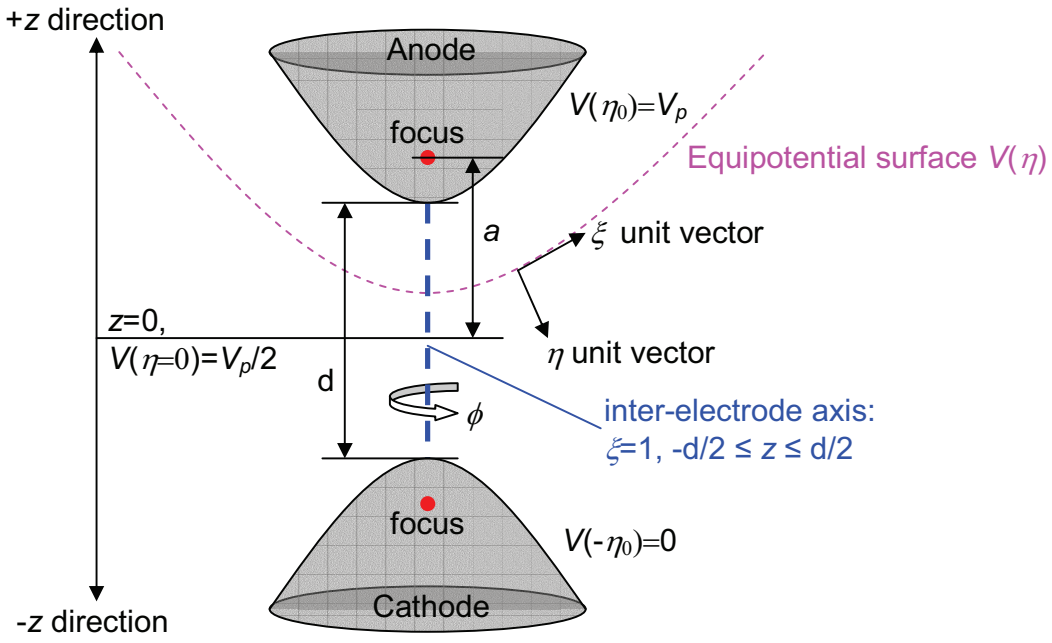

Figure 6.1: Two-sheet hyperboloid surface representation of the pin-to-pin electrode configuration in prolate spheroidal coordinates.

The literature gives solutions only for pin-plane configurations represented as a single hyperboloid electrode facing a plane surface [6.1-6.3]. The solution with the electrode at $V(\eta_0)=V_p$ and the plane at $V(0)=0$ was given by Müller *et al* [6.4]. Because of the cylindrical symmetry of the electrodes, the Laplacian potential $V(\eta, \xi, \phi)$ is independent of ξ and ϕ:

$$V(\eta) = V_p \frac{\ln\left[(1+\eta)/(1-\eta)\right]}{\ln\left[(1+\eta_0)/(1-\eta_0)\right]} \tag{6.1}$$

Recalling that $z=a\eta$, the Laplacian electric field on the inter-electrode (z) axis is:

$$E(z) = -\nabla V = -\frac{dV}{d\eta}\frac{d\eta}{dz} = -\frac{2V_p}{\ln\left[(1+\eta_0)/(1-\eta_0)\right]}\frac{a}{a^2-z^2} \tag{6.2}$$

The field and potential for a pin-plane geometry are exactly the same as those for a symmetric pin-to-pin geometry where $V(\eta_0)=V_p$ at the anode, $V(0)=0$ at mid-gap, and $V(-\eta_0)=-V_p$ at the cathode, according to the method of images. For our case, $V(\eta_0)=V_p$ and $V(-\eta_0)=0$. If we idealize the electrodes as infinite hyperboloid surfaces and place the boundaries at $V=0$ infinitely far away, then symmetry is nearly preserved, with $V(0)\approx V_p/2$ and $E(z)\approx -E(-z)$ [6.5]. Most, but not all, of the electric field lines leaving the anode will end on the cathode. Some will end at the boundaries because they are at the same

potential as the cathode. Therefore, the field is slightly stronger at the anode than at the cathode. Equations (6.1) and (6.2) must be modified to account for $V(\eta_0)=V_p$, $V(0)\approx V_p/2$, and $V(-\eta_0)=0$:

$$V(\eta) \approx \frac{V_p}{2}\left\{\frac{\ln\left[(1+\eta)/(1-\eta)\right]}{\ln\left[(1+\eta_0)/(1-\eta_0)\right]}+1\right\} \tag{6.3}$$

$$E(z) \approx -\frac{V_p}{\ln\left[(1+\eta_0)/(1-\eta_0)\right]}\frac{a}{a^2-z^2} \tag{6.4}$$

If the boundaries are at V=0 and at a far but finite distance from the electrodes, and if the electrodes are of finite length, then the potential and field become more asymmetric than for the ideal case of infinitely far away boundaries. However, since the gap distance is small compared to the distance between the electrodes and other conducting surfaces in our experiments, Equations (6.3) and (6.4) are reasonable approximations.

Figure 6.2 shows $E(z)$ calculated for several values of the radius of curvature at the electrode tip (R) using Equation (6.4), with V_p=10 kV and d=5 mm. When R is much greater than d, as demonstrated by the R=1 m case, we approach the parallel-plate electrode case, where $E(z)=V_p/d$. As R decreases, the field becomes more non-uniform, with significant field enhancement near the electrodes and a decrease in the field at mid-gap. The former is proportionally affected more than the latter. Although we did not measure R in our experiments, it is safe to say that it was between 100 μm and 1 mm.

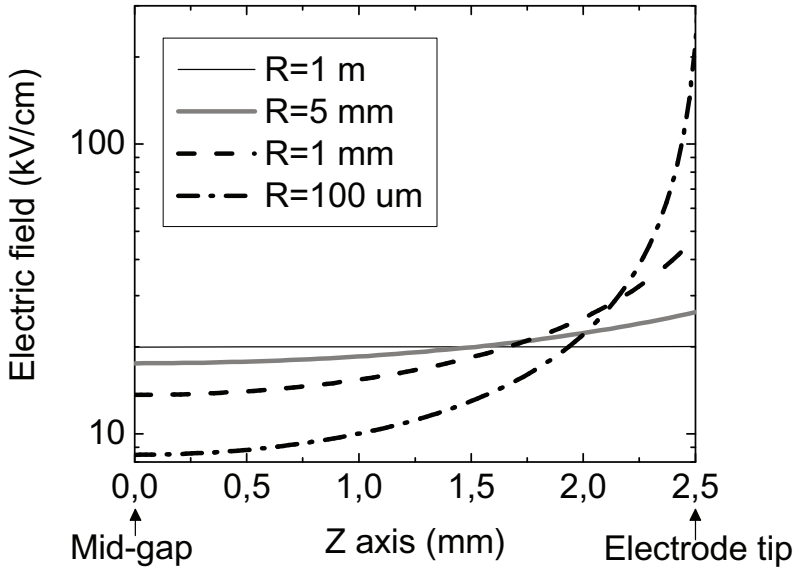

Figure 6.2: Laplacian electric field along the inter-electrode (z) axis (ξ=1) with d=5 mm and V_p=10 kV, for several values of the electrode tip radius of curvature (R). The field is symmetric about z=0.

Figure 6.3 shows $E(z)$ calculated for several values of the gap distance (d) using Equation (6.4), with V_p=10 kV and R=1 mm. The distance in the z direction has been normalized by $d/2$ to show that the field non-uniformity increases with increasing gap distance, although field enhancement at the electrode tip decreases.

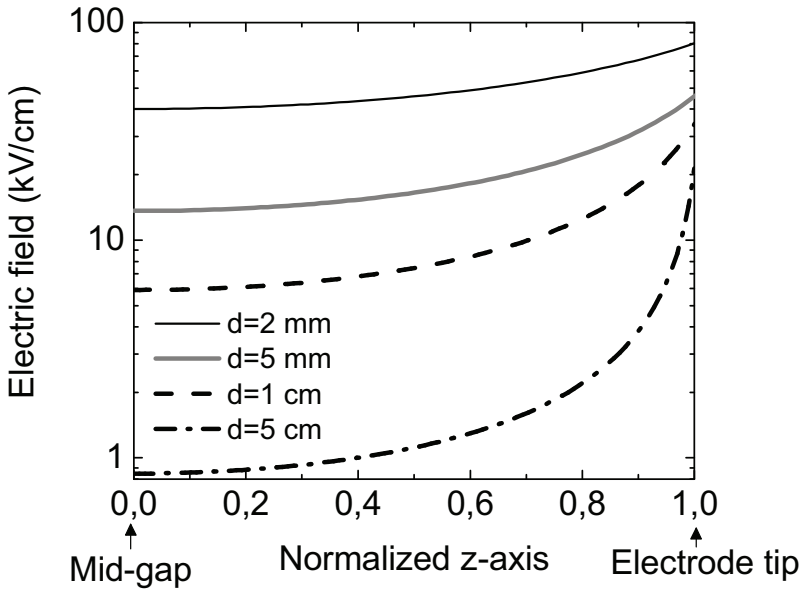

Figure 6.3: Laplacian electric field on the normalized inter-electrode (z) axis (ξ=1) with R=1 mm and V_p=10 kV, for several values of the inter-electrode distance (d). The field is symmetric about z=0.

In addition, the field at mid-gap is more sensitive to changes in gap distance than the field at the electrode tip. For d=2 mm, $E(0)$=40 kV/cm and $E(1)$=80 kV/cm, whereas for d=5 cm, $E(0)$=0.85 kV/cm and $E(1)$=20 kV/cm. Therefore, an increase by a factor of 25 in gap distance results in a decrease by a factor of 47 in the field at mid-gap and only a decrease by a factor of 4 at the tip.

Thus, we have established that changing the radius of curvature at the electrode tip primarily affects the field strength at the tip. On the other hand, changing the gap distance primarily affects the field strength in the middle of the gap. Although these conclusions were drawn from calculations based on idealized electrodes, they should remain qualitatively correct as long as the electrodes are approximately symmetric in shape and orientation.

6.3 Existence of strongly and weakly ionizing zones in the discharge gap

In this section, we consider how the non-uniformity of the Laplacian electric field affects the ionization within the discharge gap. The net ionization coefficient is $\alpha_{net}=\alpha-\eta$, where α is the ionization coefficient and η here is the attachment coefficient. The reduced electric field for breakdown (E_{br}), i.e. when α_{net}=0, is 35 V/cm/torr (E_{br}/N=99 Td) for air at 300 K [6.6]. Tanaka calculated the dependence of E_{br} on gas temperature [6.7], which is shown in Figure 6.4. E_{br} does not vary much from 300 to

1000 K, the range of temperatures for the D regime. It must be noted that these are static breakdown thresholds, and it is not clear by how much E_{br} would change in the pre-ionized or pre-excited air generated by NRP discharges.

Nonetheless, if we estimate that E_{br}/N~100 Td, then from 300 to 1000 K, E_{br} ranges from 27 kV/cm to 8 kV/cm, respectively. Given these estimates, we see from Figure 6.2 and Figure 6.3 that in the 300-1000 K range, $E(z)>E_{br}$ only in the part of the inter-electrode gap closest to the electrodes for many combinations of R and d. Thus, we can divide the discharge gap into net ionization zones near the electrodes in which $E(z)>E_{br}$ and a net attachment zone in the middle of the gap in which $E(z)<E_{br}$.

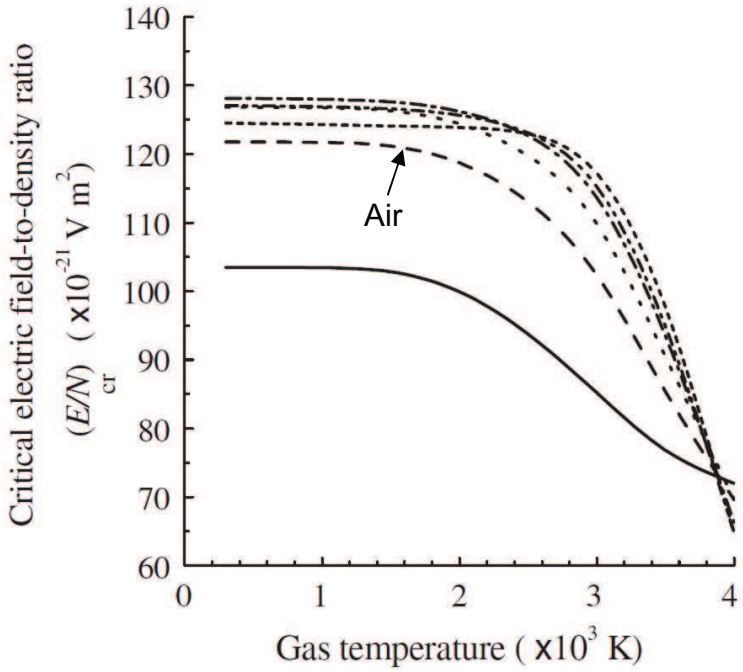

Figure 6.4: Reduced electric field (in Td) for breakdown of N_2/O_2 mixtures as a function of gas temperature at atmospheric pressure. The dashed line for air is indicated. Taken from [6.7].

Figure 6.5 shows a schematic diagram of the electrode configuration, the Laplacian electric field, and the Laplacian potential along the inter-electrode (z) axis, using the same coordinates as in Figure 6.1. In reality, the electrodes are vertically oriented. The electric field is oriented in the $-z$ direction, and the electron drift and airflow velocity in the $+z$ direction. In addition, the threshold electric field for breakdown E_{br} is indicated.

The small radius of curvature of the electrode tip causes the local field near the electrodes to be higher than the average field, and consequently ionization primarily occurs in the zones labeled Σ_a and Σ_c near the anode and cathode, respectively. In the middle of the gap, $E(z)$ is lower than the average field V_p/d. If in addition $E(z)<E_{br}$, then avalanche ionization cannot occur in the zone labeled Ω, which is bounded at z_a and z_c, the points at which $E(z)=E_{br}$. However, Ω cannot be so attaching as to eliminate the formation of the

D regime at all. Therefore, there is a range of field strengths that supports the D regime, and this was experimentally observed.

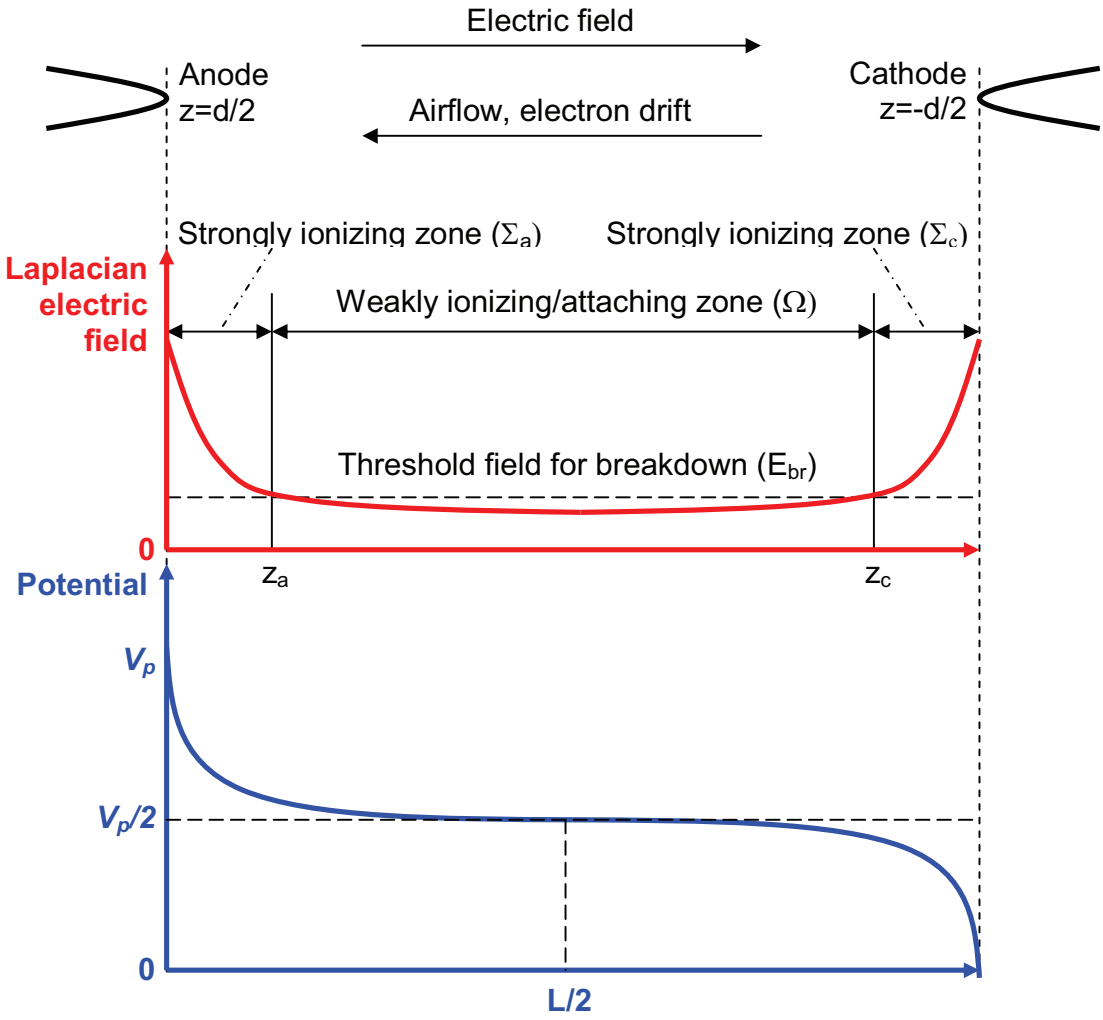

Figure 6.5: Schematic diagram of electric field and electric potential in the 1-D approximation.

Although Σ_a and Σ_c have symmetrical field profiles, the ionization behaviors of these two regions are not identical for two reasons. First, the electron drift is in the direction of increasing field strength for Σ_a but in the opposite direction for Σ_c. As a result, electron avalanche multiplication in Σ_a is stronger. In addition, the airflow is oriented such that the gas in Σ_a has crossed the entire length of the gap and been subjected to the maximum number of pulses, making it the most pre-ionized and pre-excited region of the gap. This results in more seed electrons for ionization and more step-wise ionization. On the other hand, the gas in Σ_c has experienced the least number of pulses and does not benefit as much from pre-ionization and pre-excitation. The asymmetry of pre-ionization and

pre-excitation between Σ_a and Σ_c favors stronger avalanche multiplication in Σ_a. Thus, there are two reasons for stronger ionization near the anode, which is why we observe a cathode-directed streamer originating in this region.

6.4 The D regime as a transient glow discharge

In this section we suggest an explanation for the sequence of events of D regime generation based upon the studies of ionization waves presented in Sections 4.7, 4.8, 5.3, and 5.6. For the D regime, we always observe a cathode-directed streamer that propagates at a speed of about 10^8 cm/s, followed immediately by a return wave. The uncertainty of the measured speed of the return wave is high because the standard deviation of the measured delays at the anode and cathode is large compared to the difference between them, but we estimate the return wave speed to be about 10^9 cm/s. This sequence of events, as well as the directions of propagation of these waves, is reminiscent of phenomena described in studies of streamers in atmospheric pressure air by Cernak and Odrobina [6.8], and Sigmond [6.12]. Figure 6.6 is an illustration of our hypothesis, showing events in order of their times of occurrence. We will now discuss each event in detail.

Avalanche ionization leading to streamer formation

First, the high-voltage pulse initiates an anode-directed Townsend avalanche. This direction of electron movement is expected because the electric field points toward the cathode, as indicated in Figure 6.5. The electrons accumulate near the anode and begin forming a space-charge layer. Eventually, the space-charge layer builds up sufficiently to meet Meek's criterion for the avalanche-to-streamer transition, whereby the space-charge field is approximately equal in strength to the Laplacian field. As mentioned in the previous section, we expect streamer initiation near the anode because ionization is more efficient there than near the cathode. This streamer initiation is observed as the first emission peak at the anode. The emission delays relative to the high-voltage pulse observed in Figures 4.8, 4.10, and 4.11 may be interpreted as the time required for meeting the Meek-Raether criterion at the anode. Some additional time may be required for the generation of emission, which could also contribute to the delay.

During this time, which is about 5 ns, we can neglect the ion-neutral and neutral-neutral chemistry because electron chemistry is dominant. The collision frequency ($\nu_{h\text{-}h}$) between two heavy particles is approximately:

$$\nu_{h-h} = n_h Q_{h-h} \sqrt{\frac{8k_B T_g}{\pi \mu_{h-h}}} \tag{6.5}$$

where n_h is the gas number density, $Q_{h\text{-}h}$ is the heavy-heavy cross-section for momentum transfer, k_B is Boltzmann's constant, T_g is the gas temperature, and $\mu_{h\text{-}h}$ is the reduced mass of two heavy particles. The cross-section $Q_{h\text{-}h}=\pi d_h^2=4.3\times10^{-15}$ cm^2, where $d_h=3.7\times10^{-8}$ cm is the average air particle diameter. The molecular weight of air is 29 g/mol, and therefore $\mu_{h\text{-}h}=2.4\times10^{-26}$ kg. Thus, $\nu_{h\text{-}h}=7.3\times10^9$ s^{-1} at 300 K and

3.8×10^{9} s^{-1} at 1000 K. To find the electron-heavy collision frequency ($\nu_{e\text{-}h}$) in air, we also use Equation (6.5), except that we replace $Q_{h\text{-}h}$ with $Q_{e\text{-}h}\sim10^{-15}$ cm^2, T_g with $T_e\sim30{,}000$ K, and $\mu_{h\text{-}h}$ with the electron mass (m_e). We find that $\nu_{e\text{-}h}=3\times10^{12}$ s^{-1} at 300 K and 10^{12} s^{-1} at 1000 K. Since $\nu_{e\text{-}h}>>\nu_{h\text{-}h}$ during this streamer formation period, we only need to consider electron dynamics and processes.

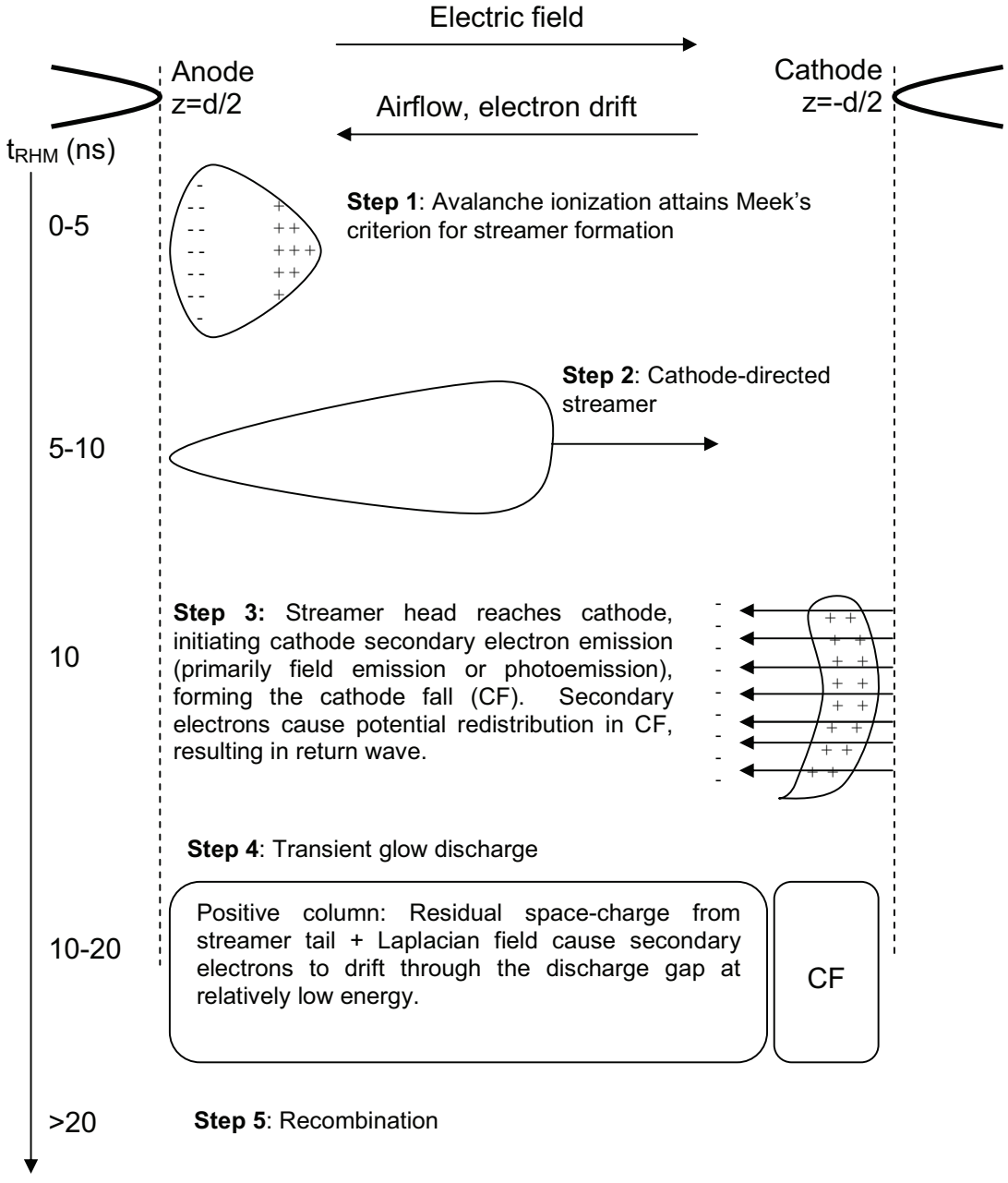

Figure 6.6: Illustration of the sequence of events of the D regime in chronological order. On the left is an axis of the time following the rising half-maximum of the high-voltage pulse, as introduced in Section 4.5.

Cathode-directed streamer propagation

Following its initiation, the cathode-directed streamer propagates across the discharge gap. Figure 6.7 shows an example of species densities and the electric field in the head/near-tail region of a positive streamer in atmospheric pressure air, as simulated by Morrow and Lowke [6.2] for a pin-plane configuration. The intensely ionizing streamer head leaves behind an ionized channel in its tail, in which there is net positive space charge and therefore an electric field pointing towards the cathode like the Laplacian field (E_L). The total field in the gap (E_{tail}) in the tail is thus the sum of the Laplacian and space charge fields and has been calculated to be in the 20-40 Td range in air at pressures from 300-760 torr for a pin-to-plane geometry by Pancheshnyi *et al* [6.13]. In addition, E_{tail} remains fairly constant in the tail region far from the anode, as shown in Figure 6.8.

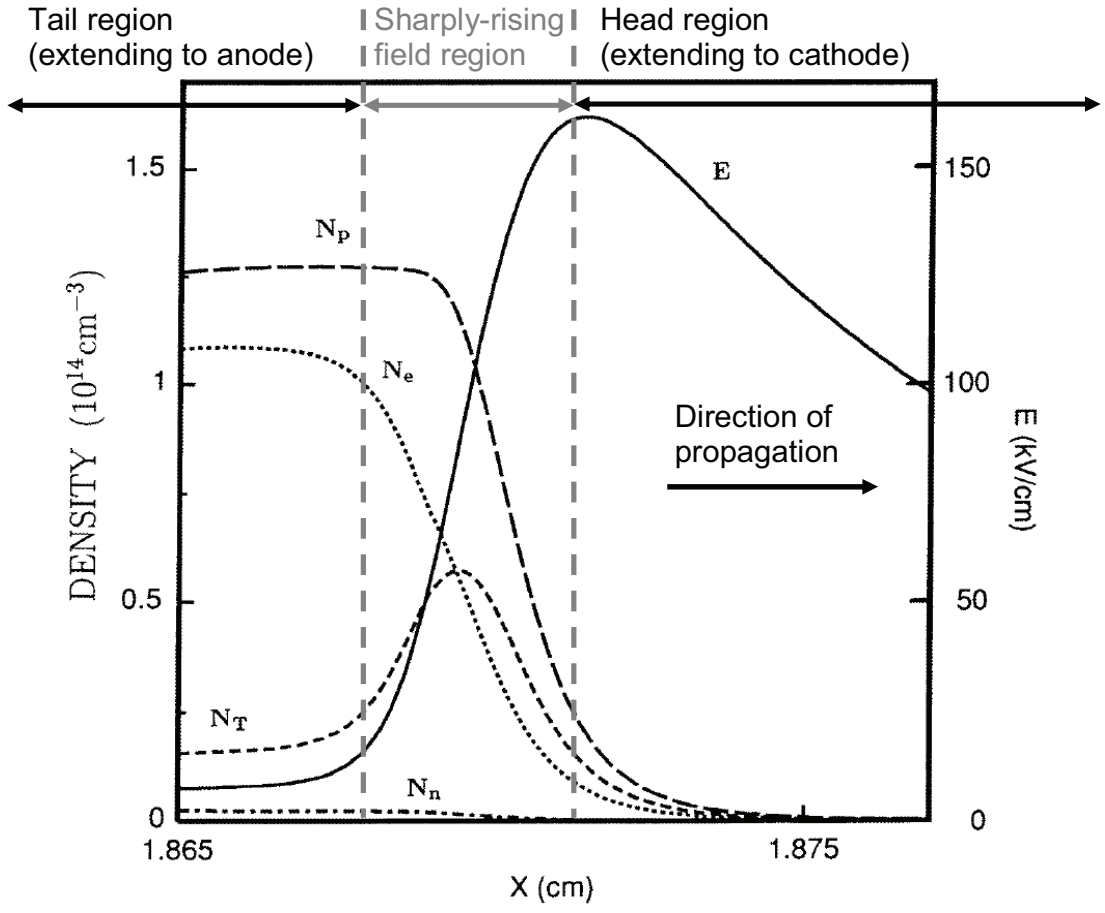

Figure 6.7: Simulated electric field (E), positive ion density (N_p), negative ion density (N_n), electron density (N_e), and net charge density (N_T) for the head and near-tail region of a positive streamer in air at atmospheric pressure. Taken from [6.2]. The tail, sharply-rising field, and head regions referred to later in this section are marked.

We cannot just sum the Laplacian and space charge fields to calculate the total field between the streamer head and the cathode (E_{head}) because the positive space charge of

the head induces negative image charge on the cathode. The head can be thought of as a moving virtual anode that progressively reduces the gap distance, producing an increasingly strong E_{head}.

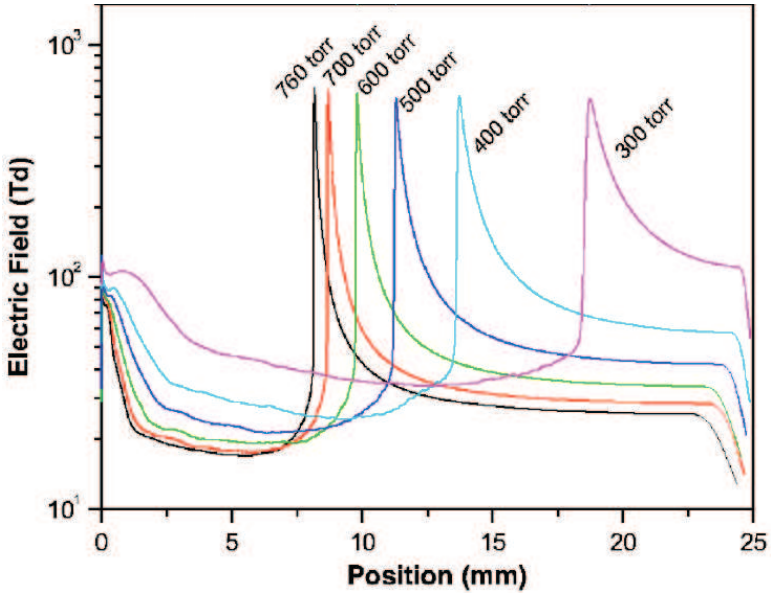

Figure 6.8: Simulated reduced electric field on the discharge axis at a moment during positive streamer propagation in air at pressures from 300-760 torr. Taken from [6.13].

Streamer-cathode interaction

By the cathode-directed streamer head reaching the cathode, we mean that it attains its closest distance from the cathode before the space charge profile that the streamer head maintained during propagation is distorted by E_{head}-induced ion drift toward the cathode. Once the streamer head reaches the cathode, there is no more gas ahead of it. It can no longer extract electrons from the gas, use them for ionization, and maintain a high space-charge field. To continue existing, the streamer head must instead extract electrons from the cathode. Thus, streamer-cathode interaction eventually leads to the formation of the cathode fall, which is characterized by secondary electron emission. One mechanism for secondary electron emission is field emission, which is described by the Fowler-Nordheim formula:

$$j_F = AE_{cath}^2 \exp\left(-\frac{B}{E_{cath}}\right) \tag{6.6}$$

where j_F is the current density generated by field emission and E_{cath} is the field at the cathode. The parameters A and B are taken from Raizer [6.6]:

$$A = 6.2\times10^{-6}\frac{\sqrt{\varepsilon_F/\varphi}}{\varepsilon_F+\varphi} \tag{6.7}$$

$$B = -6.85\times10^{7}\,\varphi^{3/2}\xi \tag{6.8}$$

where ε_F is the Fermi energy and φ is the work function unperturbed by an external field. ξ is the correction factor for the work function in an external field and is a function of $\Delta\varphi/\varphi$, where $\Delta\varphi$ is the reduction in the work function as a result of an external field. This is the Schottky effect, where $\Delta\varphi=3.8\times10^{-4}\{E[\text{V/cm}]\}^{1/2}$ eV. Raizer [6.6] gives tabulated values of ξ as a function of $\Delta\varphi/\varphi$.

To calculate j_F, we need to know E_{cath}. To our knowledge, no one has calculated the electric field for a streamer approaching a pin cathode, although it is common to find calculations for the plane cathode case [7.2, 7.8, 7.13, 7.14]. To estimate E_{cath}, we approximate the streamer as the anode and calculate the electric field using Equation (6.4), assuming that both the streamer head and the cathode have radii of curvature R=1 mm. In addition to R, we also need to know the potential of the streamer head (V_{head}). From Figure 6.7 and Figure 6.8, we see that V_{head} is:

$$V_{head} = V_p - \Delta V_{tail} - \Delta V_{rise} \tag{6.9}$$

where V_p is the potential of anode, ΔV_{tail} is the voltage drop across the tail region, and ΔV_{rise} is the voltage drop in the sharply rising field region just before the streamer head, which is marked in Figure 6.7. Recalling that E_{tail} is roughly constant throughout the tail region, ΔV_{tail} is approximately $E_{tail}d$ by the time the streamer has reached the cathode. As mentioned above, E_{tail} has been simulated to be 20-40 Td, which is equivalent to 5.4 kV/cm at 760 torr and to 4.2 kV/cm at 300 torr.

Kulikovsky showed that the field in this sharply rising region (E_{rise}) is well approximated by a linear profile [6.14]:

$$E_{rise} = E_{\max}\left(1+\frac{z'}{l_h}\right) \tag{6.10}$$

where E_{max} is the maximum field strength of the streamer head, l_h is the thickness of the head region in the z direction, and z' is the coordinate in the moving streamer head reference frame. Equation (6.10) can be integrated from $-l_h \le z' < 0$ to obtain $\Delta V_{rise}=E_{max}l_h/2$.

To estimate E_{max} and l_h, we consult Table 6.1, which summarizes the simulation results of streamer propagation air at 1 atm and 300 K, using pin-plane electrode geometries. For the simulated results in long gaps (>1 cm), the values listed were for the first 1 cm of propagation, which is the longest gap distance studied in this thesis. E_{max} decreases in strength as the streamer propagates [6.2, 6.14], and therefore it is most appropriate to take the lowest values listed in Table 6.1, as we are concerned here with the streamer after it has crossed the gap. Thus, we have average values of E_{max}=137.5 kV/cm and l_h=95 μm, which means that on average ΔV_{rise}=652 V.

Table 6.1: Parameters for several simulations of streamer propagation in atmospheric pressure air at 300 K using a pin-plane geometry and results for streamer head electron number density ($n_{e,max}$), net charge number density (ρ_{max}), and total electric field (E_{max}).

Author	d (mm)	V_p (kV)	$n_{e,max}$ (cm^{-3})	ρ_{max} (cm^{-3})	E_{max} (kV/cm)	l_h (μm)
Morrow and Lowke [6.2]	50	20	2×10^{14}-2.7×10^{14}	6.6×10^{13}	175-225	30
Kulikovsky [6.14]	10	13	2×10^{13}-5×10^{14}	7×10^{12}	100-200	160

In Section 4.8, we showed that, for the D regime, the applied voltage (V_p) as a function of the gap distance (d) is well-fitted by the linear relation:

$$V_p = V_c + E_{br} d \tag{6.11}$$

where V_c is the cathode fall voltage and E_{br} is the static breakdown field for air at a given pressure. Substituting Equation (6.11) into Equation (6.9) gives:

$$V_{head} = V_c + \left(E_{br} - E_{tail}\right) d - \Delta V_{rise} \tag{6.12}$$

From Section 4.8, V_c=1.2 kV and E_{br}=9 kV/cm for the weak D states at 1000 K. Using E_{tail}=4.2 kV/cm at 300 torr, we have V_{head} ranged from 1.5 kV for d=2 mm to 5.3 kV for d=1 cm. For the strong D states, V_c=1.9 kV and E_{br}=9 kV/cm, and thus V_{head} ranged from 2.2 kV for d=2 mm to 6 kV for d=1 cm. We note that $V_{head}>V_c$, indicating that the streamer decreases in potential during its transformation into the cathode fall. Thus, we use Equation (6.4) to calculate E_{cath} and Equations (6.6)-(6.8) to calculate j_F, using typical values ε_F=7 eV and φ=4.5 eV [6.6]. Using these parameters, Figure 6.9 shows the calculated j_F as a function of the distance of the streamer head from the cathode.

There is a very large range of values for j_F in Figure 6.9, but we must consider that experimentally, we could not measure conduction current for the D regime. Figure 6.10 shows typical measured voltage (V_p) and conduction current (I_{cond}) for a D state, and we recall from Section 3.11 that I_{cond} is found by subtracting the measured total current without plasma from the measured total current with plasma. We expect that conduction current should manifest itself as a pulse, as for the F regime, but smaller. Instead, we observe oscillations at ~500 MHz, which may be due to plasma reactance resonance. To claim that we measure I_{cond}, we must find a current pulse that rises above the amplitude of these oscillations. Therefore, the limit of detection for conduction current is ~2 A. We measured the plasma radius for a D state in Section 3.6 to be ~1 mm, which means that the limit of detection for current density is ~64 A/cm^2.

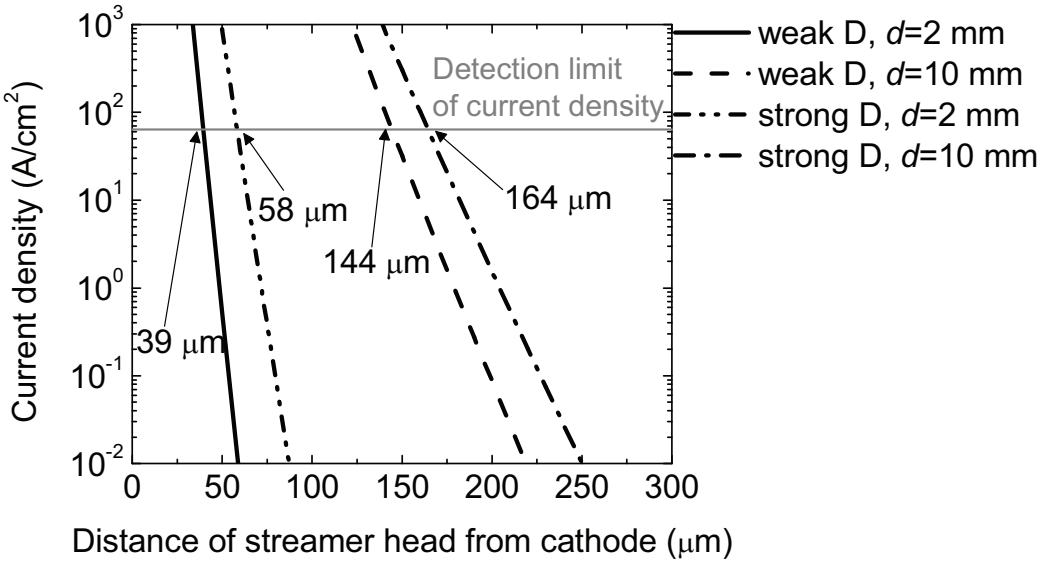

Figure 6.9: Field emission current density as a function of distance of the streamer head to the cathode for weak and strong D states with gap distances of 2 and 10 mm. The work function is 4.5 eV, and the Fermi energy is 7 eV. The distances corresponding to the detection limit of current density are indicated.

Because of this detection limit for current density, we see from Figure 6.9 that the streamer cannot be closer than 39 and 144 μm from the cathode for the weak D state with d=2 mm and 10 mm, respectively. Likewise, the streamer cannot be closer than 58 and 164 μm from the cathode for the strong D state with d=2 mm and 10 mm, respectively. Thus, calculating the field emission alone permits us establish limits for the approach of the streamer head to the cathode, regardless of other secondary emission processes.

In addition to field emission, the intense optical emission from the head that generated photo-ionization during the streamer propagation phase now generates photo-electrons from the cathode via the photo-electric effect. The contribution of ion-electron emission is minor because the time scale for initial streamer-cathode interaction is short. We observed in Figure 3.9 that the return wave occurs immediately following the arrival of the streamer at the cathode. Therefore, the streamer-cathode interaction time is less than the minimum camera gate window of 2 ns. Using Equation (6.5), we find that during a maximum interaction time of 2 ns, a heavy particle undergoes at most only 15 collisions at 300 K and 8 collisions at 1000 K.

Ions move faster than neutrals due to drift, where the ion drift velocity (v_i) is equal to the product of the ion mobility (μ_i) and the local electric field. Ellis *et al* [6.9] and Moseley *et al* [6.10] measured the mobilities of N_2^+ and O_2^+ for fields up to 200 kV/cm. The maximum ion velocity is 2×10^5 cm/s, using the fact that μ_i is about 10^{-4} m^2/V/s for both N_2^+ and O_2^+ at 200 kV/cm. For air at 300 and 1000 K, the mean free paths are 6×10^{-6} cm

and 2×10^{-5} cm [6.11], respectively, and the respective ion-heavy collision frequencies are 3.3×10^{10} s^{-1} and 10^{10} s^{-1}. Therefore, during a maximum streamer-cathode interaction time of 2 ns, an ion undergoes 66 collisions at 300 K and 20 collisions at 1000 K. We have probably underestimated the maximum number of collisions because E_{cath} is likely to be in the MV/cm range, given the distances of the streamer head from the cathode shown in Figure 6.9.

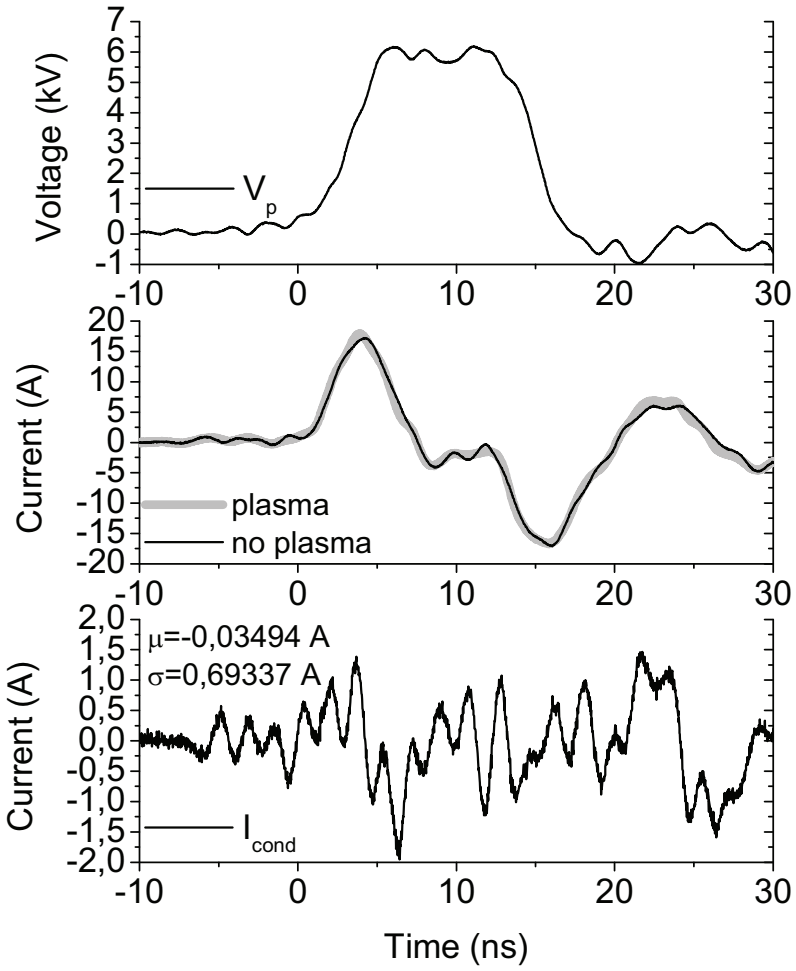

Figure 6.10: Typical measured applied voltage (top), total current with plasma (middle, thick line), total current without plasma (middle, thin line), and conduction current (bottom) for a D state. T_g=1000 K, PRF=30 kHz, d=5 mm, v=1.6 m/s. For the conduction current, μ is the mean value, and σ is the standard deviation.

Nonetheless, we should expect that secondary electron emission processes involving ions should occur more slowly than those involving electrons or photons. Indeed, Cernak and Odrobina [6.8] calculated that the current from the cathode resulting from photo-emission precedes that from ion impact by about 10 ns. As a final note, we neglect thermionic

emission effects that could enhance the field additionally, under the assumption that the electrodes remain below 1000 K in the D regime.

Transient glow discharge – Cathode fall

Following less than 2 ns of streamer-cathode interaction, the return wave to the anode is generated. At this point, the streamer head has transformed into the cathode fall. We can calculate field emission using the cathode fall voltages measured in Section 4.8 to estimate the minimum cathode fall thickness (d_c). From the experiments in Section 4.8 at T_g=1000 K and PRF=30 kHz, V_c=1.2 kV for the weak D states and V_c=1.9 kV for the strong D states. Thus, we use Equation (6.4) to calculate E_{cath} and Equations (6.6)-(6.8) to calculate j_F, using typical values ε_F=7 eV and φ=4.5 eV [6.6], assuming radii of curvature of R=1 mm for both the cathode fall "anode" and the cathode. Figure 6.11 shows the resulting calculation for E_{cath} as a function of the distance of the streamer head from the cathode.

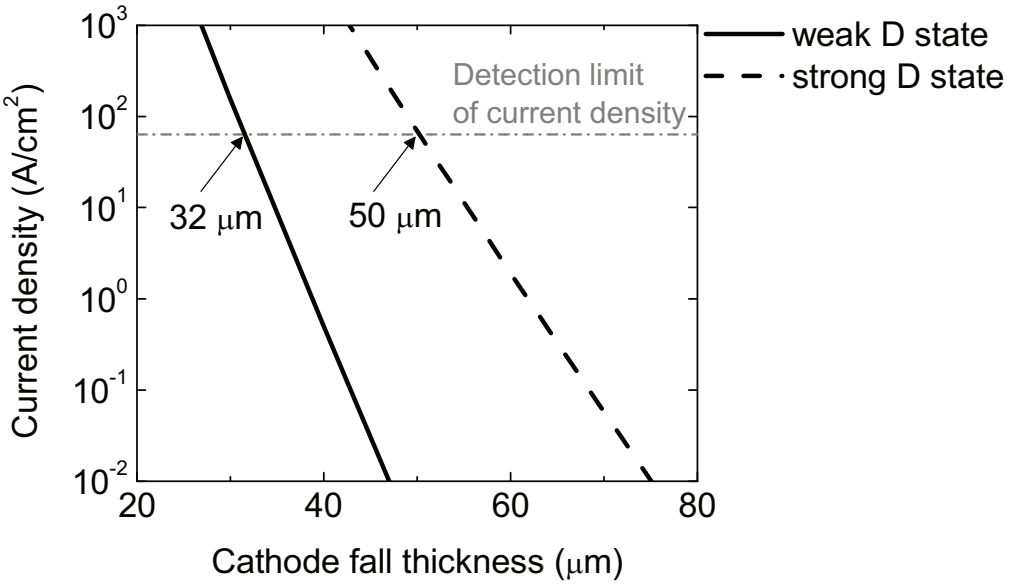

Figure 6.11: Field emission current density as a function of the cathode fall thickness, using a work function of 4.5 eV and a Fermi energy of 7 eV.

The limit of detection for current density is ~64 A/cm^2. Therefore, the cathode fall cannot be less than 32 and 50 μm thick, respectively, for the weak and strong D states. Typical normal cathode fall thicknesses (d_c) for air at room temperature are related to the gas pressure (p) by pd_c=0.25 to 0.52 torr-cm [6.6]. Using the ideal gas law to relate the gas temperature to an equivalent p, we find that d_c ranges from 3 to 23 microns from 300 to 1000 K. Cernak and Odrobina [6.8], who modeled streamer-cathode interaction, found that the streamer stopped ~100 microns in front of the cathode, for a discharge in N_2 at 26.7 kPa in a pin-plane geometry. Abnormal glows also have higher cathode fall voltages (V_c) than normal glows. In Section 4.8, we measured V_c from 1.2 to 1.9 kV for the D regime at 1000 K, which is considerably higher than the ~300 V normal cathode fall voltage for air. Therefore, the measured V_c suggest that the weak and strong D states

are in the abnormal glow regime. The abnormal glow regime leads to the glow-arc transition for DC discharges, and the same is observed in NRP plasmas.

Transient glow discharge – Return wave

The return wave is generally considered a phase of potential redistribution, during which electrons released from the cathode fall neutralize the positive space charge in the streamer tail [6.12, 6.15]. Sigmond [6.12] suggested that the charge displacement necessary for this neutralization is a phase that travels much faster than actual electron speeds. The situation is analogous to voltage traveling down a wire. Using this analogy, Sigmond modeled the return wave using the telegraph equation typically used to describe lossy transmission lines:

$$\frac{\partial^2 V}{\partial z^2} - LC\frac{\partial^2 V}{\partial t^2} - RC\frac{\partial V}{\partial t} = 0 \tag{6.13}$$

where V is the potential and R, L, and C are the per unit length plasma resistance, inductance, and capacitance, respectively. For a 100-mA streamer channel in atmospheric pressure air, R is typically about 5×10^6 Ω/m, which is high enough to dampen the lossless transmission line wave solutions to Equation (6.13). Thus, neglecting the LC term in Equation (6.13) results in a diffusion equation, which was first used for streamers by Wright [6.16] and Marode [6.17]:

$$\frac{\partial^2 V}{\partial z^2} - RC\frac{\partial V}{\partial t} = 0 \tag{6.14}$$

Streamer contact with the cathode is modeled as a voltage step function, for which the lowest and least damped mode crosses the gap in time $d^2RC/4$. This means that the return wave velocity is about 10^9 cm/s for short (<5 cm) gaps in ambient air, according to Sigmond [6.12]. This agrees well with the speeds of 7×10^8 cm/s measured in Chapter 4. Electron drift speeds in the residual streamer tail, assuming E_{tail} ranges from 20-40 Td as during initial streamer propagation, would only be 3×10^6 to 6×10^6 cm/s, using the electron mobility values found in Raizer [6.6].

However, Sigmond's work concerned why the return stroke had *not* been observed in a number of experiments, contending that Equation (6.14) produces weak-field solutions, and therefore return waves are too faint to measure. This contradicts our consistent observation of return waves in Chapter 3 and 4.

Previously, we found that the potential of the streamer head upon reaching the cathode (V_{head}) is higher than the potential of the cathode fall (V_c). It seems plausible that as secondary electrons are created and undergo avalanche ionization in the cathode fall, the net charge in the cathode fall decreases. This results in a decrease in the electric field due to space charge and a corresponding decrease in the cathode fall potential from V_{head} to V_c. This occurs in a very short time, as the return wave begins immediately after the initial streamer reaches the cathode. Therefore, such a potential drop would be well approximated by the step function used by Sigmond to solve Equation (6.14). This

voltage drop propagates through the discharge gap, generating the return wave. To estimate the field of the return wave, we use the speed calculated by Sigmond, $v_{return} \approx 10^9$ cm/s. If the time required for a burst of secondary electrons to instigate a potential drop in the cathode fall is τ_{drop}, then we can estimate the field of the return wave as:

$$E_{return} = \frac{V_{head} - V_c}{v_{return} \tau_{drop}} \tag{6.15}$$

Previously, we calculated V_{head}=1.5 kV and V_c=1.2 kV for the weak D state and V_{head}=2.2 kV and V_c=1.9 kV. As mentioned before, τ_{drop} is at most 2 ns, the gate width of the ICCD camera used to measure ionization waves. Therefore, the minimum E_{return} is 150 V/cm. To obtain a better estimate of τ_{drop}, we calculate the electron drift time through the cathode fall. The average field in the cathode fall is V_c/d_c. Using the minimum values for d_c of 32 and 50 μm for the weak and strong states respectively, we obtain an average cathode fall field of 380 kV/cm (4700 Td) for both the weak and strong D states. To our knowledge, the highest reduced field studied for electron mobility measurements is 1440 Td by Lakshminarasimha and Lucas [6.18]. In fact, they studied the ratio of the transverse electron diffusion coefficient (D_T) to the electron mobility (μ_e), with a maximum measured D_T/μ_e of about 10 V at 1440 Td. This is related to the electron temperature (T_e) by the Einstein relation:

$$\frac{D_T}{\mu_e} = \frac{k_B T_e}{e} \cong \frac{m_e \bar{v}_e^2}{3e} \tag{6.16}$$

Using D_T/μ_e=10 V, we obtain an average electron speed of 2×10^8 cm/s. Therefore, the average electron drift time through 50 μm is 20 ps. From Equation (6.15) we obtain E_{return}=15 kV/cm, which is sufficiently high to generate electronic excitation. Although there is uncertainty in the electron mobility, values of τ_{drop} in the picosecond time range appear realistic and would lead to significant fields in the return wave, according to Equation (6.15). This would lead to electron energies sufficient for electronic excitation and explain the observed emission of the return wave. Furthermore, as we did not measure significant conduction current in the D regime, the field in the return wave is probably not high enough to generate significant ionization.

These electron energies are determined in part by the Laplacian field in the gap, which varies with the applied voltage. Increasing the applied voltage increases the electron energy, resulting in the increase in the emission intensity observed for the second peak at the anode.

6.5 Role of the minimum gap distance for the existence of the D regime

The requirement of a minimum gap distance for generating the D regime means that the average electric field (V_p/d) is not a critical parameter. Otherwise, the D regime could exist in gaps smaller than the minimum using lower applied voltage. We suspect that the

non-uniformity of the electric field generated by our pin-to-pin electrode configuration plays a critical role.

Referring back to Figure 6.5, for a given gas temperature (T_g), the applied voltage must be increased until sufficient ionization occurs in Σ_a and Σ_c to sustain a D regime. The cathode region of glow discharges, which is contained in Σ_c, has been suspected as the origin of the glow-arc instability, according to Takaki *et al* [6.19]. We suggest that the instability develops initially in Σ_c and spreads through the rest of the discharge gap, thus causing the D-F transition. However, if we widen the gap, the electric fields in Σ_a and Σ_c retain their strength due to their proximity to the electrodes, while the field in Ω decreases in strength. At a critical length, the net ionization coefficient in Ω is sufficiently weak (or even negative) to extinguish the glow-arc instability as it attempts to spread through the gap. Moreover, by widening the gap, we also increase the length over which the instability must spread, further impeding its ability to complete a high-current circuit. Even intense ionization near the electrodes cannot cause excessive ionization because the Ω zone impedes high current flow through the plasma circuit. Thus, the middle attachment zone acts as a current-limiting element to prevent the D-F transition.

When T_g decreases, two effects occur that require an increase in the fields in Σ_a and Σ_c to obtain the D regime. First, detachment rates, which are generally dependent upon T_g, decrease, causing the effective ionization coefficient to decrease. Second, the density increases, thereby decreasing the reduced electric field. Therefore, we must increase the electric field strengths in Σ_a and Σ_c to compensate for these two effects. However, an increase in field strength must be accompanied by a widening of Ω to ensure that the field is weak enough in Ω to contain the glow-arc instability.

It is worthwhile to wonder whether the same phenomenon would be observed in pin-plane configurations. Typically, the plane is grounded, with the pin electrode at high positive or negative voltage. Let us consider the case of positive voltage. After switching on the voltage, electron avalanches in volume accumulate primarily near the anode because its local field is the highest of any location in the discharge gap. Space-charge develops near the anode until a positive streamer develops and propagates toward the cathode. Upon reaching the plane cathode, however, not as many secondary electrons are emanated because the Laplacian field is not as high as it is for a pin cathode. As a result, the total field at the cathode (Laplacian + streamer head) is not as powerful, and it may not be enough to enable the streamer-cathode interactions that form a cathode fall. Furthermore, for a plane cathode, there is no way to increase the cathode region field high enough to induce secondary electron emission processes while keeping the middle of the gap at comparatively low field to prevent the spread of the glow-arc instability. Therefore, the pin-to-pin configuration is more conducive than the pin-plane configuration to the formation of the non-thermal regime, and it may indeed be essential for it.

To test the extent that the electrode configuration (and hence the form of the non-uniform field) influences the ionization instability, experiments should be performed for DC discharges at 300 K, using a pin-to-pin configuration. Conversely, we should explore

whether it is possible to generate the D regime in a pin-plane electrode configuration using the NRP method. At best, the use of pin-to-pin electrode configurations with large gaps may represent a new method for controlling runaway ionization and producing non-thermal plasmas.

6.6 Conclusion

In this chapter, we have suggested the possibility that the D regime is a transient glow discharge and that the weakly ionizing middle region of the discharge gap is critical for controlling the D-F transition. We demonstrated an approximation of the Laplacian field of a pin-to-pin electrode geometry based on an analytical solution for pin-plane geometry represented by a hyperboloid-shaped electrode in prolate spheroidal coordinates. Furthermore, we showed that such a Laplacian field separates the discharge gap into strongly ionizing zones near the electrodes and a weakly ionizing, or even attaching, zone in the middle of the gap. Upon application of the high-voltage pulse, an avalanche-to-streamer transition occurs in the strongly ionizing zone near the anode. The cathode-directed streamer propagates across the gap and initiates secondary emission processes upon reaching the cathode. The streamer transforms into the cathode fall. We used the detection limit of electron field emission from the cathode to estimate the minimum distance between the streamer head and the cathode and the minimum cathode fall thickness. Based upon the cathode fall thickness and voltage drop, we concluded that the D regime is an abnormal glow discharge. As the streamer head transforms into the cathode fall, a return wave propagates to the anode. We demonstrated that the observed return wave speed agrees with previous work suggesting that it is potential wave. Furthermore, we calculated that the field of this potential wave is sufficient to produce electronic excitation.

Finally, we proposed that the weakly ionizing middle region of the discharge gap serves as a current-limiting element that contains the spread of the glow-arc instability originating from the cathode region. By widening the gap beyond a certain minimum, it is possible to have field strengths near the electrodes sufficient for ionization and simultaneously low field strengths in the middle of the gap to impede the glow-arc instability. These two conditions are required to maintain the D regime and avoid the D-F transition. Thus, we have two tools to aid with generating non-thermal atmospheric pressure air plasmas in ambient air: the use of the NRP method and the use of the pin-to-pin electrode geometry. Both tools serve to prevent the D-F transition resulting from the glow-arc instability.

6.7 References

[6.1] J. D. Zuber, K. L. Jensen, and T. E. Sullivan, *J. Appl. Phys.* **91**(11) (2002) 9379-9384.
[6.2] R. Morrow and J. J. Lowke, *J. Phys. D.: Appl. Phys.* **30** (1997) 614-627.
[6.3] G. Mesa, E. Dobado-Fuentes, and J. J. Sáenz, *J. Appl. Phys.* **79**(1) (1996) 39-44.
[6.4] E. W. Müller, Z. Phys. **108**, 668 ~1938; R. Haefer, *ibid.* **116**, 604 ~1940; A. M. Russell, J. Appl. Phys. **33**, 970 ~1962.
[6.5] S. Celestin, personal communication.

[6.6] Yu. P. Raizer, 1997 *Gas Discharge Physics* (Berlin: Springer)
[6.7] Y. Tanaka, *J. Phys. D.: Appl. Phys.* **37** (2004) 851-859.
[6.8] I. Odrobina and M. Cernak, *J. Appl. Phys.* **78**(6) (1995) 3635-3642.
[6.9] H. W. Ellis, R. Y. Pai, E. W. McDaniel, E. A. Mason, and L. A. Viehland, *Atomic Data and Nuclear Data Tables*, **17** (1976) 177.
[6.10] J. T. Moseley, R. M. Snuggs, D. W. Martin, and E. W. McDaniel, *Phys. Rev.* **178**(1) (1969) 240-248.
[6.11] W. G. Vincenti and C. H. Kruger, 1986 *Introduction to Physical Gas Dynamics* (New York: Wiley).
[6.12] R.S. Sigmond, *J. Appl. Phys.* **56**(5) (1984) 1355-1370.
[6.13] S. Pancheshnyi, M. Nudnova, and A. Starikovskii, *Phys. Rev. E* **71** (2005) 016407.
[6.14] A. A. Kulikovsky, *Phys. Rev. E* **57**(6) (1998) 7066-7074.
[6.15] F. Bastien and E. Marode, *J. Phys. D.: Appl. Phys.* **12** (1979) 249-263.
[6.16] J. K. Wright, *Proc. Roy. Soc. London Ser. A* **280** (1964) 23.
[6.17] E. Marode, *J. Appl. Phys.* **46** (1975) 2005, 2016.
[6.18] Lakshminarasimha and Lucas, *J. Phys. D.: Appl. Phys.* **10** (1977) 313-321.
[6.19] K. Takaki, D. Kitamura, and T. Fujiwara, *J. Phys. D: Appl. Phys.* **33** (2000) 1369-1375.

Chapter 7

Conclusion

7.1 Contributions of this thesis

In previous work by the Stanford group [7.1-7.3], glow plasmas in atmospheric pressure air at 2000 K were produced using the Nanosecond Repetitively Pulsed (NRP) method. In this thesis, the NRP method was implemented to generate plasma discharges in a pre-heated (T_g=300-1000 K) atmospheric pressure airflow between two bare steel electrodes in a pin-pin configuration parallel to the flow. We applied short-duration (10 ns) high-voltage (0-10 kV) pulses at Pulse Repetition Frequencies (PRFs) of 1-30 kHz across a primarily 5-mm discharge gap, although the 0.5-10 mm range was studied as well.

We used optical emission spectroscopy and voltage-current measurements to examine the chemistry and electrodynamics of NRP discharges. We observed the C, D, and F discharge regimes, which are akin to corona, glow, and spark discharges, respectively. We defined the discharge regimes according to the applied voltage. In particular, the D regime is lower-bounded by the C-D transition voltage and upper-bounded by the D-F transition voltage. Our findings are summarized as follows:

D regime

Experimentally, the populations of the excited species $N_2(B)$, $N_2(C)$, $N_2^+(B)$, NO(A), and O(3p ^{5}P) in the middle of the gap all recombined within nanoseconds except for NO(A), which persisted at all times. Based upon the relative emission intensity of the $N_2^+(B)$ state, we inferred that the maximum electron density was about 10^{13} cm^{-3}. The emission radius expanded up to ~1 mm. Beginning in the second half of the high voltage pulse, an initial ionization wave of constant emission intensity propagated from the anode to the cathode. This is followed by a return wave whose intensity varied with the applied voltage. We were unable to detect the conduction current, which was therefore presumed to be small, i.e. in the mA range. Most importantly, the gas heating was not significant.

Based on these findings, we proposed an explanation concerning the nature of D regime and the D-F transition. The non-uniform Laplacian electric field generated by the pin-pin geometry creates high-field regions near the electrodes where strong ionization occurs. The D regime initiates in the anode high-field region with a cathode-directed streamer, whose head transforms into a cathode fall, thus creating a transient glow discharge. The cathode-streamer interaction also causes potential redistribution across the gap, which manifests itself as the observed return wave.

F regime

The chemistry remains active long after the application of the pulse, including as yet unidentified species that emerge about 10 μs afterwards. Emission filled the discharge gap at once without distinguishable ionization wave propagation, at the time resolution of the present experiments (2 ns). The gas heats up to ~5000 K within a few nanoseconds after the pulse. There is significant conduction current, indicating a high electron density. Based on these findings, we hypothesize that the F regime is a spark discharge.

Influence of T_g and PRF on D and F regimes and the D-F transition

In the range T_g=300-1000 K and PRF=1-30 kHz, the regimes were more sensitive to T_g than to PRF. For a fixed set of operating conditions, there is a minimum T_g for D regime generation. The emission intensity and energy curves simply shifted to higher applied voltages with decreasing PRF and T_g. Thus, two states occupying the same relative place within a regime were equivalent in terms of their emission intensity and energy. In addition, the D regime expanded and the D-F transition became more gradual with decreasing PRF. The emission delay following the application of the high-voltage pulse decreased noticeably with increasing PRF, but no trend as a function of T_g was found. Finally, for a given T_g, there is a minimum gap distance for the generation of the D regime. Using this fact, we generated an intermittent D state in ambient air.

We tentatively explained the minimum gap distance for D regime existence based upon our aforementioned explanation of the nature of the D regime. The weakly ionizing low-field region between the electrodes can inhibit the spread of the glow-arc instability and prevent the D-F transition, acting as a current-limiting element.

In conclusion, we have successfully demonstrated that non-thermal plasma discharges can be generated in atmospheric pressure air from 300 to 1000 K using the NRP method with a power budget of just 2-20 W/cm^3 and over gap distances from millimeters to several centimeters.

The generation of diffuse non-thermal discharges capable of producing active species in air at atmospheric pressure appears therefore possible. One way to fill a large volume would be to use several diffuse NRP discharges between pins placed in parallel, as already demonstrated by Packan [7.2] in air at 2000 K. This may open the way for new applications, such as those mentioned in Chapter 2, for plasma treatment in cold air over a large volume.

7.2 Perspectives and future work

The usefulness of a plasma depends strongly on its electron density. Therefore, measuring the electron recombination time is still a priority, despite fruitless earlier efforts. Previously, a DC circuit was inserted in series with the NRP circuit to measure the dynamic plasma resistance during the recombination period following the application

of the pulses. We had sought to deduce the electron density from the plasma conductance, which is calculable from the resistance. However, noise from the high-voltage pulse dominated the measured signal during the first 2 μs, with no sign of the plasma current. A different approach must be found to eliminate this noise problem.

A natural complement to electron number density measurements would be studies of the attachment and detachment processes, which primarily involve oxygen. Measurements of O, O_3, O_2^-, O^-, and the long-lived metastable states $O_2(a^1\Delta_g)$ and $O_2(b^1\Sigma_g^+)$ would form a solid data set for understanding the oxygen chemistry. At the time of this writing, Two-photon Laser-Induced Fluorescence (TALIF) measurements are underway at the Laboratoire EM2C to measure ground-state atomic oxygen. Preliminary results indicate the presence of atomic oxygen in both the D and F regimes up to 1 μs after the pulse. Previously, we were unsuccessful in measuring $O_2(a^1\Delta_g)$ by IR emission spectroscopy, since emission from this state is weak, as it is a dipole-forbidden transition. Therefore, an absorption technique such as off-axis Integrated Cavity Output Spectroscopy (ICOS) may be more appropriate. In addition, opto-galvanic spectroscopy could be performed to measure O_2^- and O^-. A single-pass absorption spectroscopy experiment using a UV source may suffice to measure ozone. Finally, one other way to verify the role of oxygen in the chemistry is to generate NRP plasma discharges in nitrogen and compare them with those in air.

Expanding the data set for the nitrogen chemistry is another priority. Upcoming experiments at EM2C include Cavity Ring-Down Spectroscopy (CRDS) to measure $N_2(A^3\Sigma_u^+)$. Because it is a long-lived metastable state, we expect its population to be significant following accumulation over many pulse cycles. With its high energy of 6.2 eV (see Appendix E), $N_2(A)$ may participate in important processes such as dissociative quenching of O_2, step-wise ionization, and the formation of NO.

It is also important to acquire images of single discharges to verify that the D regime is indeed diffuse. All spectroscopic measurements presented in this thesis were accumulated over many discharge events. It is possible that the diffuse aspect of the D regime is in fact the temporal average of several filaments, such that at high PRF the discharge appears diffuse in accumulated measurements. However, this would be a contradiction with the images of a D state obtained by Packan [7.2] in air at 2000 K, which clearly showed a diffuse discharge structure.

In many respects, the NRP discharge exhibits numerous similarities with the prevented spark discharge of Bastien and Marode [7.4]. A comparative study would be useful to further elucidate the behavior of these discharges.

Finally, the discovery that the D regime is possible at 300 K certainly invites further investigation. As we observed it only intermittently, conditions need to be found for stable operation.

7.3 References

[7.1] C. H. Kruger, C. O. Laux, L. Yu, D. M. Packan, and L. Pierrot, *Pure Appl. Chem.* **74**(3) (2002) 337-347.
[7.2] D. M. Packan, Ph.D. Thesis, Stanford University, 2003.
[7.3] M. Nagulapally, G. V. Candler, C. O. Laux, L. Yu, D. M. Packan, C. H. Kruger, R. Stark, K. H. Schoenbach, *31st AIAA Plasmadynamics and Lasers Conference*, AIAA Paper 2000-2417, Denver, Colorado, June 19-22, 2000.
[7.4] F. Bastien and E. Marode, *J. Phys. D: Appl. Phys.* **12** (1979) 249-263.

Annexe A

Fonctionnement du générateur d'impulsions nanosecondes à haute tension

A.1 Introduction

Dans cette annexe nous exposons les principes du fonctionnement du générateur d'impulsions (FID FPG 10-30MS) utilisé dans les études expérimentales présentées dans cette thèse. L'objectif est d'arriver à dessiner notre propre générateur, à partir du schéma général du générateur FID. Dans la Section A.2, nous présentons une introduction générale du générateur FID. Dans la Section A.3, nous utilisons la méthode développée dans l'Annexe B pour analyser son circuit, afin de comprendre le rôle de chaque composant et le choix de sa valeur.

A.2 Mode opératoire du générateur FID FPG 10-30MS

Dans cette section nous présentons un bilan général du générateur d'impulsions FID. Ce générateur n'est pas de type Marx, qui est limité aux basses Fréquences de Répétition des Impulsions (FRI). Il n'est pas non plus de type Blumlein, qui est limité à des conditions de charge assez spécifiques. Afin d'atteindre des FRI supérieure à 1 kHz et une grande gamme des conditions de charge, le générateur FID utilise une diode spéciale développée par Grekhov *et al* [1], appelée la « Drift Step Recovery Diode » (DSRD). Puisque la DSRD est le composant qui permettait l'évolution de ce type de générateur, nous allons maintenant résumer les aspects importants de la DRSD avant discuter le dessin du générateur FID.

Physique de la « Drift Step Recovery Diode » (DSRD)

Quand une diode change de l'état conducteur « forward bias » vers un état isolant « reverse bias », elle ne devient pas isolante toute suite mais continue d'être conductrice pendant une période appelée le « reverse recovery time ». Les DSRD ont la propriété de posséder un « reverse recovery time » très court, de l'ordre de la nanoseconde. Les détails de la physique des semi-conducteurs derrière cette propriété se trouve dans la thèse de Chudobiak [2]. La Figure A.1 montre le comportement d'une DSRD d'après des simulations réalisées par Prokhoreko *et al* [3]. Dans leur circuit, la DRSD est installée de manière à ce qu'il faille appliquer une tension E positive pour la mettre en mode « forward bias ». Pendant la phase $E>0$, la DSRD accumule la charge Q_d, qui la rend conductrice, elle passe alors un courant I_d.

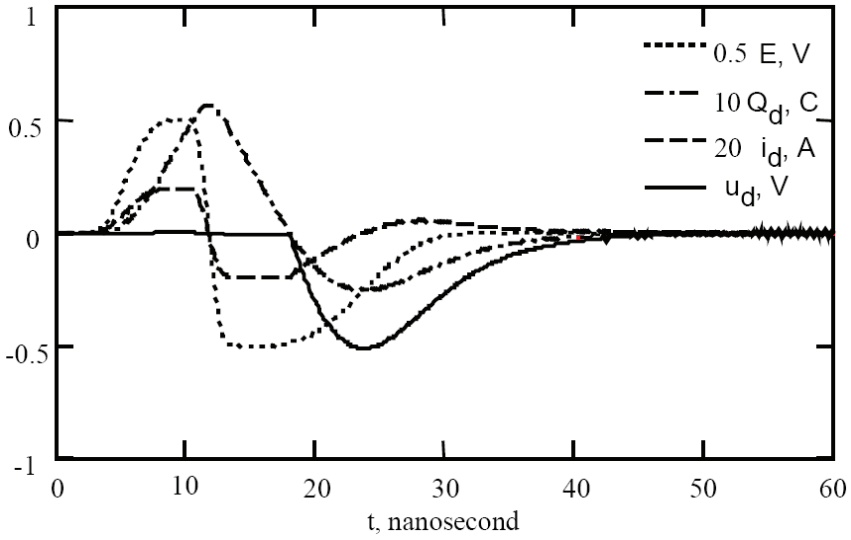

Figure A.1 : Résultats des simulations d'une DSRD pendant une séquence où elle est d'abord mis en « forward bias » et ensuite en « reverse bias ». Le courant (I_d), la charge (Q_d), la tension de la DRSD (u_d) et la tension appliquée (E) sont indiqués. Ces résultats proviennent de Prokhorenko *et al* [3].

Le temps de l'impulsion de courant en « forward bias » doit être inférieur au temps de vie du porteur de charge minoritaire, qui détermine en partie la longueur de diffusion. Dans ce cas, les charges injectées sont faiblement diffusées et elles restent concentrées près des jonctions où elles sont créées. Cette localisation permet à la charge accumulée d'être rapidement enlevée lorsque le courant change de direction, afin d'effectuer un « reverse recovery time » (τ_r) très rapide, entre 1 et 10 ns [2]. Ces effets sont observables dans la Figure A.1, où le changement de polarité de la tension E amène une décroissance de la charge Q_d. Quand Q_d retombe à zéro, la phase de « reverse recovery » est complète, et le courant I_d est rapidement coupé. Cette coupure de courant induit une réponse transitoire du circuit autour de la DSRD qui produit l'impulsion de la tension désirée sur la DSRD u_d.

Prokhorenko *et al* [3] ont modélisé la DSRD comme une résistance ou un condensateur en « forward bias» ou « reverse bias », respectivement. La capacité d'une diode en « reverse bias » est dominé par la capacité de jonction C_j [4] :

$$C_j = \frac{C_{jo}}{\left(1 - \frac{V_d}{\phi}\right)^m} \tag{A.1}$$

Où C_{jo} est la valeur à tension zéro, V_d est la tension par la diode et ϕ est la tension « built-in » et m est un facteur qui varie entre 1/3 et 1/2. Typiquement, C_{jo} et ϕ prennent des valeurs de 1-100 pF et ~1 V, respectivement. Dans le mode « reverse bias », $V_d < 0$ et donc $C_j < C_{jo}$. Nous allons supposer que C_j=10 pF comme approximation dans le reste de cette annexe.

Schéma général du générateur FID

Les générateurs d'impulsions à haute tension du type DSRD ne sont pas différents en principe de ceux à basse tension basés sur le « Step Recovery Diode » (SRD) [5]. Dans les deux cas, le « reverse recovery » d'une diode coupe le courant, ce qui induit une oscillation d'un circuit résonant RLC. La première demi-période de cette oscillation forme l'impulsion, et la deuxième demi-période est interrompue parce que la diode revient en « forward bias ». Pour induire le « reverse recovery », il faut un signal bipolaire qui conduit la DSRD d'abord en « forward bias » et ensuite en « reverse bias », comme montré dans la Figure A.1.

La Figure A.2 montre le diagramme du circuit équivalent du générateur FID, qui a été obtenue en consultation avec FID Technology [6]. Le circuit peut être découpé en deux grandes parties : un générateur « step » et un réseau passif. Le générateur « step » de tension est indiqué sur les Figure A.2. Il est composé d'une partie pour stocker l'énergie modélisée comme un condensateur C_{dc} initialement chargé à une tension V_{dc} par une alimentation continue externe, et de la diode idéale D_{dc}. Les conditions initiales sont alors $V_{step} = V_{dc}$ et $V_x = V_{out} = 0$. Un banc de transistors M contrôlé par un trigger externe V_{trig} déclenche le « step ». Quand M est dans la mode « on », C_{dc} se décharge et D_{dc} se met tout de suite en « reverse bias » jusqu'à la fin de la génération de l'impulsion à haute tension.

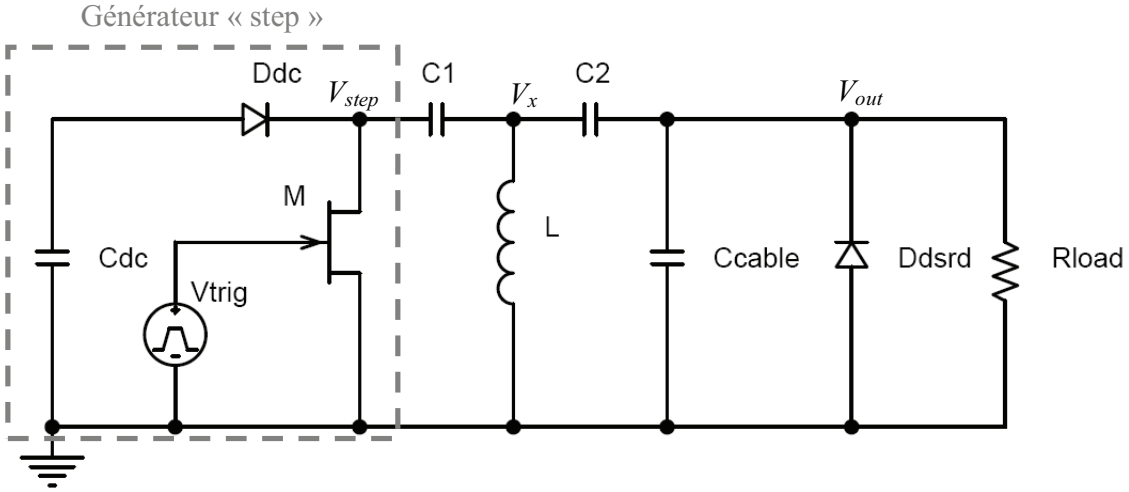

Figure A.2 : Le circuit du générateur des impulsions à haute tension FID FPG 10-30MS.

Le réseau passif génère le signal qui conduit le mode de la DSRD et les impulsions à haute tension. Il est composé principalement des condensateurs C_1 et C_2, de l'inductance L et de la DSRD. Les condensateurs C_1 et C_2 sont de type film métallique avec une tolérance de tension jusqu'à quelques dizaines de kilovolts. La DSRD D_{dsrd} est modélisée par une résistance R_{dsrd} dans le mode « forward bias ». Dans le mode « reverse bias », elle est modélisée par le condensateur C_{dsrd}. Il existe aussi un câble coaxial, modélisé comme le condensateur C_{cable}, qui sert à modifier l'impulsion d'une forme sinusoïdale vers une forme trapézoïdale. La résistance R_{load} représente une charge extérieure du générateur,

comme un plasma par exemple. Le Tableau A.1 montre les ordres de grandeurs donnés par FID Technology [6] pour les valeurs des composants indiqués sur la Figure A.2.

Tableau A.1 : Estimations des valeurs des composants du circuit équivalent du générateur FID, suivant le schéma de la Figure A.2.

Composant	Valeur estimée
R_{dsrd}	Inconnue
R_{load}	Arbitraire
C_1	10 nF
C_2	10 nF
C_{cable}	10 pF
C_{dsrd}	10 pF
L	100 nH

La description du fonctionnement du générateur FID présentée ci-dessus est validée par les mesures. La Figure A.3 montre les tensions mesurées aux nœuds V_{step}, V_x et V_{out} indiqués dans la Figure A.2. Le signal « step » V_{step} induit une oscillation amortie sur V_x. Entre les temps t = -140 ns et t = -75 ns, cette oscillation est dans une phase de tension négative, qui met la DSRD en « forward bias ». À t = -75 ns, un changement de signe de V_x démarre le « reverse recovery » du mode « forward bias » vers le mode « reverse bias ».

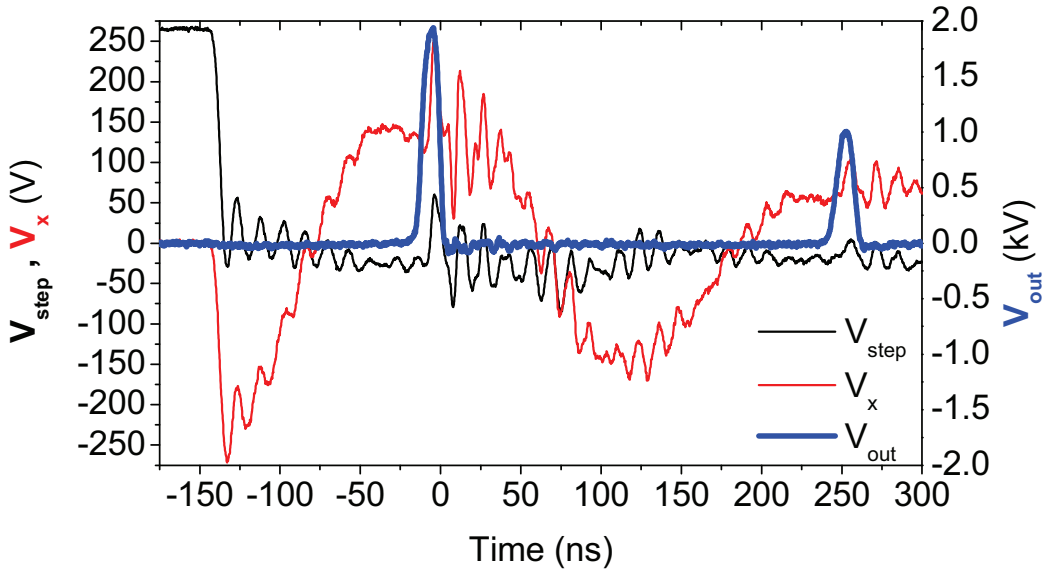

Figure A.3 : Les tensions mesurées aux nœuds correspondants de la Figure A.2.

Nous voyons que le signal bipolaire nécessaire pour changer le mode de la DSRD, est approximé par l'oscillation de V_x. Nous aimerions produire une impulsion à haute tension pour chaque signal bipolaire. Mais le générateur FID n'arrive pas à amortir l'oscillation après le premier cycle, et donc nous voyons que le deuxième cycle génère une impulsion secondaire à t = 250 ns. Le « reverse recovery » est complet à t = -15 ns, et à ce moment, la DSRD n'est plus conductrice. Le résultat est une coupure du courant, qui induit l'impulsion à haute tension à V_{out}.

A.3 Analyse du circuit du générateur FID

Dans cette section nous cherchons à comprendre le choix des valeurs des composants du circuit du générateur FID, montrés dans le Tableau A.1. Nous allons utiliser la méthode présentée dans l'Annexe B pour faciliter cette analyse. D'abord nous considérons la première phase de la génération d'impulsions, où la DSRD est en « forward bias » afin de générer une oscillation qui changera le mode de la DSRD. Comme la DSRD est en « forward bias », elle est modélisée par R_{dsrd}. Le circuit équivalent est présenté dans la Figure A.4, où $R_1 = (R_{dsrd}R_{load})/(R_{dsrd} + R_{load})$. Pendant cette phase, le banc de transistors M montré dans la Figure A.2 est « on », et donc le générateur « step » et modélisé comme un court circuit. En conséquence, C_1 est relié à la masse dans la Figure A.4.

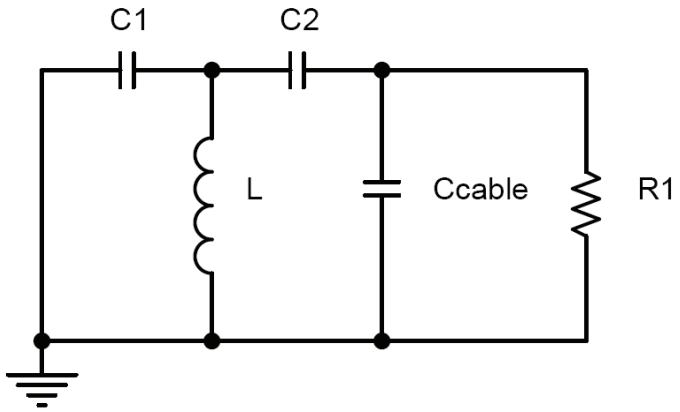

Figure A.4 : Le circuit équivalent du générateur FID pendant que la DSRD est en « forward bias ».

Suivant la méthode de l'Annexe B, nous trouvons les fréquences caractéristiques du circuit de la Figure A.4 :

(A.2) $$\omega_1 = \frac{1}{\sqrt{L\left[C_1 + \left(\frac{1}{C_2} + \frac{1}{C_{cable}}\right)^{-1}\right]}} \approx \frac{1}{\sqrt{LC_1}}$$

(A.3) $$\omega_2 = \frac{1}{\sqrt{L\left(C_1 + C_2\right)}}$$

(A.4) $$\alpha = \frac{1}{R_1\left[C_{cable} + \left(\frac{1}{C_1} + \frac{1}{C_2}\right)^{-1}\right]} \approx \frac{1}{R_1\left(\frac{1}{C_1} + \frac{1}{C_2}\right)^{-1}}$$

Les expressions simplifiées des équations (A.2) et (A.4) sont dues au fait que C_{cable} est petit devant C_1 et C_2, d'après le Tableau A.1. Nous pouvons également calculer le facteur de qualité Q_1 :

$$Q_1 = \sqrt{3}\frac{\omega_1}{\alpha} \approx \sqrt{3}\frac{R_1\left(\frac{1}{C_1}+\frac{1}{C_2}\right)^{-1}}{\sqrt{LC_1}} \tag{A.5}$$

Pour produire des oscillations, il faut que $Q_1 > \sqrt{3}$. Avec les valeurs de C_1, C_2 et L données par le Tableau A.1, l'équation (A.5) donne $R_1 > 6\ \Omega$. Donc il faut d'abord choisir une DSRD avec $R_{dsrd} > 6\ \Omega$. Il faut aussi que la charge $R_{load} > 6\ \Omega$. Sinon, le générateur FID risque de ne plus fonctionner correctement, ce qui est montré par les expériences de la section 3.9.

Les équations (A.2) à (A.5) nous indiquent les rôles des composants. L et C_1 forment un oscillateur et déterminent sa fréquence ω_1. Nous cherchons pour chaque trigger V_{trig} à générer seulement une impulsion, mais toutes les oscillations suivant la première peuvent relancer des « reverse recovery » et produire des impulsions secondaires. Donc il faut amortir les oscillations, sur un temps $1/\alpha$. L'équation (A.4) montre que C_2 facilite l'optimisation du « reverse recovery » de la DSRD car il permet d'ajuster α sans changer ω_1.

Après le « reverse recovery », le mode de la DSRD devient « reverse bias » et le circuit équivalent est alors montré dans la Figure A.5. La DSRD est maintenant modélisée par C_{dsrd}. Nous avons aussi $C_3 = C_{dsrd} + C_{cable}$. Pendant cette phase, le banc de transistors M montré dans la Figure A.2 est « off », et il est modélisé comme un circuit ouvert. Comme la diode D_{dc} est en circuit ouvert aussi, C_1 n'est plus connecté au circuit et donc il est négligé.

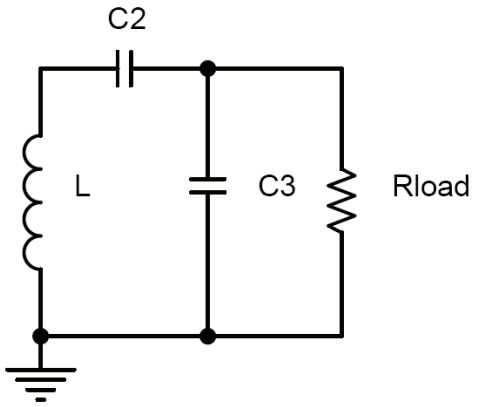

Figure A.5 : Le circuit équivalent du générateur FID pendant que la DSRD est en « reverse bias ».

Pour le circuit équivalent de la Figure A.5, nous avons les fréquences caractéristiques suivantes :

$$\omega_1 = \frac{1}{\sqrt{L\left(\frac{1}{C_2}+\frac{1}{C_3}\right)^{-1}}} \approx \frac{1}{\sqrt{LC_3}} \tag{A.6}$$

(A.7) $$\omega_2 = \frac{1}{\sqrt{LC_2}}$$

(A.8) $$\alpha = \frac{1}{R_{load}C_3}$$

Les équations (A.6) et (A.8) nous donnent le facteur de qualité Q_1 :

(A.9) $$Q_1 \approx \sqrt{3}\frac{R_{load}C_3}{\sqrt{LC_3}}$$

Il faut que $Q_1 > \sqrt{3}$ pour obtenir des oscillations. Le premier demi-cycle de la première oscillation est l'impulsion à haute tension que nous cherchons à générer. Le deuxième demi-cycle, qui est négatif, remet la DSRD en « forward bias ». Les oscillations sont alors arrêtées.

Maintenant nous pouvons dessiner le générateur pour nos besoins. La durée de l'impulsion τ_p est l'inverse de la fréquence de l'oscillation $\omega_1/2\pi$ donnée par l'équation (A.6) :

(A.10) $$\tau_p = 2\pi\sqrt{L\left(C_{dsrd} + C_{cable}\right)}$$

Il faut que la DSRD soit fabriquée avec une petite valeur de C_{dsrd} pour obtenir des impulsions courtes. Les valeurs de L, C_{dsrd} et C_{cable} données sur le Tableau A.1 donnent $\tau_p \approx 9$ ns, ce qui est proche à la valeur expérimentale de 10 ns. De plus, nous trouvons d'après l'équation (A.9) que si $R_{load} < 71\ \Omega$, il n'y aurait pas d'oscillations et le générateur n'aurait plus fonctionné correctement. Selon la Section 3.9, nous avons mesuré que les impulsions fournies par le générateur FID commencent à être déformés entre $R_{load} = 60\ \Omega$ et $R_{load} = 100\ \Omega$.

De plus, nous pouvons calculer l'amplitude de l'impulsion V_p en supposant que l'énergie dissipée pendant la génération de l'impulsion est négligeable devant l'énergie disponible initialement. Toute l'énergie initiale U est stockée dans le condensateur C_1 :

(A.11) $$U = \frac{C_1 V_{dc}^2}{2}$$

Toute cette énergie est dans le condensateur $C_3 = C_{dsrd} + C_{cable}$ quand la DSRD est en « reverse bias ». La conservation d'énergie donne la relation suivante :

(A.12) $$V_p = V_{dc}\sqrt{\frac{C_1}{C_{dsrd} + C_{cable}}}$$

La Figure A.6 montre les mesures de l'amplitude des impulsions V_p en fonction de la tension de l'alimentation continue V_{alim}, pour plusieurs fréquences de répétition (FRI). Il

faut remarquer que toutes les courbes ont la même pente V_p/V_{alim}=17.6; elles sont seulement décalées. Avec les valeurs de C_1 et C_{dsrd} données par le Tableau A.1, l'Equation (A.12) donne un rapport V_p/V_{dc}=22.4, qui est proche à la valeur expérimentale. Le décalage est du au déchargement de C_{dc} entre chaque impulsion. Pour générer une impulsion, C_{dc} n'a plus d'énergie et doit être réalimentée par l'alimentation continue externe. Normalement, $V_{alim}=V_{dc}$. Mais la phase de réalimentation est suivie par un déchargement capacitif qui se passe lentement entre les impulsions. En baissant la FRI, nous permettons une plus longue période de déchargement de C_{dc}, qui donne $V_{dc}<V_{alim}$. Nous voyons cet effet sur la Figure A.6.

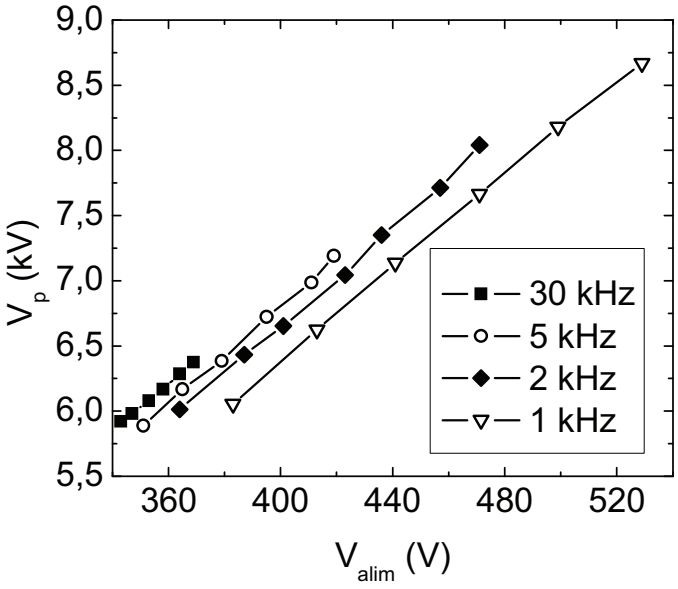

Figure A.6 : Mesures de l'amplitude des impulsions (V_p) en fonction de la tension de l'alimentation continue externe (V_{alim}) pour FRI=1, 2, 5 et 30 kHz.

A.4 Références

[1] I. V. Grekhov, V. M. Efanov, A. F. Kardo-Sysoev et S. V. Shenderei, *Solid-State Electronics* **28** (1985), 597-599.

[2] M. J. Chudobiak, Ph.D. Thesis, Carleton University, 1996.

[3] V. Prokhorenko et A. Boryssenko, *SPIE Proceedings* **4084** (2000) 277-281, *8th International Conference on Ground Penetrating Radar*, Gold Coast, Australia, May 23-26, 2000.

[4] R. T. Howe et C. G. Sodini 1996 *Microelectonics : An Integrated Approach* (Upper Saddle River, NJ: Prentice Hall).

[5] « Pulse and Waveform Generation with Step Recovery Diodes », Application Note 918, Hewlett-Packard.

[6] Communication privée avec Pavel Yarin.

Annexe B

Analyse des circuits passifs par la méthode des temps caractéristiques

B.1 Introduction

Dans cette annexe nous développons une méthode afin d'identifier par inspection les temps caractéristiques d'un circuit passif et de déterminer les conditions d'oscillation. Cette annexe est complémentaire à l'annexe A, où nous utilisons les résultats obtenus ici afin de comprendre le fonctionnement des générateurs d'impulsions. Dans la Section B.2, nous discutons la dynamique temporelle des circuits de deuxième et troisième ordre. Dans les Sections B.3 et B.4, nous définissons des facteurs de qualité pour des circuits de deuxième et troisième ordres. Enfin, dans la Section B.5, nous utilisons les résultats des Sections B.2 à B.4 afin de développer une méthode pour identifier par inspection les temps caractéristiques d'un circuit passif.

B.2 Dynamique temporelle des circuits passifs

Dans cette section la méthode d'« espace des états » [1] est appliquée au traitement rigoureux de la dynamique temporelle des circuits passifs. Tout d'abord, nous considérons le circuit de troisième ordre schématisé sur la Figure B.1. V_{in} est une source de tension idéale et arbitraire. Les tensions des condensateurs C_1 et C_2 sont respectivement V_{C1} et V_{C2}. Le courant de l'inductance L est i_L.

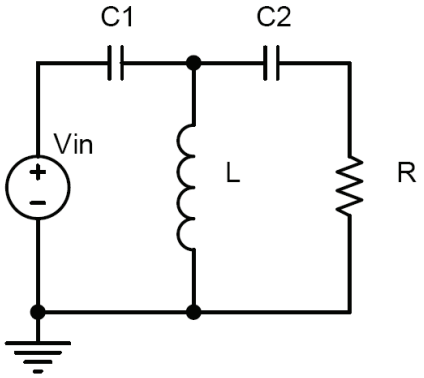

Figure B.1 : Schéma d'un circuit passif de troisième ordre (circuit *d* dans la Figure B.2).

Nous écrivons le système d'équations de la dynamique du circuit sous la forme matricielle:

$$\underbrace{\frac{d}{dt}\begin{bmatrix} V_{C1} \\ V_{C2} \\ I_L \end{bmatrix}}_{X} = \underbrace{\begin{bmatrix} -1/RC_1 & -1/RC_1 & 1/C_1 \\ -1/RC_2 & -1/RC_2 & 0 \\ -1/L & 0 & 0 \end{bmatrix}}_{A} \underbrace{\begin{bmatrix} V_{C1} \\ V_{C2} \\ I_L \end{bmatrix}}_{X} + \underbrace{\begin{bmatrix} 1/RC_1 \\ 1/RC_2 \\ 1/L \end{bmatrix}}_{B} V_{in} \qquad \text{(B.1)}$$

Le système (B.1) montre que « l'équation d'état » prend la forme $dX/dt = AX + BV_{in}$, où $X(t)$ est le « vecteur d'état », et où V_{C1}, V_{C2} et I_L représentent l'état du circuit. La matrice A est la « matrice d'état » et B est un vecteur qui couple la source V_{in} au circuit. Il n'est pas nécessaire de résoudre le système (B.1) pour obtenir des informations sur la présence d'oscillations et leur temps d'amortissement. En effet, celles-ci peuvent être obtenues à partir des temps caractéristiques du circuit, comme nous le détaillons ci-dessous.

Nous pourrions réduire la dynamique du circuit en deux parties. La première est la matrice d'état A, qui donne la solution homogène des équations différentielles du circuit. Physiquement, c'est la réponse naturelle du circuit sans source. La deuxième partie est le terme BV_{in}, qui décrit comment la source influence la dynamique du circuit.

Ici nous traitons uniquement l'équation homogène $dX/dt = AX$. Il faut trouver les valeurs propres de A pour résoudre cette équation. Utilisant l'analyse des systèmes dynamiques linéaires [2], nous appliquons la transformée de Laplace à la partie $dX/dt = AX$ du système d'équations (B.1) afin d'écrire le polynôme caractéristique de A sous forme de déterminant :

$$\det\left(sI - A\right) = \det\left(\begin{bmatrix} s+1/RC_1 & 1/RC_1 & -1/C_1 \\ 1/RC_2 & s+1/RC_2 & 0 \\ 1/L & 0 & s \end{bmatrix}\right) = 0 \qquad \text{(B.2)}$$

Nous l'écrivons également dans sa forme algébrique :

$$s^3 + \frac{1}{R}\left(\frac{1}{C_1} + \frac{1}{C_2}\right)s^2 + \frac{1}{LC_1}s + \frac{1}{LC_1RC_2} = 0 \qquad \text{(B.3)}$$

Les racines de l'équation (B.3) sont les valeurs propres de la matrice A. Appliquant la même technique, nous avons également calculé les polynômes caractéristiques des circuits schématisés sur la Figure B.2, listés sur le Tableau B.1. Tous les circuits considérés sont de deuxième ou de troisième ordre. Ces polynômes sont également les dénominateurs des fonctions de transfert dans le domaine de fréquence [2].

Si nous trouvons les racines des polynômes listés sur le Tableau B.1, nous pouvons décrire exactement la réponse naturelle des circuits de la Figure B.2. Cependant, il est plus pratique de déterminer les types des racines (réelles ou complexes), qui nous révèlent le comportement du circuit, c'est-à-dire s'il est oscillatoire et le degré d'amortissement des oscillations. Il existe une quantité pour nous aider à déterminer ces propriétés : le facteur de qualité Q. Nous parlerons de Q plus en détail dans les Sections B.3 et B.4.

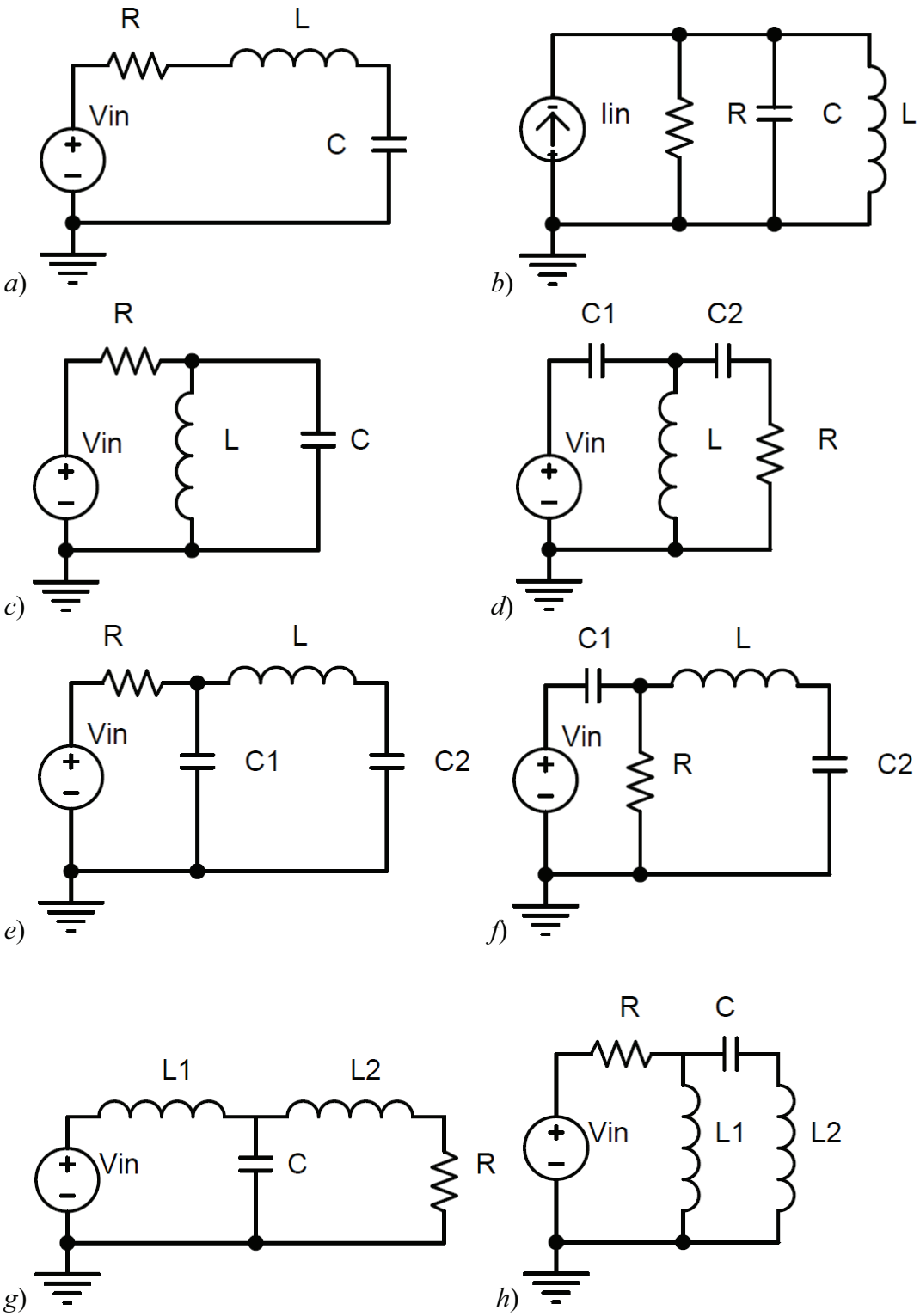

Figure B.2 : Les schémas des circuits des deuxième et troisième ordres dont les polynômes caractéristiques se trouvent sur le Tableau B.1.

Tableau B.1 : Les polynômes caractéristiques et les temps caractéristiques des circuits présentés dans la Figure B.2.

Indice de circuit	Polynôme caractéristique
a	$s^2 + \frac{R}{L}s + \frac{1}{LC} = 0$
b, c	$s^2 + \frac{1}{RC}s + \frac{1}{LC} = 0$
d	$s^3 + \frac{1}{R\left(1/C_1 + 1/C_2\right)^{-1}}s^2 + \frac{1}{LC_1}s + \frac{1}{LC_1RC_2} = 0$
e, f	$s^3 + \frac{1}{RC_1}s^2 + \frac{1}{L\left(1/C_1 + 1/C_2\right)^{-1}}s + \frac{1}{LC_1RC_2} = 0$
g	$s^3 + \frac{R}{L_2}s^2 + \frac{1}{\left(1/L_1 + 1/L_2\right)^{-1}C}s + \frac{R}{L_1L_2C} = 0$
h	$s^3 + \frac{R}{\left(1/L_1 + 1/L_2\right)^{-1}}s^2 + \frac{1}{L_2C}s + \frac{R}{L_1L_2C} = 0$

B.3 Facteur de qualité des circuits de deuxième ordre

Les circuits *a*, *b* et *c* de la Figure B.2 sont du deuxième ordre. Les circuits *a* et *b* sont des circuits RLC classique respectivement série et parallèle. Pour tous ces circuits, le polynôme caractéristique prend la forme :

$$s^2 + 2\alpha s + \omega_0^2 = 0 \tag{B.4}$$

Où $\omega_0 = 1/(LC)^{1/2}$ est la fréquence d'oscillation, ou fréquence résonante, et α est la fréquence caractéristique d'amortissement. Pour le circuit *a*, $\alpha = R/(2L)$, et pour les circuits *b* et *c*, $\alpha = 1/(2RC)$. Sans trouver les racines de l'équation (B.4), nous pouvons déterminer le comportement général du circuit en utilisant la discriminante de deuxième ordre Δ_2 :

$$\Delta_2 = \left(2\alpha\right)^2 - 4\omega_0^2 = 4\left(\alpha^2 - \omega_0^2\right) \tag{B.5}$$

Le signe de Δ_2 nous indique si le circuit allait produire des oscillations :

$\alpha = \omega_0 \rightarrow \Delta_2 = 0 \rightarrow$ racine réelle double $\rightarrow$ critiquement amorti.
$\alpha > \omega_0 \rightarrow \Delta_2 > 0 \rightarrow$ deux racines réelles $\rightarrow$ sur-amorti.
$\alpha < \omega_0 \rightarrow \Delta_2 < 0 \rightarrow$ deux racines complexes $\rightarrow$ sous-amorti.

Sans calculer Δ_2, nous pouvons obtenir la même information sur le circuit utilisant le rapport entre l'énergie stockée et dissipée par cycle, exprimé par le facteur de qualité Q :

$$Q \approx 2\pi \frac{\text{Energie stockée par cycle d'oscillation}}{\text{Energie dissipée par cycle d'oscillation}} \tag{B.6}$$

Dans un circuit avec des éléments de stockage et de dissipation, il faut environs Q cycles pour dissiper toute l'énergie stockée. Une autre façon d'interpréter Q : si le temps de dissipation est plus grand que le temps d'oscillation, il y aura des oscillations qui seront progressivement

réduites à cause de la dissipation. Si le temps d'oscillation est plus grand, l'énergie sera dissipée trop rapidement pour qu'on obtienne des oscillations. En termes des fréquences caractéristiques du circuit *a* de la Figure B.2 et du Tableau B.1 :

$$Q = \frac{\omega_0}{2\alpha} = \frac{L/R}{\sqrt{LC}} = \frac{1}{R}\sqrt{\frac{L}{C}} \tag{B.7}$$

Et pour les circuits *b* et *c*, nous avons:

$$Q = \frac{\omega_0}{2\alpha} = \frac{RC}{\sqrt{LC}} = R\sqrt{\frac{C}{L}} \tag{B.8}$$

Les équations (B.7) et (B.8) montrent que si $Q > 1/2$, le circuit est sous-amorti. Le circuit est critiquement amorti si $Q = 1/2$, et il est sur-amorti si $Q < 1/2$. Nous aimerions maintenant trouver une quantité similaire à Q pour les circuits de troisième ordre.

B.4 Facteurs de qualité des circuits de troisième ordre

Les circuits *d* à *h* de la Figure B.2 sont de troisième ordre avec des polynômes caractéristiques de la forme suivante :

$$s^3 + a_2 s^2 + a_1 s^1 + a_0 = 0 \tag{B.9}$$

Remarquons d'après le Tableau B.1 que a_0, a_1, $a_2 > 0$. La discriminante d'un polynôme de troisième ordre Δ_3 peut être exprimée de la manière suivante [3,4] :

$$\Delta_3 = a_2^2 a_1^2 - 4a_1^3 - 4a_2^3 a_0 - 27a_0^2 + 18a_2 a_1 a_0 = -\left(Y^3 + P^2\right) \tag{B.10}$$

Où :

$$Y = 12\left(3a_1 - a_2^2\right) \tag{B.11}$$

$$P = 54a_2 Y + 2\left(a_2^3 - 27a_0\right) \tag{B.12}$$

Le signe de Δ_3 indique la nature des racines de l'équation (B.9) :

$\Delta_3 = 0 \rightarrow$ racine réelle double ou triple $\rightarrow$ critiquement amorti.
$\Delta_3 > 0 \rightarrow$ trois racines réelles $\rightarrow$ sur-amorti.
$\Delta_3 < 0 \rightarrow$ une racine réelle et deux racines complexes $\rightarrow$ sous-amorti.

Il est nécessaire (mais il n'est pas suffisant) que $Y < 0$ pour que $\Delta_3 > 0$, qui implique :

$$3a_1 < a_2^2 \tag{B.13}$$

Il y a plus de chance que $\Delta_3 > 0$ si $Y < 0$ et si le deuxième terme de P est positif (afin de minimiser P^2 dans l'équation (B.10)), ce qui implique :

$$a_2^3 > 27a_0 \tag{B.14}$$

Par exemple, pour le circuit *d* de la Figure B.2, les équations (B.13) et (B.14) impliquent que les conditions qui favorisent que le circuit *d* soit sur-amorti ($\Delta_3 > 0$) sont :

$$R\left(\frac{1}{C_1}+\frac{1}{C_2}\right)^{-1} < \sqrt{\frac{LC_1}{3}} \tag{B.15}$$

$$R\left(\frac{1}{C_1}+\frac{1}{C_2}\right)^{-1} < \frac{1}{3}\sqrt{\frac{L\left(C_1+C_2\right)}{3}} \tag{B.16}$$

Il suffit que l'inégalité de l'équation (B.13) soit inversée pour assurer que le circuit est sous-amorti ($\Delta_3 < 0$). Les équations (B.15) et (B.16) expriment les relations entre les éléments de stockage et de dissipation du circuit *d*. D'après l'équation (B.6), nous pouvons maintenant définir des facteurs de qualités pour le circuit *d* :

$$Q_1 = \sqrt{3}\,\frac{R\left(\frac{1}{C_1}+\frac{1}{C_2}\right)^{-1}}{\sqrt{LC_1}} \equiv \sqrt{3}\,\frac{\omega_1}{\alpha} \tag{B.17}$$

$$Q_2 = 3\sqrt{3}\,\frac{R\left(\frac{1}{C_1}+\frac{1}{C_2}\right)^{-1}}{\sqrt{L\left(C_1+C_2\right)}} \equiv 3\sqrt{3}\,\frac{\omega_2}{\alpha} \tag{B.18}$$

Les équations (B.17) et (B.18) montrent qu'il y a deux fréquences caractéristiques d'oscillation ω_1 et ω_2, ainsi qu'une fréquence caractéristique de dissipation α.

Ainsi, les conditions $Q_1 < 3^{1/2}$ et $Q_2 < 27^{1/2}$ *favorisent* le fait que le circuit *d* soit sur-amorti. Physiquement, cela signifie que la probabilité qu'un circuit soit sur-amorti augmente si le temps de dissipation est plus court que tous les temps d'oscillation. Par contre, la condition $Q_1 > 3^{1/2}$ *garantie* que le circuit est sous-amorti, car le temps de dissipation est plus grand que le temps d'oscillation. Les temps caractéristiques ainsi que les Q_1 de tous les circuits de la Figure B.2 sont listés dans le Tableau B.2. Pour les circuits de *a* à *h*, qui ont tous une seule résistance, l'oscillateur qui apparaît dans Q_1 est celui dont le temps d'oscillation est le plus court et qui partage un composant avec le dissipateur. Il est en effet logique du point de vue physique que le couplage soit plus fort pour un couple oscillateur-dissipateur qui partage un composant qu'un couple qui n'a aucun composant en commun.

Tableau B.2 : Le facteur de qualité Q_1 pour les circuits de la Figure B.2.

Indice de circuit	Temps caractéristiques	$Q_1/\sqrt{3}$
a	L/R, $(LC)^{1/2}$	$(L/R)/(LC)^{1/2}$
b, c	RC, $(LC)^{1/2}$	$(RC)/(LC)^{1/2}$
d	$R(1/C_1 + 1/C_2)^{-1}$, $(LC_1)^{1/2}$, $(L(C_1 + C_2))^{1/2}$	$(R(1/C_1 + 1/C_2)^{-1})/(LC_1)^{1/2}$
e, f	RC_1, $(LC_2)^{1/2}$, $(L(1/C_1 + 1/C_2)^{-1})^{1/2}$	$(RC_1)/(L(1/C_1 + 1/C_2)^{-1})^{1/2}$
g	L_2/R, $(L_1C)^{1/2}$, $((1/L_1 + 1/L_2)^{-1}C)^{1/2}$	$(L_2/R)/((1/L_1 + 1/L_2)^{-1}C)^{1/2}$
h	$(1/L_1 + 1/L_2)^{-1}/R$, $(L_2C)^{1/2}$, $((L_1 + L_2)C)^{1/2}$	$((1/L_1 + 1/L_2)^{-1}/R)/(L_2C)^{1/2}$

B.5 Méthode pour identifier les temps caractéristiques d'un circuit passif

Les temps caractéristiques α et ω proviennent des ensembles des composants facilement identifiés dans la Figure B.2 comme des amortisseurs (type *RL* ou *RC*) et des oscillateurs (type *LC*). Ces ensembles jouent respectivement des rôles de dissipation et de stockage d'énergie. Il serait pratique de trouver par inspection ces ensembles afin de calculer Q_1 en utilisant l'équation (B.17).

Cependant nous remarquons que les temps L/R et RC_1 ne se trouvent pas dans les équations (B.15)-(B.16). De plus, LC_1 et $L(C_1 + C_2)$ sont des éléments secondaires mais pas LC_2. Ainsi, il semble qu'il existe des « règles de sélection » pour identifier les amortisseurs et les oscillateurs parmi toutes les combinaisons possibles. En regardant la Figure B.2, le Tableau B.1 et le Tableau B.2, il est possible de développer les règles suivantes :

1) *Eteindre les sources*. Afin de trouver les temps caractéristiques, il faut étudier la réponse naturelle du circuit. Pour mettre l'équation d'état générale $dX/dt = AX + BV_{in}$ ou $dX/dt = AX + BI_{in}$ sous la forme homogène $dX/dt = AX$ qui donne la réponse naturelle du circuit, il faut éteindre les sources.
2) *Les circuits équivalents « sans sources » ont les même temps caractéristiques, mais ils n'ont pas forcement les mêmes réponses aux excitations.* Par exemple, les circuits *c* et *d* de la Figure B.2 sont équivalents si nous mettons V_{in}=0 pour le circuit *c* et I_{in}=0 pour circuit le *d*. Les circuits *e* et *f* sont également équivalents sans sources. Mais si le circuit est très dissipatif, tel qu'il n'y a pas d'oscillations, ce serait les éléments trouvés dans le vecteur *B* qui contrôleraient la réponse du circuit soumis aux excitations V_{in} ou I_{in}.
3) *On trouve les oscillateurs lorsque les résistances sont mises en circuit ouvert ou en court circuit.* Sans mécanismes dissipatifs, les éléments *LC* auraient conservé leurs énergies totales. Cette situation aurait lieu si aucune énergie n'était dissipée par les résistances, c'est-à-dire si le courant ou la tension étaient nuls. Par exemple, pour le circuit *d* de la Figure B.2, la résistance *R* en circuit ouvert nous donne l'élément LC_1 et en court circuit nous donne l'élément $L(C_1 + C_2)$.
4) *Chaque résistance est associée à un seul temps caractéristique de dissipation.*
5) *En mettant les condensateurs en court circuit, nous trouvons des dissipateurs de type RL.* Comme l'énergie stockée dans un condensateur est égale à $CV_C^2/2$, si $V_C = 0$ il n'échange aucune énergie avec les résistances, et il ne participe donc pas à la dissipation. Par exemple, pour le circuit *g* de la Figure B.2, nous trouvons un circuit composé par RL_2 si $V_C = 0$.
6) *En mettant les inductances en circuit ouvert, nous trouvons des dissipateurs de type RC.* Comme l'énergie stockée dans une inductance est égale à $LI_L^2/2$, si $I_L = 0$ elle n'échange aucune énergie avec les résistances, et elle ne participe pas à la dissipation. Par exemple, pour le circuit *d* de la Figure B.2, nous trouvons un circuit composé par $R(1/C_1 + 1/C_2)^{-1}$ si $I_L = 0$.
7) *Le facteur de qualité Q_1 est calculé en utilisant l'équation* (B.17)*, où les fréquences caractéristiques correspondant aux oscillateurs et aux dissipateurs obtenus par les règles au-dessus.*

Les conseils ci-dessus sont strictement valables pour les circuits de troisième ordre qui contiennent une seule résistance. Cette méthode de détermination des temps caractéristiques des réseaux passifs ressemble à la méthode « Open Circuit Time Constant » qui est habituellement utilisée pour estimer le passe bande des amplificateurs [5].

B.6 Références

[1] A. Agarwal et J. H. Lang 2005 *Foundations of Analog and Digital Electronic Circuits* (San Mateo, CA: Elsevier).
[2] G. Birkhoff et S. MacLane 1996, *A Survey of Modern Algebra* (New York: Macmillan).
[3] R. S. Irving 2004, *Integers, Polynomials, and Rings* (New York: Springer-Verlag).
[4] E. W. Weisstein, MathWorld, http://mathworld.wolfram.com/CubicFormula.html.
[5] M. T. Thompson 2006, *Intuitive Analog Circuit Design* (Oxford : Elsevier).

Annexe C

Analyse des sources d'erreur dans les mesures par spectroscopie d'émission

Dans cette annexe nous déterminons par spectroscopie d'émission l'erreur associée aux variations de températures dans les mesures des espèces moléculaires excitées. Nous discutons surtout les résultats expérimentaux de la Section 4.5 concernant le régime D.

Dans la Section 4.5, les mesures des populations des espèces excitées résolues en temps ont été réalisées à partir des intensités d'émission absolue à certaines longueurs d'onde. Pour l'espèce atomique excitée O(3p ^{5}P), cette méthode est précise. Cependant, pour les molécules, l'intensité d'émission à une raie ne représente que la population d'un niveau rotationnel et vibrationnel particulier. Il faut intégrer les populations de tous les niveaux rotationnels et vibrationnels pour arriver à la population totale d'une espèce moléculaire excitée. Afin de prendre en compte tous ces niveaux, nous utilisons le logiciel SPECAIR pour calculer des spectres modélisés, à partir des températures du gaz (T_g), rotationnelle (T_r), vibrationnelle (T_v) et électronique (T_{elec}). Il faut également spécifier la longueur du milieu émissif (l_m) et la fonction d'appareil. Avec ces informations, SPECAIR calcule des spectres numériques en intensité absolue, ainsi que les populations des espèces divisées par leur dégénérescence de l'état quantique, g. Ensuite, les spectres calculés sont comparés aux spectres mesurés, afin d'associer les populations des espèces excitées avec les spectres.

En traitant les données pour arriver aux populations des espèces résolues en temps, comme dans la Figure 4.8, nous aurions idéalement dû comparer le spectre mesuré avec le spectre calculé à chaque temps. Ce traitement est assez lourd, vu le nombre des points de données. Nous prenons donc seulement le profil en temps de l'intensité mesurée à une raie. Sur ce profil, nous appliquons une normalisation par la population déterminée par comparaison mesure/calcul, mais uniquement à un instant donné. L'erreur provenant de cette simplification est la variation d'intensité de la raie induite par les variations des températures de la décharge. Dans cette annexe, nous cherchons à déterminer les variations des températures de la décharge à partir des spectres mesurés (correspondants aux données dans la Figure 4.8), qui ont été obtenues pour une décharge dans le régime D.

Avant de comparer les spectres mesurés et calculés, il faut faire quelques remarques concernant les paramètres que nous avons utilisés dans SPECAIR. D'abord, l'intensité d'émission est donnée après la convolution du spectre avec une fonction d'appareil triangulaire de largeur à mi-hauteur de 0,35 nm (d'après la mesure présentée dans la Figure 3.11). L'intensité d'émission est alors donnée avec les unités mW/cm^2/sr au lieu de mW/cm^2 /nm/sr, les unités de l'intensité d'émission avant convolution avec la fonction d'appareil. De plus, nous avons utilisé une longueur du milieu émissif de l_m = 2 mm, d'après la Section 4.6, où nous avons trouvés que le rayon de la décharge est 1 mm au maximum d'intensité d'émission. La variation de l'intensité d'émission, et donc la population de l'espèce, est proportionnelle à la variation du rayon de la décharge, qui varie de 0,88 mm à 1,25 mm. Tous les spectres calculés dans cette annexe ont été calculés avec l_m = 2 mm, et sa variation est prise en compte par les barres d'erreurs dans la Figure 4.8.

Nous traitons maintenant le cas de la tête de bande pour la transition N_2 (C-B) 0-0, à partir duquel nous pouvons déduire la population de l'espèce $N_2(C)$. La Figure C.1 présente le spectre mesuré au temps du maximum d'intensité d'émission, ainsi qu'un spectre calculé avec $T_g=T_r=1100$ K, $T_v=2950$ K et $T_{elec}=7070$ K. Nous remarquons que T_g est bonne en accord avec les mesures de la température du gaz du régime D de la Section 4.9. Nous utilisons les bandes N_2 (C-B) 1-2 et 0-1 pour déterminer T_v. Ensuite nous choisissions T_{elec} pour avoir un bon accord avec l'intensité à la tête de bande N_2 (C-B) 0-0. Il y a un léger désaccord avec les bandes 1-2 et 0-1, qui est probablement dû aux erreurs minimes dans la calibration (voir la Section 3.4). Pour ces conditions, SPECAIR calcule que la population de $N_2(C)$ à l'instant du maximum d'intensité d'émission est $n_{max}=6{,}5\times10^{11}$ cm^{-3}, comme présenté dans le Tableau C.1 et également dans la Figure 4.8.

Avant de normaliser toutes les intensités d'émission à la tête de bande N_2 (C-B) 0-0 par n_{max} afin de déterminer le profil en temps de $N_2(C)$, il faut trouver la variation de l'intensité de cette bande avec la température vibrationnelle. Le Tableau C.2 présente la gamme de T_v trouvée pour chaque espèce moléculaire excitée étudiée dans cette thèse, où les températures ont été trouvées par comparaisons des spectres mesurés avec des spectres calculés. Pour $N_2(C)$, T_v varie de 1300 K à 3400 K. Le graphe de gauche sur la Figure C.2 montre que l'intensité d'émission à la tête de bande N_2 (C-B) 0-0 à $T_v=1300$ K est alors 1,5 fois supérieure à celle obtenue à $T_v=3400$ K. Cette diminution pour les températures élevées est due au fait que la fraction molaire de $N_2(C)$ dans l'état fondamental v=0 diminue en fonction de T_v, ce qu'on observe à la Figure D.1. D'après la Figure 4.8, la population de $N_2(C)$ varie de sept ordres de grandeur, et donc une erreur relative de $\varepsilon_v=1{,}5$ est mineure. Nous avons quand même pris en compte cette variation par les barres d'erreur dans la Figure 4.8.

Il faut également trouver la variation de l'intensité de cette bande avec la température rotationnelle. Pour $N_2(C)$, nous avons trouvés que T_r varie de 1000 K à 1200 K. Le graphe à droite sur la Figure C.2 montre que l'intensité d'émission à la tête de bande N_2 (C-B) 0-0 à $T_r=1000$ K est alors 1,1 fois supérieure à celle obtenue à $T_r=1200$ K. Cette diminution pour les températures élevées est due au fait que la fraction molaire de $N_2(C)$ des états rotationnels qui forme la tête de la bande 0-0 diminue en fonction de T_r. D'après la Figure 4.8, la population de $N_2(C)$ varie de sept ordres de grandeur, et donc une erreur relative de $\varepsilon_r=1{,}1$ est négligeable.

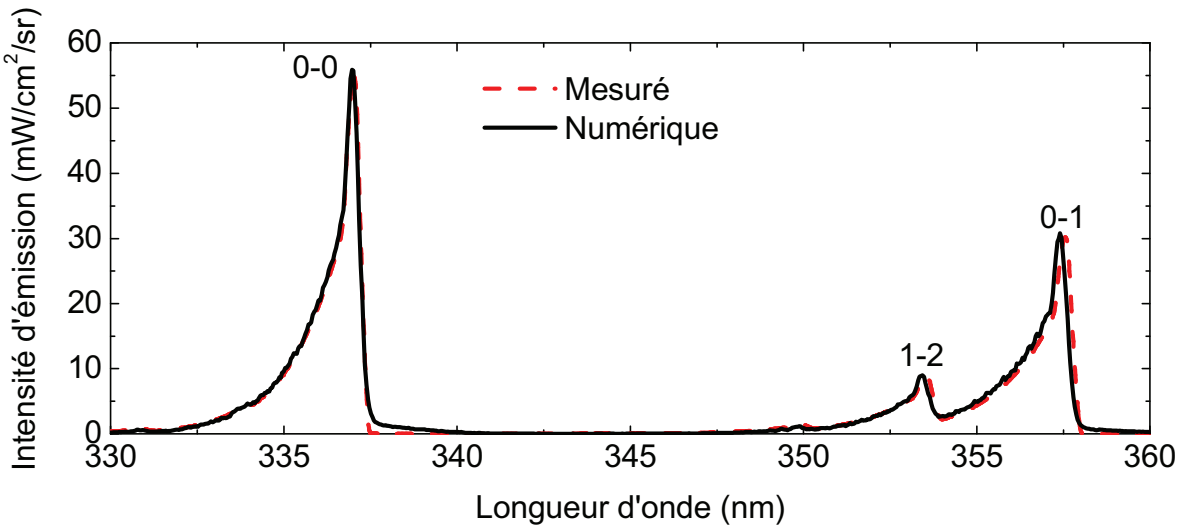

Figure C.1 : Spectre mesuré à l'instant du maximum d'intensité d'émission de la transition N_2(C-B) 0-0, et le spectre calculé par SPECAIR avec $T_g=T_r=1100$ K, $T_v=2950$ K, $T_{elec}=7070$ K et $l_m=2$ mm.

Tableau C.1 : Paramètres de SPECAIR utilisés pour calculer les spectres correspondants à l'instant du maximum d'intensité d'émission pour des espèces excités moléculaires. La dégénérescence de l'état quantique est donnée par *g*, et SPECAIR fournit la population normalisée par *g*, n_{max}/g. Les étoiles (*) indique que pour NO(A), la population ne correspond pas au maximum, mais 8 ns après.

Espèce	T_g (K)	T_r (K)	T_v (K)	T_{elec} (K)	*g*	n_{max}/g (cm^{-3})	n_{max} (cm^{-3})
$N_2(C)$	1100	1100	2950	7650	6	$4{,}3\times10^{11}$	$2{,}6\times10^{12}$
$N_2(B)$	1000	1000	8000	5725	6	$4{,}05\times10^{12}$	$2{,}4\times10^{13}$
NO(A)*	1100*	1900*	6000*	3340*	2	$6{,}36\times10^{9}$ (*)	$1{,}3\times10^{10}$ (*)
$N_2^+(B)$	1000	1000	1000	1790	2	$3{,}94\times10^{9}$	$7{,}9\times10^{9}$

Tableau C.2 : Valeurs minimales et maximales mesurées des températures vibrationnelles des espèces excitées.

Espèce	Valeur minimale de T_v (K)	Valeur maximale de T_v (K)	Erreur relative au maximum de l'intensité d'émission (ε_v)
$N_2(C)$	1300	3400	1,5
$N_2(B)$	2000	12000	2,7
NO(A)*	1500	6000	2,4
$N_2^+(B)$	1000	2000	1,2

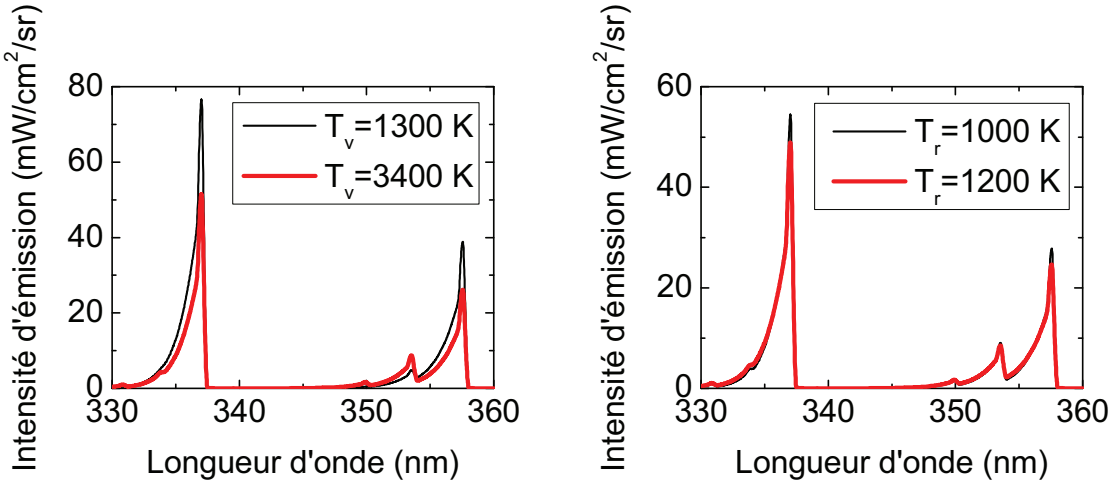

Figure C.2 : Spectres calculés de la transition N_2 (C-B), calculés par SPECAIR pour T_r=1100 K fixée (à gauche) et pour T_v=3400 K fixée (à droite). T_g=1100 K et T_{elec}=7070 K sont fixée pour les deux graphes, avec l_m=2 mm.

Le maximum de population des autres espèces moléculaires excitées et leur gammes de températures vibrationnelles et sont listés sur les Tableau C.1 et Tableau C.2, respectivement. Les spectres avec les températures vibrationnelles maximales sont présentés dans les Figure C.3 à Figure C.5, ainsi que les spectres numériques correspondants. Remarquons sur le Tableau C.2 que parmi toutes les espèces, l'erreur relative causée par la variation en T_v ne dépasse pas 3, ce qui est petit par rapport aux ordres de grandeur des variations en temps des populations (d'après la Figure 4.8). De plus, toutes les espèces possèdent une température rotationnelle près de celle de $N_2(C)$, sauf NO(A) qui varie de 1400 à 1900 K en T_r, pour une erreur relative de $\varepsilon_r = 1{,}15$. Enfin, il faut prendre en compte les variations en intensité d'émission à cause de la variation en température du gaz. Il était mentionné précédemment que pour $N_2(C)$, T_r varie de 1000 K à 1200 K. Dans cette thèse, nous avons fait la supposition

que T_r=T_g, grâce aux transferts rapides d'énergie entre les motions cinétique et rotationnelle. L'erreur relative de ε_g = 1,2 est alors proportionnelle à la variation de T_g.

En conclusion, nous avons déterminés les erreurs relatives causées par les variations en T_v, T_r et T_g. Elles ne sont pas significatives en comparaison aux variations des populations des espèces (montrés sur la Figure 4.8). Nous pouvons maintenant définir l'erreur relative totale ε_T qui est le somme des erreurs relatives causées par T_v, T_r et T_g :

$$\varepsilon_T = \varepsilon_v + \varepsilon_r + \varepsilon_g \tag{C.1}$$

Dans la Figure 4.8, les barres d'erreur des populations des espèces sont calculées et notées par ε_T.

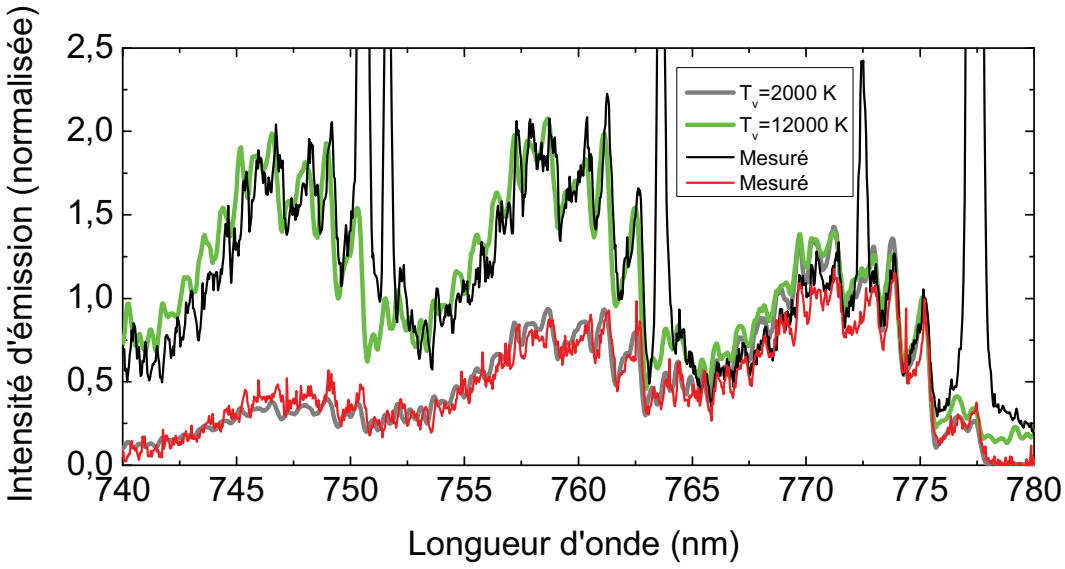

Figure C.3 : Spectres mesurés de la transition N_2(B-A) avec le minimum et le maximum de la température vibrationnelle, et les spectres correspondants calculés par SPECAIR avec T_g=T_r=1000 K et l_m=2 mm.

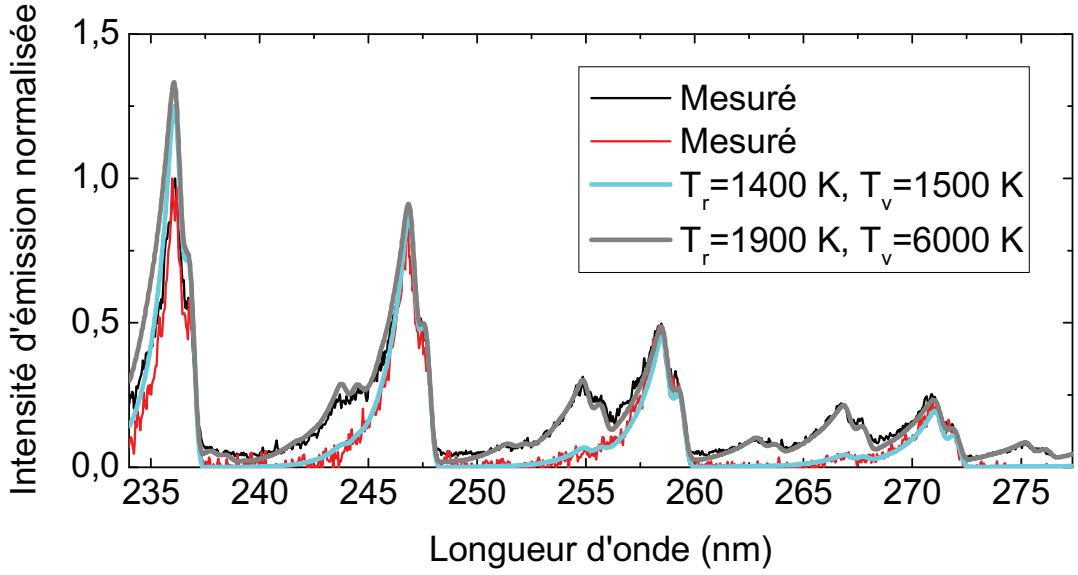

Figure C.4 : Spectres mesurés de la transition NO (A-X) avec le minimum et le maximum de la température vibrationnelle, et les spectres correspondants calculés par SPECAIR avec l_m=2 mm.

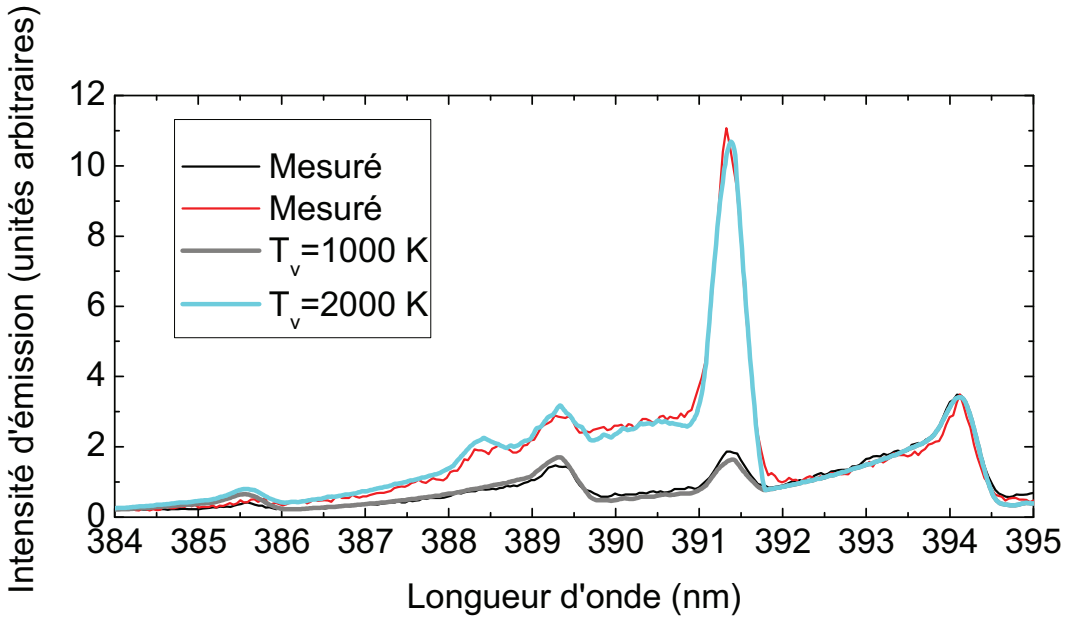

Figure C.5 : Spectres mesurés de la transition N_2^+ (B-X) avec le minimum et le maximum de la température vibrationnelle, et les spectres correspondants calculés par SPECAIR avec T_g=T_r=1000 K et l_m=2 mm.

Appendix D

Self-absorption

D.1. Introduction

This appendix on optical self-absorption supplements Section 4.9, where we discussed how gas temperatures measured from the emission of the N_2 (C-B) (0,0) band could be affected by self-absorption. In Section D.2 we present the fundamentals of self-absorption, and in Section D.3 we discuss the effect of vibrational temperature.

D.2. Fundamentals of self-absorption

Self-absorption reduces the N_2 (C-B) (0,0) band-head intensity relative to the rest of the band, and such distortion of measured spectra can result in false rotational temperature fits to simulated spectra calculated by SPECAIR. One way to determine the degree of self-absorption is to compare the band-head intensities of the strongly self-absorbed N_2 (C-B) (0,0) band, $I_{(0,0)}$, and the less self-absorbed N_2 (C-B) (0,1) band, $I_{(0,1)}$.

We can show how $I_{(0,1)}/I_{(0,0)}$ depends on temperature from the fundamental principles of radiative transfer. Let $n(e,\mathrm{v},J)$ be the number density of a rovibronic state with electronic level e, vibrational level v, and rotational level J. The upper state u of a transition has levels e', v′, and J'. The lower state l of a transition has levels e'', v″, and J''. For light of intensity $I_{(u,l)}(x=0)$ normally incident upon a slab of gas of length l_a at $x=0$, the intensity $I_{(u,l)}(x=l_a)$ exiting the slab at $x= l_a$ is:

$$I_{(u,l)}\left(x=l_a\right)=\int_0^{l_a}\varepsilon_{ul}\exp\left[-\alpha_{lu}\left(l_a-x\right)\right]dx=\frac{\varepsilon_{ul}}{\alpha_{lu}}\left(1-\exp\left(-\alpha_{lu}l_a\right)\right) \tag{D.1}$$

For simplicity, we have assumed that the net absorption coefficient α_{lu} and the spectral radiance ε_{ul} are constant throughout the slab, where the spectral radiance is:

$$\varepsilon_{ul}=n\left(e',\mathrm{v}',J'\right)A_{ul}E_{ul}\phi_{ul} \tag{D.2}$$

A_{ul} is the Einstein A coefficient for spontaneous emission for the u-l transition, E_{ul} is its energy, and ϕ_{ul} is the spectral width. B_{lu} is the Einstein B coefficient for absorption for the l-u transition, and the net absorption coefficient taking to account both absorption and stimulated emission is:

$$\alpha_{lu}=\left[n\left(e'',\mathrm{v}'',J''\right)-n\left(e',\mathrm{v}',J'\right)\right]B_{lu}E_{ul}\phi_{ul} \tag{D.3}$$

Now we formulate the band-head intensity ratio $I_{(0,1)}/I_{(0,0)}$ for the N_2 (C-B) transition. For the (0,1) transition, the upper state is written as $n(e=C,\mathrm{v}=0,J=J'_{01})$ to indicate the

$N_2(C)_{v=0}$ state at the rotational level of interest at the (0,1) band head, J'_{01}. The Einstein A coefficient (without the Hönl-London factor) for this transition is $A_{01}=8.905\times10^6$ s^{-1}, and its energy is $E_{01}=3.47$ eV [D.1]. The emission from the (0,0) transition is from the upper state population $n(e=C,v=0,J=J'_{00})$, the $N_2(C)_{v=0}$ state at the rotational level of interest at the (0,0) band head, J'_{00}. For this transition, $A_{00}=1.337\times10^7$ s^{-1} (without the Hönl-London factor) and $E_{00}=3.69$ eV [D.1]. The absorption coefficient involves the lower state population $n(e=B,v=0,J=J''_{00})$, the $N_2(B)_{v=0}$ state at the rotational level of interest at the (0,0) band head, J''_{00}, and the Einstein B coefficient for the transition back up to J'_{00} state, B_{00}. Now we can use Equation (D.1) to write the intensity ratio of interest:

$$\frac{I_{(0,1)}}{I_{(0,0)}}=\frac{A_{01}E_{01}}{A_{00}E_{00}}\frac{\alpha_{00}}{\alpha_{01}}\frac{1-\exp\left(-\alpha_{01}l_a\right)}{1-\exp\left(-\alpha_{00}l_a\right)} \tag{D.4}$$

The band head is actually the superposition of a number of individual rotational lines. The rigorous treatment of the band head intensity must also account for the convolution of these lines with the spectral width ϕ_{ul} as well as the fact that the P branch "wraps" around the band head wavelength. We will not perform such a detailed calculation here. Instead, we will use the intensity ratio of two individual lines given by Equation (D.4) to provide insight when analyzing modeled spectra.

For the given absorption length l_a, the temperature dependence of Equation (D.4) is dictated entirely by the number densities of the upper and lower states of a transition. The number density of a state is $n(e,v,J)$ can be written as a product of its rotational, vibrational, and electronic state populations:

$$n\left(e,\mathrm{v},J\right)=n_g\frac{g_{elec}\exp\left(-\frac{E_{elec}}{k_BT_{elec}}\right)}{Q_{elec}}\frac{g_{rot}\exp\left(-\frac{E_{rot}}{k_BT_r}\right)}{Q_{rot}}\frac{g_{vib}\exp\left(-\frac{E_{vib}}{k_BT_v}\right)}{Q_{vib}} \tag{D.5}$$

Where n_g is the gas density and k_B is Boltzmann's constant. E_{elec}, E_{rot}, and E_{vib} are the energies of levels e, J, and v, respectively. Likewise, Q_{elec}, Q_{rot}, and Q_{vib} are their partition functions, and g_{elec}, g_{rot}, and g_{vib} are their degeneracies. The degeneracy of the electronic state is $g_{elec}=\Lambda(2S+1)$, where S is the molecular spin quantum number ($\Lambda=1$ if the molecular angular momentum quantum number is zero, and $\Lambda=2$ otherwise). In addition, $g_{vib}=1$ and $g_{rot}=2J+1$. The general expression for the partition function over i states is:

$$Q=\sum_i g_i\exp\left(-\frac{E_i}{k_BT}\right) \tag{D.6}$$

The summations comprising Q_{rot} and Q_{vib} have simple expressions:

$$Q_{rot}=\frac{1}{\sigma}\frac{T_r}{\Theta_r} \tag{D.7}$$

Where σ=2 is the symmetry factor for homonuclear molecules. Θ_r is the characteristic temperature for rotation:

$$\Theta_r \equiv \frac{h^2}{8\pi^2 Mk} \tag{D.8}$$

Where $M=\mu R_0^2$ is the moment of inertia. μ is the reduced mass, and R_0 is the bond length. Even though we are concerned with the excited electronic states, we use Θ_r=2.9 K for N_2 in the ground state [D.2]. This is a reasonable approximation because Θ_r does not change significantly for excited states. The vibrational partition function is:

$$Q_{vib} = \frac{1}{1-\exp\left(-\frac{\Theta_v}{T_v}\right)} \tag{D.9}$$

Where Θ_v is the characteristic temperature for vibration in terms of the harmonic oscillator frequency ν_{vib}:

$$\Theta_v \equiv \frac{h\nu_{vib}}{k_B} \tag{D.10}$$

Θ_v=3390 K for N_2 [3.2]. Unfortunately, there is not a simple expression for the electronic partition function because of the irregularity of the degeneracy and energy levels. Instead, we approximate Q_{elec} in the form given by Equation (D.6) by considering as many of the electronic levels as possible whose energies are known. These states, their degeneracies, and their characteristic temperatures for electronic excitation $\Theta_{elec}=E_{elec}/k_B$ are summarized in Table D.1.

The rotational and vibrational energies are:

$$E_{rot} = \frac{\hbar^2}{2M} J\left(J+1\right) = k_B \Theta_r J\left(J+1\right) \tag{D.11}$$

$$E_{vib} = \left(\mathrm{v}+\frac{1}{2}\right) h\nu_{vib} = \left(\mathrm{v}+\frac{1}{2}\right) \Theta_v k_B \tag{D.12}$$

Using Equations (D.6) to (D.12), we rewrite Equation (D.5) as:

$$n\left(e,\mathrm{v},J\right) = n_0 F_{rot} f_{vib} f_{elec} \tag{D.13}$$

Where n_0=2.69×10^{19} cm^{-3} is the density of air in standard conditions. f_{elec} and f_{vib} are the population fractions for the electronic level e and vibrational level v, respectively:

$$f_{elec}\left(e,T_{elec}\right)=\frac{2\left(2S_e+1\right)\exp\left(-\frac{\Theta_{elec,e}}{T_{elec}}\right)}{\sum_{i=X^1\Sigma_u^+}^{c'_4{}^1\Sigma_u^+} g_{elec,i}\exp\left(-\frac{\Theta_{elec,i}}{T_{elec}}\right)} \tag{D.14}$$

$$f_{vib}\left(\mathrm{v},T_v\right)=\left(1-\exp\left(-\frac{\Theta_v}{T_v}\right)\right)\exp\left(-\frac{\Theta_v}{T_v}\mathrm{v}\right) \tag{D.15}$$

Table D.1: The energies, degeneracies, and characteristic temperatures for electronic excitation for the electronic states of N_2 included in the approximation for the electronic partition function of N_2. Taken from [D.3] and [D.4]. Data from the former are in parentheses and are used whenever available because it is a more recent publication.

Electronic state of N_2	E_{elec} (in eV)	$g_{elec}=\Lambda(2S+1)$	Θ_{elec} (in K)
$X^1\Sigma_g^+$	0	1	0
$A^3\Sigma_u^+$	6.17 (6.22)	3	72100
$B^3\Pi_g$	7.35 (7.39)	6	85700
$W^3\Delta_u$	7.36	6	85300
$B'^3\Sigma_u^-$	8.16	3	94600
$a'^1\Sigma_g^-$	8.4 (8.57)	1	99400
$a^1\Pi_g$	8.55	2	99130
$w^1\Delta_u$	8.89	3	103000
$C^3\Pi_u$	11.03 (11.05)	6	128000
$E^3\Sigma_g^+$	11.88	3	138000
$a''^1\Sigma_g^+$	12.25	1	142000
$b^1\Pi_u$	12.5	2	145000
$b'^1\Sigma_u^+$	12.85	1	149000
$D^3\Sigma_u^+$	12.85	3	149000
$c'_4{}^1\Sigma_u^+$	12.94	1	150000

F_{rot} is the product of the rotational population fraction f_{rot} and the scaling factor of the gas density from standard conditions as a function of the gas temperature, where we have assumed $T_g=T_r$, as dictated by the ideal gas law:

$$F_{rot}\left(J,T_r\right)=\left(\frac{300\text{ K}}{T_r}\right)f_{rot}=\left(\frac{300\text{ K}}{T_r}\right)\left\{\left(2J+1\right)\frac{2\Theta_r}{T_r}\exp\left(-J\left(J+1\right)\frac{\Theta_r}{T_r}\right)\right\} \quad \text{(D.16)}$$

Since we are concerned with the band-head intensities, we must choose the appropriate $J = J_{head}$ which is the rotational level for the upper state of the N_2(C-B) (0,0) transition. For a rovibronic transition for given *e* and v levels, the Hönl-London factor shown in Equation 4.1 does not vary much with *J* and therefore neither does the Einstein A coefficient. It follows that the intensities of the rotational lines within a given band depend mostly on the population of the level *J*. Thus the band-head wavelength must correspond to the *J* at which the population fraction is a maximum, $J = J_{head}$. Given the rotational constants $\beta_u = 1.8153$ cm^{-1} and $\beta_l = 1.62872$ cm^{-1} for the $N_2(C)_{v=0}$ and $N_2(B)_{v=0}$ states [D.5], respectively, it can be shown that J_{head} is:

$$J_{head}=\frac{\beta_l+\beta_u}{2\left(\beta_u-\beta_l\right)} \quad \text{(D.17)}$$

Equation (D.17) gives $J_{head} \approx 9$ for both the (0,0) and (0,1) transitions.

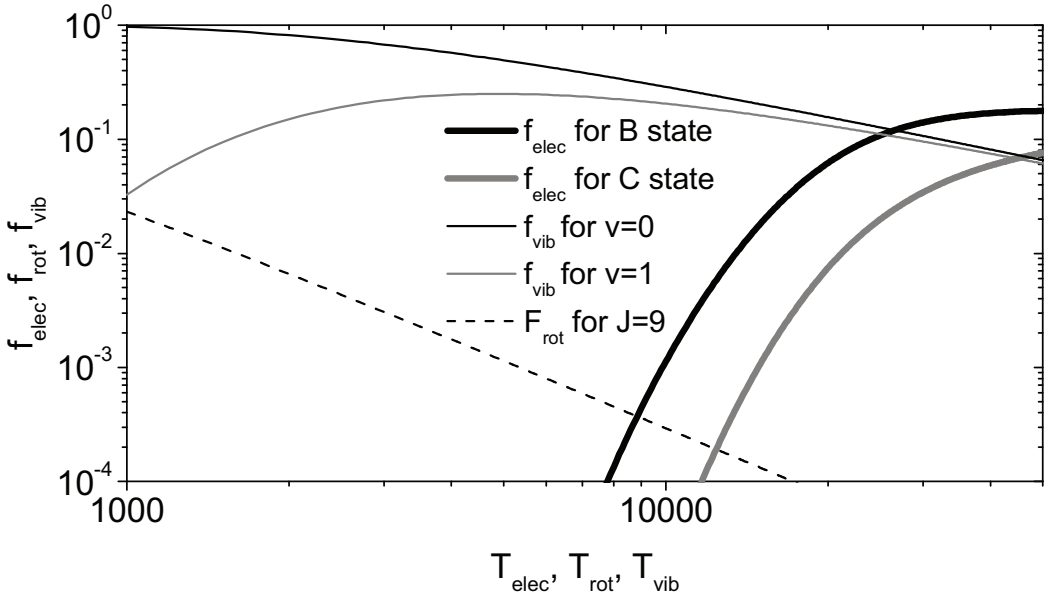

Figure D.1: The population fraction functions f_{elec}, f_{vib}, and f_{rot} as a function of T_{elec}, T_r, and T_v, respectively, calculated using Equations (D.14)-(D.16).

Finally, we can evaluate Equations (D.14)-(D.16) for the state of interest, where *e* is the $B^3\Pi_g$ level, v=0, and $J = J_{head}$. Figure D.1 shows the resulting $f_{elec}(B^3\Pi_g,T_{elec})$, $f_{vib}(0,T_v)$, and $f_{rot}(J_{head},T_r)$ as a function of their respective temperatures, in addition to several other population fraction functions. First, it shows that the $B^3\Pi_g$ level population fraction climbs from 0.0011 at 10,000 K to 0.177 at 50,000 K, the range of electronic temperatures considered in Figures 4.17 and 4.18. Thus, for fixed T_v and T_r, the increase

in T_{elec} across this range results in sharp rises in the populations of the lower states for absorption, $n(e=B,v=0,J=J_{head})$ and $n(e=B,v=1,J=J_{head})$, which serve to increase the net absorption coefficient. The resulting increase in absorption of the (0,0) and (0,1) band heads is shown in Figure 4.18. In addition, Figure D.1 shows that F_{rot} for $J = J_{head}$ decreases from 0.023 at T_r=1000 K to 8×10^{-4} at T_r=6000 K, the range of T_r considered. Increasing T_r across this range serves to decrease $n(e=B,v=0,J=J_{head})$ and $n(e=B,v=1,J=J_{head})$, resulting in the "dampening" of the plots of $I_{(0,1)}/I_{(0,0)}$ with increasing T_r that is shown in Figure 4.17. It is important to observe that this dampening is due to both the depopulation of the J_{head} state as well the decrease in gas density, since $n(e,v,J)$ depends on F_{rot} and not just on f_{rot}.

D.3. Influence of vibrational temperature on self-absorption

Another important consideration in evaluating $I_{(0,1)}/I_{(0,0)}$ is the vibrational temperature. Figure D.1 shows that f_{vib} for v=0 decreases from 0.97 at T_v=1000 K to 0.49 at T_v=5000 K, whereas f_{vib} for v=1 increases from 0.03 at T_v=1000 K to 0.25 at T_v=5000 K. The much larger proportional change in f_{vib} for v=1 implies that the (0,1) band head's degree of absorption varies significantly more than that of the (0,0) band head over the 1000-5000 K temperature range. It follows that variations in $I_{(0,1)}/I_{(0,0)}$ as a function T_v are largely due to the absorption of the (0,1) band head and not that of the (0,0) band head. Figure D.2 shows $I_{(0,1)}/I_{(0,0)}$ as a function of T_v for several values of T_e, with T_r=2700 K held constant.

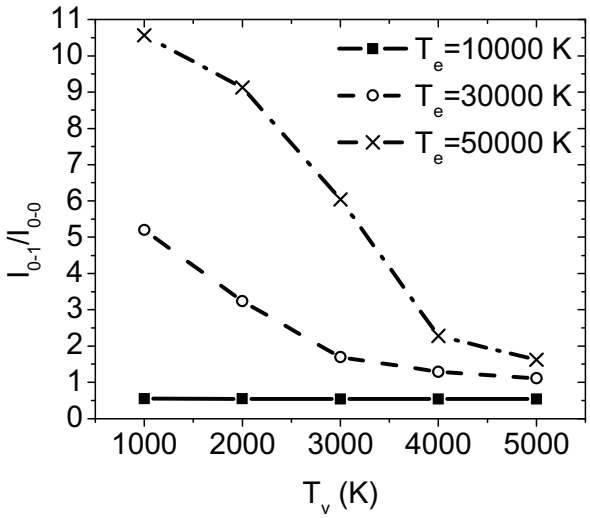

Figure D.2: Ratios of intensities between the N_2 (C-B) (0,0) and (0,1) band heads of modeled N_2 spectra as a function of T_v for several T_{elec}, calculated using SPECAIR. T_r=T_g=2700 K. The absorption length is l_a=1 mm.

Figure D.3 displays the I_{thick}/I_{thin} for the (0,0) and (0,1) band heads that correspond to the data points in Figure D.2. These two figures demonstrate that the decrease of $I_{(0,1)}/I_{(0,0)}$ with increasing T_v is in fact due to increased absorption of the (0,1) band head. I_{thick}/I_{thin} for the (0,0) band head remains relatively unaffected by T_v. This is in contrast to

Figure 4.18, in which I_{thick}/I_{thin} for (0,0) and (0,1) varied in a coordinated fashion, such that changes in $I_{(0,1)}/I_{(0,0)}$ always at least partially reflected changes in the degree of self-absorption of the (0,0) band head.

Thus, the usage of $I_{(0,1)}/I_{(0,0)}$ as an indicator of self-absorption of the (0,0) band head is hampered by the fact that at high T_v, the attenuation of the (0,1) band head due to self-absorption yields a low value for $I_{(0,1)}/I_{(0,0)}$, masking the significant absorption of the (0,0) band head.

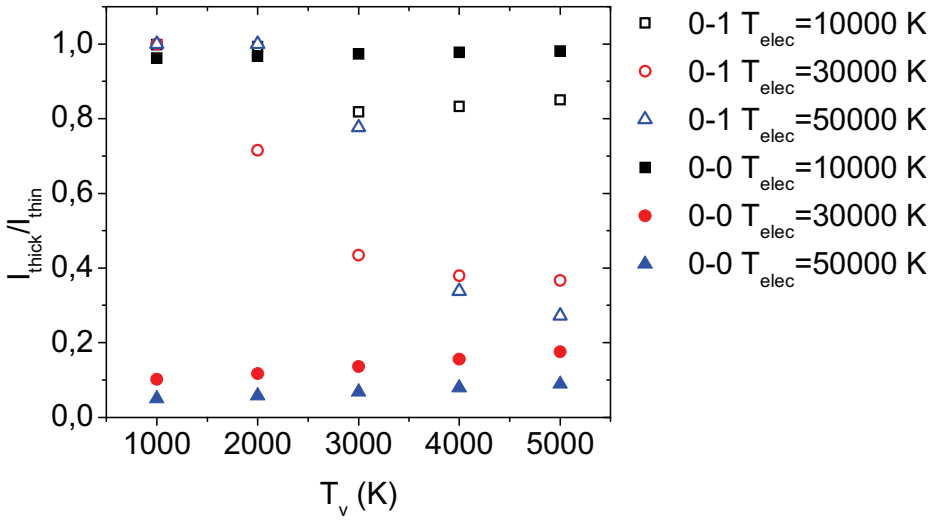

Figure D.3: Ratio of optically thick to optically thin band-head emission intensities of modeled N_2 (C-B) (0,1) and (0,0) spectra as a function of T_v for several T_{elec}, calculated using SPECAIR. T_r=T_g=2700 K. The absorption length is l_a=1 mm.

D.4. References

[1] C.O. Laux, Ph.D. Thesis, Stanford University, 1993

[2] W.G. Vincenti and C.H. Kruger 1986 *Introduction to Physical Gas Dynamics* (New York: Wiley).

[3] K.H. Becker, U. Kogelschatz, K.H. Schoenbach, and R.J. Barker 2004 *Non-Equilibrium Air Plasmas at Atmospheric Pressure* (Briston: IOP Publishing).

[4] M. Capitelli, C.M. Ferreira, B.F. Gordiets, and A.I. Osipov 2000 *Plasma Kinetics in Atmospheric Gases* (Berlin: Springer-Verlag).

[5] F. Roux and F. Michaud, *J. Molecular Spectroscopy* **158** (1993) 270-277.